Fall 2016

An improved measurement of the Muon Neutrino charged current Quasi-Elastic cross-section on Hydrocarbon at Minerva

Dun Zhang
College of William and Mary - Arts & Sciences, dzhang@email.wm.edu

An Improved Measurement of the Muon Neutrino Charged Current Quasi-Elastic Cross-Section on Hydrocarbon at MINERνA

Dun Zhang

Lianyungang, Jiangsu, China

Master of Science, College of William & Mary, 2009
Bachelor of Science, University of Science and Technology of China, 2007

A Dissertation presented to the Graduate Faculty
of The College of William & Mary in Candidacy for the Degree of
Doctor of Philosophy

Department of Physics

College of William & Mary
May 2017

APPROVAL PAGE

This Dissertation is submitted in partial fulfillment of
the requirements for the degree of

Doctor of Philosophy

Dun Zhang

Dun Zhang

Approved by the Committee, November, 2016

Committee Chair
Associate Professor Michael A. Kordosky, Physics
The College of William and Mary

Professor Jeffrey K. Nelson, Physics
The College of William and Mary

Professor Keith A. Griffioen, Physics
The College of William and Mary

Professor Todd D. Averett, Physics
The College of William and Mary

Associate Scientist Laura J. Fields
Fermi National Accelerator Laboratory

ABSTRACT

Long baseline neutrino oscillation experiments measure the flavor and energy of neutrinos to determine the neutrino mass spectrum and mixing parameters (the PMNS matrix). The flavor of a neutrino is determined by identifying the lepton in the final state of a charged current (CC) interaction. The energy is most generally determined by summing the energy of the lepton and hadronic recoil system. At energies below the pion production threshold, the dominant reaction is quasi-elastic (QE) scattering — $\nu_l n \to l^- p$. This process is advantageous because the neutrino energy can be determined from knowledge of the incoming neutrino's angle, and the energy and angle of the outgoing lepton. At energies above the pion production threshold QE scattering gradually becomes less important but serves as a standard candle for oscillation experiments, at least in principle. In practice, oscillation experiments are made of heavy nuclei (C, Fe, Ar) so the QE process occurs on nucleons that are embedded in the nuclear environment. Predictions of the QE cross-section suffer from significant uncertainties due to our understanding of that nuclear environment and the way it is probed by the weak interaction.

This thesis improves knowledge of the CCQE process by presenting measurements of the differential cross-section ($d\sigma/dQ^2$) for scattering on hydrocarbon. The data comes from MINERνA, a dedicated neutrino-scattering experiment based at Fermi National Accelerator Laboratory (Fermilab). Neutrinos are provided to the experiment by the Neutrinos at the Main Injector (NuMI) neutrino beam. The data used in this thesis were taken between March 2010 and April 2012 in the "low energy" beam configuration that has previously been used to measure the CCQE cross-section [1]. The measurement technique has been improved in this thesis in a few ways. First, the inelastic background to CCQE was reduced by identifying the "Michel electron" produced by the $\pi^+ \to \mu^+ \to e^+$ decay chain. Additionally an updated neutrino flux was used to extract the cross-section and estimates for some sources of systematic uncertainty have been improved. The measured cross-section is compared to several theoretical models and the effect that the signal definition ("CCQE" vs "CCQE-like") has on the measurement is also explored.

TABLE OF CONTENTS

ACKNOWLEDGMENTS

I would like to thank my advisor, Dr. Michael Kordosky, for his guidance through more than seven years of research. Without his professional great help and patience, I could not reach this far. I also want to express appreciation to those who have helped me and contributed to my research including Laura Fields, Arturo Fiorentini, and Jyotsna Osta. In particular, I must thank Minerba Betancourt, who is extremely patient and willing to help all the time.

To my family, Dad, Mom, my sister Yu, my niece Jingyuan, and my nephew Yihan, I owe them many thanks for all of their love and support. Their words make me feel warm and strong.

I present this thesis in honor of my parents.

LIST OF TABLES

LIST OF FIGURES

AN IMPROVED MEASUREMENT OF THE MUON NEUTRINO CHARGED CURRENT QUASI-ELASTIC CROSS-SECTION ON HYDROCARBON AT MINERνA

CHAPTER 1

Introduction

Neutrino physics has been the most attractive field in particle physics recently. One important discovery is neutrino oscillations, a phenomenon in which neutrinos switch between flavors as they propagate through space. The oscillation indicates that neutrinos have mass and that the flavor eigenstates are superpositions of the mass eigenstates. It also raises many questions about neutrino physics, like where the neutrino mass comes from? how mass eigenstates are mixed? and if neutrinos violate charge conjugation parity symmetry? Many experiments are currently taking data and others will be built aiming to answer these questions.

The knowledge of neutrino cross-sections at neutrino energies in the few GeV region is critical for those oscillation experiments. Unfortunately, our current knowledge is relatively poor, relaying on limited datasets (mostly from bubble chambers) and out-of-date theoretical models. This situation motivates the MINERνA experiment, which is being conducted to study neutrino interactions on various nuclei in the 1 to 50 GeV range [2]. This thesis presents an improved measurement of the differential cross-section $d\sigma/dQ^2$ for charged current muon neutrino quasi-elastic scattering from the MINERνA experiment.

A tool to tag Michel electrons is developed to improve the measurement, described in Chapter 5. This chapter describes aspects of the Standard Model, neutrino oscillation, and neutrino scattering, with emphasis on the charged current quasi-elastic scattering at few-GeV energies. It also describes a way to improve the current measurements. The remaining chapters in this dissertation are as follows:

- **Chapter 2** gives an overview of the neutrino beam and the detectors used to collect data for this analysis.
- **Chapter 3** summarizes the detector's calibration and event reconstruction in MINERνA.
- **Chapter 4** describes the methods to simulate events in MINERνA.
- **Chapter 5** details the Michel electrons tagging procedure and its performance.
- **Chapter 6** explains the methods for selecting the ν_μ charged-current quasi-elastic like candidates and the step-by-step calculation of the cross-section, as well as the illustration of systematic uncertainties.
- **Chapter 7** concludes and discusses the results.

1.1 The Standard Model

The Standard Model of particle physics is a theoretical framework that describes all the known fundamental particles and their interactions via three of four forces: the electromagnetic, weak, and strong forces. Gravity, the fourth force, is not included in the Standard Model.

1.1.1 Fundamental Particles

The fundamental particles consist of mediator particles (gauge bosons) and matter particles (fermions). Fermions have half-integer spin while bosons have integer spin, 0 or 1. Fermions obey Fermi statistics while bosons obey Bose-Einstein statistics. One consequence of Fermi statistics is the Pauli exclusion principle, which forbids two identical fermions from having the same quantum numbers and occupying the same state. There are two types of fermions: quarks and leptons. Quarks have six species —up (u), down (d), strange (s), charm (c), bottom (b), and top (t). These six species are divided into three pairs called generations: ud, cs, and tb. There are three charged leptons —electron (e), muon (μ), and tau(τ), and three corresponding neutrinos —electron neutrino (ν_e), muon neutrino (ν_μ), and tau neutrino (ν_τ). Tab. 1.1 summarizes the properties of fermions.

TABLE 1.1: A list of the three generations of fundamental fermions and their properties. Only limits exist on the masses of neutrinos [3].

Type of Particle	Spin	Charge	Mass
Quarks			
u	$\frac{1}{2}$	$\frac{2}{3}$	2.3 MeV/c^2
d	$\frac{1}{2}$	$-\frac{1}{3}$	4.8 MeV/c^2
c	$\frac{1}{2}$	$\frac{2}{3}$	1.275 GeV/c^2
s	$\frac{1}{2}$	$-\frac{1}{3}$	95 MeV/c^2
t	$\frac{1}{2}$	$\frac{2}{3}$	173.5 GeV/c^2
b	$\frac{1}{2}$	$-\frac{1}{3}$	4.65 GeV/c^2
Leptons			
e	$\frac{1}{2}$	-1	0.5486 MeV/c^2
ν_e	$\frac{1}{2}$	0	$\sum_{\alpha=e,\mu,\tau} m_{\nu_\alpha}$<0.3 − 1.5 eV/c^2
μ	$\frac{1}{2}$	-1	105.7 MeV/c^2
ν_μ	$\frac{1}{2}$	0	$\sum_{\alpha=e,\mu,\tau} m_{\nu_\alpha}$<0.3 − 1.5 eV/c^2
τ	$\frac{1}{2}$	-1	1.777 GeV/c^2
ν_τ	$\frac{1}{2}$	0	$\sum_{\alpha=e,\mu,\tau} m_{\nu_\alpha}$<0.3 − 1.5 eV/c^2

There are two varieties of bosons: one type acts as the mediator of the three fundamental forces; the other one is the Higgs boson (H). The Higgs boson has spin 0 and is responsible for the masses of the charged leptons, the quarks, and maybe the neutrinos. It is also responsible for the masses of the $W^{\pm}$ and Z. The mediator bosons have spin 1 and consist of the W and Z bosons mediating the weak force, the photon γ mediating the electromagnetic force, and the gluon g mediating the strong force. Tab. 1.2 summarizes the properties of bosons.

TABLE 1.2: A list of the fundamental bosons in the Standard Model [3].

Boson	Spin	Charge	Mass(GeV/c^2)	Force or Effect
photon	1	0	0	Electromagnetic force
$W^{\pm}$	1	± 1	80.385	Charged current weak interactions
Z	1	0	91.188	Neutral current weak interactions
gluons	1	0	0	Strong interactions
Higgs	0	0	125	Provides mass to particles

1.1.2 Fundamental Interactions

The Standard Model describes three of four fundamental forces, the electromagnetic, weak, and strong forces. Each force is mediated by gauge bosons, listed in Tab. 1.2. Each force can only affect particular particles with the quantum number conserved in the interaction.

The electromagnetic force is mediated by the massless photon. Because of the masslessness of the photon, the electromagnetic force has an infinite range. The quantum number required in the electromagnetic interaction is electric charge, which is carried by leptons, quarks, and W bosons. The strong force is mediated by massless, self-coupling gluons. Analogous to electric charge, the quantum number required in strong interactions is color charge, which is carried by quarks and gluons.

The weak force is mediated by massive gauge bosons, the $W^{\pm}$ and Z. The quantum

number required in the weak interaction is weak isospin, which is carried by W bosons and left-handed fermions. Interactions mediated by $W^{\pm}$ (Z) are referred to as charged (neutral) current. The weak force is short-ranged due to the Heisenberg Uncertainty Principle, $\Delta E \Delta t \geq \frac{\hbar}{2}$. When a massive virtual weak boson is exchanged in a low energy reaction, the principle limits the interaction time, and consequently limits the interaction distance to a very short range.

A quark can be switched for another quark in the same or another generation in the charged current interaction. The quark states that couple to the weak interaction Hamiltonian (d', s', and b') are different than the quark mass states (d, s, and b). The quark mass states are eigenstates of the free quark Hamiltonian. The relationship between weak eigenstates and free mass eigenstates are given by the Cabibbo-Kobayashi-Maskawa (CKM) matrix

$$\begin{pmatrix} d' \\ s' \\ b' \end{pmatrix} = \begin{pmatrix} V_{ud} & V_{us} & V_{ub} \\ V_{cd} & U_{cs} & V_{cb} \\ V_{td} & U_{ts} & V_{tb} \end{pmatrix} \begin{pmatrix} d \\ s \\ b \end{pmatrix}.$$

The weak force breaks the combined symmetry of charge conjugation and parity, CP symmetry. Charge-parity symmetry describes that the physics would not change if a particle is converted to the antiparticle with opposite spin. CP violation is governed by an independent parameter (δ_{13}) in the CKM matrix. Currently the best known values for the CP violating phase in quarks is 1.20 ± 0.08 rad [4].

1.2 Neutrino Oscillations

Neutrino oscillations, a quantum mechanical phenomenon that is not included in the Standard Model, was directly detected more than a decade ago [5]. Neutrino oscillation implies that neutrinos have mass with mass eigenstates, ν_1, ν_2, and ν_3. Neutrinos propagate

through space in mass eigenstates that are time dependent. Neutrinos also have flavor eigenstates, ν_e, ν_μ, and ν_τ. The flavor eigenstates can be inferred for neutrinos produced from weak interactions. In other words, a neutrino produced from a weak interaction has a definite flavor eigenstate. Take π^+ decay for example. Fig. 1.1 shows the Feynman diagram of this process, where a muon neutrino is produced. If neutrino oscillation does not exist, after traveling a certain distance, the flavor eigenstate and mass eigenstate of a neutrino would be identical (i.e. the flavor of this muon neutrino would stay unchanged). Actually, observation of electron/tau neutrinos from muon neutrinos traveling a certain distance proves neutrino oscillations.

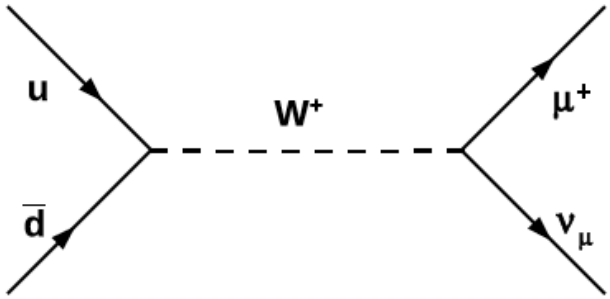

FIG. 1.1: The Feynman diagram for pion decay.

The flavor eigenstates are the superpositions of mass eigenstates. They are related by the Pontecorvo-Maki-Nakagawa-Sakata (PMNS) matrix, which is a 3×3 unitary matrix, given as

$$\begin{pmatrix} \nu_e \\ \nu_\mu \\ \nu_\tau \end{pmatrix} = \begin{pmatrix} U_{e1} & U_{e2} & U_{e3} \\ U_{\mu 1} & U_{\mu 2} & U_{\mu 3} \\ U_{\tau 1} & U_{\tau 2} & U_{\tau 3} \end{pmatrix} \begin{pmatrix} \nu_1 \\ \nu_2 \\ \nu_3 \end{pmatrix},$$

or expressed as three mixing angles θ_{ij} and a phase δ,

$$\begin{pmatrix} c_{12}c_{13} & s_{12}c_{13} & s_{13}e^{-i\delta} \\ -s_{12}c_{23} - c_{12}s_{23}s_{13}e^{i\delta} & c_{12}c_{23} - s_{12}s_{23}s_{13}e^{i\delta} & s_{23}c_{13} \\ s_{12}s_{23} - c13c_{23}s_{13}e^{i\delta} & -c_{12}s_{23} - s_{12}c_{23}s_{13}e^{i\delta} & c_{23}c_{13} \end{pmatrix},$$

where δ is the CP violating phase, $s_{ij} = \sin\theta_{ij}$, $c_{ij} = \cos\theta_{ij}$ and $\theta_{ij} = \theta_{12},\ \theta_{23},\ or\ \theta_{13}$. These are the neutrino mixing angles that determine the combination of mass eigenstates that form a neutrino flavor eigenstate.

The time evolution of a mass eigenstate is given by the Schrödinger equation,

$$|\nu_i(t)\rangle = e^{-iE_i t}\,|\nu_i(0)\rangle\,, \tag{1.1}$$

where E_i is the total energy of the neutrino and i = 1, 2, or 3.

The probability of oscillation of one type of neutrino to another, assuming oscillation between only two flavors, is given by

$$P(\nu_\alpha \to \nu_\beta) = \sin^2(2\theta)\sin^2\left(\frac{1.267\Delta m^2_{ij}(eV^2)L(km)}{E(GeV)}\right), \tag{1.2}$$

where ν_α and ν_β are neutrino flavor eigenstates, θ is the relevant mixing angle that characterizes the two neutrino oscillation model, L is the distance of propagation in units of kilometers, E is the energy of the neutrino in units of GeV, and Δm^2_{ij} is the difference of the square of the two neutrino mass eigenstates, $m_i^2 - m_j^2$, in the model.

Eq. 1.2 shows that oscillations depend on several factors: the ratio $\frac{L}{E}$ between the propagating distance and the neutrino's energy, mass splitting Δm^2_{ij}, and mixing angles θ_{ij}. Tab. 1.3 lists the values of $\sin^2 2\theta_{ij}$ as well as the values of Δm^2_{ij}. The relative values of mass splittings Δm^2_{ij} are:

$$\left|\Delta m^2_{12}\right| \ll \left|\Delta m^2_{23}\right| \approx \left|\Delta m^2_{13}\right|.$$

However, the signs of Δm^2_{23} and Δm^2_{13} are not known. More specifically, whether ν_3 is the heaviest or lightest mass eigenstate is not known. The scenario where ν_3 is the heaviest (lightest) mass eigenstate is referred to as an normal (inverted) neutrino mass ordering [3],

TABLE 1.3: The current best measurements of different parameters in neutrino oscillation [6].

Parameter	Value
$\sin^2 2\theta_{12}$	$0.857^{+0.023}_{-0.025}$
$\sin^2 2\theta_{23}$	< 0.95 (90% confidence)
$\sin^2 2\theta_{13}$	0.098 ± 0.013
Δm^2_{12}	$7.5^{+0.19}_{-0.20} \times 10^{-5}$ eV^2
$\lvert\Delta m^2_{23}\rvert$	$2.32^{+0.12}_{-0.08} \times 10^{-3}$ eV^2
$\lvert\Delta m^2_{13}\rvert$	$2.32^{+0.12}_{-0.08} \times 10^{-3}$ eV^2
δ	Unkonwn

shown in Fig. 1.2.

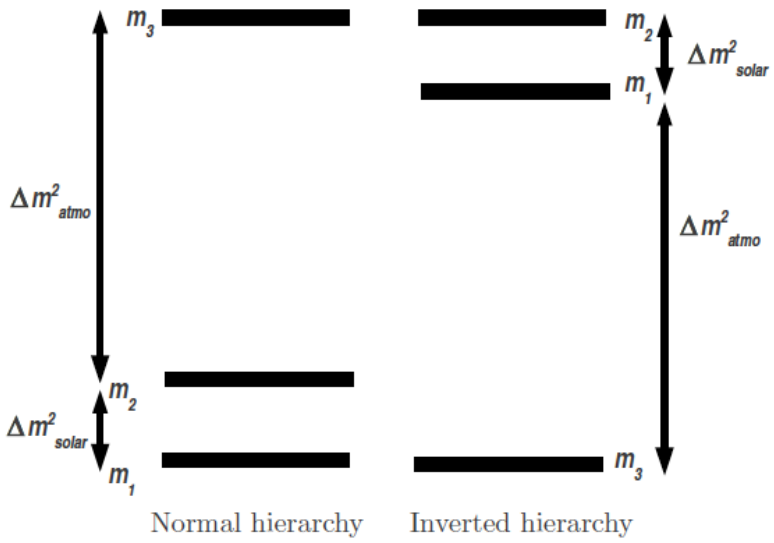

FIG. 1.2: Normal and inverted mass hierarchy in neutrino oscillations. Reprinted from [7].

To measure the mass hierarchy and search for CP violation, the best candidates are accelerator based oscillation experiments, such as the Tokai to Kamioka (T2K) experiment [8], the NuMI Off-Axis ν_e Appearance (NOvA) experiment [9], and Super Kamiokande (Super-K) using atmospheric neutrinos [10]. Such experiments focus on neutrinos with energies in the few GeV region. Uncertainties on cross-sections of neutrinos in this region

are significant and sometimes contradictory. Thus the MINERνA experiment was built to improve the knowledge of cross-sections of neutrinos in this region.

1.3 Neutrino Quasi-Elastic Scattering

Neutrinos participate in weak interactions only, via exchanging either a neutral Z or charged W boson, which is a neutral current or charged current interaction, respectively. This dissertation presents an analysis of a charged current cross-section. Therefore, only charged current weak interactions are discussed in this section.

The ways that neutrinos interact within nuclei or with nucleons depend on the energies of the neutrinos. Interactions are categorized into "channels" according to the contents of the hadronic system after each interaction has occurred. These channels include:

- **Quasi-elastic Scattering**: $\nu_\alpha N \rightarrow l_\alpha N'$. This Feynman diagram for this process is shown in Fig. 1.3. The neutrino scatters off the entire nucleon inside a nucleus.

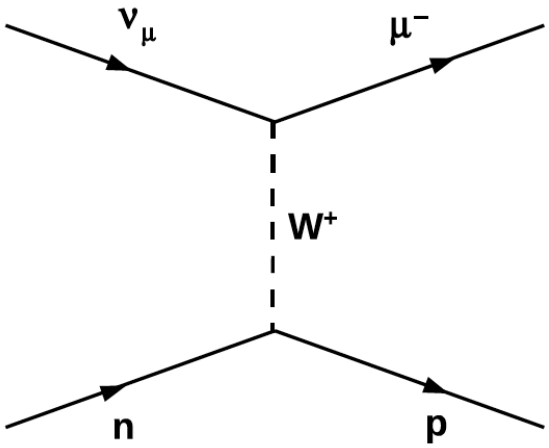

FIG. 1.3: The Feynman diagram of the charged-current quasi-elastic neutrino-nucleus scattering.

- **Single Pion Production**: The Feynman diagram is shown in Fig. 1.4. This channel includes **Nuclear Resonance Production** $\nu_\alpha N \rightarrow l_\alpha N'\pi$ and **Coherent Scattering**

$\nu_\alpha A \to l_\alpha A' \pi$. The resonance production occurs when the neutrino scatters inelastically from a nucleon. The inelastic scattering creates a baryonic excited state, Δ or N^*, and the baryon decays quickly into a nucleon and one pion via the strong interaction. Coherent scattering is the channel where the neutrino interacts with the whole nucleus and transfers a small amount of momentum. Pions are also produced through the diffractive mechanism.

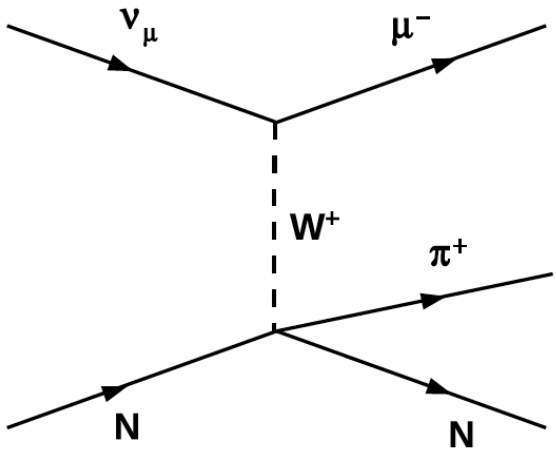

FIG. 1.4: The Feynman diagram of the single pion production.

- **Deep Inelastic Scattering**: $\nu_\alpha N \to l_\alpha N' + hadrons$. Fig. 1.5 shows the Feynman diagram for this channel. The neutrino scatters off a quark in the nucleus. Usually multiple pions are produced by the hadronization of the ejected quark.

1.3.1 Introduction to Elastic Scattering

The description of the elastic scattering begins with the cross-section, an important quantity in particle physics. For two body elastic scattering, the differential cross-section can be calculated using the Feynman rules [11], and set $c = \hbar = 1$ as is customary:

$$d\sigma = |\mathcal{M}|^2 \frac{(2\pi)^4}{4\sqrt{p_1 \cdot p_2 - m_1 m_2}} \delta^4(p_3 + p_4 - p_1 - p_2) \frac{d^3 p_3}{(2\pi)^3 2E_3} \frac{d^3 p_4}{(2\pi)^3 2E_4}, \qquad (1.3)$$

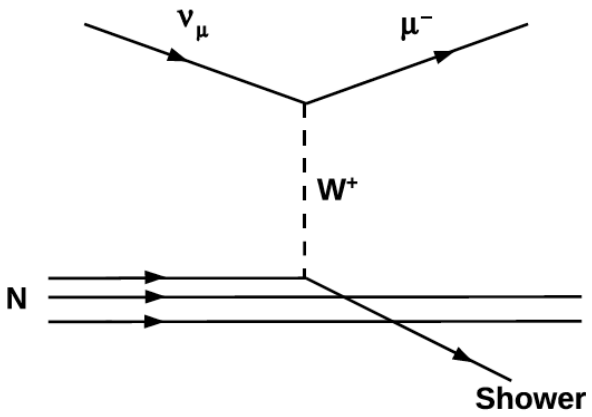

FIG. 1.5: The Feynman diagram of the charged-current deep inelastic neutrino-nucleus scattering.

where $\mathcal{M}$ is the matrix amplitude determined by the interaction's particulars, such as the types of the initial state particles involved in the interaction and the interaction channel is, and p_i (i=1,2,3,4) are kinematic momenta of incoming and outgoing particles, and E_j (j=3,4) are energies of outgoing particles. This matrix amplitude $\mathcal{M}$ can be calculated analytically for point-like particles. Take a muon neutrino quasi-elastically scatters off an electron as an example with the Feynman diagram shown in Fig. 1.6. The matrix element is

$$\mathcal{M} = \frac{g_W^2}{8}(\bar{u}(3)\gamma^\mu(1-\gamma^5)u(1))\frac{-i(g_{\mu\nu} - \frac{q_\mu q_\nu)}{M_W^2})}{q^2 - M_W^2}(\bar{u}(4)\gamma^\nu(1-\gamma^5)u(2)). \tag{1.4}$$

Assuming the momentum transferred, $q^2 \ll M_W^2$, the matrix amplitude can be calculated to be

$$\begin{aligned} <|\mathcal{M}|^2> = \frac{1}{2}\sum_{spins}|\mathcal{M}|^2 = \left(\frac{g_W^2}{8M_W^2}\right)^2 & Tr[\gamma^\mu(1-\gamma^5)(\not{p_1} + m_e)\gamma^\nu(1-\gamma^5)\not{p_3}] \\ & \times Tr[\gamma_\mu(1-\gamma^5)(\not{p_2} + m_e)\gamma_\nu(1-\gamma^5)\not{p_4}], \end{aligned} \tag{1.5}$$

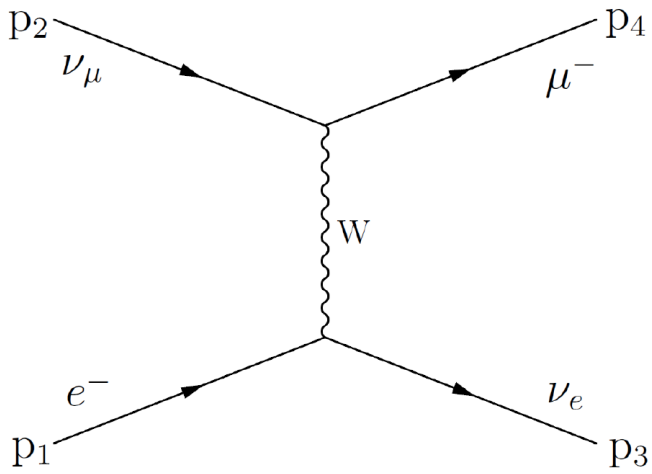

FIG. 1.6: The Feynman diagram of $\nu_\mu e^- \to \nu_e \mu^-$. The four momenta are indicated in the plot.

where the amplitude is averaged over initial spins and summed over final spins. Using trace theorems, Eq. 1.5 can be reduced to

$$< |\mathcal{M}|^2 > = 2 \left(\frac{g_W}{M_W} \right)^4 (p_1 \cdot p_2)(p_3 \cdot p_4) \tag{1.6}$$

Considering relativistic energies where $\frac{m_e}{E_\nu}$ is small, the differential cross-section can be inferred from Eq. 1.3 and Eq. 1.6. In the center of mass frame, the form is

$$\frac{d\sigma}{d\Omega} = \frac{1}{2} \left(\frac{g_W^2 E_\nu^*}{4\pi M_W^2} \right) \left(1 - \left(\frac{m_\mu}{2E_\nu^*} \right)^2 \right)^2, \tag{1.7}$$

where the electron's mass and momentum are neglected, and $E_\nu^* = \frac{E_\nu}{2}$.

1.3.2 Neutrino Charged Current Quasi-Elastic Scattering

In this section, parameters in the differential cross-section of neutrino charged current quasi-elastic scattering on free nucleons are described. Distributions of these parameters are shown, calculated using $m_A = 1.0$ GeV. The cross-section is given in Eq. 1.8, in the

form introduced by C.H. Llewellyn Smith [12],

$$\frac{d\sigma}{dQ^2} = \frac{M^2 G_F^2 \cos^2\theta_c}{8\pi E_\nu^2}\left(A(Q^2) \mp B(Q^2)\frac{(s-u)}{M^2} + \frac{C(Q^2)(s-u)^2}{M^4}\right). \tag{1.8}$$

Here Q^2 is the square of the momentum transferred from the incident (anti-)neutrino to the free nucleon, G_F is the weak coupling constant, M is the mass of the free nucleon, E_ν is the energy of the incident (anti-)neutrino, θ_c is the Cabibbo angle, s and u are two Mandelstam variables, $s - u = 4ME_\nu - Q^2 - m_l^2$, the $\mp$ term is negative for neutrinos and positive for anti-neutrinos. The terms $A(Q^2)$, $B(Q^2)$, and $C(Q^2)$ (Fig.1.8) are given by Eq. 1.9, 1.10, and 1.11,

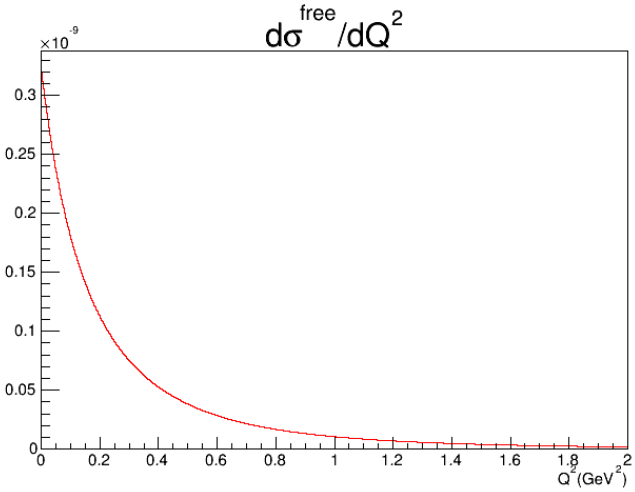

FIG. 1.7: The distribution of the differential cross-section as a function of Q^2 for a free neucleon.

$$\begin{aligned} A(Q^2) = \frac{(m_l^2+Q^2)}{M^2}[(1+\tau)\left|F_A\right|^2 - (1-\tau)\left|F_V^1\right|^2 + \tau(1-\tau)\left|F_V^2\right|^2 \\ + 4\tau F_V^1 F_V^2 - \frac{m_l^2}{4M^2}(\left|F_V^1 + F_V^2\right|^2 + \left|F_A + 2F_P\right|^2 - 4(1+\tau)\left|F_P\right|^2), \end{aligned} \tag{1.9}$$

$$B(Q^2) = \frac{Q^2}{M^2}F_A(F_V^1 + F_V^2), \tag{1.10}$$

$$C(Q^2) = \frac{1}{4}(|F_A|^2 + \left|F_V^1\right|^2 + \tau \left|F_V^2\right|^2), \tag{1.11}$$

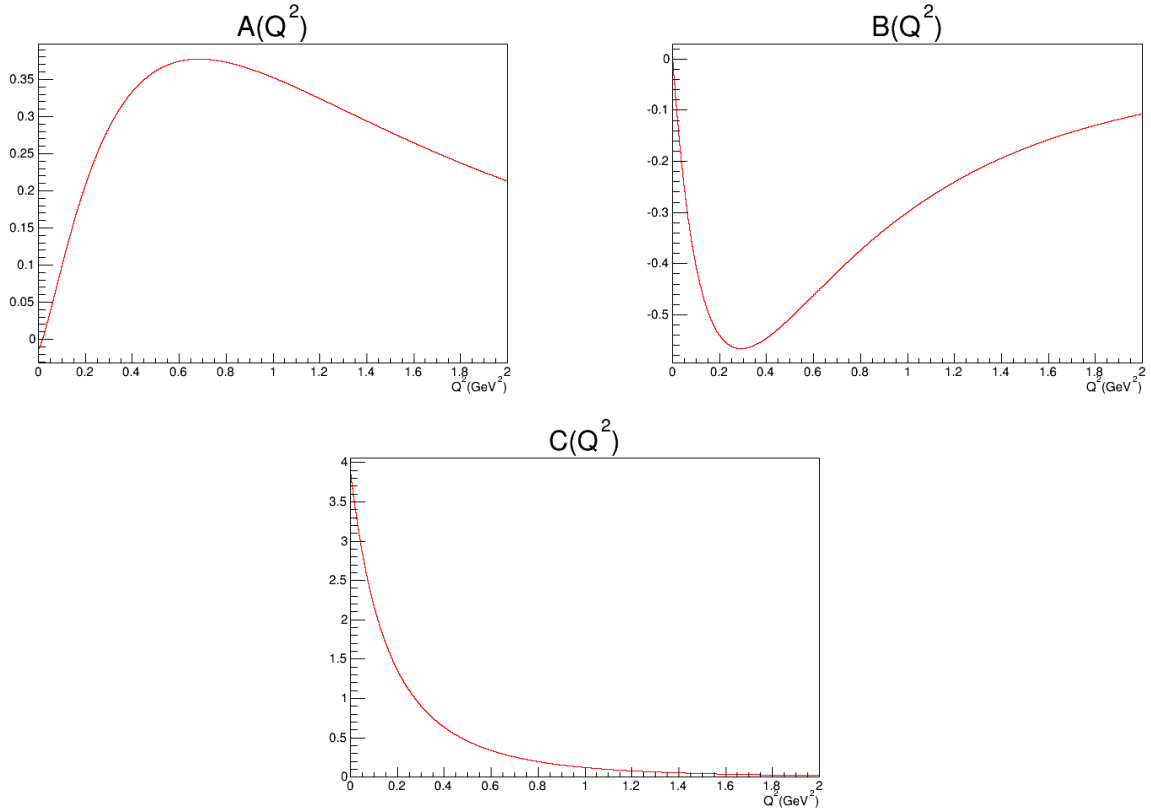

FIG. 1.8: The distribution of $A(Q^2)$ (top left), $B(Q^2)$ (top right), and $C(Q^2)$ (bottom).

where F_V^1 and F_V^2 are vector form factors, F_P is the psuedo-scalar form factor, F_A is the axial vector form factor, and $\tau = \frac{Q^2}{4M^2}$.

Vector Form Factors

The vector form factors, F_V^1 and F_V^2 (Fig.1.9), are related to the nucleon electromagnetic form factors by the conserved vector current (CVC) hypothesis. This hypothesis assumes that the vector components in neutrino nucleus scattering and charged lepton

nucleon scattering are the same. The vector form factors can be written in the forms of

$$F_V^1(Q^2) = \frac{G_E^V(Q^2) + \tau G_M^V(Q^2)}{1+\tau}, \tag{1.12}$$

and

$$F_V^2(Q^2) = \frac{G_M^V(Q^2) - G_E^V(Q^2)}{1+\tau}, \tag{1.13}$$

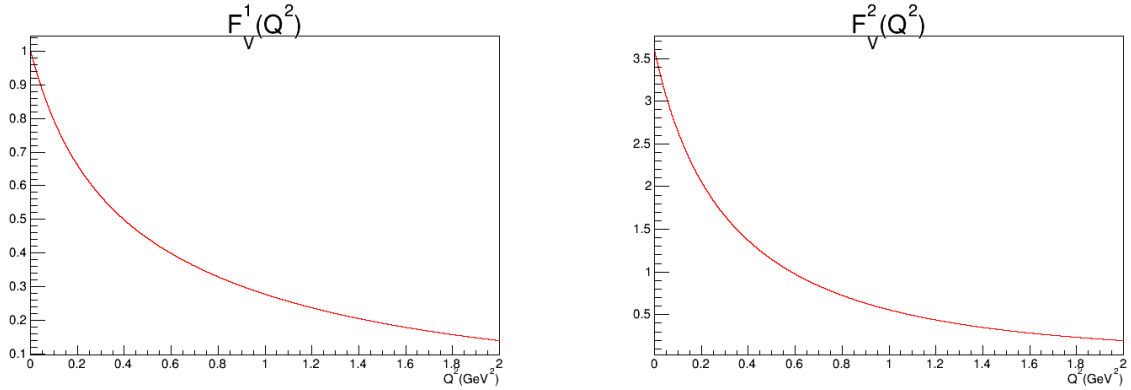

FIG. 1.9: The distribution of $F_V^1(Q^2)$ (left) and $F_V^2(Q^2)$ (right).

where M is the nucleon mass, $\tau = \frac{Q^2}{4M^2}$, and G_E^V and G_M^V (Fig.1.10) are the electromagnetic form factors given by

$$G_E^V(Q^2) = G_E^p(Q^2) - G_E^n(q^2), \tag{1.14}$$

and

$$G_M^V(Q^2) = G_M^p(Q^2) - G_M^n(Q^2). \tag{1.15}$$

In Eq. 1.14 and 1.15, $G_E^p(Q^2)$, $G_E^n(Q^2)$, $G_M^p(Q^2)$, and $G_M^n(Q^2)$ (Fig. 1.11) are respectively the electric and magnetic Sach's form factors of nucleons (proton and neutron). The values of those factors are extracted from data by fitting to the electron nucleon elastic scattering, and the version used in this analysis referred to as BBBA07 form fac-

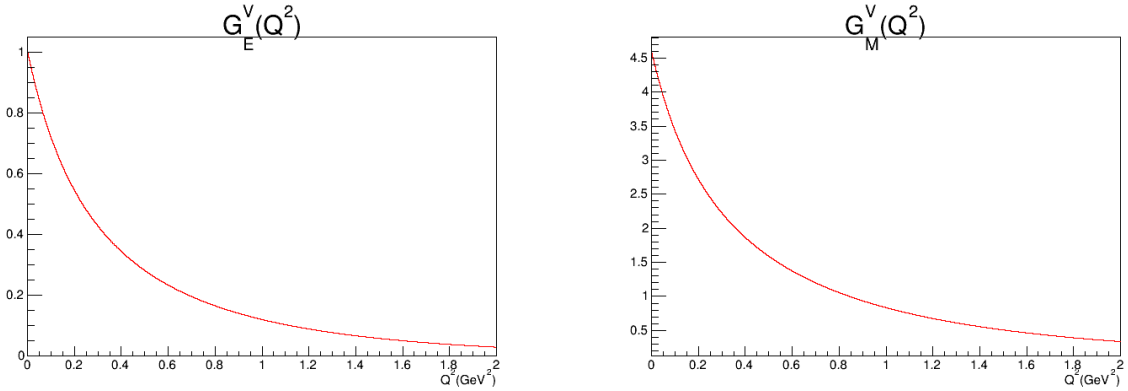

FIG. 1.10: The distribution of $G_E^V(Q^2)$ (left) and $G_M^V(Q^2)$ (right).

tors [13]. The Galster parametrization [14] is utilized in generating the sequential plots in this section, in the forms of

$$G_E^p(Q^2) = G_D(Q^2),$$

$$G_M^p(Q^2) = \mu_p G_D(Q^2),$$

$$G_M^n(Q^2) = \mu_n G_D(Q^2),$$

$$G_E^n(Q^2) = -\mu_n \frac{0.942\tau}{1+4.61\tau} G_D(Q^2),$$

where the magnetic momenta of proton and neutron are $\mu_p = 2.793$ and $\mu_n = -1.793$, and the dipole form factor $G_D(Q^2)$ is given by

$$G_D(Q^2) = \frac{1}{\left(1+\frac{Q^2}{M_\nu^2}\right)^2},$$

with the vector mass parameter $M_V^2 = 0.71$ GeV^2.

In the low Q^2 regime, up to 2.0 GeV, G_E and G_M can be thought of as Fourier transforms of the charge and magnetization current densities inside the proton and nucleon,

and the dipole form describes the Q^2-dependence of the electric and magnetic form factors of nucleons very well [15]. Originally, the dipole form was introduced empirically. When trying to incorporate the non-zero size of the proton into the form factors, the lowest-order attempt yields the dipole approximation [13].

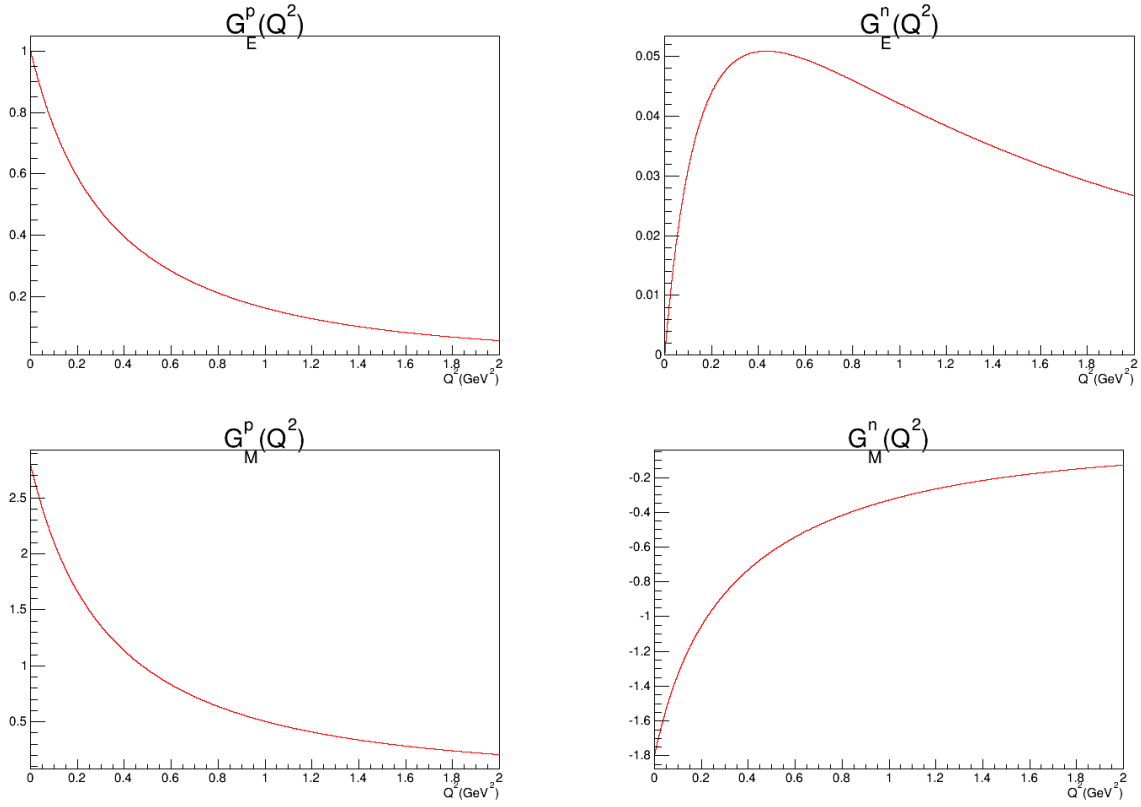

FIG. 1.11: The distribution of $G_E^p(Q^2)$ (top left), $G_E^n(Q^2)$ (top right), $G_M^p(Q^2)$ (bottom left), and $G_M^n(Q^2)$ (bottom right).

Pseudo-Scalar Form Factor

The pseudo-scalar form factor F_P (Fig.1.12) is related to the axial form factor $F_A(Q^2)$ by the partially conserved axial current (PCAC) hypothesis. The PCAC hypothesis predicts that the non-conserved weak axial current is nearly conserved in nuclear interactions [11]. Using the Goldberger-Treiman relation [16], the relation predicted by the PCAC

hypothesis is given by

$$F_P = \frac{2M^2}{Q^2 + m_\pi^2} F_A(Q^2), \tag{1.16}$$

where m_π is the charged pion mass, M is the mass of the nucleon, and $F_A(Q^2)$ is the axial form factor. Notice that, in the cross-section formula Eq. 1.9, the pseudo-scalar form factor is multiplied by the ratio between the masses of lepton and nucleon. Therefore, the pseudo-scalar form factor contributes little to the cross-section for the electron nucleon elastic scattering and neutrino nucleon quasi-elastic scattering.

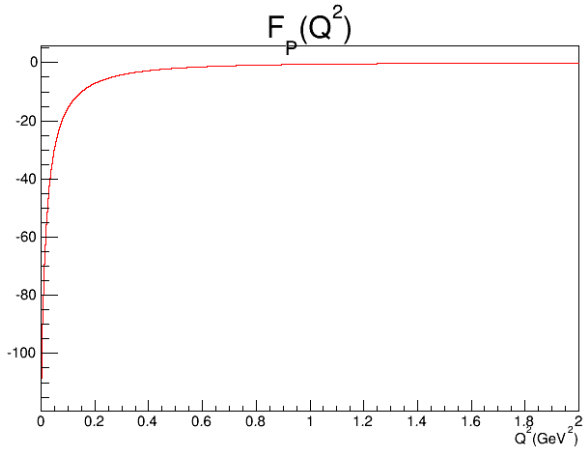

FIG. 1.12: The distribution of $F_P(Q^2)$.

Axial Form Factor

Using the dipole parameterization, the axial form factor (Fig.1.13) is given by

$$F_A(Q^2) = \frac{g_A}{\left(1 + \frac{Q^2}{M_A^2}\right)^2}, \tag{1.17}$$

where a single free parameter M_A is referred as the axial mass and g_A is the axial coupling constant with a value of 1.257±0.003, which is found in beta decay experiments [3].

Neutrino and anti-neutrino quasi-elastic experiments are utilized to measure the axial

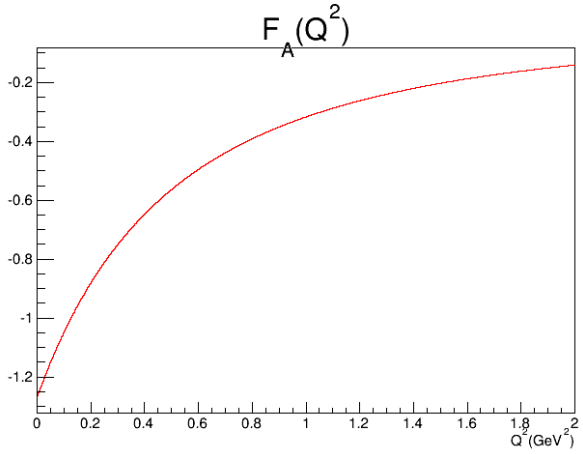

FIG. 1.13: The distribution of $F_A(Q^2)$.

mass precisely. Various experiments were built to extract the value of the axial mass. Fig. 1.14 shows the measured values of the axial mass with the world average value: $M_A = 1.026 \pm 0.021$ GeV.

1.4 Nuclear Effects

Nuclear effects play important roles in extracting the differential cross-sections. Eq. 1.8 calculates the differential cross-section for a free nucleon. For other materials with multiple nucleons combined in a nucleus, the calculation of the cross-section is affected by several nuclear effects, such as final state interactions, Pauli blocking, and meson exchange currents.

Final State Interactions

In neutrino scattering, the term "final state interactions" (FSI) refers to the possible hadronic interactions between hadrons and the nucleus in which they were produced. The possibility of FSIs is very high in neutrino physics because that the hadronic cross-sections are large and heavy nuclei are commonly used as targets in neutrino experiments. FSIs change the hadronic system produced in neutrino interactions, i.e. directions and

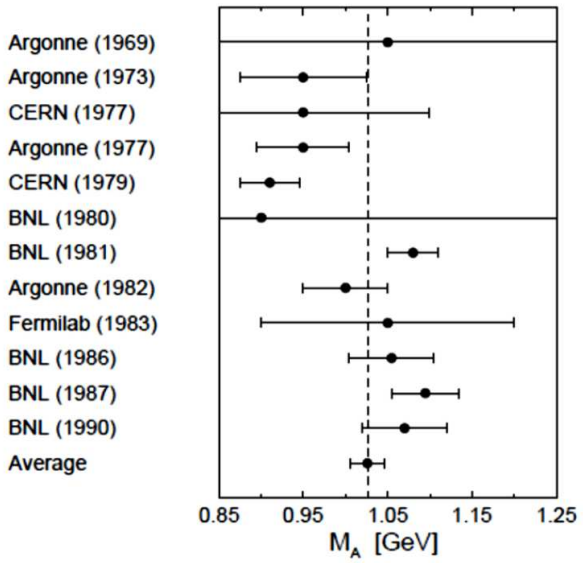

FIG. 1.14: Values of the axial mass extracted from various (anti)neutrino quasi elastic scattering experiments. These experiments include (anti)neutrino scattering off protons, deuterons, and other nuclei (Al, Fe). Reprinted from [17].

momentums of the outgoing particles, and they may change the number of hadrons in the final state. In general, there are four types of FSIs: **elastic scattering**, where hadrons scatter off a nucleus which remains in its ground state; **inelastic scattering**, where hadrons excite the nucleus or eject nucleons from the nucleus; **absorption**, where hadrons are absorbed; and, finally, **charge exchange**, where hadrons change charge, such as a final state π^+ becoming a π^0 by scattering off a proton.

Relativistic Fermi Gas Model

The Relativistic Fermi Gas (RFG) model is often used to model the nucleus [18]. This model posits that the nucleons (protons and neutrons) within a nucleus obey Fermi statistics, do not interact, and are confined in a potential well. The potential well is due to the forces from all nucleons. In the ground state, all nucleons occupy the lowest possible energy levels. The maximum energy of a nucleon in the ground state is referred to as the Fermi energy. The RFG model can explain many effects including Pauli blocking and binding energy suppression. In the case of Pauli blocking, the cross-section is significantly

suppressed at low Q^2 due to the Pauli exclusion principle. An interaction at low Q^2 possibly imparts energy to a final-state nucleon and pushes it into an already occupied state, which is forbidden by the Pauli exclusion principle. Binding energy is the minimum energy that the hadronic system requires in order to eject a nucleon from the nucleus. This minimum energy requirement suppresses particular processes and changes the cross-section. The RFG model in our simulation utilizes a step function. If a final state nucleon's momentum is below the Fermi momentum, the step function is zero and the consequently the cross-section is zero.

The limitation of the RFG model is that this model assumes the non-interacting nucleons, which is not realistic. Short range correlations can lead to nucleons having a momentum above the Fermi momentum. This model was extended to partially take Nucleon-Nucleon correlations into account by Bodek and Richie [19] by adding high momentum tails to the nucleon momentum distribution, which is flat in RFG model.

Meson Exchange Currents

The meson exchange currents (MEC) are two-body currents that are mediated by a virtual meson that is exchanged between correlated nucleons in the nucleus. A neutron and a proton are the most frequent correlated pair. This process is a possible explanation to the size of the MiniBooNE CCQE cross-section measurement [20]. Considering some final state nucleons are below detection threshold and not necessarily observed in the detector, the final states of MEC may appear as a CCQE event. Therefore, the presence of MEC enhances the overall CCQE cross-section.

Besides MEC enhancement, the transverse enhancement model (TEM) is also introduced. It is an empirical approach using electron-nucleus quasi-elastic cross-section to enhance the CCQE cross-section for the bound nucleon [19].

Random Phase Approximation

Nucleon-nucleon correlations play roles in modeling the nucleus. The interactions

between particles lead to a screening of the interactions, where screening implies a charge redistribution. The random phase approximation (RPA) is a technique to account for the long-range interactions between nucleons and study the superpositions of particle-hole and hole-particle configurations [21]. RPA corrects the nucleon excitation energy and binding energy by taking multiple nucleons interaction into account. The cross-section that is small at low energy transfer is consistent with the long range nucleon-nucleon correlations [21], i.e. the RPA effect, shown in Fig. 1.15.

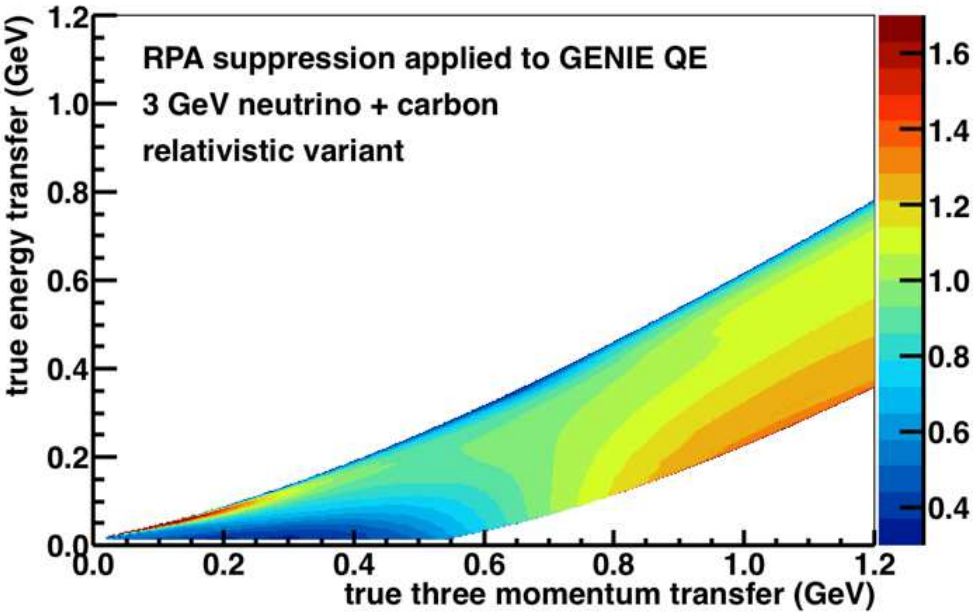

FIG. 1.15: Suppression of the QE cross-section with RPA effect and low energy transfer and enhancement at high Q^2, compared to not having RPA effect. The figure was made for 3 GeV neutrinos interacting with carbon. Reprinted from [22].

In conclusions, we still see that this CCQE-like analysis confirms simulations with the RPA model are favored when comparing to simulations without the RPA model.

1.5 Motivation to Remeasure the Cross-section

Previously, MINERνA published a measurement of the flux-averaged muon neutrino quasi-elastic differential cross-section on a hydrocarbon target at $E_\nu = 3.5$GeV, $d\sigma/dQ^2_{QE}$ [1], shown in Fig. 1.16.

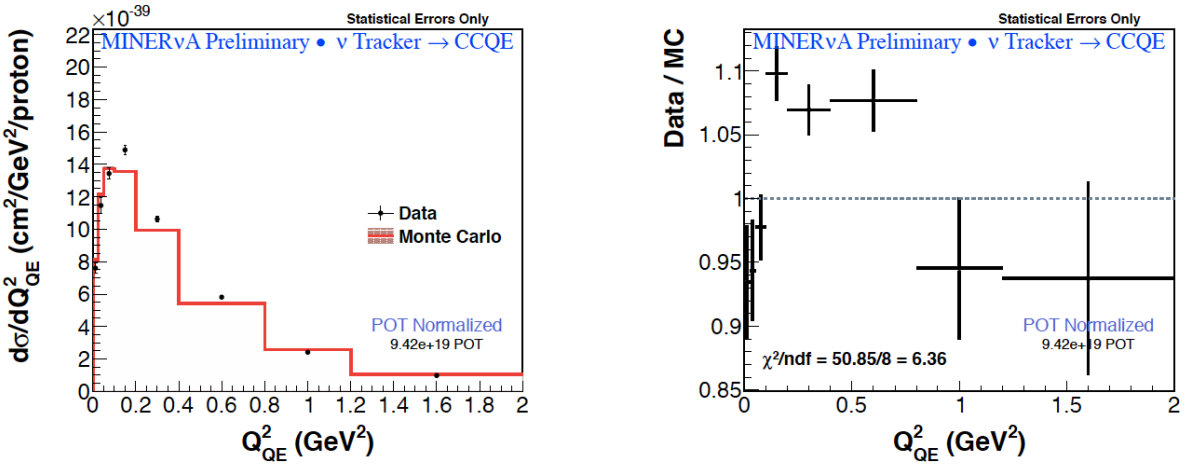

FIG. 1.16: Previous results of the differential cross-section as a function of Q^2. Reprinted from [23].

Since then, I have developed a new technique to reject the background. A newer and better version of the neutrino flux prediction is also available [24]. Many techniques for estimating the systematic errors have been updated. Event selection has changed slightly. Beside that, additional data is available for this analysis. All of these facts motivate an improved differential cross-section measurement not only on the CCQE channel but also on the CCQE-like channel, which was not measured in the previous published analysis.

CHAPTER 2

The NuMI Beamline and The MINERνA Detector

The Main INjector ExpeRiment: ν-A (MINERνA) is a neutrino-nucleus scattering experiment designed to measure low-energy neutrino interactions. It is located at Fermi National Accelerator Laboratory (Fermilab), in Batavia, IL. MINERνA runs in the NuMI beamline, observing large samples of muon neutrino and anti-neutrino interactions in the 1 to 20 GeV energy range. In this chapter, details of the NuMI beamline and the MINERνA detector are discussed.

2.1 The NuMI Beamline

The neutrino and anti-neutrino beam utilized by MINERνA comes from the NuMI beamline, which is part of the Fermilab Accelerator Complex, shown in Fig. 2.1. The 120 GeV/c proton beam is directed onto a graphite target. pC interactions make mesons and these mesons are focused by magnetic horns and decay in a long two-meter-wide pipe to produce

neutrinos. This section describes the creation of the proton beam and the design of the NuMI beamline.

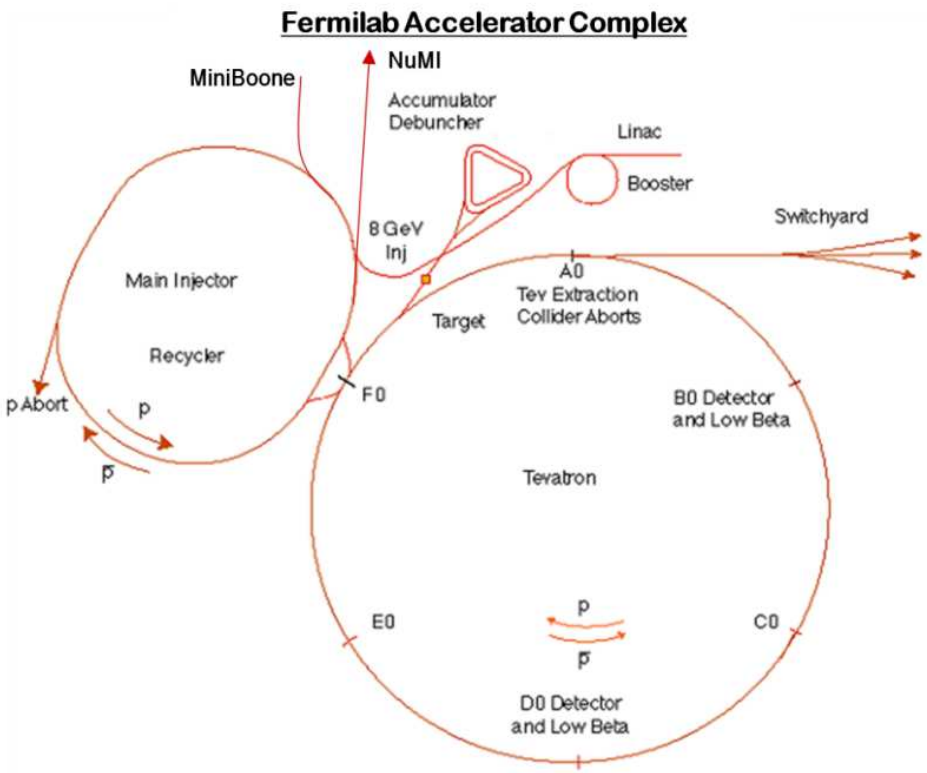

FIG. 2.1: The layout of different beam facilities at the Fermi National Accelerator Laboratory. The Linac, Booster, and Main Injector shown in this plot accelerate protons. Reprinted from [25].

2.1.1 The Proton Beam

The first step in creating the proton beam is to ionize diatomic hydrogen into H^- ions. A Cockcroft-Walton generator accelerates the H^- ions to 750 KeV. Next, the H^- ions are fed to the Linac (Linear Accelerator) that accelerates them to an momentum of 400 MeV/c. The beam passes through a carbon foil that strips away the electrons and converts the ion beam into protons, and then it travels to the Booster, a 150-meter diameter synchotron. The Booster accelerates the proton to an momentum of 8 GeV/c in about 67 ms. These

protons are then transported to the Main Injector, which accelerates the beam to an momentum of 120 GeV/c. The Main Injector separates the beam in six batches. When the Tevatron was operating, one batch was used by the Tevatron and the other five batches were delivered to the NuMI beamline. More recently the Tevatron stopped operations so all six batches were used by NuMI. The structure of the six batches in the neutrino beam is shown in Fig. 2.2.

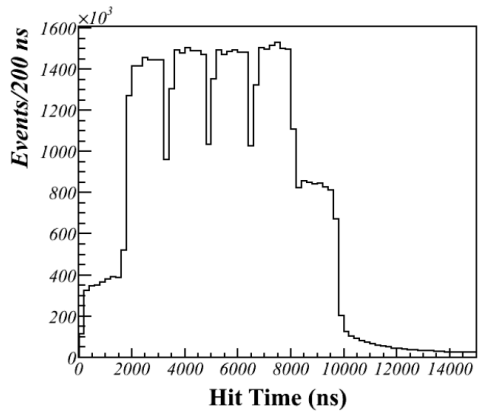

FIG. 2.2: Time distribution of hits in MINERνA, which demonstrates the batch structure for the NuMI beamline. The tail in the plot is from particle decays within the detector.

A typical five-batch beam spill contains 3.5×10^{13} protons per pulse and lasts 8.4 μs. A typical six-batch beam spill contains 4.2×10^{13} protons per pulse and lasts 10 μs. After acceleration in the Main Injector, the batches are extracted from the ring and transferred to the NuMI beamline.

2.1.2 The Neutrino Beam

The NuMI facility is diagrammed in Fig. 2.3. Protons for the NuMI beamline are extracted from the Main Injector and directed downward at an angle of 58 milliradians with respect to the Earth's surface. This angle was selected to point the beam at the MINOS far detector, located in Soudan, MN.

The Main Injector delivers protons with a momentum of 120 GeV/c to the NuMI graphite production target. The collisions between protons and carbon nuclei produce pions and kaons which are focused in magnetic horns and subsequently decay in flight within the decay pipe to produce a tertiary ν_μ or $\bar{\nu_\mu}$ beam. More details of the NuMI beamline are described below.

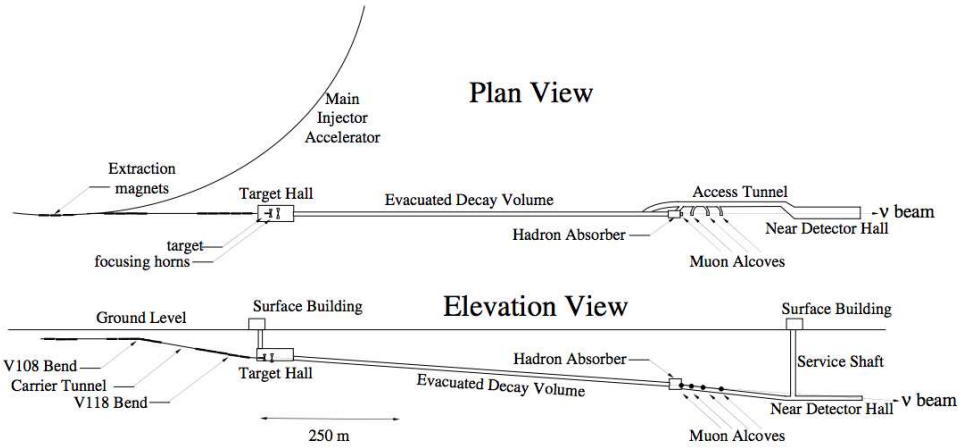

FIG. 2.3: An overhead and cut-away view of the NuMI facility. Reprinted from [26].

The Production Target

The proton beam, which is injected into the NuMI beamline from the Main Injector, first passes through a collimator baffle and is focused to a 1.1×1.1 mm^2 profile in the dataset used in this thesis [26] with a maximum divergence of 60 microradians before colliding with the NuMI target. The NuMI target (Fig. 2.4) is made of 47 pieces of 2 cm long graphite (carbon) fins with a 0.3 cm gap between each fin. These graphite fins are mounted to two stainless steel water cooling pipes that run along the beam direction. The total size of the NuMI target is 95.38 cm in length (roughly two interaction lengths), 15 mm in height and 6.4 mm in width [27]. Pions and kaons produced by pC collisions can reinteract within the target, and the reinteractions can shift the energy spectrum of pions and kaons, reducing the number of neutrinos with energy useful to MINOS. Thus, the target was built thin to minimize these reinteractions. The entire target is enclosed in

an aluminum vacuum case mounted within a helium-filled steel canister. This container is electrically isolated so that an extra 48th fin can serve as a beam monitor, the so-called "Budal monitor" [26]. The Budal monitor is used to measure the shape of the beam profile and the beam intensity by detecting delta-ray charge created by interactions in the fin. Another important feature of the NuMI target is that it can move longitudinally so that the energy spectrum of mesons can be changed by changing the target-horn spacing.

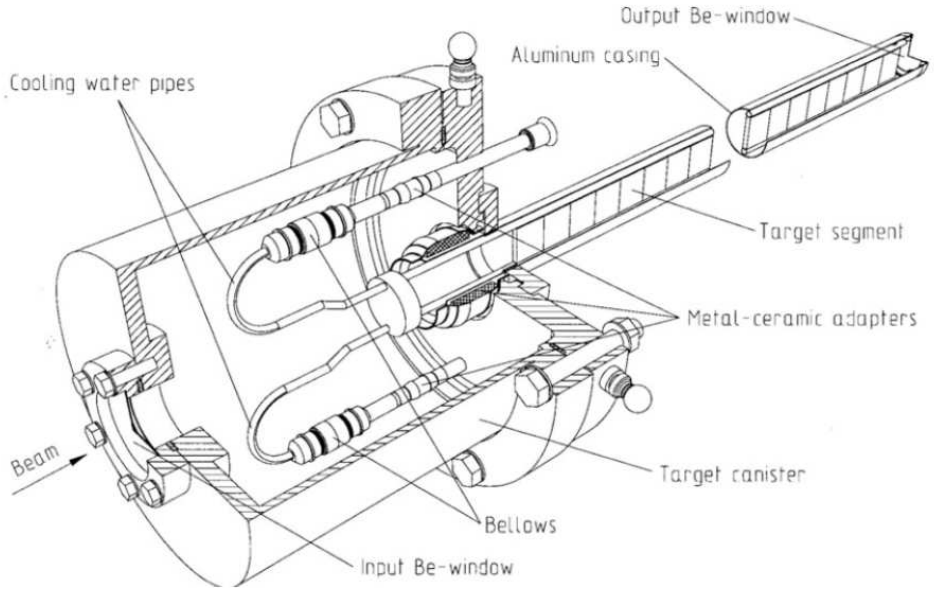

FIG. 2.4: A diagram of the NuMI target. Reprinted from [7].

The Magnetic Horns

The spray of mesons, mostly pions and kaons, and any leftover protons, resulting from the pC collisions with the production target, travels toward the NuMI horns (Fig. 2.5, 2.6). The NuMI focusing system consists of two 3 m long magnetic parabolic focusing horns placed downstream of the NuMI target. A toroidal magnetic field of 30 kG is produced inside the horn by a 200 kA current running along its inner and outer surfaces [26]. The lens's focal length is proportional to the incoming hadron momentum [28]. As mentioned above, the target can move to change the distance between the target and the horn. This

changes the beam energy by selecting the momentum range of charged particles focused by the magnetic field. Hadrons with certain momentum values and angles are refracted by the second horn. In addition, changing the sign of the current allows the choice of focusing positive or negative mesons, which in turn creates a neutrino or anti-neutrino beam. In this analysis, the target-horn system with the configuration of Forward Horn Current (FHC) mode is used. In the FHC mode, positive particles are focused and a ν_μ enhanced beam is created.

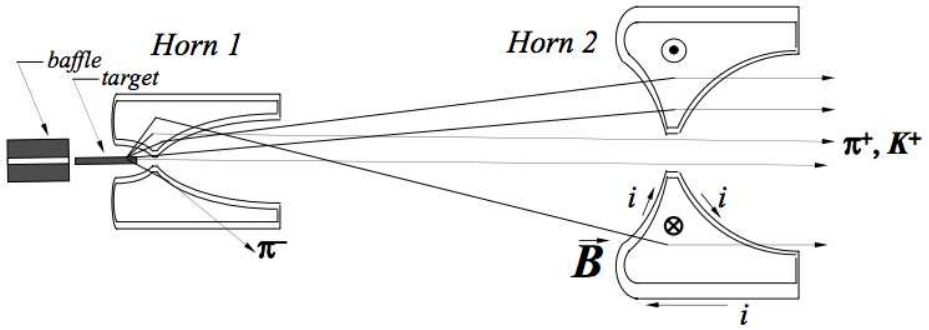

FIG. 2.5: A schematic of the two magnetized parabolic NuMI horns used to focus the pions and kaons prior to decay. Reprinted from [26].

The Decay Pipe

After passing the focusing horns, the beam, which consists mostly of pions and kaons, and any leftover protons, enters a decay pipe, 675 m in length, and 2 m in diameter. The decay pipe is filled with 13.2 PSI of helium (Fig. 2.7). The purpose of the helium is to minimize the pion absorption and pion interactions with air [26]. The length of the decay pipe corresponds to the decay length of a 10 GeV pion. The pions and kaons decay into neutrinos and muons in the modes summarized in Tab. 2.1.

The Hadron Monitor and Absorber

As shown in Fig. 2.7, the hadron monitor and absorber sit downstream of the decay pipe. The hadron monitor is a 7×7—array of ion chambers, 1×1 m^2 in size, filled with

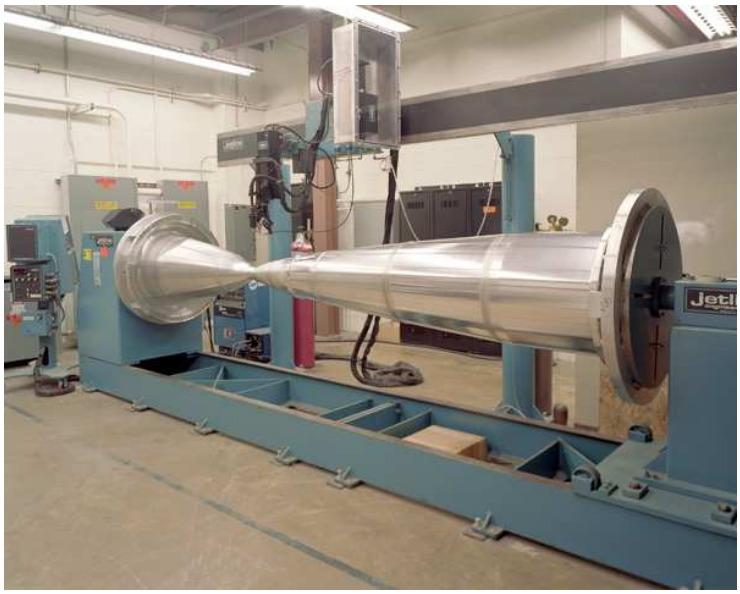

FIG. 2.6: NuMI horn 2 inner conductor on the welding machine.

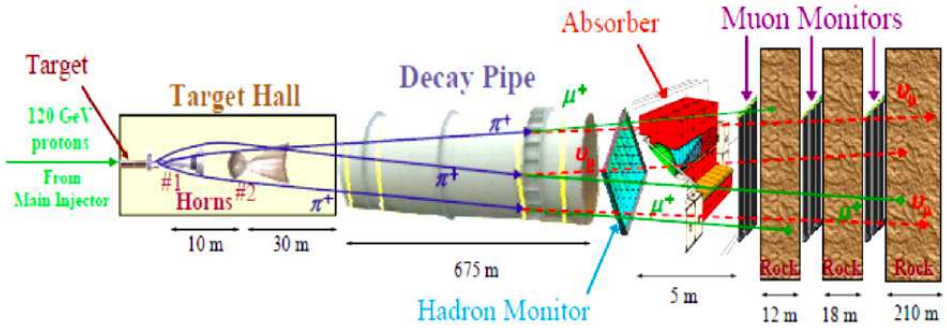

FIG. 2.7: A diagram of the NuMI beamline. Reprinted from [29].

helium gas. It is used to monitor the intensity and position of protons at the end of the decay pipe. All protons and mesons that do not decay are stopped by the hadron absorber (HA), which is composed of aluminum, steel and concrete. Considering that muons in the few-GeV energy range are minimum ionizing particles, most muons pass through the HA. Thus the beam, after traveling through the HA, is mostly muons and neutrinos.

The Muon Monitors

The muon and neutrino beam meets three muon monitors sitting downstream of the hadron absorber, as shown in Fig. 2.8. The muon monitors, each $2 \times 2\ m^2$ in size, are 9×9

TABLE 2.1: Decay modes of π^+ and K^+ resulting in neutrinos relevant in the NuMI beam [3].

Decay Mode	Fraction
$\pi^+ \to \mu^+\nu_\mu$	99.99%
$\pi^+ \to \mu^+\nu_\mu\gamma$	2.00×10^{-4}
$\pi^+ \to e^+\nu_e$	1.23×10^{-4}
$K^+ \to \mu^+\nu_\mu$	63.55%
$K^+ \to \pi^0 e^+\nu_e$	5.07%
$K^+ \to \pi^0\mu^+\nu_\mu$	3.35%

—arrays of ion chambers filled with the helium gas, similar to the hadron monitor. The three muon monitors are embedded in dolomite rock and are centered on the beam. Since muons must have higher energy to pass through increasing amounts of rock, the energy threshold for a muon increases with each successive monitor. The information about the kinematics of the parent mesons can be obtained by comparing the muon rates at each monitor. This information can be used to constrain the prediction of pion and kaon spectra and consequently the expected neutrino energy spectrum [30].

Downstream of the muon monitors there is an additional 240 m of rock between the decay pipe and the Near Detector Hall, which is sufficient to stop all muons originating from the beamline. The neutrino beam then enters the MINERνA detector.

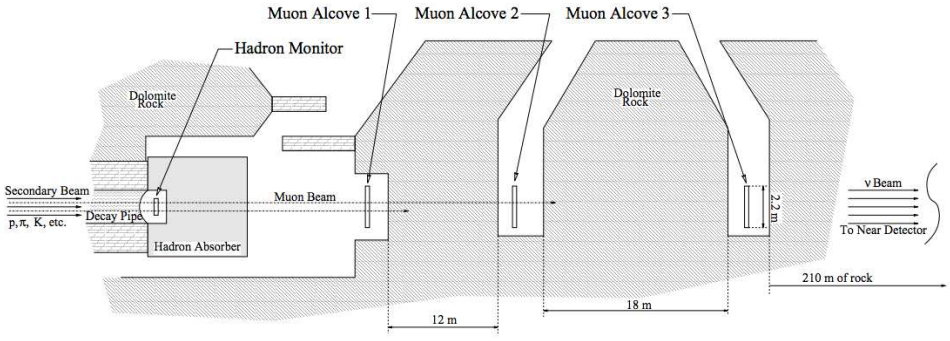

FIG. 2.8: The locations of the Hadron Monitor and three Muon Monitors in the NuMI facility. Reprinted from [26].

2.2 The MINERνA Detector

The MINERνA detector is placed 100 m underground in the NuMI beamline and 2.1 m upstream of the MINOS detector. Measuring low-energy neutrino interactions requires the MINERνA detector to resolve multi-particle final states, track low energy charged particles with energies greater than 100 MeV [31], contain electromagnetic showers and high-energy final states up to at least 10 GeV [31], and resolve multiple interactions in a single beam spill. The MINERνA detector is designed with fine-grained polystyrene scintillator strips to meet these goals.

Fig. 2.9 shows the major regions of the MINERνA detector. The core is a regular hexagonal cylinder that consists of a series of fine-grained, fully-active tracking scintillator modules, as shown in Fig. 2.11. The cylinder is 5 m long with an apothem of approximately 1.7 m. The apothem is the distance from the center to the midpoint of one side of the hexagon. The inner detector's apothem is 1.07 m and is radially enclosed by the outer detector. The outer detector consists largely of steel frames and serves as the side hadronic calorimeter. The upstream region of the detector consists of various solid (carbon, iron, and lead) and liquid (water) nuclear targets that are used to study the A-dependence of neutrino interactions. The downstream regions of the detector are electromagnetic and hadronic calorimeters used for the observation of electromagnetic and hadronic showers, respectively.

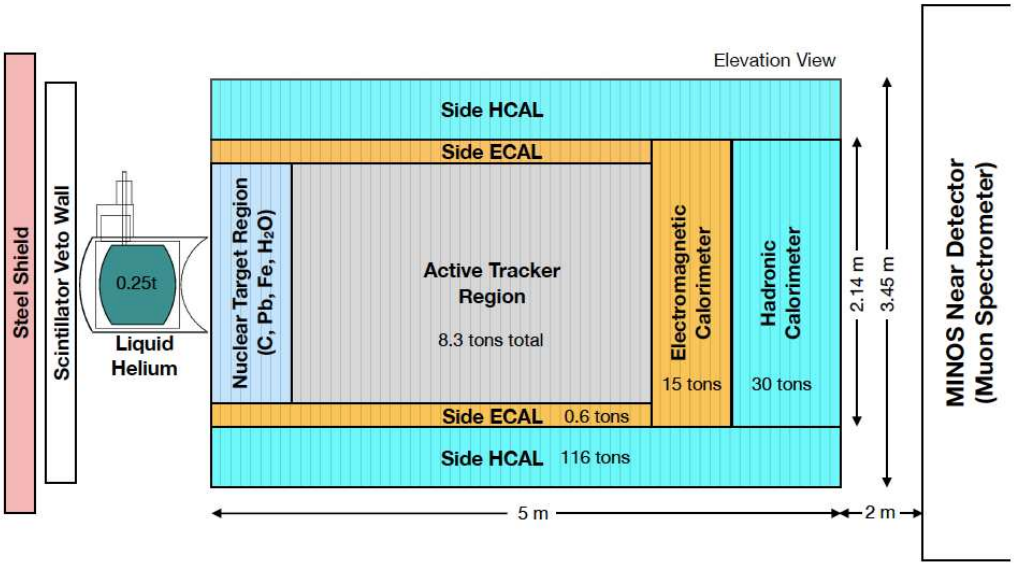

FIG. 2.9: An elevation view of the entire detector. Reprinted from [31]. Note: MINOS and the distance to MINOS is not to scale.

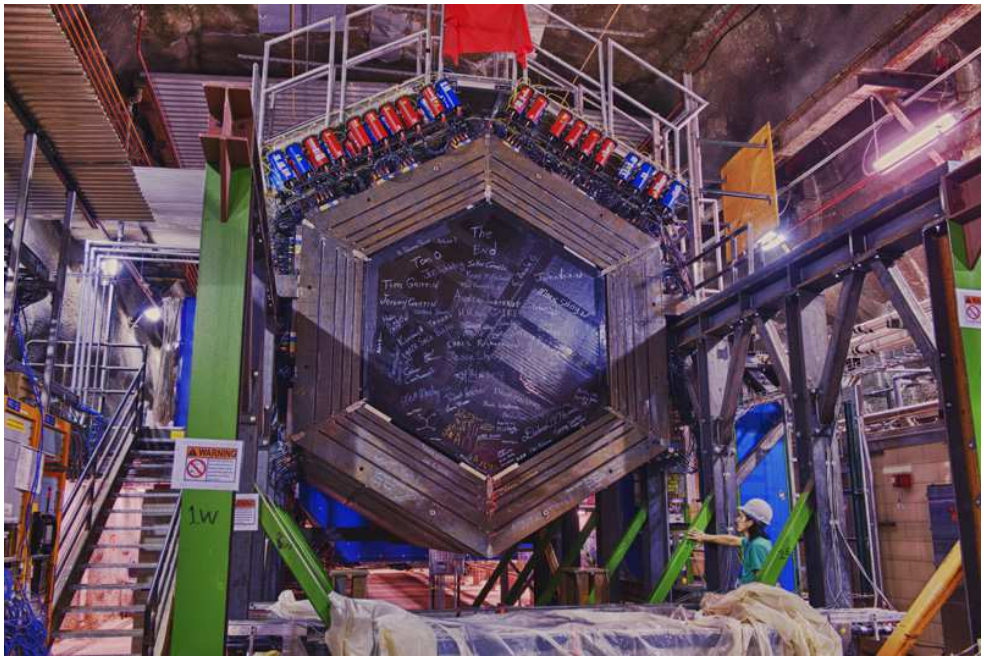

FIG. 2.10: A photo of the MINERνA detector in the NuMI near hall, in front of the MINOS near detector. The photo looks downstream to the MINOS detector.

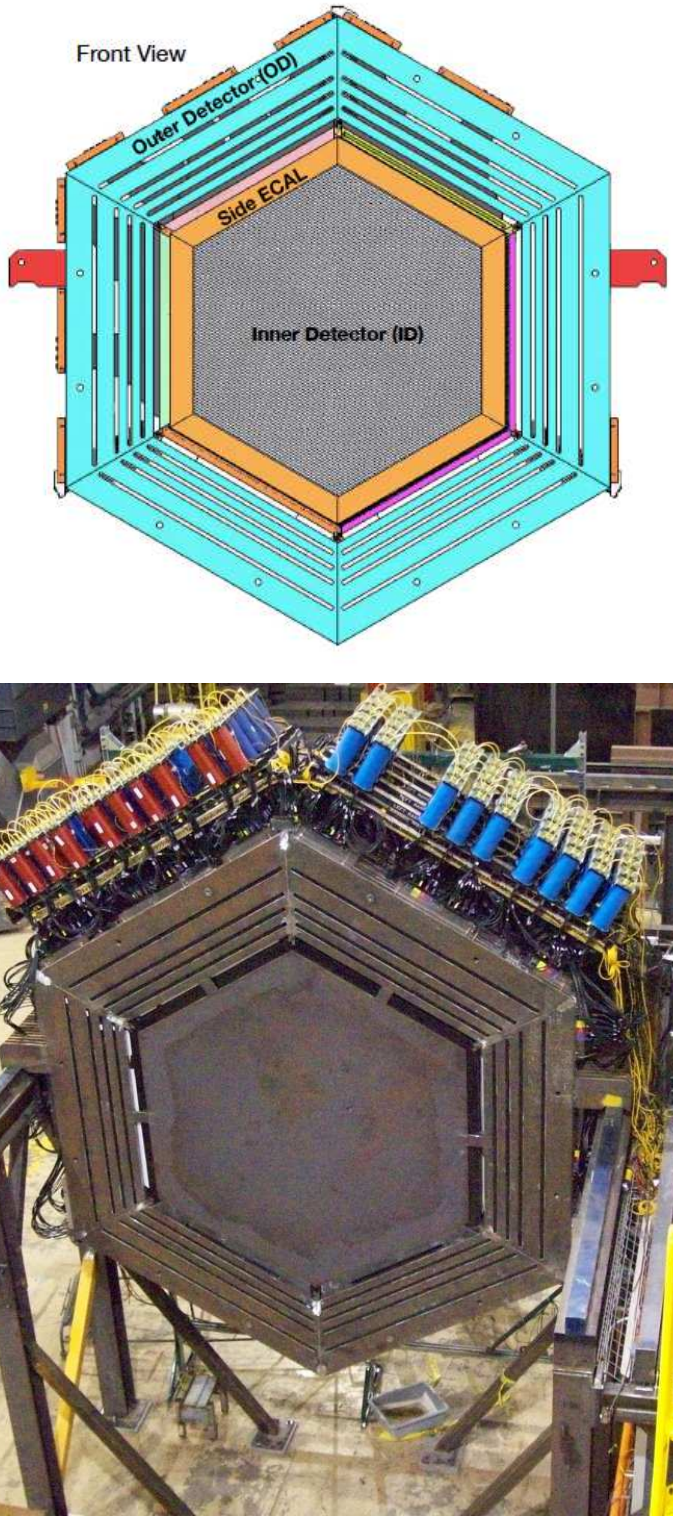

FIG. 2.11: An example of a tracking module mounted in an outer detector frame. The width of the tracking module is about 3.4 m. Reprinted from [31].

Fig. 2.12 shows the right-handed coordinate system used in MINERνA. The z direction is horizontal along the neutrino beam direction through the center of the detector. There is 3 degree different between the beam direction and the z direction. The y direction is upward to the Earth's surface. The x direction is to the left from the perspective of the beam.

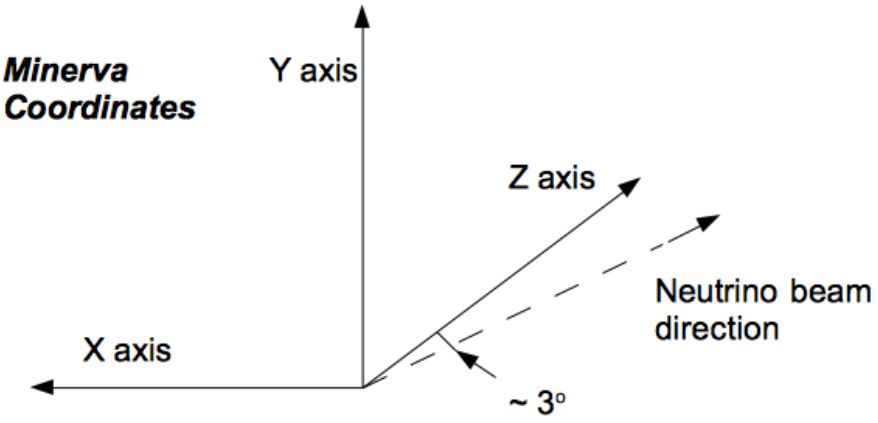

FIG. 2.12: A schematic diagram of the MINERνA coordinate system.

2.2.1 Inner Detector

There are four regions in the inner detector: the nuclear target region, the tracking region, the downstream ECAL, and the downstream HCAL, in order from upstream to downstream, as shown in Fig. 2.9. A total of 120 hexagonal modules are installed orthogonal to the z-axis and are numbered -5 to 114. These modules are divided into four types: passive target modules, tracking modules, ECAL modules, and HCAL modules. Tab. 2.2 shows the arrangement of modules in the four regions.

Scintillator Planes

Each scintillator plane is 1.7 cm thick, and contains 127 polystyrene triangular strips, and is rotated in one of three orientations (views) with respect to the coordinate system,

TABLE 2.2: Modular composition of regions in the inner detector. Reprinted from [29]. †:One passive target modules in Target 3 occupies the space of two modules. Therefore, the nuclear target region occupies the space of 28 modules.

Regions	Module Type	Module Numbers	No. of Scint. Planes
Nuclear Targets	22 tracking, 5 passive	-5 — 22†	44
Tracking Region	62 tracking modules	23 — 84	114
ECAL	10 ECAL	85 — 94	20
HCAL	20 HCAL	95 — 114	20

as shown in Fig. 2.13. In the X view the strips are parallel to the y-axis, thus enabling the MINERνA detector to measure the position along the x-axis. Rotating the strips in the X-Y plane by 60 degrees clockwise and counterclockwise to the X view forms the U and V views, respectively. The three different views allow for the reconstruction of three-dimensional objects.

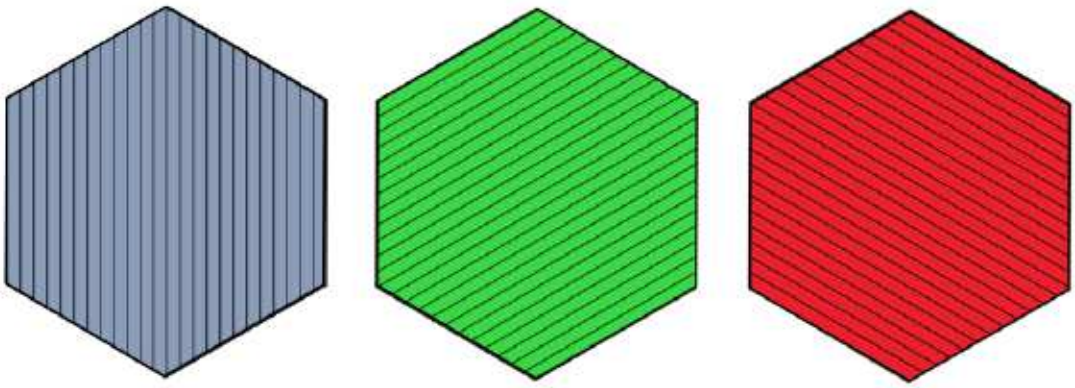

FIG. 2.13: The X (left)/ U (middle) / V (right) views in MINERνA from beam respective. Reprinted from [32].

The triangular scintillator strips are 33 mm wide, 17 mm high, and of various lengths in order to fit in the hexagonal planes. They are glued together with 3M-DP190 translucent epoxy (Fig. 2.14). On both sides of the planes, sheets of Lexan (GE polycarbonate, $C_{10}H_{12}O_3$) are glued with 3M-DP190 gray epoxy to make the planes light tight. Additionally, black PVC (C_2H_3Cl) electrical tape is used to control light leaks. Tab. 2.3 shows the

various element fractions in a scintillator plane. Each plane has an areal density of 2.02 ± 0.03 g/cm^2.

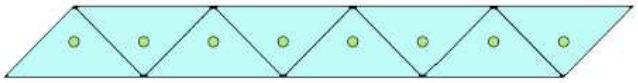

FIG. 2.14: The cross section view of the triangular scintillator strips. Each strip contains a WLS fiber. Reprinted from [32].

TABLE 2.3: Density and composition by mass percentage of scintillator plane materials [31].

Material	Density (g/cm^3)	H	C	N	O	Al	Si	Cl	Ti
Scintillator	1.043 ± 0.002	7.6	92.2	0.06	0.07	-	-	-	-
Coating	1.52	6.5	78.5	-	6.0	-	-	-	9.0
Lexan	1.2	6.7	66.7	-	26.7	-	-	-	-
PVC tape	1.2	4.8	38.7	-	-	-	-	56.5	-
Transl. Epoxy	1.32	10.0	69.0	2.6	17.0	-	-	0.5	-
Gray Epoxy	1.70	5.0	47.0	1.7	27.0	6.0	6.0	0.05	-

The X, U, and V view planes are arranged in alternating order. Each tracking module is composed of two scintillator planes. The downstream plane is in the X view and the upstream plane is in the U or V view. The 62 tracking modules are stacked in alternating UX/VX orientations. As shown in Fig. 2.11, a 2 mm thick hexagonal lead ring with an inner apothem of 90 cm and an outer apothem of 105 cm covers the outermost 15 cm of each plane's upstream side. This ring and the scintillator it covers form the side ECAL.

The ECAL region contains 10 ECAL modules, each composed of two scintillator planes and two hexagonal lead planes. The lead planes, 2 mm thick with an apothem identical to the scintillator planes, is installed upstream of each scintillator plane. The lead planes help contain electromagnetic showers. The ECAL modules are assembled in the same pattern as the tracking modules with alternating UX/VX orientations.

Twenty HCAL modules are installed in the HCAL region. An HCAL module consists

of one scintillator plane and a 2.54 cm thick hexagonal steel plane placed upstream of the scintillator plane. The steel planes help stop most hadrons originating from neutrino interactions in the low energy NuMI beam configurations. The HCAL modules are assembled in this order: Fe/X Fe/V Fe/X Fe/U.

The nuclear target region contains 22 tracking modules, 5 solid passive targets, and a water target. Fig. 2.15 shows a schematic diagram of the nuclear targets of MINERνA where the solid targets are numbered 1-5 upstream to downstream and the water target is not included. There are four scintillator planes before the first target and between the Carbon/Iron/Lead targets. The exception is between the fourth and fifth solid targets where only two scintillator planes are installed. These hexagonal scintillator planes are utilized to reconstruct the vertices, tracks, and showers in the nuclear target region.

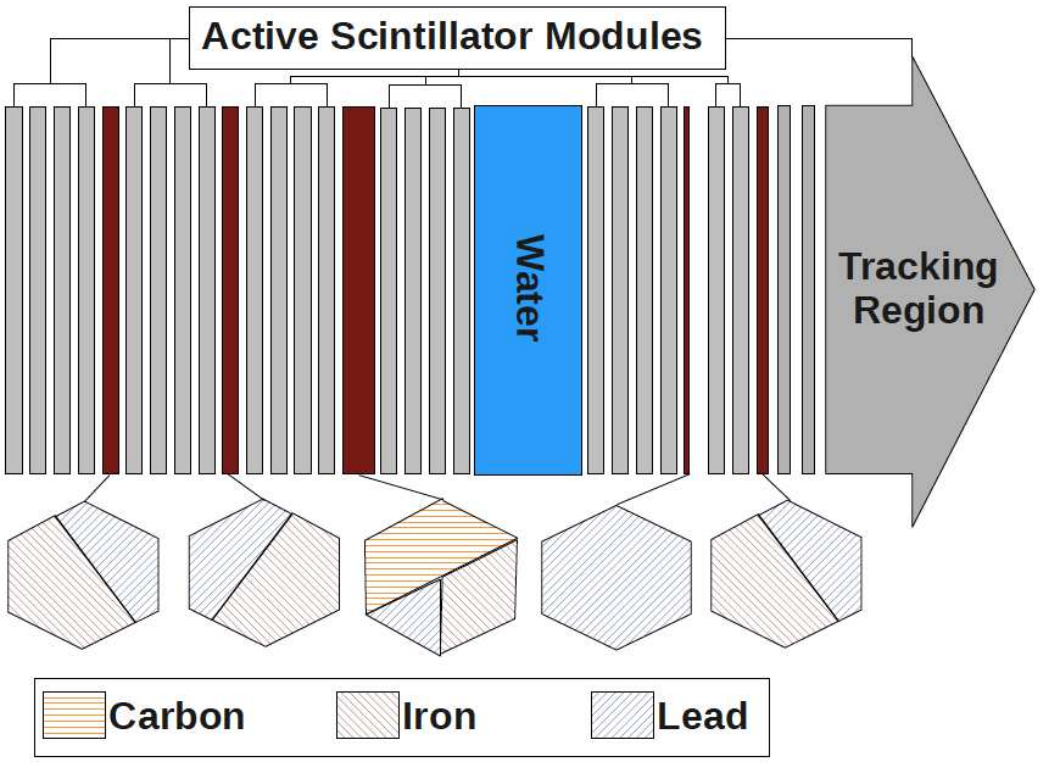

FIG. 2.15: Nuclear target region of MINERνA. Reprinted from [31]

The passive nuclear targets consist of plates of carbon, iron, and lead. For targets 1,

2, and 5, a pair of iron and carbon plates, are divided diagonally on a 20.5 cm offset from the center of the hexagon. For target 3, carbon, iron, and lead plates, occupy one half, one third, and one sixth of the target area, respectively. The carbon layer is approximately 3 times thicker than the iron and lead layers, which ensures equal nuclear interaction length for all three materials. Target 4 has only one composition, lead. Thicker targets are placed upstream to minimize the interaction of hadrons produced in neutrino interactions. The water target is placed between the third and fourth solid targets. Tab. 2.4 lists the geometrical composition of each nuclear target.

TABLE 2.4: The Nuclear Targets and Geometrical Description.

Target Number	Nucleus	Fiducial Mass (kg)	Thickness (cm)
Target 1	Iron	322	2.567 ± 0.006
	Lead	263	2.578 ± 0.012
Target 2	Iron	321	2.563 ± 0.006
	Lead	263	2.581 ± 0.016
Target 3	Carbon	158	2.573 ± 0.004
	Iron	107	2.563 ± 0.004
	Lead	160	7.620 ± 0.005
Target 4	Lead	225	0.795 ± 0.005
Target 5	Iron	162	1.289 ± 0.006
	Lead	134	1.317 ± 0.007

2.2.2 Outer Detector

The outer detector (OD) serves as a hadronic calorimeter that consists of hexagonal steel frames instrumented with scintillator strips. The steel frames that support the tracking and ECAL modules are 3.49 cm thick, whereas the frames supporting the HCAL modules are 3.81 cm thick. The outmost layer in Fig. 2.11 shows an OD frame. It is composed of six towers, approximately 56 cm wide at their halfway positions. A tower has four slots,

each of which is instrumented with a pair of scintillator strips (OD bars). In contrast to the inner detector, the scintillator strips in the OD are rectangular, as shown in Fig. 2.16. Two 2.54 × 2.54 cm^2 strips with WLS fibers form an OD bar (19.00 mm wide and 16.6 mm high) in the tracker and ECAL region. The OD bars in the HCAL region are larger due to the thickness of the iron absorber.

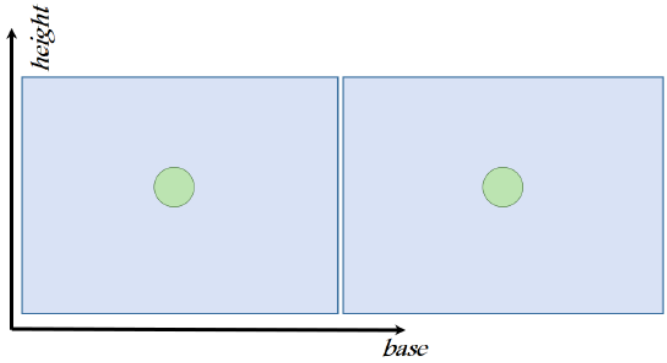

FIG. 2.16: A schematic diagram of the cross section of an OD bar. Reprinted from [7].

2.2.3 Upstream Region

The region upstream of MINERνA is not utilized in this analysis and hence not described in detail. Basically, the upstream region contains a veto wall followed by a cryogenic helium target. The veto wall contains iron slabs and scintillator paddles, which are used to absorb and identify charged particles entering the front face of the detector. Neutrinos can undergo charged and neutral current interactions with the rock before entering the Near Detector Hall. The steel slabs can stop the low energy particles from these interactions and possibly induce showers so that they may be detected by the scintillator paddles. The paddles can also detect muons from the neutrino interactions with the rock. The cryogenic helium target sits between the veto wall and the main detector.

2.2.4 The Scintillator Strips

Scintillator strips in MINERνA are triangular shaped bars of varying lengths according to their positions in the planes. The scintillator is composed of Dow Styron 663 (W) polystyrene ($(C_8H_8)_n$) [33]. Two dopants exist in the strips: PPO and POPOP. PPO, short for 2,5-diphenyloxazole ($C_{15}H_{11}NO$), comprises 1% of the scintillator mass. POPOP, short for 1,4-bis (5-Phenyloxazole-2-yl) benzene ($C_{24}H_{16}N_2O_20$), comprises 0.03% of the scintillator strips by weight. Energy deposits within a strip are converted to light by these dopants, and that light is collected by the WLS fiber. The strips are covered by a 0.25 mm thick layer of reflective layer that is composed of polystyrene and titanium dioxide (TiO_2). The TiO_2 makes up 15% of the outer layer by weight.

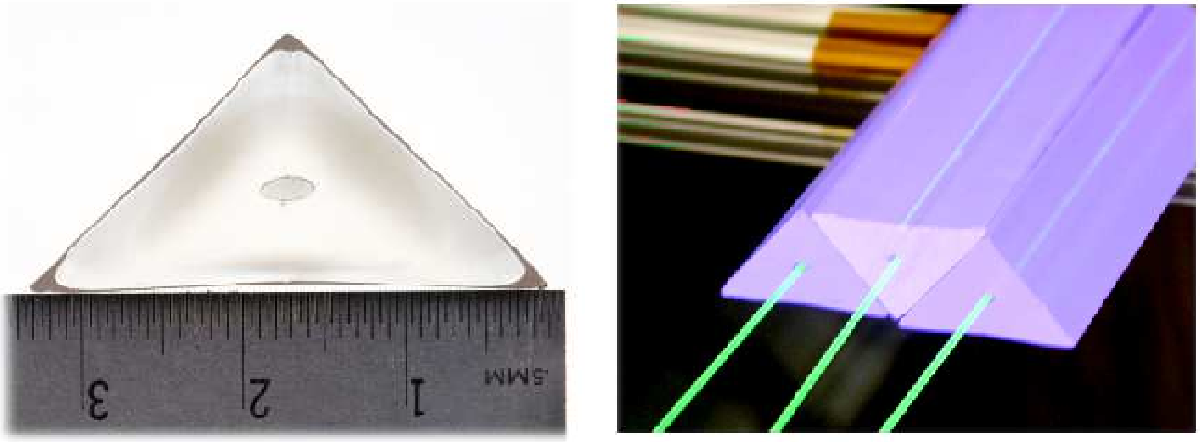

FIG. 2.17: Pictures of scintillator strips.

As shown in Fig. 2.17, the scintillator strips are 3.3 cm in width and 1.7 cm in height. There is a hole 0.26 cm in diameter through each scintillator strip. The hole is centered on the base and is positioned halfway (0.85 cm) above the base. A 175 ppm Y-11 doped, S-35 multi-cade WLS optical fiber (1.2 mm in diameter) fills each hole and is held in place by optically clear epoxy (Epon Resin 815C and Epicure 3234). The WLS fibers collect light from the scintillator strips, shift light from blue to green, and direct light out of the strips.

This shifted light spectrum more closely matches to the photosensitivity of the PMTs in MINERνA. Only one end of a WLS fiber is read out, connected to a PMT tube, while the other end is mirrored by vacuum sputtering of Aluminum. This technique increases the total amount of light seen by the PMT by reflecting light traveling away from the PMT tube back toward the PMT.

The read-out end of each WLS fiber connects to a clear optical fiber. The fibers are 1.2 mm diameter, S-35 multi-clad, optical fibers. The length of the fibers in the inner detector is 1.4 m, on average. Eight fibers are bundled together into a connector that mates to a connector on a PMT box.

2.2.5 The Photomultiplier Tubes

The clear optical fibers connect the WLS fibers to the 64-anode Hamamatsu R5900-m64 PMTs used by MINERνA. Fig. 2.18 shows a picture of a PMT box. There are eight connectors in a PMT box and one connector can mate to one eight-fiber connector. Therefore, a PMT box allows up to 64 fiber connections. Each PMT contains an array of 8×8 pixels in a grid with 2mm pitch. A "cookie", a plastic component inside the box, is used to mate the fibers to PMT pixels. The cookie connects to a weave of 64 fibers and align these fibers aiming to mitigate the optical cross talk in the neighboring channels. The PMT is mounted to a circuit board, which directs the signal to the front-end electronics. In MINERνA, there are in total 507 PMTs providing approximately 32000 readout channels. The PMT boxes are placed atop the detector.

2.2.6 Readout Electronics and the Data Acquisition System

The MINERνA readout electronics system reads the electrical pulses from more than 32,000 channels from PMTs that are connected to scintillator strips. Each pulse con-

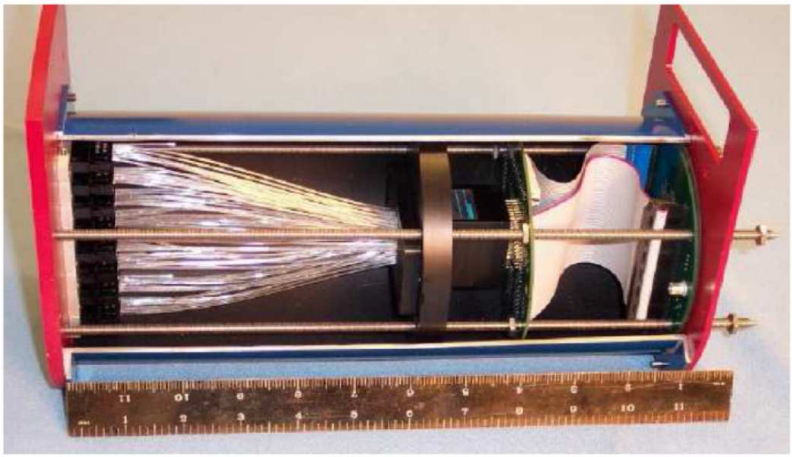

FIG. 2.18: A picture of a PMT box containing a weave of fibers connecting to a 64-anode PMT. Reprinted from [6].

tains the timing information and the amplitude, which is proportional to the light signals that pass through the scintillator strips. This section describes the MINERνA readout electronics and the DAQ system. See Ref. [34] for more details.

Recall that PMTs are connected to the front end electronics. A Front End Board (FEB) is attached to front face of the PMT optical box. The FEBs perform two major functions: supply the high voltage to the PMTs with an on-board Cockroft-Walton generator, and digitize the anode charge signals from the PMTs. A FEB contains six Application-Specific Integrated Circuit (ASIC) chips, known as TriP-t chips. The TriP-t chips integrate the charge from the PMT over a time window to determine whether the integrated charge passes the discriminator threshold. The threshold is a minimum amount that triggers the chips to record the signal.

The read out is organized into gates, which last approximately 16 μs, starting 0.5 μs before the arrival of the beam spills and ending 5.5 μs after the beam spills end. When the discriminator is fired by any channel, the TriP-t chips begin to integrate charge and record hit times. The integration window is about 150 ns, during which all channels on

the Trip-t chip are read out. There is a 188 ns reset window when no charge is read out in any channels (deadtime). Channels can be read out up to five times in one gate.

With standard ethernet cables, nine or ten FEBs are daisy-chained into groups. Both ends of the chain are connected to the Chain Readout Controller (CROC), a custom VME module. Timing information is communicated among the VME modules by the CROC Interface Module (CRIM). Timing information comes from two resources: MINOS, which is used to match events between MINOS (see below) and MINERνA, and from the MINERνA Timing Module (MvTM), which receives information from the Main Injector. The MvTM controls the gates starting time relative to the beam spill. CROCs and a CRIM are mounted in a VME crate, which communicates with the DAQ computers.

2.2.7 MINOS Detector

Main Injector Neutrino Oscillation Search (MINOS) is a neutrino oscillation experiment located in the beamline with a near detector, 2.1 m downstream of the MINERνA detector, and a far detector approximately 735 km away in the Soudan Mine in Minnesota. The plastic scintillator modules and the frame steel used to construct the MINOS detectors are similar to ones used in MINERνA. A significant difference between the MINERνA detector and the MINOS detectors is that the MINOS detectors are magnetized and capable of reconstructing the charge and momentum of muons.

The near detector, shown in Fig. 2.19, is a one kiloton magnetized, course-grained, steel/scintillator detector and calorimeter. It is divided into two regions. One is the calorimetry region, with 120 planes where one scintillator plane is placed before each steel plane. The other one is the muon spectrometer region, with 162 planes where a fully-instrumented scintillator plane is affixed every fifth steel plane. The MINOS modules are rotated 45 degree with respect to the positive y-axis, clockwise and counterclockwise

respectively in the successive planes. The scintillator planes are 1 cm thick and the steel planes are 2.54 cm thick. The scintillator strips are rectangular with a cross sectional area of 1.0×4.1 cm^2, but of the same compositions as the strips in MINERνA.

The MINOS near detector serves as the magnetic spectrometer for MINERνA. A 40 kA current generates a magnetic filed with an average strength of 1.3 T. The polarity of the current is adjustable so that the sign of muons can be chosen to be contained in the detector.

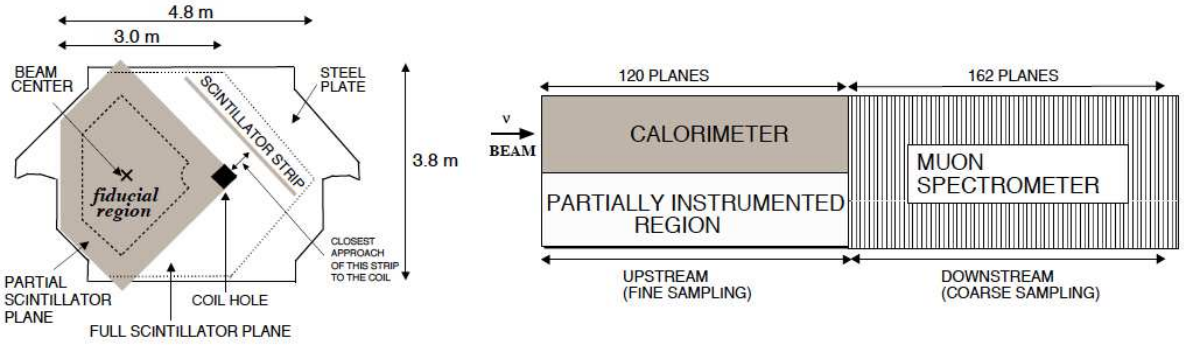

FIG. 2.19: The MINOS near detector. The right plot shows a top view of the detector and the left plot shows a beam view of the detector. Reprinted from [31].

FIG. 2.20: Photo of the MINOS detector.

CHAPTER 3

Calibration and Reconstruction in MINERνA

Neutrinos do not participate in electromagnetic processes so they cannot be detected by direct observation, but only from the energy they deposit after weak interaction. The presence, energy, and kinematics of interaction of neutrinos, can only be inferred from the final state products of their interactions. Therefore, reconstruction of detector activities is critical for analyzing neutrino scattering. The reconstruction is based on the MINERνA detector's measurements of the energy deposition, position, and time of hits that are caused by charged particles traveling through the detector's mass. The energy deposition is stored as a digitized PMT anode charge. The position is the location of the scintillator strip where the energy deposition produces photoelectrons, which we call a hit. The time is the gap between an FEB clock tick and the start of the read out gate. These three quantities are not directly read out, but must be inferred from the digitized data stored by the detector and calibrated. This chapter describes the calibration process in MINERνA and the subsequent reconstruction work. More details can be found in Ref. [31].

3.1 Calibration

Fig. 3.1 shows a schematic diagram of an optical readout channel. A particle travels through the MINERνA detector, deposits energy into a scintillator strip, and produces photons. The photons propagate in the wave-length fiber (WLF) and the clear optical fiber, and reach a Photo Multiplier Tube (PMT) where they are converted to photoelectrons. The PMT stands on a front-end-board (FEB) that reads the raw time and covert it to TDC (time-to-digital), and digitize the analog charge to ADC (analog-to-digital) counts.

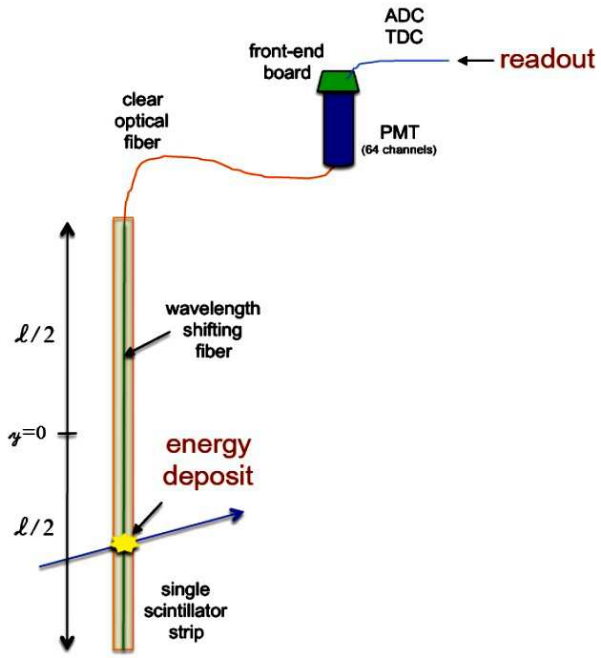

FIG. 3.1: A schematic diagram of an optical readout channel. Reprinted from [31].

A timing calibration accounts for the transportation time in fibers and the time response of electronics. The conversions from ADC counts, ADC_i, to the energy deposited, E_i per scintillator strip i, is computed as

$$E_i = ADC_i \times [C(t) \cdot S_i(t) \cdot \eta_i^{att} \cdot e^{l_i/\lambda_{clear}} \cdot G_i(t) \cdot Q_i(ADC)], \tag{3.1}$$

where

- $C(t)$ —absolute energy scale factor, dependent on time, converting the measured photoelectrons into units of energy in MeV.
- $S_i(t)$ —relative channel to channel energy scale factor, dependent on time, correcting the energy variations that may come from the extrusion of scintillator, bubbles in epoxy around optical fibers, connection of the fibers to the PMT, environmental conditions across the detector, etc.
- η_i^{att} —attenuation correction factor in the WLS fiber, dependent on the position in the fiber. The position is not known initially, so the calibration is done to the center of the strip. After reconstructing the position successfully, the attenuation correction is adjusted accordingly.
- $e^{l_i/\lambda_{clear}}$ —exponential attenuation correction factor in the clear optical fiber, where the attenuation length $\lambda_{clear} = 7.83$ m and l_i is the length of the clear optical fiber i.
- $G_i(t)$ —the PMT gain per channel, dependent on time.
- $Q_i(ADC)$ —Conversion of an analog charge to the number of photoelectrons.

All terms listed above are discussed in detail in the rest of this section.

There are two sets of calibrations in the MINERνA experiment, the *Ex situ* and the*In situ*. The *Ex situ* calibrations were measured from different components before they were installed on the MINERνA detector, including calibrations of the front-end boards (FEBs), the photomultiplier tubes (PMTs), and the module mapper. The *In situ* calibrations were measured from the fully installed detector.

3.1.1 *Ex situ* Calibration

Front-End Broads

The term $Q_i(ADC)$ in Eq. 3.1 is directly related to the measurement on the high, medium, and low gain of FEBs. The measurement was done by injecting 10 capacitors at various known voltages into FEBs and fitting the output ADC count responses using a tri-linear function for each channel. The fitting results of a typical FEB are shown in Fig. 3.2.

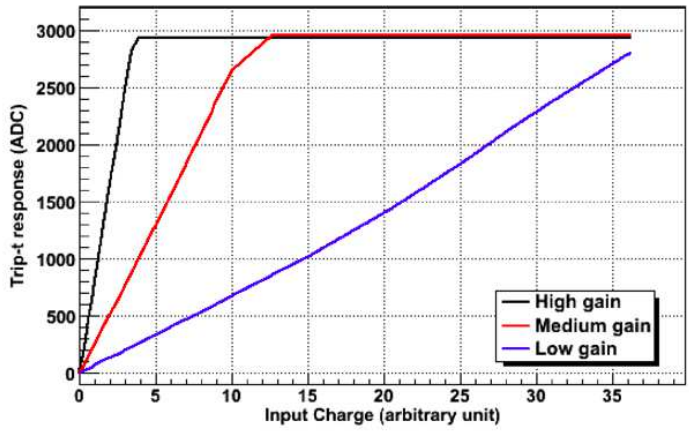

FIG. 3.2: A typical MINERνA FEB's high, medium, and low gain response of one electronics channel as a function of input charge. Reprinted from [31].

Module Mapper

The term η_i^{att} in Eq. 3.1 is the optical attenuation in the WLS fiber, which is measured in the module mapper, shown in Fig. 3.3, using γ radiation of a ^{137}Cs source. The source was put up and down the scintillator strips in the module while the PMT responses were recorded. It measured the η_i^{att} for each channel as a function of the longitudinal position of the source along the strip.

Photomultiplier Tubes

The purpose of testing PMTs is to ensure PMT quality before installing them in the

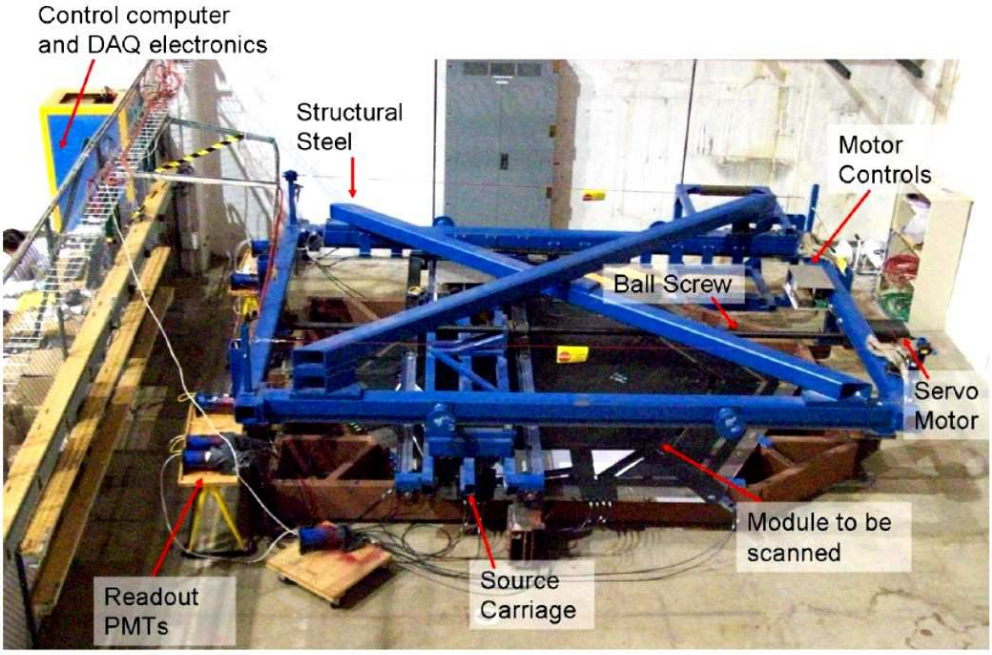

FIG. 3.3: The picture of the Module Mapper. Reprinted from [31].

cylindrical steel boxes. The tests were done on the test stand, shown in Fig. 3.4. The quality requirements include linearity, efficiency, dark noise, channel-to-channel amplification variation, and optical cross-talk. After all of the different parts are assembled in the PMT box, additional assurance checks were done to ensure the unit was fully functionally and the different components were properly aligned. The gain on each PMT as a function of time was also calibrated *in situ*, which is discussed in the next subsection.

3.1.2 *In situ* Calibration

Aside from the measurements conducted prior to the full installation of the MINERνA detector, some terms in Eq. 3.1 needed to be estimated in the assembled detector. The reason for *in situ* calibration is that these factors can vary over long time runs and the time dependence needed to be taken into account in the detector's simulation and reconstruction. A natural calibration resource is the rock muons, which are the products from

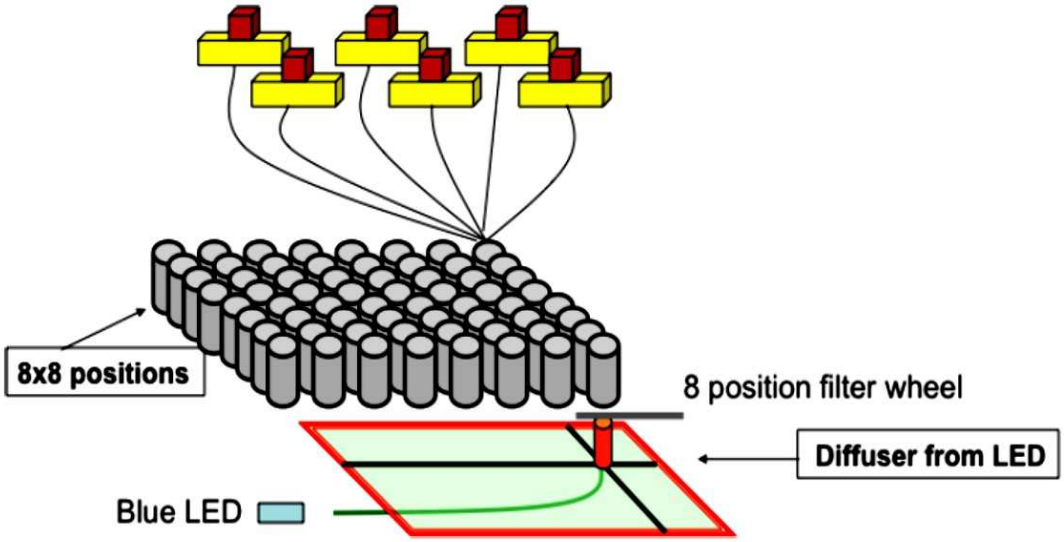

FIG. 3.4: A schematic diagram of the PMT test stand. Light from LED is directed through a green WLS fiber and illuminates one pixel in each of six PMTs (represented by red cubes) mounted on fiber cookies (represented by the Yellow rectangular boxes). Reprinted from [31].

neutrino interactions with the rock that sits upstream of, and around, the MINERνA detector. Rock muons can be used to calibrate the overall energy scale, timing, cross-talk between PMT pixels, relative alignment of the ID modules, and the relative light yield of scintillator strips in the detector. Not surprisingly, rock muons are not the solution to all problems. There are other factors that need to be calibrated with special triggers. For example, the pedestal value of each channel is best measured when the beam is off. The PMT gain can not be measured accurately using the normal beam, so a separate system to inject light into the boxes is utilized to measure the PMT gain. The various types of *in situ* calibration are described in this subsection, including those using rock muons and special triggers.

Pedestal Subtraction

Pedestal is a reference point reflecting the noise of the detector in the absence of the beam. The noise is caused by cosmic rays, radioactivity, electronic source, and the PMT's dark current. The pedestal needed to be subtracted from the signals for each read out interactions. The pedestals differ in every channel and needed to be calibrated for each channel individually. During the standard run, pedestal levels were measured for all channels in the special subrun, which is in a mixed mode of the neutrino beam and pedestal, for every 10.5 hours. Fig. 3.5 shows a histogram of pedestal data collected in a single channel.

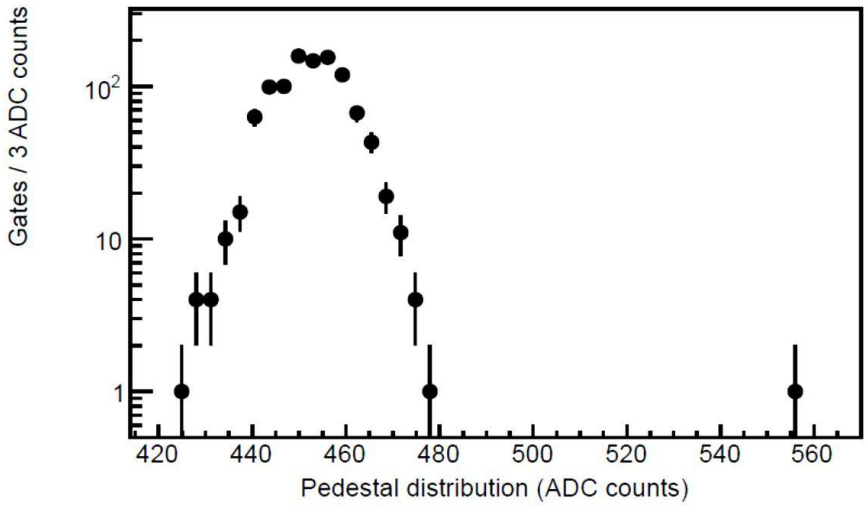

FIG. 3.5: Example of a channel for a single pedestal gate with a measured signal of about 100 ADC counts above the pedestal level. Reprinted from [31].

PMT Gains

PMT gains are calibrated since they change over time (Fig. 3.6) by taking data daily to monitor fluctuations in the single PE PMT gain for all channels. The calibration is done within a separate system, a light injection (LI) system, which is triggered once after each beam spill. A special calibration source is used here, which is the ultra-violet LED light. Each PMT box has two ports connecting to optical fibers that connect to the LED light. A polypropylene diffuser is embedded in each port to spread that the light across

the entire face of the PMT. The LED light in the LI system can flash varying strength signals roughly at the level of several photoelectrons into each pixel. The PMT gain is calculated assuming a probabilistic model for amplification in the dynode chain.

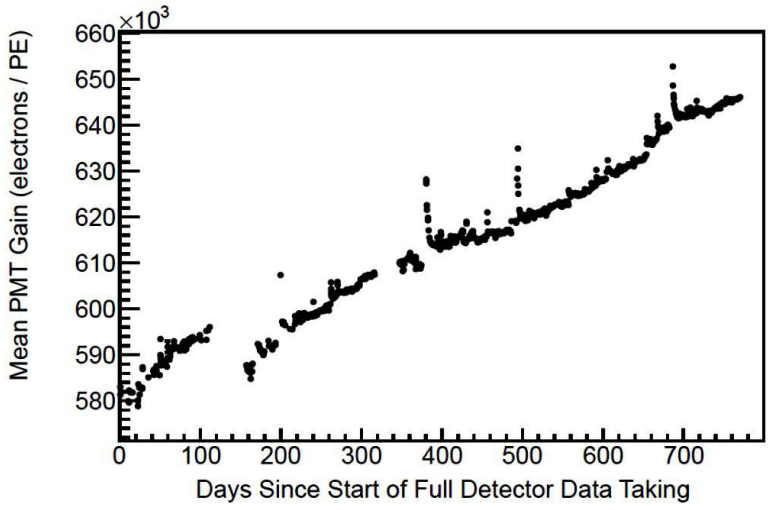

FIG. 3.6: The average PMT gain as a function of time for one pixel. Reprinted from [31].

Scintillator Plane Alignment

Variations in the relative module positions are taken into account, including the two planes within a module and module-to-module. Two planes in one module could suffer from stresses and strain differently in the frame even though they hang on the same frame. Module-to-module mis-placement could be the rotation about the z-axis and the translation in the direction of the measurement. Rock muons that enter the front of MINERνA and exit the back of the detector (referred to as through-going rock muons) are used to estimate offsets based on these effects. The through-going rock muons that travel along the beam direction are selected. Consider two facts here: first, the maximum path length in the triangular strip is from the center of the triangular base to the peak; second, the longer the path, the more energy deposits in the strip. Therefore, the peak in the energy deposited in the histogram is indicated by the peak of the triangle. Fig. 3.7

shows an example of the plane alignment. Typical offsets are at the level of strip width of 33 mm, and they are determined by the alignment procedure and corrected for in the event reconstruction.

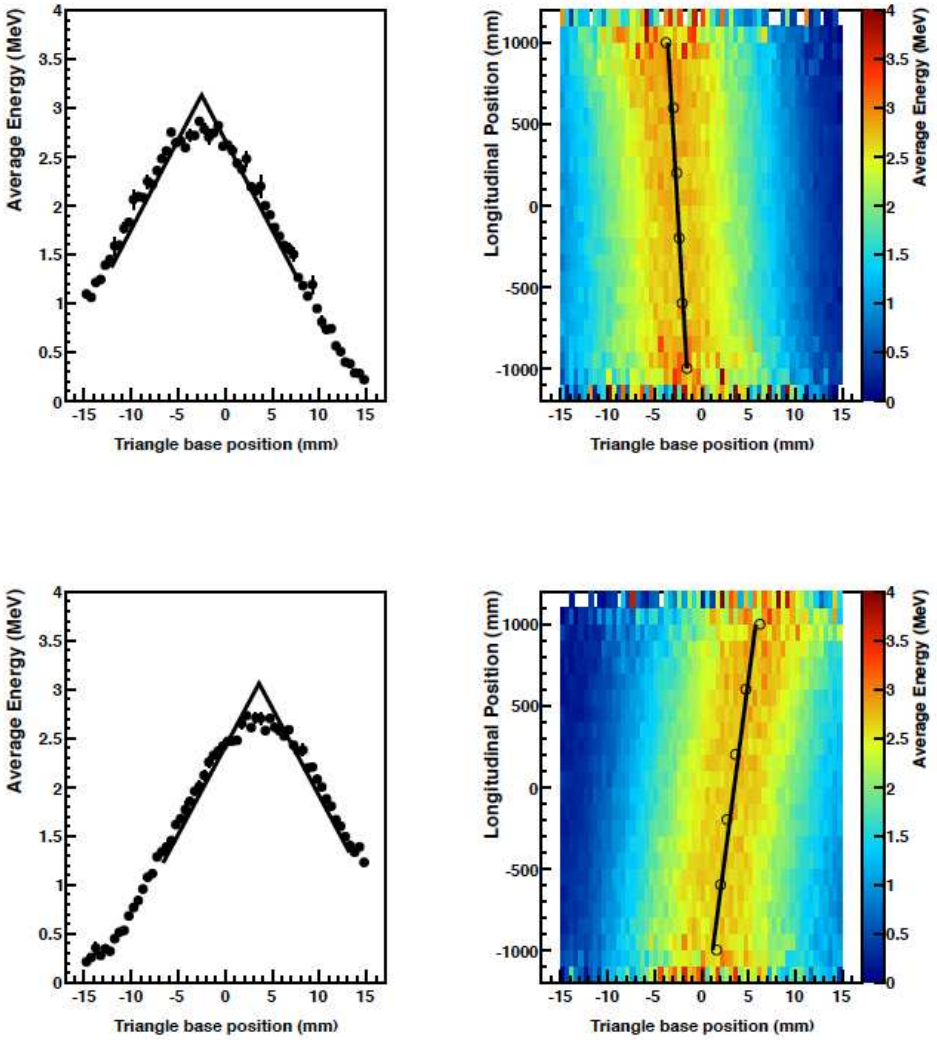

FIG. 3.7: The plots show the alignment fits for module 50, plane 2 (top) and module 61, plane 1 (bottom). Left plots show the offset of the peak with respect to the nominal position (0 mm in the plots). Right plots show the base position change with respect to the longitudinal position in the strip, and the slopes indicate a rotational misalignment. Reprinted from [31].

Relative Strip-to-Strip Response Variations

There are still some effects that are not considered in the calibrations that cause strip-to-strip variations in the measured light level. For example, the scintillator material can differ from batch to batch and air bubbles exist when coupling the WLS fiber in a strip using optical epoxy. These remaining variations need a strip-to-strip calibration using the through-going rock muons. It is an iterative procedure to develop multiplicative constants to normalize the measured light in each strip. The energy per length, dE/dx, of scintillator strip is measured. Fig. 3.8 shows the consistency in the energy response of modules after strip-to-strip calibration.

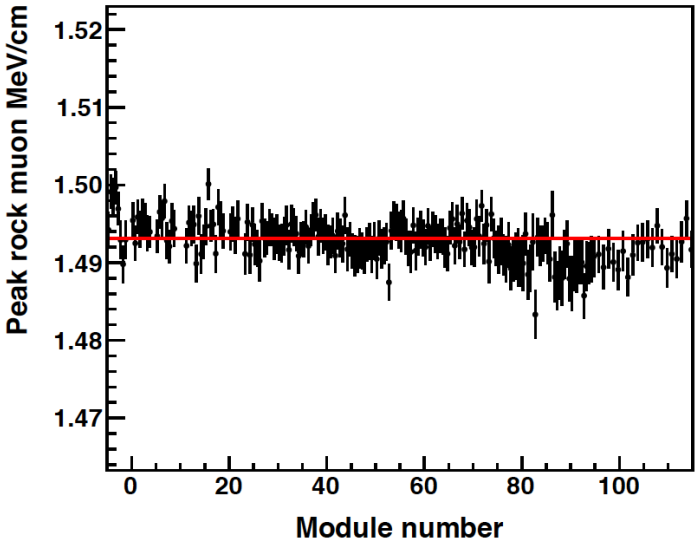

FIG. 3.8: Linear fit on the distribution of peak energy per unit path length for each plane. Reprinted from [31].

Absolute Energy Scale

The well understood energy loss of muons in the active scintillator is used to calibrate the absolute energy scale of MINERνA. The through-going rock muons are the calibration source. The absolute energy scale factor, term $C(t)$ in Eq. 3.1, is set by comparing the simulated dE/dx to the measured dE/dx after applying all other energy calibrations. The

distributions in Fig. 3.9 are fitted to a fifth-order polynomial, and $C(t)$ is the ratio of the simulated fitted peak to the measured fitted peak. This energy scale is time dependent because of the detector's aging and the energy scale is calculated in two-day intervals.

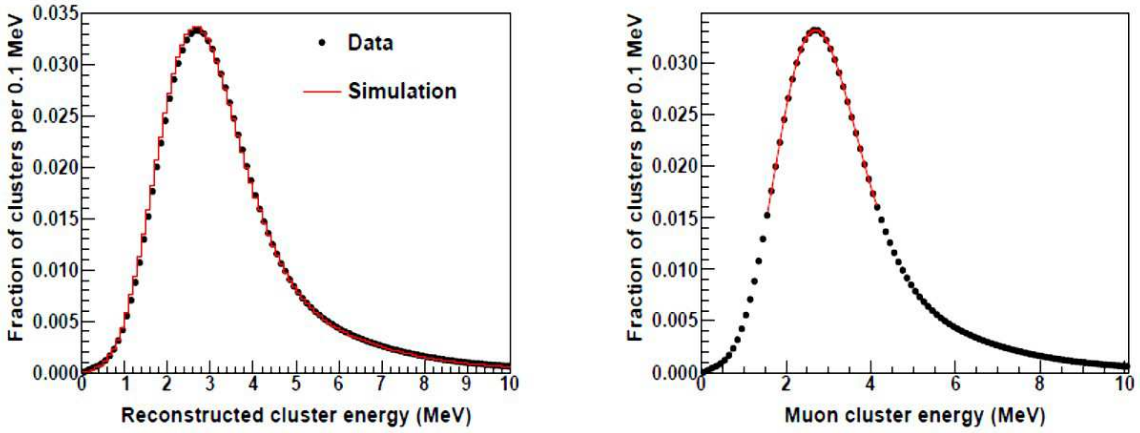

FIG. 3.9: Comparison of muon energy in data and simulation (left) and fits to the peaks (right). Reprinted from [31].

Timing

Through-going rock muons are also the source of the timing calibration, which includes correction for transport time in the optical fiber, time slewing, and channel-to-channel time offsets. The optical fibers connected to each PMT pixel are of various lengths, so the different transport times in each fiber need to be measured. Time slewing is due to the scintillator decay, which varies in time as a function of energy deposition. Time slewing is a function of the PE yield in scintillator strips. Fig. 3.10 shows an example of time slewing as a function of photoelectrons. Channel-to-channel time offsets include the time delays in propagation between FEBs and read out chains.

The calibration procedure is iterative. It extracts the time constants by fitting the time residual that is the difference between the calibrated time of each hit and the truncated-mean time of hits along the through-going rock muon tracks, until convergence. Fig. 3.11 shows the time residual after the final iteration, where the peak is fitted to a Gaussian with a width of 3 ns.

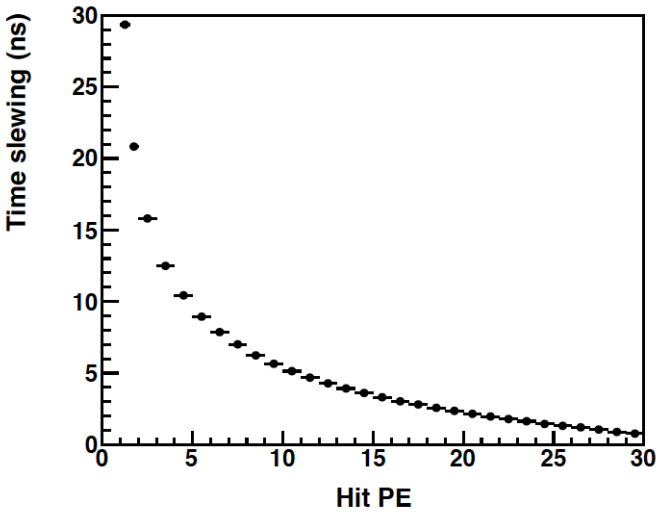

FIG. 3.10: Time slewing vs. number of photoelectrons for through-going rock muons. Reprinted from [31].

Cross-Talk

Cross talk is identified as the response in one channel induced by signals in other channels. Again, through-going rock muons play the role of calibration source here. The reason is simply that muons usually deposit energy into only two strips per plane. The procedure is to compare the frequency and energy distributions of cross talk in data and simulation to calibrate the probabilistic algorithm in the simulation. Fig. 3.12 shows the comparison of $f_{xt,NN}$ in data and simulation, where $f_{xt,NN}$ is the ratio of the energy of cross talk candidate hits to the energy of hits along the track.

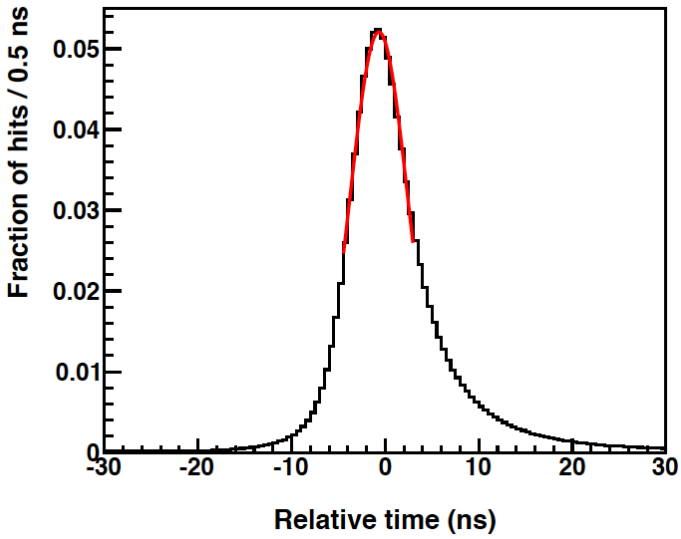

FIG. 3.11: Time residual for through-going rock muons after applying the timing calibration. Reprinted from [31].

3.2 Reconstruction

Through a series of low and high level calibration techniques described in the previous section, energy depositions in the detector are readied to be reconstructed into the particles' activities in MINERνA using pattern recognition algorithms. The activities relating to this analysis, include clusters, tracks, vertices, and some other groupings of energy deposits, all of which are discussed in this section. The reconstruction of Michel electrons is different and will be discussed in Chap. 5.

3.2.1 TimeSlice Reconstruction

The NuMI beam is a very intense neutrino source and usually produces multiple events in one readout gate. The neutrino events here could be either rock muons coming into the MINERνA detector or neutrinos scattering in the detector. The beginning of the reconstruction chain is grouping raw hits in a gate into "time slices" using their timing

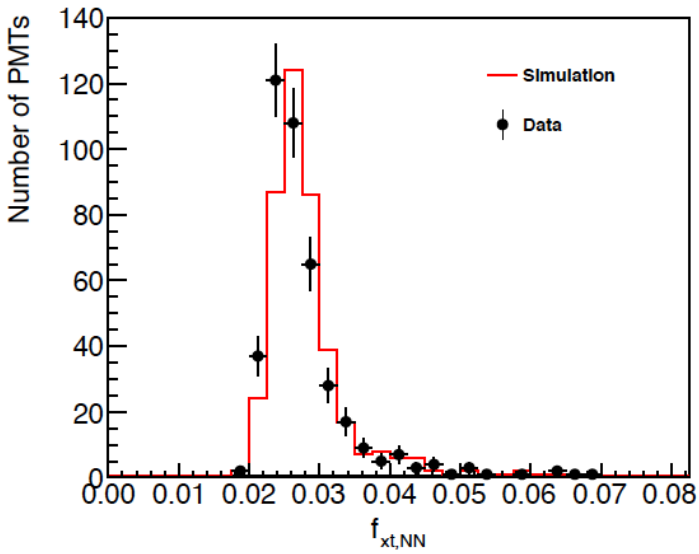

FIG. 3.12: Comparison of cross talk fraction in data and simulation. $f_{xt,NN}$ is the ratio of the energy of cross-talk candidates to the energy of hits along the track. Reprinted from [31].

information. A time slice in MINERνA usually has the collection of raw hits corresponding to only one neutrino event. Hits in different time slices do not interfere [1] and subsequent reconstructions are conducted in single time slices.

The time slice forming algorithm starts with a 30 ns time window moving forward on the time distribution of raw hits. The photoelectrons within the roaming time window are integrated. If the integration is greater than 10 MeV, a time slice candidate is created with raw hits within the time window. Activities in 30 ns windows are added to the slice until the integrated photoelectrons in a window does not exceed 10 MeV. The time window is then moved forward to look for more time slices. Typically, the width of a time slice is approximately 150 ns and there are between 5 and 12 time slices in a readout gate.

Fig. 3.13 shows the hit time profile of a typical readout gate that corresponds to a single 10 μs spill of the MuMI beam. The colored groupings of hits are time slices. The

[1] This does not hold for Michel electrons, which are different, as mentioned before. The typical time gap between a Michel electron and its parent muon is approximately 2 μs which is longer than the typical separation time between time slices.

black entries are the hits that are below the threshold for forming a time slice candidate.

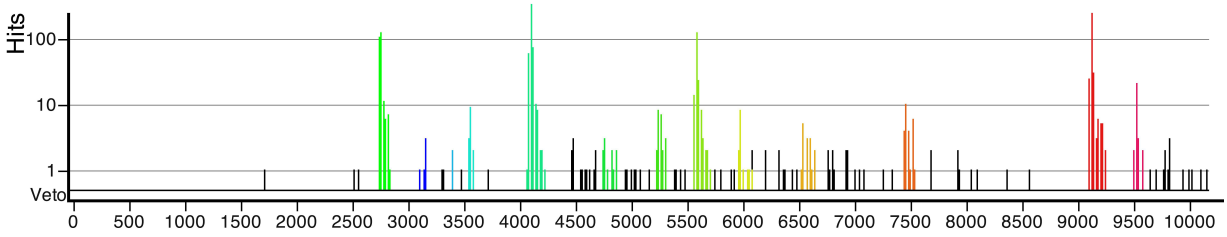

FIG. 3.13: Time profile of hits in a typical readout gate. Reprinted from [31].

3.2.2 Cluster Formation

A cluster is a collection of energy deposits (hits or digits) in consecutive scintillator strips in one plane within a time slice. The energy of a cluster is the sum of the energies of its constituent hits. The time of a cluster is the time of the hit with highest energy. The position of a cluster is the energy-weighted mean position of all hits. This analysis only utilizes ID clusters that are the clusters identified in the inner detector of MINERνA.

Every hit is added to one and only one cluster. A cluster may contain only one hit if it has no neighboring hits. Based on the number (N_{hit}) and the energy of hits ($E_{cluster}$) that the clusters contain, the topological classifications of clusters are listed as follows:

- **Cross-Talk** —clusters are induced by hits in the adjacent PMT pixels that are correlated to particular clusters.
- **Low Activity** —clusters' energies, $E_{cluster} < 1$ MeV.
- **Trackable** —clusters with $N_{hit} \leqslant 4$ and 1 MeV $< E_{cluster} <$ 12 MeV. The number of hits with energy above 0.5 MeV, $N_{hit}(E_{hit} > 0.5 \text{ MeV}) \geqslant 1$. If there are two such hits, $N_{hit}(E_{hit} > 0.5 \text{ MeV}) == 2$, they must be adjacent. This topology is consistent with a single minimum ionizing particle crossing the plane at an angle less than 70 degrees.

- **Heavy-Ionizing** —clusters with $N_{hit} \leqslant 4$ and $E_{cluster} \geqslant 12$ MeV. The number of hits with energy above 0.5 MeV, $1 \leqslant N_{hit}(E_{hit} > 0.5 \text{ MeV}) \leqslant 3$. If there are two or three such hits, $N_{hit}(E_{hit} > 0.5 \text{ MeV}) == 2 \,||\, 3$, they must be adjacent. This topology is consistent with several types of particles, such as high-angle particles, spatially-overlapping particles and the large energy deposits from non-minimum-ionizing particles.

- **Supercluster** —clusters that do not fit into any of the above conditions. This topology is consistent with hadronic on electromagnetic showers. Typical superclusters are wide and have large energy deposits.

3.2.3 Track Formation

In MINERνA, a track is a reconstruction object that is a collection of clusters approximating the trajectory of a charged particle. In general, there are two pattern recognition schemes to form a track: long track and short track patterns. Given that this analysis only utilizes the muon tracks that are matched in MINOS, only long track pattern recognition is discussed in this section.

The long track pattern recognition begins by building possible track seeds on a set of trackable and heavy-ionizing clusters (see top left plot in Fig. 3.14) within a single time slice, where a track seed is a collection of three clusters, all in the same view (X, U or V), which meets the following criteria (see top right plot in Fig. 3.14):

- Clusters must be in different scintillator planes,

- Clusters must be in consecutive scintillator planes,

- Clusters must be fitted by a two-dimensional straight line successfully.

Next, track candidates are built by the merger of two track seeds (see middle left plot in Fig. 3.14). The merging procedure starts from the downstream end of the detector and stops towards the upstream region. The track candidates must meet the following criteria:

- Share one cluster or more,
- Share no multiple clusters in the same plane,
- Have consistent slopes.

After all track candidates are built, similar criteria are applied to join these track candidates in the same view into larger track candidates. The join occurs when two track candidates project to each other.

The last step is to combine these larger track candidates (see middle right plot in Fig. 3.14) in different views into three-dimensional track objects, executed by two different techniques sequentially: three-view tracking and two-view tracking. Three-view tracking is attempted first on all possible combinations of three candidates from three different views. If a combination fully overlaps along the z-direction and is consistent to a three-dimensional line, the combination is formed into a track. After testing all possible combinations of three candidates, two-view tracking is attempted on all remaining candidates unused in the previous step. The remaining candidates are formed into pairs that are two candidates in different views. If a pair fully overlaps along the z-direction, a possible track object is constructed. Then, in the view other than the views in the pair, all unused clusters are searched to detect those with the z position consistent with the possible track object. If there is a sufficient number of clusters found, the pair is formed into a track.

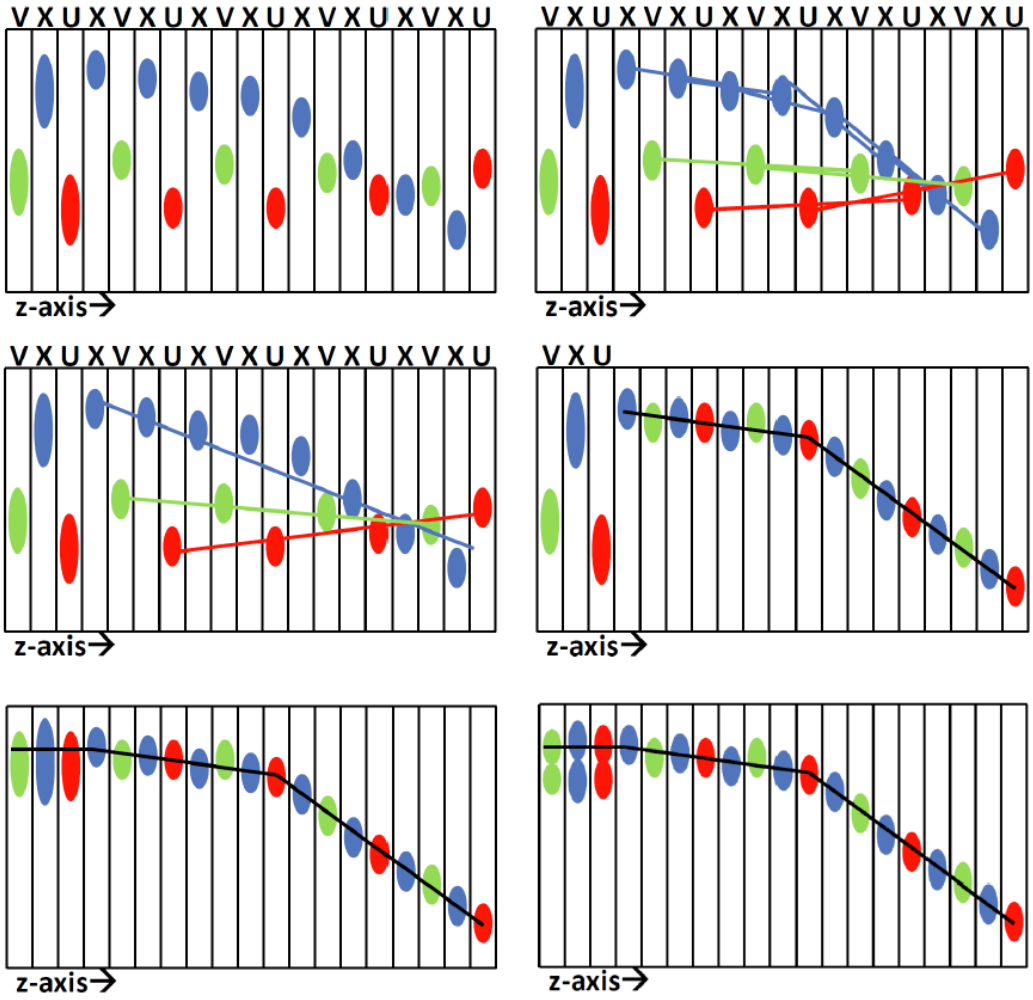

FIG. 3.14: A cartoon example of three-view long track reconstruction in each step. The top left plot shows formed clusters in X/U/V views. The top right plot shows track seeds formed in each view. Superclusters are not being used yet. The middle left plot shows track candidates are built from merged track seeds. The middle right plot shows a three-dimensional track formed from candidates in each view. The bottom left plot shows projecting the track back to claim the superclusters. The bottom right plot shows the track cleaning procedure to break the superclusters. Reprint from [32].

There is more work after the tracks' reconstruction. A Kalman filter is used to fit the reconstructed tracks [35]. This fit assigns the three-dimensional position and the slope to each cluster on the tracks. Fig. 3.15 shows the tracking position resolution after the fit. The purpose of the fit is to add any clusters missing from the tracks by exploiting the fitting results. The fitted track is projected to both upstream and downstream and unused clusters are added to the track when the projection intersects the unused clusters. Superclusters can be used here by breaking them into smaller clusters and assigning the fraction of the cluster energy to each track based on dE/dx of each track near the supercluster.

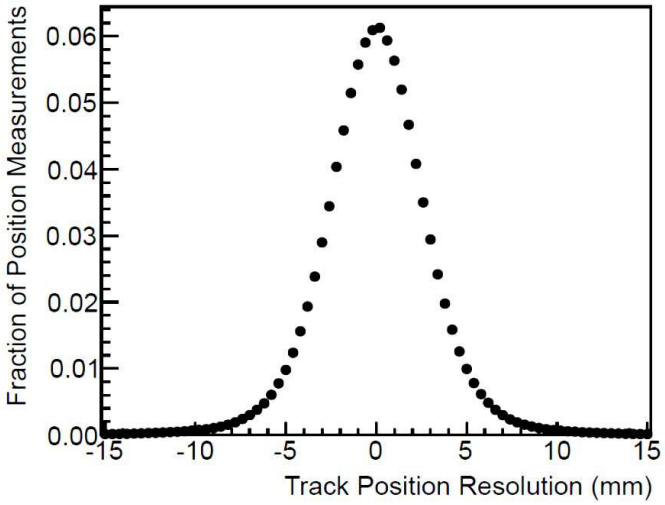

FIG. 3.15: Resolutions of the fitted position along a track relative to the measured cluster positions for a sample of rock muons in data. The RMS of the distribution is 3.1 mm. Reprinted from [31].

3.2.4 Vertex Fitting

A vertex is a reconstruction object that is either a starting point or an ending point of one or more tracks. The vertex where the neutrino interaction occurs is named as the primary vertex. MINERνA utilizes the point of closest approach (POCA) to reconstruct vertices. The POCA procedure implements the Kalman filter method [35], which is a local

least-squares estimator. The outputs of the Kalman filter are the position, slope, and covariance matrix for each cluster. For the cases with more than two tracks, the POCA method estimates the vertex positions using every pair of tracks. The raw position of the vertex is the weighted average of all positions. The raw position is then refitted using an adaptive Kalman filter minimization routine [36]. This routine uses an adaptive fitter scheme to weigh down the tracks which are not compatible with the vertex. Thus, tracks with poor compatibility influence the vertex reconstruction to a lesser extent. For more details about this fitting procedure, see Ref. [29].

3.2.5 Track-Based Event Building

The event building described in this subsection is mainly about the charged current events (i.e., events with a muon track), which are the event candidates in this analysis. MINERνA has developed an algorithm to form the track-based events, and it has several steps to create high quality tracks (Fig. 3.16).

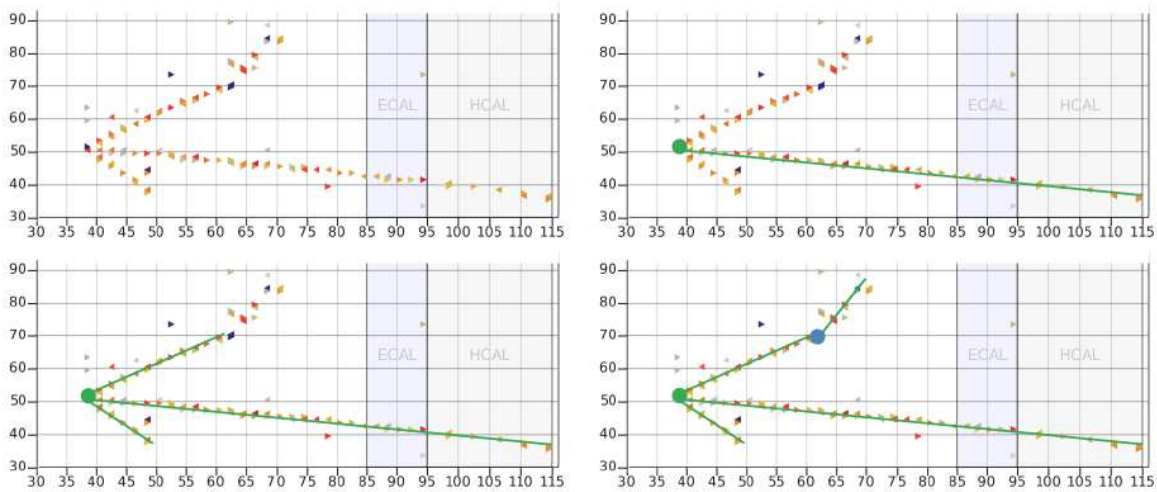

FIG. 3.16: Track-based event building example. Top left, step 0, shows the clusters in one slice. Top right, step 1, shows identifying the anchor track. Bottom left, step 2, shows creating the anchored tracks. Bottom right, step 3, shows creating secondary tracks. Reprinted from [32].

Step 1: Identify the Anchor

The anchor track is almost always a muon in the charged current neutrino interaction. It is created using the long-track pattern recognition scheme discussed above, using trackable and heavy ionizing clusters. The longest track is selected as the anchor track, which usually has more than 25 nodes. The origin of the anchor track is taken as the primary vertex. Around the primary vertex, any energy inconsistent with a minimum ionizing particle (MIP) is discarded. Superclusters are always broken and only the energy portion consistent with a MIP is retained.

Step 2: Create Anchored Tracks

To reconstruct tracks, pattern recognition loops again over clusters not used in creating the anchor track or other anchored tracks. If a track has a vertex compatible with the anchor track, the anchored track is created and the new fitted vertex replaces the previous vertex. This process is repeated until no more anchored tracks are reconstructed. Here vertex compatibility means:

- The distance between the vertex and the track's projection is less than 100 mm,
- The distance between the vertex and the track's origin is less than 250 mm.

Step 3: Create Secondary Tracks

A similar process is used to create the secondary tracks, often referred as kinked or forked tracks, which could be caused by a hadronic collision or decay. The only difference is that the secondary tracks are compared to the end points of the tracks, which are reconstructed in the previous two steps instead of the vertex. The process for creating secondary tracks continues until no more are found.

3.2.6 Muon Reconstruction

In this analysis, the signal events are the ones that have one muon track. Therefore, the reconstruction of muons is extremely crucial. This section describes how muons are reconstructed in the analysis.

Matching Tracks to MINOS

In MINERνA, it is rare for a charged hadron created in a ν interaction to exit the back of the detector without stopping in, or interacting with, ECAL and HCAL. Therefore muons can be identified by requiring that tracks in MINERνA match with those in MINOS. The matching details include:

1. The MINERνA track has at least one cluster in the five most downstream MINERνA planes,

2. The MINOS track contains at least one hit in the four most upstream MINOS planes,

3. The time gap between the MINERνA track and the MINOS track is less than 200 ns.

The matching procedure starts by projecting the MINERνA track to the first active MINOS plane and projecting the MINOS track to the last active MINERνA plane. It requires that the distance between the projection and the other track activity is less than 40 cm in both cases. If more than one projection satisfies the requirements, the one with the shortest distance is selected. If no projection satisfies the requirements, then the POCA method is used along the projections. The goal is to identify the cases where the muon scatters in the passive material between the MINERνA and MINOS detectors.

Charge and Momentum Reconstruction

Since the MINERνA detector is not magnetized, it can not measure the momentum or charge of exiting muons. This work is done with measurements in the MINOS detector.

The muon charge is determined by the deflection of the matched track in the MINOS magnetic field. The charge of the muon is directly related to the sign of curvature of the deflection. The muon momentum is usually measured in two ways: range and curvature. For the low energy muons contained in the MINOS detector, the more precise range method is used. The curvature method calculates the initial result using the equation:

$$p_\mu = 0.3BR, \tag{3.2}$$

where p_μ is the momentum of muon (MeV/c), B is the magnetic field in MINOS (kGauss), and R is the radius of curvature (cm). Then the momentum of the muon is approximated using a Kalman filter.

In order to reconstruct the muon's momentum at the interaction vertex, the energy loss in the passive material between two detectors must be added. The energy loss is calculated using the Bethe-Bloch equation [3]. More details can be found in Ref. [37] and [38].

3.2.7 Recoil System Reconstruction

The recoil system in this analysis consists of the clusters passing the following criteria:

1. They are not associated with the muon track.

2. They are not low activity clusters or cross talk candidates.

3. They are within a time window (-20 ns, +35 ns) of the event time.

The recoil energy is the sum of all of these clusters' energy with some corrections, including a correction accounting for traveling through passive materials, a scaling correction

from tuning to the simulation, and a polyline correction from applying an energy-dependent scale factor. The result can be written in the form:

$$E_{recoil} = poly(E_{recoil}) \cdot \alpha \cdot \sum_{i}^{hits} E_i^{vis} \cdot f_i^{pass}, \tag{3.3}$$

where $poly(E_{recoil})$ is the polyline correction, α is a constant scale factor dependent on the primary vertex position (for the active detector, $\alpha = 1.60$), E_i^{vis} is the visible energy of a hit, and f_i^{pass} is the correction on the energy loss in passive material near the hit.

Passive Material Correction

The assumption in the calculation of the passive material correction is that the number of MEUs per g/cm^2 deposited in scintillator is the same as the deposits in the passive material. The number of MEUs deposited in scintillator is

$$n_{meu} = \frac{e_{vis}}{f_{active} \cdot M_{Sc} \cdot dEdx_{Sc}}, \tag{3.4}$$

where e_{vis} is the visible energy of a hit, M_{Sc} is the mass of scintillator that recorded the hit in g/cm^2, and $dEdx_{Sc}$ is the energy lost in scintillator by MIP in MeV/g/cm^2.

The total energy deposited is estimated to be

$$E = n_{meu} \cdot \sum_{i}^{materials} \left(M_i \cdot dEdx_i\right), \tag{3.5}$$

where the sum is over materials near the hit and the dE/dx values are listed in Tab. 3.1.

TABLE 3.1: dE/dx for materials in the MINERνA detector [37]

Material	Scintillator	Carbon	Iron	Lead
dE/dx (MeV/g/cm^2)	1.936	1.742	1.451	1.122

Multiplicative Scale Factor

An additional correction of a scale factor α is needed to account for additional visible energy losses, such as finite containment, neutral particles, and final-state interactions. The procedure is to minimize the difference between the reconstructed recoil energy and the true hadronic energy, as well as tune the results to the Monte Carlo, where the true hadronic energy is defined as $E_{had} = E_\nu - E_\mu$. Only the events passing all cuts in this analysis are used in tuning and the scale factor α is 1.60 in this analysis since only interactions in the tracker region are used.

Polyline Correction

The polyline correction is also added to account for the residuals in bins of E_{had} in the Monte Carlo. The polyline is formed with the points $(X, Y) = (\bar{E}_{had}(1 + \mu), \bar{E}_{had})$ from (0, 0) to (50, 50) in unit of GeV, where $\bar{E}_{had}$ is the true hadronic energy in that bin and μ is the mean of the Gaussian fit for the residual $\frac{E_{recoil} - E_{had}}{E_{had}}$ in that bin. Note that bins with $E_{had} < 0.3$ GeV are interpolated linearly to 0.

Uncertainties on recoil reconstruction will be discussed in Chap. 6.4.3.2.

CHAPTER 4

Simulation

The simulation of the MINERνA experiment is accomplished in four steps. The first step is to simulate particle production and transport in the NuMI beamline, with neutrinos produced via weak decays. The neutrino flux is predicted by the G4numi beam Monte Carlo simulation. Then the interactions of those neutrinos are generated in the MINERνA detector by the GENIE simulation [39]. The third step is to handle transport of the particles produced in the neutrino interactions, including energy loss, hadronic reinteractions, and the effect of MINOS's magnetic field with a GEANT-based package. The final step is to model the response of the detector to energy depositions and create 'hits' and 'digits' in the same format as real data.

In this chapter, a step by step overview of simulation is presented.

4.1 Beam Simulation

The NuMI beamline is simulated using the G4numi (Geant4 version 9.2.p03 NuMI) package. G4numi is a Geant4-based implementation of the NuMI beamline and the MINERνA specific version uses the FTFP_BERT (Fritiof with Pre-compound and Bertini cascade)

hadronic physics list for modeling hadron production by pC collisions in the target, reinteractions within the production target and magnetic horns, and further propagation down the beamline. For energies greater than 5 GeV, FTFP_BERT uses the FRITIOF string model to generate the primary hadronic interactions, the Lund model for fragmentation into hadrons, and precompound splines to de-excite the remnant nucleus. For energies less than 5 GeV, FTFP_BERT uses the Bertini model to simulate the intranuclear cascade.

The output of the beam simulation includes the information of the neutrino production, such as the position and kinematics, and record of upstream interactions and material transversed. Fig. 4.1 shows the raw output of the beam simulation.

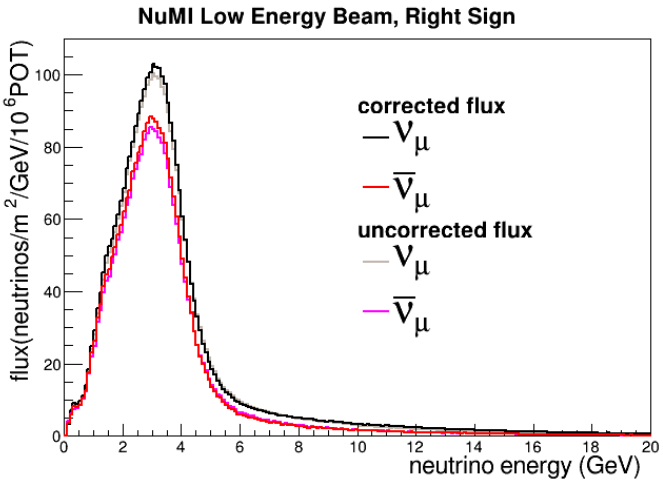

FIG. 4.1: The dotted lines show the raw output of the beam simulation, the uncorrected flux.

The hadronic models used in the simulation are expected to be not accurate because low Q^2 interactions followed by hadronization are not well predicted due to the strong coupling of QCD. Data constraints are needed. Therefore, a new procedure to reweight the flux prediction was developed using the external hadron production data [40].

Hadron Production Reweighting

In order to predict the neutrino flux more accurately, MINERνA corrects the prediction by reweighting events based on the measurements from external pC hadron production data. The external data used to reweight the process $pC \to \pi^{\pm}X$, $pC \to K^{\pm}X$, $pC \to pX$ are from the following experiments:

- NA49 is a large acceptance hadron detector used to investigate p-p, p-A, and A-A reactions. It collected $p - C$ data at 158 GeV/c in the CERN north area.
- Barton et. al collected p-A data at 100 GeV/c using the Fermilab Single Arm Spectrometer in the M6E beamline.

In the NA49 and Barton experiments, the cross-section was measured as a function of the transverse momentum P_T, and Feynman x, described as [41]

$$x_F \sim \frac{2P_L}{\sqrt{s}},$$

where P_L is the longitudinal momentum of the produced particle and $\sqrt{s}$ is the total center of mass energy. The comparisons of cross-sections for $pC \to \pi^{\pm}X$ between FTFT_BERT and NA49 are shown in Fig 4.2. In NuMI, hadrons with x_F=[0.05, 0.15] and P_T=[0.1, 0.6] GeV/c are focused nearly parallel to the beam direction, allowing them to enter the decay pipe. This produces a peak in the flux in the energy range E_ν=[1.0, 5.0] GeV, shown in Fig. 4.1. Note that the discrepancy between data and the simulation becomes larger as p_T increases.

Recall that the NuMI beamline is produced by a 120 GeV/c proton beam that is different from the experiments listed above, so an energy scaling is applied to account for the difference using the Monte Carlo package FLUKA [41] [42].

The reweighting factor is the ratio of data to FTFP_BERT values of the invariant

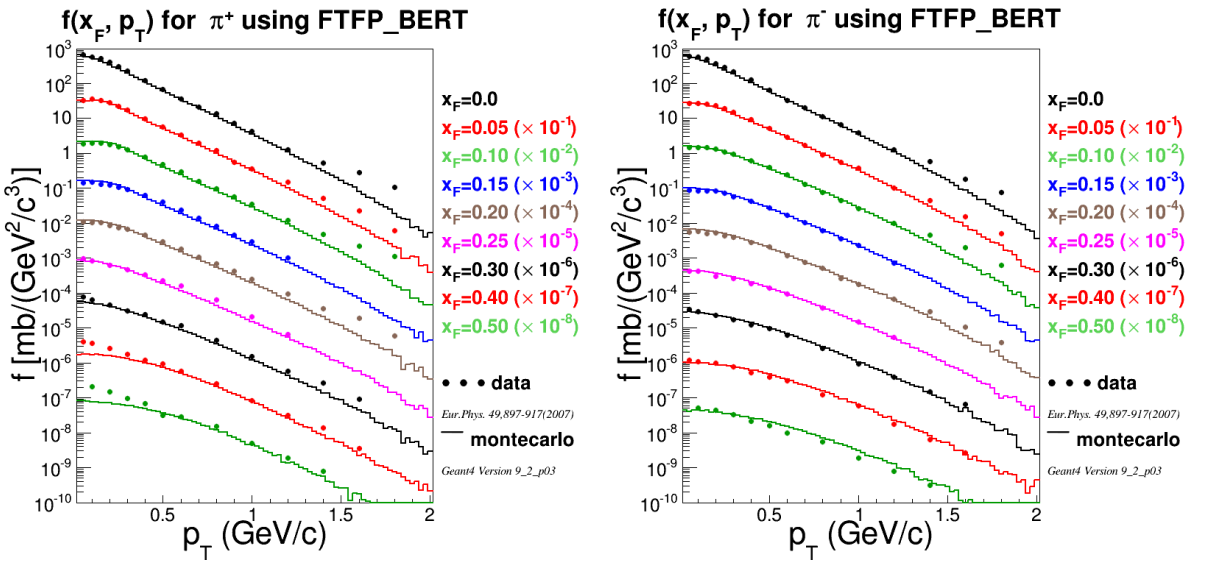

FIG. 4.2: A comparison of NA49 and FTFP_BERT predicted hadron cross-sections for $pC \to \pi^+ X$ (left) and $pC \to \pi^- X$ (right) [24].

cross-section

$$f(E, x_F, p_t) = E\frac{d^3\sigma}{dp^3},$$

and can be written as

$$RW = \frac{f(x_F, p_t, E = 158\text{GeV})_{data}}{f(x_F, p_t, E)_{g4numi}} \cdot \frac{f(x_F, p_t, E)_{fluka}}{f(x_F, p_t, E = 158\text{GeV})_{fluka}}.$$

This factor is applied to hadronic production, particles re-interactions, and attenuation of the proton beam in the NuMI target. Kaons are subject to similar reweighting. Proton production outside the target remains unchanged, and it is a very small component of the neutrino flux [24]. Therefore, there is no correction on such events.

Events with energy outside of the kinematic range of the data and interactions producing a final state that was not measured, are not constrained or reweighted. In this case, the reweighting factor is set to be 1. The kinematics that are reweighted are summarized in Tab. 4.1.

TABLE 4.1: A summary of hadron production interactions constrained by data sets

Process	Proton Energy(GeV)	Kinematics	Data Set
$pC \to \pi^{\pm}X$	158	$x_F < 0.5$	NA49 [43]
$pC \to K^{\pm}X$	158	$x_F < 0.2$	NA49 [44]
$pC \to pX$	158	$x_F < 0.95$	NA49 [45]
$pC \to \pi^{\pm}X$	100	$x_F > 0.5$	Barton [46]

The Flux Results

Fig. 4.3 shows results of the predicted NuMI flux for both neutrino and anti-neutrino mode, although this analysis utilizes neutrino mode only. The distributions only show the energy spectrum up to 20 GeV because this analysis does not exclude events with higher incoming neutrino energy. This analysis utilizes the neutrino flux from 0 GeV to 100 GeV with an integrated number of $2.90883 \times 10^{-9}/\text{cm}^2/\text{POT}$. The high values of the neutrino weighted/unweighted flux ratio come from the significant data-MC discrepancy in NA49 results (Fig. 4.2).

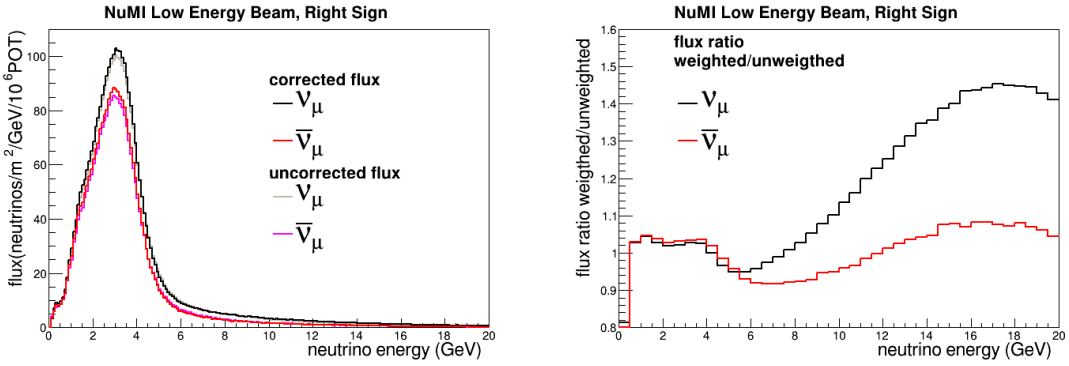

FIG. 4.3: Results of the flux prediction (left) and the reweighting factors (right).

4.2 Neutrino Interactions Simulation

MINERνA utilizes GENIE (Generates Events for Neutrino Interaction Experiments version 2.6.4), a Monte Carlo event generator, to generate neutrino interactions in nuclear matter, as well as modeling the propagation of the produced hadrons through the nucleus [47]. GENIE generates neutrino interactions in the energy range of 100 MeV to 500 GeV (although it is capable in the energy range of 1 MeV to 100 TeV), in a geometrical description of the MINERνA detector, with the predicted flux. There are three steps in GENIE's simulation: nuclear medium modeling, neutrino interactions, and final state interactions (FSI). The output of the neutrino interactions simulation is the species and four-momentum of each particles produced in the final state and the interaction. The output becomes the input to the detector response simulation, which will be discussed in the next section. This section describes GENIE models implemented in each step.

4.2.1 Cross-section Models

GENIE provides the cross-section as a function of E_ν on event-by-event basis for different interaction channels. To simulate a neutrino interaction, GENIE calculates the probability of the interaction where the neutrino carries the energy E_ν. There are several steps in the calculation. First is to calculate the total cross-section for all interaction channels,

$$\sigma_{tot}\left(E_\nu\right) = \sum_i \sigma_i\left(E_\nu\right)$$

where i represents different interaction channels, such as scattering from the nucleus, individual nucleons, quarks, and atomic electrons. The calculation of $\sigma_{tot}\left(E_\nu\right)$ in GENIE has been tuned to available world data, shown in Fig. 4.4. Then the neutrino is traced through the detector and GENIE determines whether it interacts accounting for variations

in density and atomic number. If the neutrino undergoes a scattering process GENIE samples the interaction by the probability function

$$P_i\left(E_\nu\right) = \sigma_i\left(E_\nu\right)/\sigma\left(E_\nu\right).$$

Once the interaction channel is determined, the event kinematics is modeled in that particular process. In this subsection, the interaction channels, that are relevant to this analysis, are discussed, including *quasi-elastic scattering, charged current resonance production, and charged current deep inelastic scattering.*

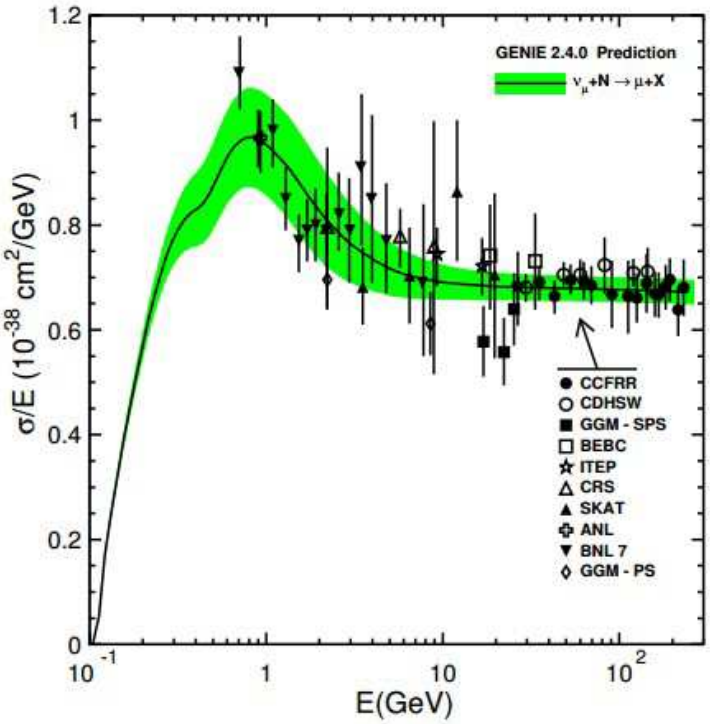

FIG. 4.4: GENIE's ν_μ CC inclusive NuMI cross-section on an isoscalar target compared with the world's data. Reprinted from [47].

4.2.1.1 Quasi-elastic Scattering

Quasi-elastic scattering includes the processes $\nu_\mu n \to \mu^- p$ and $\bar{\nu}_\mu p \to \mu^+ n$. The former one with the neutron embedded in carbon is the signal in this analysis. GENIE utilizes the Llewellyn-Smith formalism to model quasi-elastic scattering [12]. Recall that in Chap. 1 1.3.2, the differential cross-section is given as

$$\frac{d\sigma}{dQ^2} = \frac{M^2 G^2 cos^2\theta_c}{8\pi E_\nu^2}\left(A(Q^2) \mp B(Q^2)\frac{(s-u)}{M^2} + \frac{C(Q^2)(s-u)^2}{M^4}\right), \tag{4.1}$$

where Q^2 is the square of the momentum transferred from the incident (anti-)neutrino to the free nucleon, G is the weak coupling constant, M is the mass of the free nucleon, E_ν is the energy of incident (anti-)neutrino, θ_c is the Cabibbo angle, s and u are two Mandelstam variables, $s - u = 4ME_\nu - Q^2 - m_l^2$. The $\mp$ term is negative for neutrinos and positive for anti-neutrinos.

The hadronic current is parameterized in terms of Lorentz-invariant form factors that are modeled in GENIE using experimental results. Two vector form factors are related to electromagnetic form factors, that is parameterized according to the prescription of BBBA2005 [48]. The axial form factor is modeled as a dipole with $M_A = 1.01$ GeV/c^2,

$$F_A\left(Q^2\right) = \frac{F_A\left(0\right)}{\left(1 + Q^2/M_A^2\right)^2} \tag{4.2}$$

where $F_A(0)$ = -1.267 is measured from neutron decay and the axial mass $M_A = 0.99$ GeV/c^2 is measured by bubble chamber experiments. Using the partially conserved axial vector hypothesis (PCAC) [49], the pseudo-scalar form factor is related to the axial form factor

$$F_P = \frac{2M_n^2 F_A}{M_\pi^2 + Q^2}. \tag{4.3}$$

As mentioned before, Pauli blocking in the RFG is implemented for quasi-elastic scattering and the momentum of outgoing nucleon is required to be above p_F before final state interactions are simulated.

4.2.1.2 Resonance Production

In the channel of resonance production, the neutrino interacts with a nucleon and excites it to a Δ or N^* resonance. This channel is the main background in this analysis. GENIE utilizes the Rein-Sehgal formalism for modeling the differential cross-section of neutrino-induced baryon resonance production [50]. The total resonance production cross-section is the sum of 16 resonances which include:

$$P_{33}(1232), S_{11}(1535), D_{13}(1520), S_{11}(1650),$$

$$D_{13}(1700), D_{15}(1675), S_{31}(1620), D_{33}(1700),$$

$$P_{11}(1440), P_{13}(1720), F_{15}(1680), P_{31}(1910),$$

$$P_{33}(1920), F_{35}(1905), F_{37}(1905), P_{11}(1671),$$

where the resonances are labeled with the incoming partial wave $L_{2I,2J}$ where I is the isospin and J is the total angular momentum.

The $P_{33}(1600)$ and $F_{17}(1900)$ are included in Rein-Seghal model, but are omitted in GENIE because the PDG considers them to be ambiguous [3]. The axial form factor is taken to be a dipole with axial mass $M_A^{RES} = 1.12$ GeV/c^2.

4.2.1.3 Continuum Scattering

In the continuum scattering, the neutrino interacts with a single quark. The quark is ejected from the nucleon and hadronizes. GENIE calls all such inelastic events that do not

produce a resonance 'DIS', in contrast to the common definition of $Q^2 > 1$ (GeV/c)^2 and $W > 2$ GeV. GENIE utilizes the Quark Parton Model to calculate the DIS cross-section, in the form of

$$\frac{d^2\sigma^{\nu,\bar{\nu}N}}{dxdQ^2} = \frac{G_F^2}{2\pi x}\left(\frac{m_W^2}{Q^2+m_W^2}\right)^2 \times \frac{1}{2}\left(Y_+ F_2^{\nu,\bar{\nu}N} - y^2 F_L^{\nu,\bar{\nu}N} \pm xY_- F_3^{\nu,\bar{\nu}N}\right), \qquad (4.4)$$

where $Y_\pm = 1 \pm (1-y)^2$, G_F is coupling constant, x and y are Bjorken variables ($x = Q^2/(2\nu)$, $y = (p\cdot q)/(p\cdot k)$), and F_1, F_2, F_3 are form factors.

The low Q^2 regime is modified by the Bodek-Yang model. The Bodek-Yang model extends DIS to low Q^2 and E_ν but it may double count some interactions predicted by Rein-Sehgal. GENIE avoids the double counting by limiting the Rein-Sehgal model to $W_{cut} < 1.7$ GeV/c^2 and then reducing the prediction from the Bodek-Yang model for $W_{cut} < 1.7$ GeV/c^2 to agree with measurements of 1π production, 2π production, and the total cross-section. The 1π production and 2π production are also sources of background in this analysis. Various parameters in the GENIE DIS models are used to evaluate uncertainties.

4.2.2 Nuclear Medium Modeling

GENIE utilizes the formalism of the Relativistic Fermi Gas (RFG) to model the nuclei [18]. The neutrino-nucleon scattering modeling utilizes the impulse approximation, where the recoil nucleons are assigned an average binding energy. The Fermi momentum p_F and the binding energy E_b for some nuclei as examples are listed in Tab. 4.2. GENIE includes the Bodek-Ritchie model to describe the high momentum tail in the nucleon momentum distribution. In addition, GENIE implements Pauli blocking by prohibiting quasi-elastic nucleon production in the final state where the nucleon's momentum is inside the Fermi sea ($p_N < p_F$). Resonance baryon production is not subject to Pauli-blocking. The

deep inelastic scattering structure functions are modified to account for shadowing, anti-shadowing, and the EMC effect by the Bodek-Yang procedure [51].

TABLE 4.2: The Relativistic Fermi Gas Model parameters for the Quasi-elastic Scattering

Nucleus	p_F for neutron (proton)(MeV/c)	E_b(MeV)
Carbon	221 (221)	25
Iron	263 (251)	36
Lead	283 (245)	44

4.2.3 Final State Interactions

GENIE utilizes an intra-nulcear cascade model (INC) to simulate final state interactions, which is performed by the INTRANUKE subpackage. The INC model treats the nucleus as an ensemble of quasi-free nucleons that contain Fermi motion and binding energy. The cascade is implemented as a series of possible encounters where a hadron can interact with nucleons in the nucleus. The INC model tracks the hadron in steps of 0.05 fm through the nuclear environment. At each step, the probability of the hadron interacting is related to mean free path, which is a convolution of the hadron cross-section and the density of the nuclear medium. If the hadron is determined to interact, the interaction type is selected randomly according to relative cross-sections [47], shown in Fig. 4.5.

There are two implementations INTRANUKE in GENIE, denoted hA and hN. The previous paragraph describes the hA model implementation and it is used in this analysis. The hA model uses the mean free path to determine whether and how FSI occurs. This model has been tested and verified extensively with data [47] [52]. The hN model considers interactions with nucleons in the nuclear environment and simulates the complete particle cascade. Fig. 4.6 shows the difference between hA and hN models. This analysis does not use the hN model.

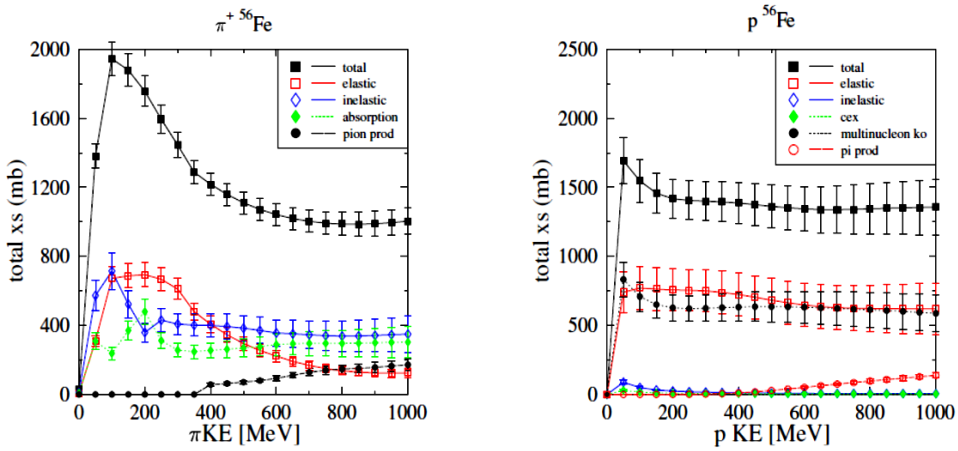

FIG. 4.5: Relative cross-sections for π^+-Fe (left) and p-Fe (right), utilized in the hA INC model. Reprinted from [47].

4.3 Simulating Events in the Detector

Geant4 is used by MINERνA to simulate the propagation of particles through the mass of the detector [39]. All processes but hadron physics are simulated by the default Geant4 modules by propagating particles in time steps and determining the interactions with the material. The hadron physics is simulated with the QGSP_BERT module, which uses a Bertini intranuclear cascade model for describing the hadron transportation in the nuclear environment at energies below 10 GeV.

The MINERνA simulation framework also models the optical readout and electronics systems. The simulation converts the energy deposited in scintillator into photoelectrons using a comparison of $\frac{dE}{dx}$ of muon between the data and MC. Saturation of the scintillator in regions with large $\frac{dE}{dx}$ is simulated with the Birk's law [53]. Then the simulation framework propagates the photoelectrons through a simulated optical readout channel.

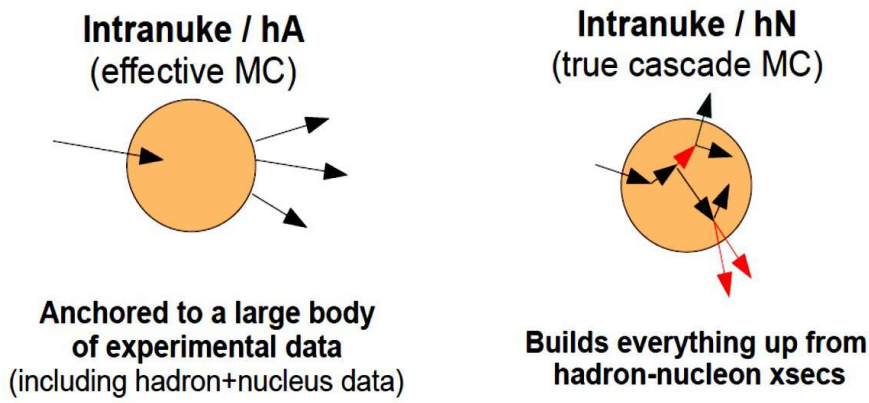

FIG. 4.6: An illustration of hA and hN INC models. Reprinted from Ref. [47].

.

Decalibrations are applied so that the light output matches the data.

Some aspects of the data are not simulated in the Geant4, such as rock muons, dead time, and event overlap in the detector. To adequately model the complicated environment within a NuMI beam spill, a data overlay procedure was developed, which pairs each generated neutrino event with one spill of real data that comes from the run period being modeled. Beam spill information from the gate and hits within the time window (-50 ns, 200 ns) around the simulated neutrino events are used throughout the rest of simulation. By overlaying with data, the simulated events now account for the unsimulated aspects.

The simulated particles exit the back from MINERνA and may enter the MINOS near detector. A MINOS-written GEANT3 simulates such particles in the MINOS near detector, including the passage of charged particles through the magnetic field and the readout of energy deposit in active elements. The simulated information is used to match a reconstructed track from MINERνA into MINOS.

CHAPTER 5

Muon Tagging

A robust procedure for identifying Michel electrons is essential to the MINERνA experiment. By tagging Michel electrons, the muon and pion tracks can be identified from the decay products: muons decay into Michel electrons, and pions decay into Michel electrons by first decaying to muons. Michel tagging plays a crucial role in many analyses. For example, the analysis of single pion production tags events with Michel electrons as the signal [32]. Tagging events with Michel electrons can also be used to reject background events, such as in the CCQE two tracks analysis [7]. Other examples include the systematic uncertainty estimation on EM energy scale (see Sec. 6.4.3.2) using Michel electrons.

In this chapter, the muon decay properties are listed and the Michel tagging procedure is described in detail. In addition, the `MichelTool` performance and efficiency/purity estimation are shown, as well as the possible background to this tagging procedure.

5.1 Muon and Michel Electron

The muon was first discovered in cosmic rays by Neddermeyer and Anderson in 1937. It is an unstable elementary particle, with a unitary negative charge, and is classified as a

lepton. It has a mass about 200 times the mass of an electron. Muons decay via a simple and well-known process described in the Standard Model. In 1948, when searching for the muon decay products, a continuous spectrum of electrons in the decay final products was found, which indicated a three-body decay accompanied by two neutral particles. These neutral particles are now known as muon neutrino and electron anti-neutrino. The experimentally measured mass of a muon is 106.66 MeV/c^2 and the muon lifetime in vacuum is 2.197 μs. In the framework of the Standard Model, there is no substructure to the muon and the lifetime (τ_μ) is related to the Fermi coupling constant (G_F), including QED corrections. The lifetime is given by,

$$\tau_\mu^{-1} = \frac{G_F^2 m_\mu^5}{192\pi^3} F(\frac{m_e^2}{m_\mu^2})(1 + \frac{3}{5}\frac{m_\mu^2}{m_W^2}[1 + \frac{\alpha(m_\mu)}{2\pi}(\frac{25}{4} - \pi^2)], \tag{5.1}$$

where $F(x) = 1 - 8x + 8x^3 - x^4 - 12x^2 \log x$, and m_μ and m_e are the masses of the muon and the electron, respectively. The fine-structure constant α value at the m_μ scale, $\alpha(m_\mu)$, is given by

$$\alpha(m_\mu) = \alpha^{-1} - \frac{2}{3\pi} ln(\frac{m_\mu}{m_e} + \frac{1}{6\pi}) \approx 136, \tag{5.2}$$

Due to lepton number conservation and charge conservation, a muon decays through weak interaction — into one electron, one electron antineutrino, and one muon neutrino — described as the virtual W boson coupling to a lepton and a neutrino. Considering the masses of various leptons, the W boson can only couple to the electron and corresponding neutrino in muon decay. The electron in the final state of muon decay is known as a Michel electron. The decay process can be written as:

$$\mu^- \to \nu_\mu + \bar{\nu}_e + e^- \text{ and } \mu^+ \to \bar{\nu}_\mu + \nu_e + e^+.$$

The Feymann diagram of muon decay in the mode above is shown in Fig. 5.1:

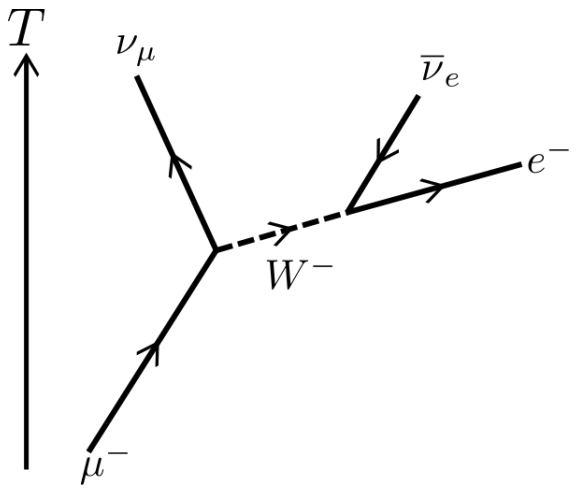

FIG. 5.1: Muon Decay Fermi Diagram

If the general four fermion interactions with no derivatives is assumed, the muon differential decay rate is given by [54],

$$\frac{d^2\Gamma(\mu^\pm \to e^\pm \nu\bar{\nu})}{dx\, d\cos\theta_e} = \frac{m_\mu}{4\pi^3} W_{e\mu}^4 G_F^2 \sqrt{x^2 - x_0^2}(F_{IS}(x) \pm P_\mu \cos\theta_e F_{AS}(x)), \tag{5.3}$$

where $W_{e\mu} = (m_\mu^2 + m_e^2)/2m_\mu$, $x = E_e/W_{e\mu}$, and $x_0 = m_e/W_{e\mu} (= 9.7\times10^{-3}) \leq x \leq 1$, E_e is the energy of the $e^\pm$, and m_e and m_μ are the masses of the positron and muon, respectively. The plus and minus signs correspond to positive and negative muon decay. θ_e is the angle between the muon polarization ($\overrightarrow{P}_\mu$) and the electron (or positron) momentum. The functions $F_{IS}(x)$ and $F_{AS}(x)$ are the isotropic and anisotropic parts of the $e^\pm$ energy spectrum, respectively. They are given by

$$F_{IS}(x) = x(1-x) + \frac{2}{9}\rho(4x^2 - 3x - x_0^2) + \eta x_0(1-x), \tag{5.4}$$

and

$$F_{AS}(x) = \frac{1}{3}\xi\sqrt{x^2 - x_0^2}[1 - x + \frac{2}{3}\delta(4x - 3 + (\sqrt{1 - x_0^2} - 1))], \tag{5.5}$$

where ρ, η, ξ, and δ are called Michel parameters [55]. The Michel parameters in the Standard Model are $\rho = \frac{3}{4}$, $\eta = 0$, $\xi = 1$, and $\delta = \frac{3}{4}$.

The differential branching ratio in the Standard Model, shown in Fig. 5.2, can be written in a simple form

$$\frac{d^2\Gamma(\mu^{\pm} \to e^{\pm}\nu\bar{\nu})}{dx\, d\cos\theta_e} = \frac{m_\mu^5 G_F^2}{192\pi^3} x^2[(3-2x) \pm P_\mu \cos\theta_e(2x-1)] \tag{5.6}$$

if electron or positron polarization is not measured and x_0 is ignored.

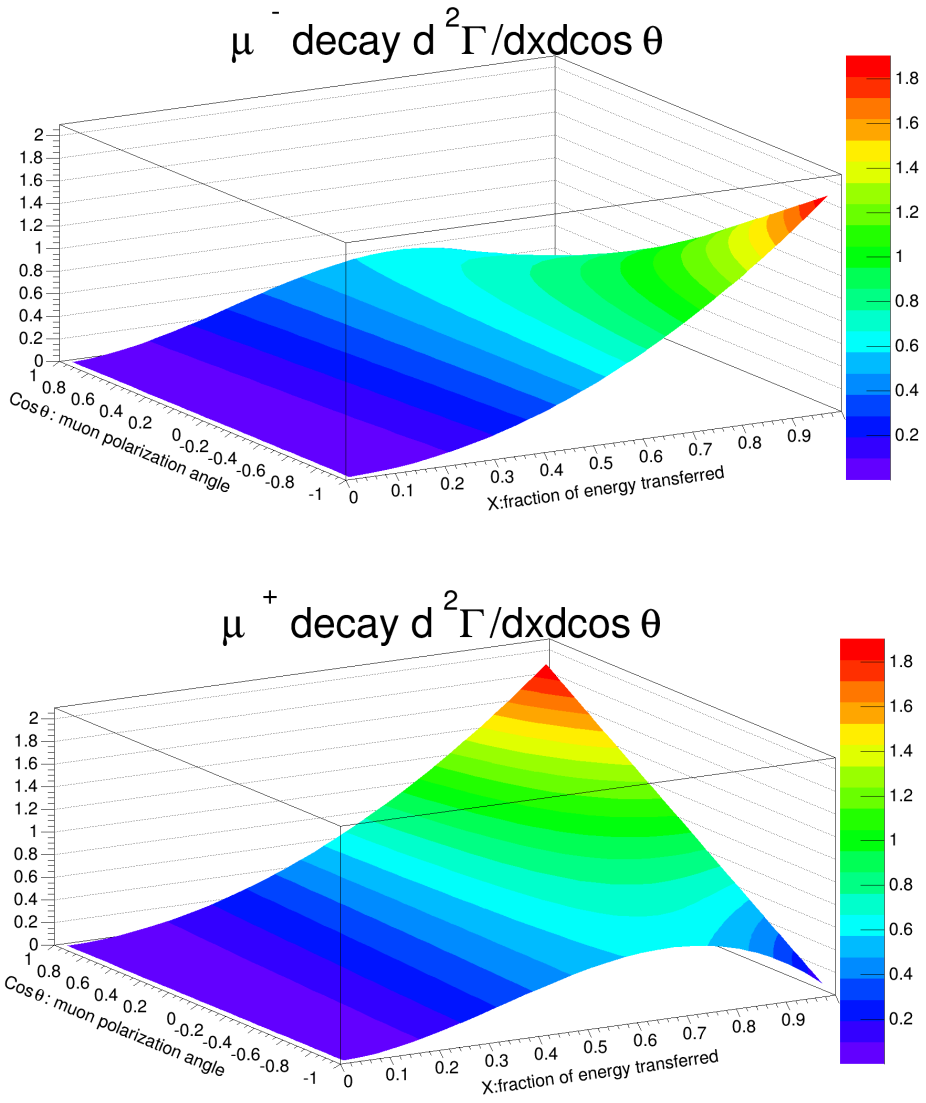

FIG. 5.2: The double differential Cross-section of negative muon (top) and positive muon (bottom) decay as a function of x, fraction of energy transferred, and $\cos\theta$, the muon polarization angle.

By integrating Eq. 5.6 over the angle, the differential cross-section of negative/positive muon decay is a function of the energy of electron, shown in Fig. 5.3, in the form of

$$\frac{d\Gamma}{dE_e} = \frac{m_\mu^5 G_F^2}{96\pi^3}[3(\frac{E_e}{W_{e\mu}})^2 - 2(\frac{E_e}{W_{e\mu}})^3].$$

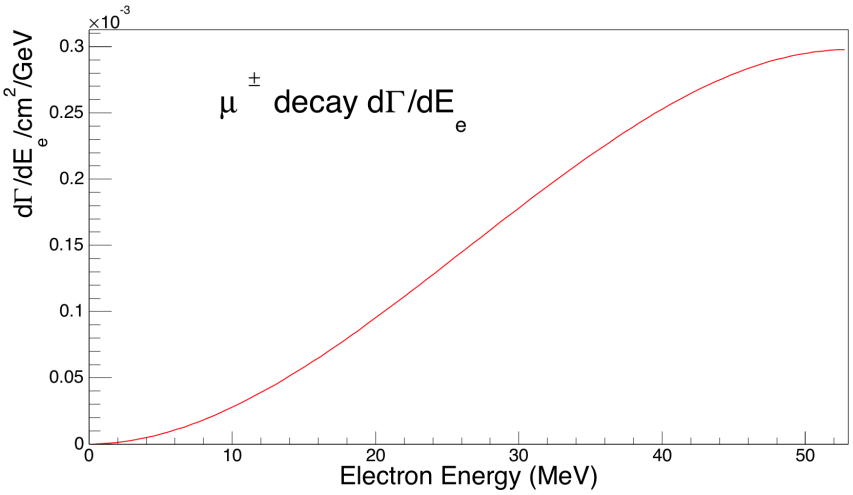

FIG. 5.3: The differential Cross-section of muon decay as a function of the electron energy E_e.

5.1.1 Muons in the MINERνA Detector

As mentioned in Chap. 3, there are generally two fates for negative muons entering the MINERνA detector:

Go through the detector — Most muons going through the detector will be caught either by the outer detector or by the MINOS detector (Fig. 5.4). The MINOS-matching procedure is utilized to identify the muon tracks that go out of the MINERνA inner detector and enter the MINOS detector. In CCQE-like one track analysis, it identifies the *one track*. Recall that, going-through rock muons are the calibration source for many effects.

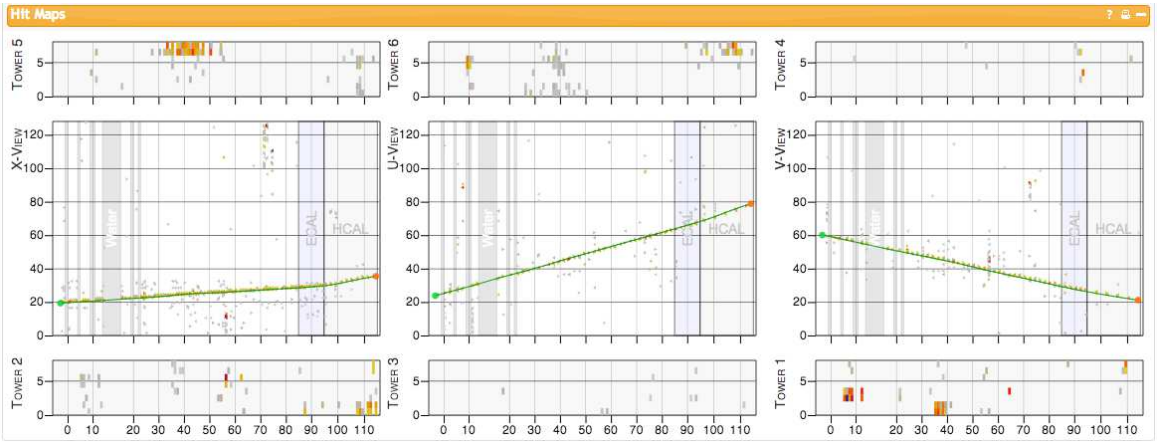

FIG. 5.4: Rock Muon that traveled through the MINERνA detector. Run 2000, Subrun 1, Gate 594, TimeSlice 1.

Stop in the detector — Muons with lower momentum can stop in the MINERνA detector (Fig. 5.5). In this case, MINOS matching does not work. Negative stopping muons face two fates: absorption and decay.

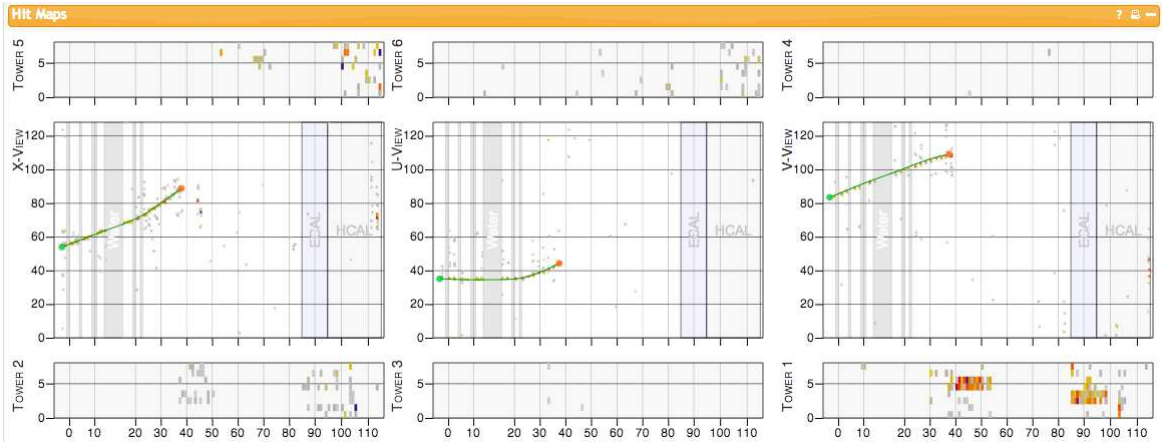

FIG. 5.5: Rock Muon that stopped in the MINERνA detector. Run 2160, Subrun 1, Gate 597, TimeSlice 1.

- **Absorption**. 4% of negative muons are captured by atoms in the scintillator detector (mostly C_8H_8 [31]). Captured muons lose energy by emitting photons and transmitioning to a lower energy level. Muon's orbits have much shorter radii when compared to electrons because muons have much larger mass than electrons, 105.69

MeV to 0.51 MeV. Thus, muons could possibly fall onto the nucleus. At this point, the interaction between the muon and the proton producing neutron is called a "capture".

- **Decay**. 96% of μ^- decay into Michel electrons, which can possibly be identified by the tagging procedure.

For positive muons, all of them are expected to decay into Michel electrons (positrons) because positive muons can not be captured by the nucleus.

Muons are common in the MINERνA experiment. When the incoming neutrino beam travels through the rock, which sits upstream of the MINERνA detector, some of the neutrinos interact with the rock and produce muons, which are called rock muons. Most rock muons will travel through the MINERνA detector (Fig. 5.4), while some of them stop in the detector, which can produce Michel electrons (Fig. 5.5). Another source of the muons in MINERνA is neutrino interactions within the detector, such as the CCQE interactions ($\nu_\mu + n \rightarrow \mu^- + p^+$) considered in this thesis.

5.1.2 Michel Electron Properties

The properties of Michel electrons and the corresponding measurable quantities in the MINERνA detector are described in this section, including the energy spectrum, the maximum travel distance, and the lifetime.

- Michel electrons from stopping muons carry up to 54 MeV kinematic energy in the center of the mass coordinate system.

- The electrons with 54 MeV of energy can travel up to 30 cm in the scintillator detector. As shown in Fig. 5.6, the continuous slowing down approximation (CSDA) range of electrons with 54 MeV kinematic energy is 22.33 g/cm^2. Considering that the density

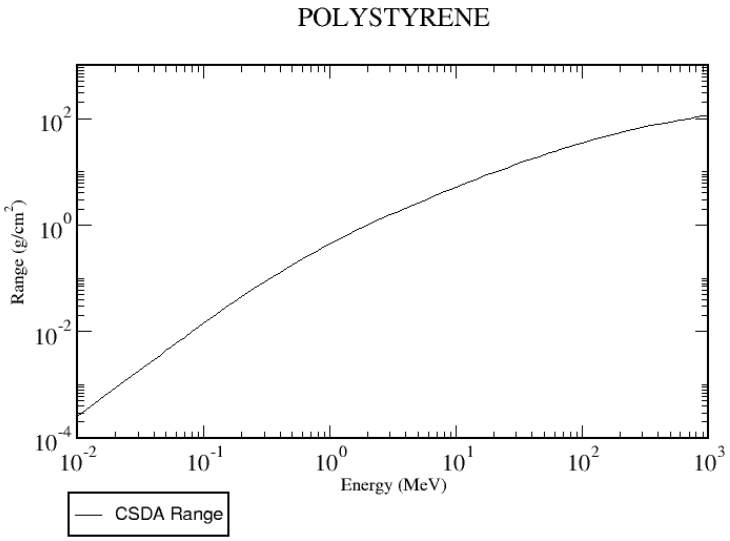

FIG. 5.6: The CSDA range of electrons in the plastic scintillator. Reprinted from [56].

of the plastic scintillator is 1.043 g/cm^3 [57], the maximum distance an electron with 54 MeV can travel is roughly calculated as

$$\frac{22.33\text{g/cm}^2}{1.043\text{g/cm}^3} = 21.41\text{cm}.$$

A sightly larger number, 30 cm, was chosen in the reconstruction stage of `MichelTool` to account for the effects that are not included in this simple calculation, such as the photon radiation of Michel electrons, and the gaps between detector modules.

- The lifetime of a Michel electron is 2190 ns in a vacuum and 2026 ns in carbon.

All of these measurable quantities are utilized to develop the requirements in the tagging procedure of `MichelTool`, described in the following section.

5.2 MichelTool

The `MichelTool` is a software module written to tag Michel electrons in MINERνA. The user of the tool inputs the position in the detector at which to look for a Michel electron and the time during the beam spill at which to begin the search. In this thesis, the event vertex and event time are input to the tool so as to identify low energy π^+ in inelastic events that would otherwise mimic quasi-elastic events. Random positions and times are also fed in to study the misidentification rate.

This tool operates in two stages: the search stage and the reconstruction stage. In the search stage, the `MichelTool` finds the most significant portion of the energy deposited by the electron. Then the reconstruction stage refines the search, potentially collecting additional energy. The output of the reconstruction stage is a Michel "prong" consisting of the energy depositions (hits) associated with the Michel electron, as well as other quantities calculated by the tool, such as total energy, position, and timing.

The details of both stages are described in this section. In the following section, the tool's performance is shown including the efficiency, purity, and distributions of Michel electrons. In the last section of this chapter, a procedure to measure the mis-identification rate is discussed. The pseudo-code of the `MichelTool` is listed in App. B and a flowchart of the `MichelTool` is shown in Fig. 5.7.

5.2.1 Search Stage

In the search stage, the tool looks for the significant energy depositions by possible Michel electron candidates in three different views, the X/U/V views. This stage consists of two sequential sets of selections. Instead of treating the clusters in three different views

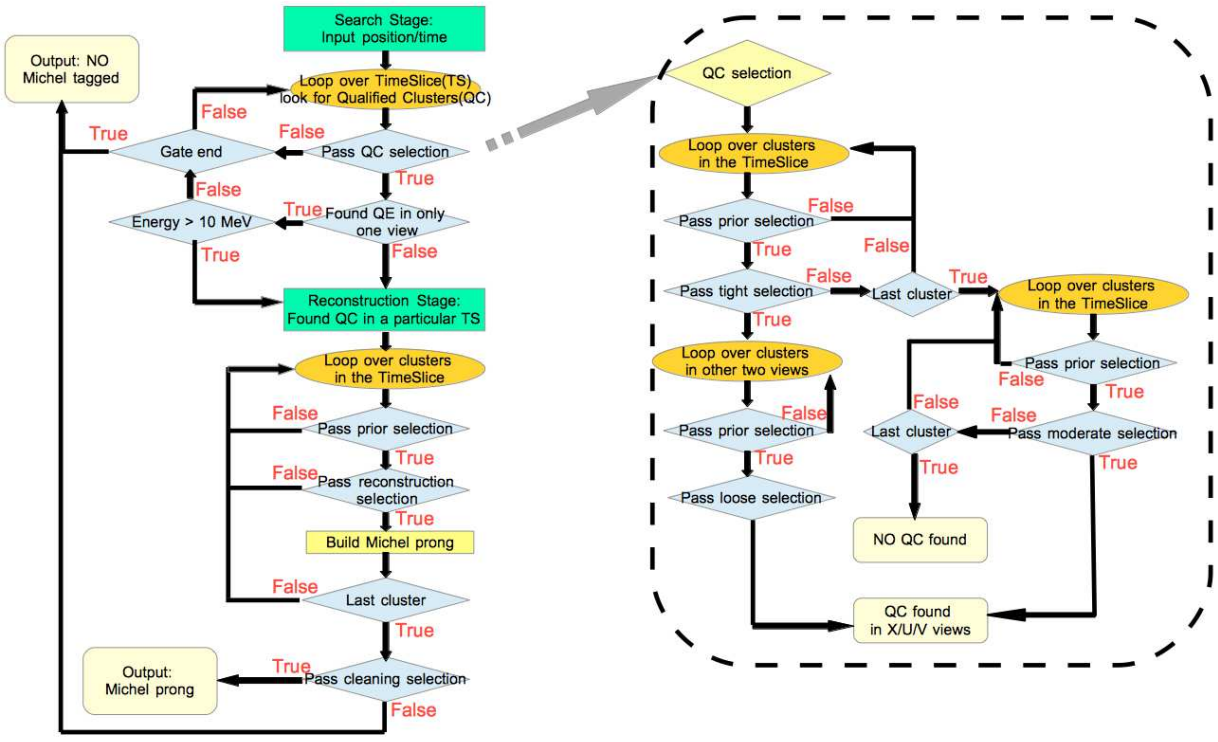

FIG. 5.7: The flowchart of the `MichelTool`.

equally, the tool tries to use tight selections to look for Michel electron candidates in one of three views, and if significant energy is found, the tool uses loose selections to search for significant energy deposited in the other two views. If the tool finds no significance energy using the tight/loose combination, then the tool treats the three views equally and uses moderate selections to search for the candidates. A new term ***Qualified Clusters***, is introduced here. Details of tight/loose/moderate selections are given following the Qualified Clusters description.

Qualified Clusters

Qualified Clusters are the clusters that pass a series of selections, including prior selections, tight/loose selections or moderate selections. This is the key concept in the search stage of the `MichelTool`, which indicates the significance of the energy deposited in the X/U/V views. The presence of Michel electrons is judged by the presence of Qualified

Clusters.

The series of selections used to identify Qualified Clusters include:

- **Prior Selections**:

  1. A Qualified Cluster is required to be an unused cluster that is not considered as a low activity or a cross talk candidate. Unused means that the cluster has not been reconstructed as part of a track or a prong. The Michel electron candidate hits should not come from muon tracks or pion tracks that have been reconstructed in MINERνA.
  2. Qualified Clusters are required to appear later than the times that users supplied to the tool.
  3. Qualified Clusters are required to be within a fiducial volume bounded by module 27 and 85 in the Z direction, and a hexagon with 850 mm apothem in the X,Y plane. This insures that the cluster's energy is well measured.
  4. A Qualified Cluster is required to have at least one digit with the discriminator "fired". Fired in this content means that at least one discriminator in the pair is triggered due to energy above the threshold, so that the timing is measured correctly.
  5. A Qualified Cluster should carry visible energy above 1 MeV. This is a requirement that aims to exclude random hits.

- **Tight/Loose Selections**:

  Tight selections : Along the z direction, a Qualified Cluster should be located within 30 mm of the position that the user supplied to the tool, and along one of the X/U/V directions, it should be located within 50 mm of the position.

When energy deposits (above 1 MeV) are found in one of the X/U/V views, the tool then uses loose selections to search for qualified clusters in the other two views.

Loose Selections : Along the z direction, a Qualified Cluster should be located within 200 mm of the position that the user supplied to the tool, and along the X/U/V directions, it should be located within 250 mm of the position.

If no significant energy depositions are found in any views using tight/loose selections, the tool then moves to moderate selections to look for Qualified Clusters in all three views.

- **Moderate Selections**: Along the z direction, a Qualified Cluster should be located within 125 mm of the position that the user supplied to the tool, and along the X/U/V directions, it should be located within 175 mm of the position.

The sequential plots (Fig. 5.8, Fig. 5.9, Fig. 5.10, Fig. 5.11, Fig. 5.12, and Fig. 5.13) of different quantities in the selections series used to select Qualified Clusters were produced on both the data (black dots in plots) and on the simulation (red lines in plots). The pink areas in the following plots represent the clusters due to true Michel electrons in simulation. The red areas represent the primary clusters in the Michel electrons. Here, the primary cluster in a Michel electron is defined as the cluster with the highest energy in all Michel clusters. These plots are in the same order: left plots are area-normalized and right plots are normalized to the beam exposure; bottom plots are the log scale of the corresponding top plots.

Fig. 5.8 shows distributions of discriminators of all clusters passing prior selection 1, 2, and 3. In the distributions, 0 means the none of discriminators of the cluster are fired. 1 means at least one discriminator of the cluster is fired. Fig. 5.9 shows distributions of clusters' energies, where the clusters pass prior selection 1, 2, 3, and 4 (discriminator

fired). Fig. 5.10, Fig. 5.11, Fig. 5.12, and Fig. 5.13 show distributions of clusters passing all prior selections, i.e. prior selection 1, 2, 3, 4 (discriminator fired), and 5 (cluster energy). Fig. 5.10 shows the distribution of the distance between the cluster and the user input position along the Z direction. Fig. 5.11, Fig. 5.12, and Fig. 5.13 show distributions of such distance along directions of X, U, and V, respectively.

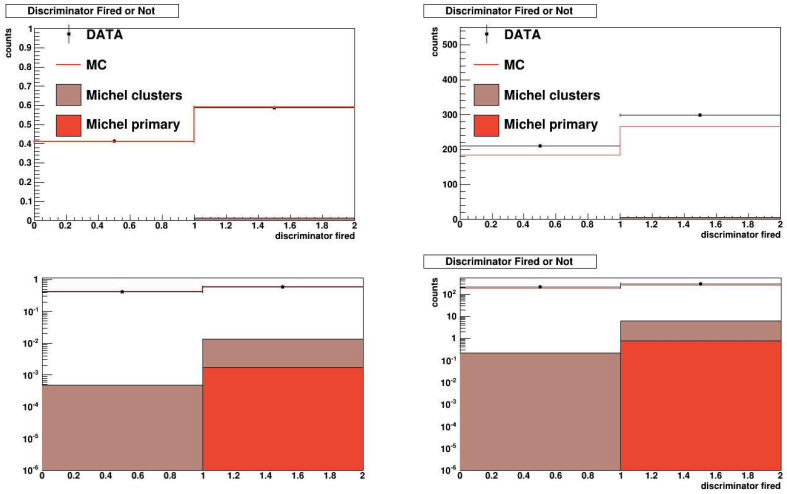

FIG. 5.8: Distributions of discriminators' values of all clusters passing the first three prior selections. 1 means the discriminator was fired and 0 means it was not fired. Left plots are area normalized and right plots are POT normalized.

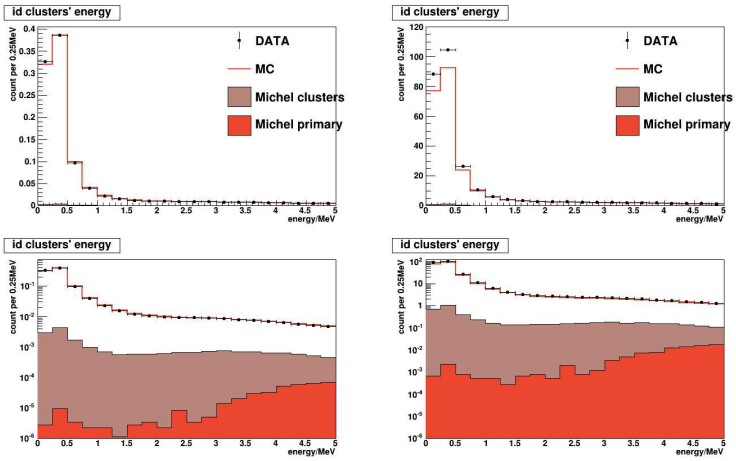

FIG. 5.9: Energy distributions of clusters passing the first four prior selections. Left plots are area normalized and right plots are POT normalized.

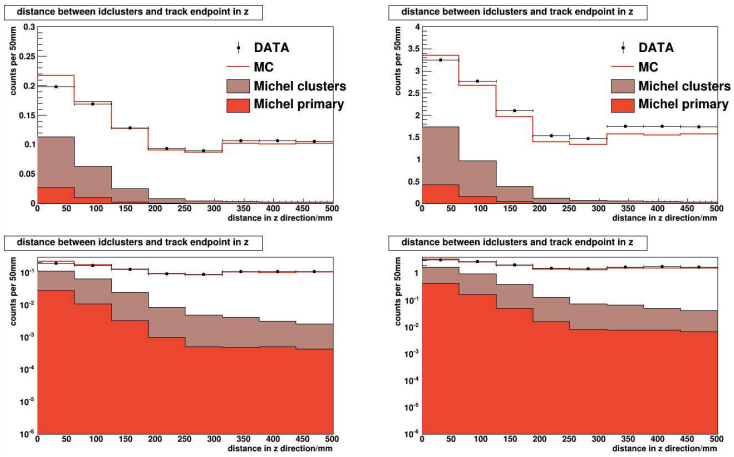

FIG. 5.10: Distribution of the distance along Z direction between user input position and clusters passing all prior selections. Left plots are area normalized and right plots are POT normalized.

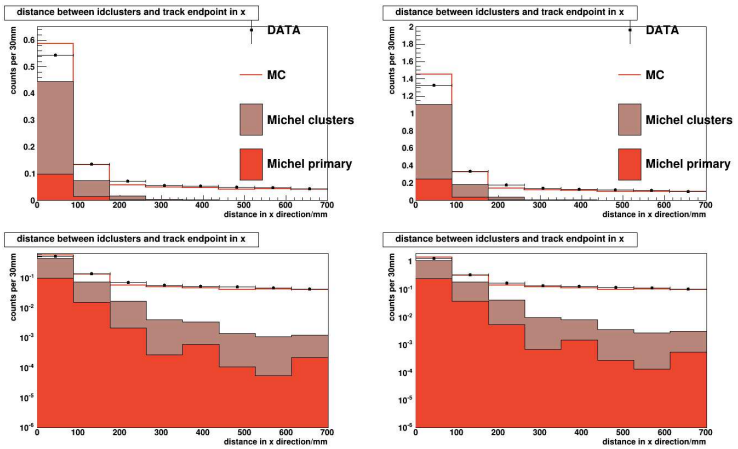

FIG. 5.11: Distribution of the distance along X direction between user input position and clusters passing all prior selections. Left plots are area normalized and right plots are POT normalized.

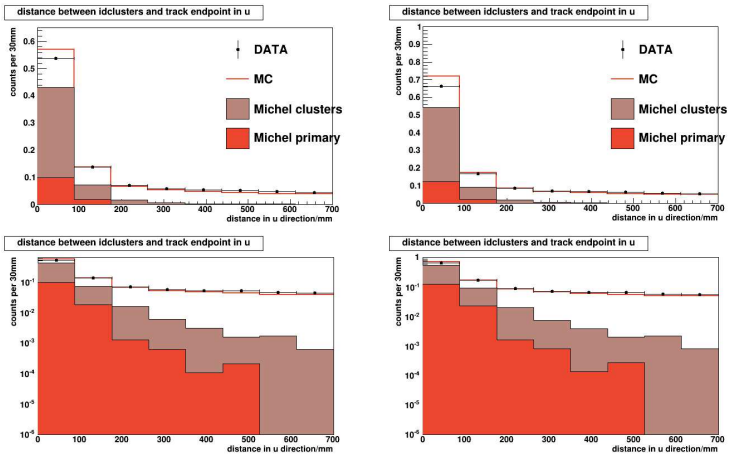

FIG. 5.12: Distribution of the distance along U direction between user input position and clusters passing all prior selections. Left plots are area normalized and right plots are POT normalized.

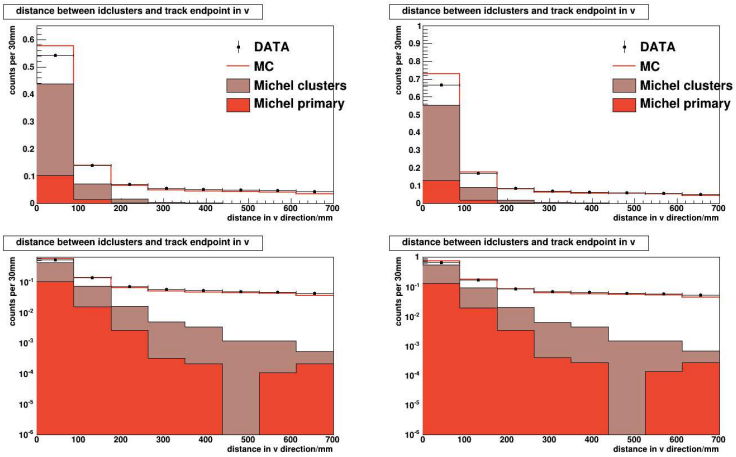

FIG. 5.13: Distribution of the distance along V direction between user input position and clusters passing all prior selections. Left plots are area normalized and right plots are POT normalized.

Candidate Formation

If Qualified Clusters are found in two views or in all three views, the `MichelTool` considers them as Michel electron candidates. If Qualified Clusters are found in only one view, the `MichelTool` requires that the summed energy of the Michel prong be larger than 10 MeV. Michel candidates with less energy are discarded.

5.2.2 Reconstruction Stage

If Qualified Clusters are identified in the previous search stage, then the tool proceeds to the reconstruction stage. In this stage, a Michel prong is constructed with clusters passing prior selections and reconstruction selections. Here, the prior selections are the same as the prior selections used in the search stage. Reconstruction selections require clusters appearing in the time window (50 ns earlier and 50 ns later than the user input time), and locating within a sphere with 30 cm radius and centered at the user input position.

In addition, some basic reconstruction quantities of a Michel electron are calculated in the reconstruction stage. These output quantities are:

Category — The Michel electron's category is the number of views with Qualified Clusters. Category 0 means no Michel electron candidate is tagged by the `MichelTool`. Category 1,2, and 3 correspond to OneView, TwoView and ThreeView Michel electrons, respectively.

Energy — The Michel electron's energy is the summation of visible energy of all clusters that are reconstructed into the Michel electron prong. The visible energy is corrected by the attenuation coefficients.

Time — The Michel electron's time is the difference between the average time of all qualified clusters and the time supplied by the user (eg, the parent track time, the

event time, or a given random time).

Distance — The Michel electron's distance is the distance between the average position of all qualified clusters and the user input position. Note that, for OneView Michel electrons, only two dimensional distance is calculated. The positions of Michel electrons are calculated using $U = \frac{X - Y \times \sqrt{3}}{2}$ and $V = \frac{X + Y \times \sqrt{3}}{2}$.

Number of Digits — By definition, it is the number of all digits in the Michel electron's prong.

Slice Energy — Michel electron's slice energy is the total energy of all clusters in the timeslice where the Michel electron is tagged.

5.2.2.1 Cleaning Selections

After reconstructing the Michel electron prong, the `MichelTool` utilizes a cleaning procedure that uses various selections on energy and the number of digits in the reconstructed prong to reject the background to Michel electrons. These cleaning selections were introduced by the background study, which is described in Sec. 5.4. The main sources of the background to Michel electrons are afterpulsing, cross-talk, and clusters with unusually large energy due to muons and protons.

The cleaning selections are: (a) the reconstructed energy is required to be less than 55 MeV, (b) the number of digits in the prong is required to be fewer than 35, (c) the total energy of the Michel electron time slice is required to be below 100 MeV, (d) the reconstructed energy and the number of digits should satisfy $N_{digits} < 0.7 \times E_{Michel} + 3$ and $N_{digits} > 0.2 \times E_{Michel} - 1$.

5.2.3 Characterizing the `MichelTool` Using Stopping Muons

The `MichelTool` returns the reconstructed prongs of Michel electrons and some basic quantities described in the reconstruction stage. Distributions of these quantities including energy, time, and distance, generated from the stopping rock muon samples, are shown in this section. Before showing the various distributions, the grouping strategies on Michel electrons are discussed.

All distributions are made from data files from MINERνA playlist 1 and combined data-driven simulation samples that are 8.26% positive muons and 91.74% negative muons. The positive/negative muon portions are calculated from the ratio between positive and negative muons (0.09 ± 0.04) in MINOS, assuming ratios are the same in MINOS and MINERνA.

Rock Muon Selection

The muons are simulated by a data-driven procedure that extracts the useful information including the start point, the momentum, the energy, and the angle, from the rock muon tracks in data and then injects this information into GEANT4 to mimic the particles' path through the MINERνA detector. Michel electrons are tagged near the end of rock muon tracks. Rock muon tracks are required to pass the `RockMuonCheckTool`, which requires that tracks start within the first module of the MINERνA detector and have at least 170 nodes in the track. However, this study focuses on stopping rock muons only. Therefore, for this study the requirement was reduced to 100 nodes. In addition, rock muon tracks are required to: stop in the fiducial volume, be the single track in the timeslice, have no dead downstream channels (ddead), and have fewer than 3 hits with energy greater than 1 MeV ($N(E > 1 \text{ MeV}) < 3$), aiming to exclude hadron tracks. This scan cut is very tight but it renders the background of hadrons negligible.

5.2.3.1 Michel Electrons Characterization

Michel electrons in MINERνA can be characterized using different strategies.

Based on the number of views with energy depositions, Michel electrons are characterized into three categories: **OneView Michel electrons**, **TwoView Michel electrons** and **ThreeView Michel electrons**. If the `MichelTool` identifies a Qualified Cluster in one of three X/U/V views, the reconstructed Michel electron is a OneView Michel electron (Fig. 5.14). Similarly, if Qualified Clusters are found in two of three views or in all three views, the reconstructed Michel electron is a TwoView or ThreeView Michel electron, respectively (Fig. 5.15 5.16). In general, the more views that a Michel electron deposits energy in, the higher the quality of the Michel electrons reconstruction.

Based on the location where they are tagged, Michel electrons are characterized into two types: **Track-end Michel electrons** and **Vertex Michel electrons**. Track-end Michel electrons are literally tagged near the end of tracks (Fig. 5.14 5.15 5.16). Those tracks are muon tracks and pion tracks. Vertex Michel electrons are tagged near the interaction vertices (Fig. 5.17) and can come from pions produced with low enough energy that they were not reconstructed into tracks.

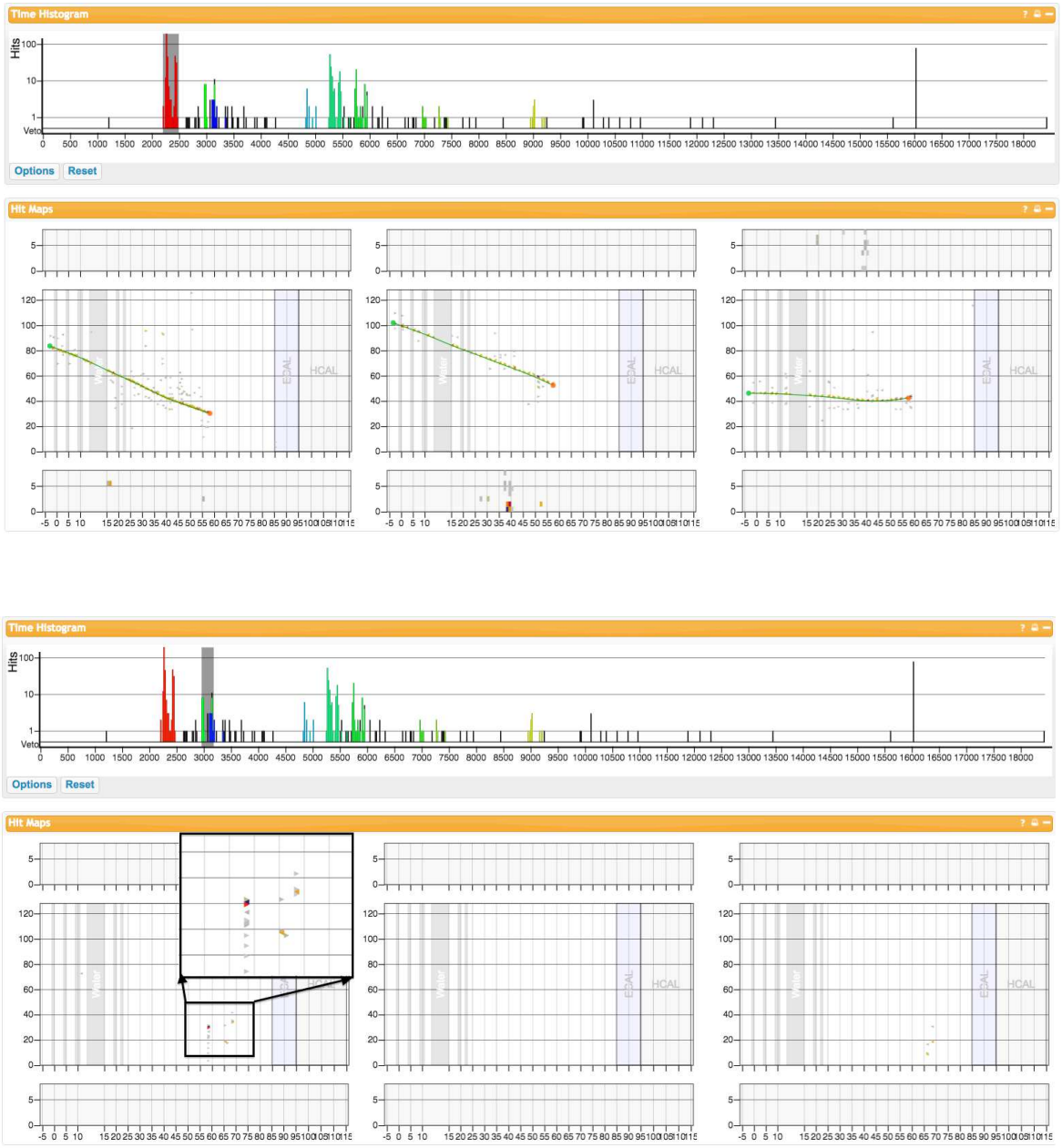

FIG. 5.14: An example of a OneView Michel electron in Run 2017, Subrun 5, Gate 70. It is found in X view. The upper plot shows a muon track stopping in fiducial in timeslice 1 (parent time slice). The lower plot shows the OneView Michel electron in timeslice 2.

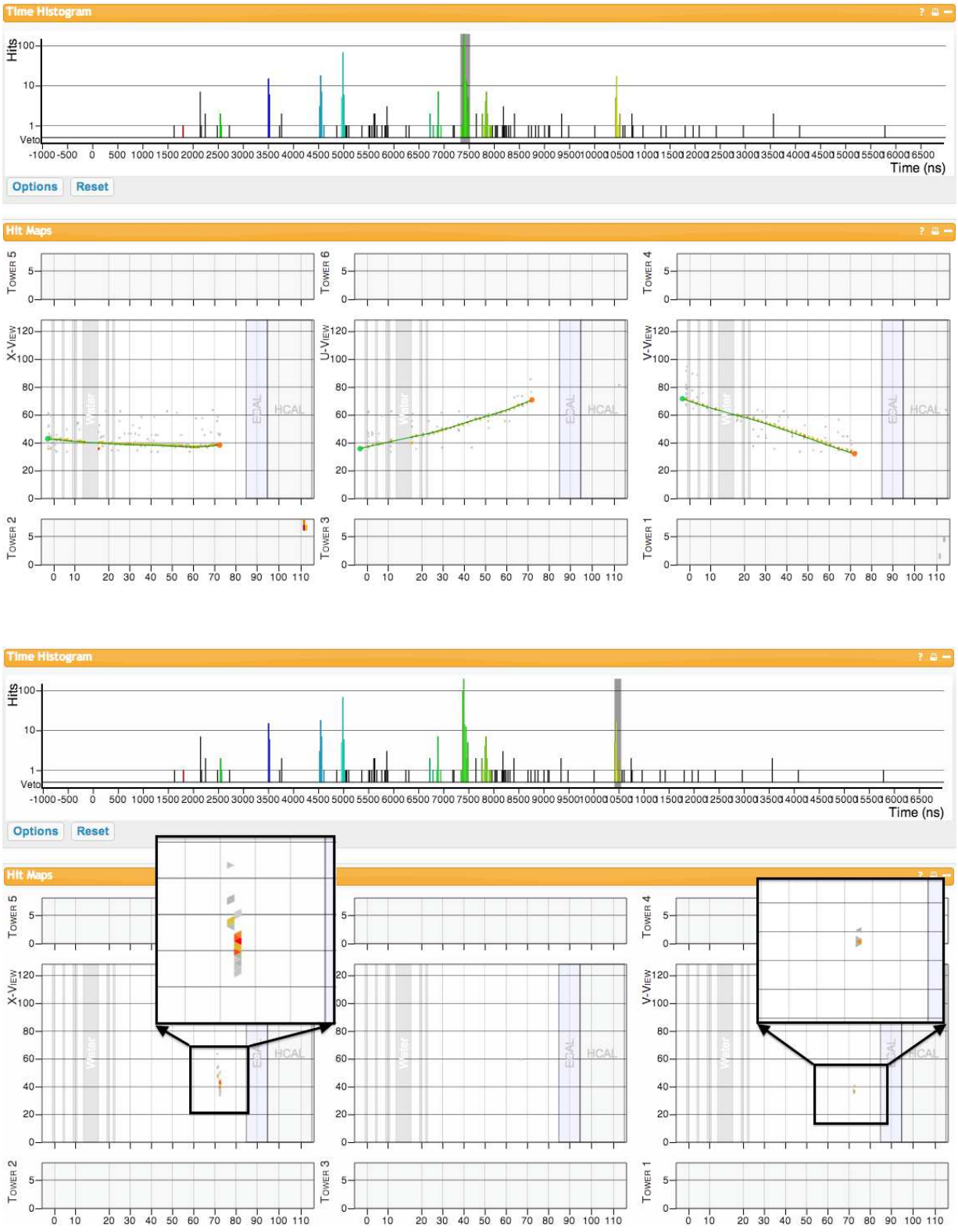

FIG. 5.15: An example of a TwoView Michel electron in Run 2000, Subrun 1, Gate 583. The upper plot shows a muon track stopping in fiducial in timeslice 8. The lower plot shows the TwoView Michel electron in X and V view in timeslice 10.

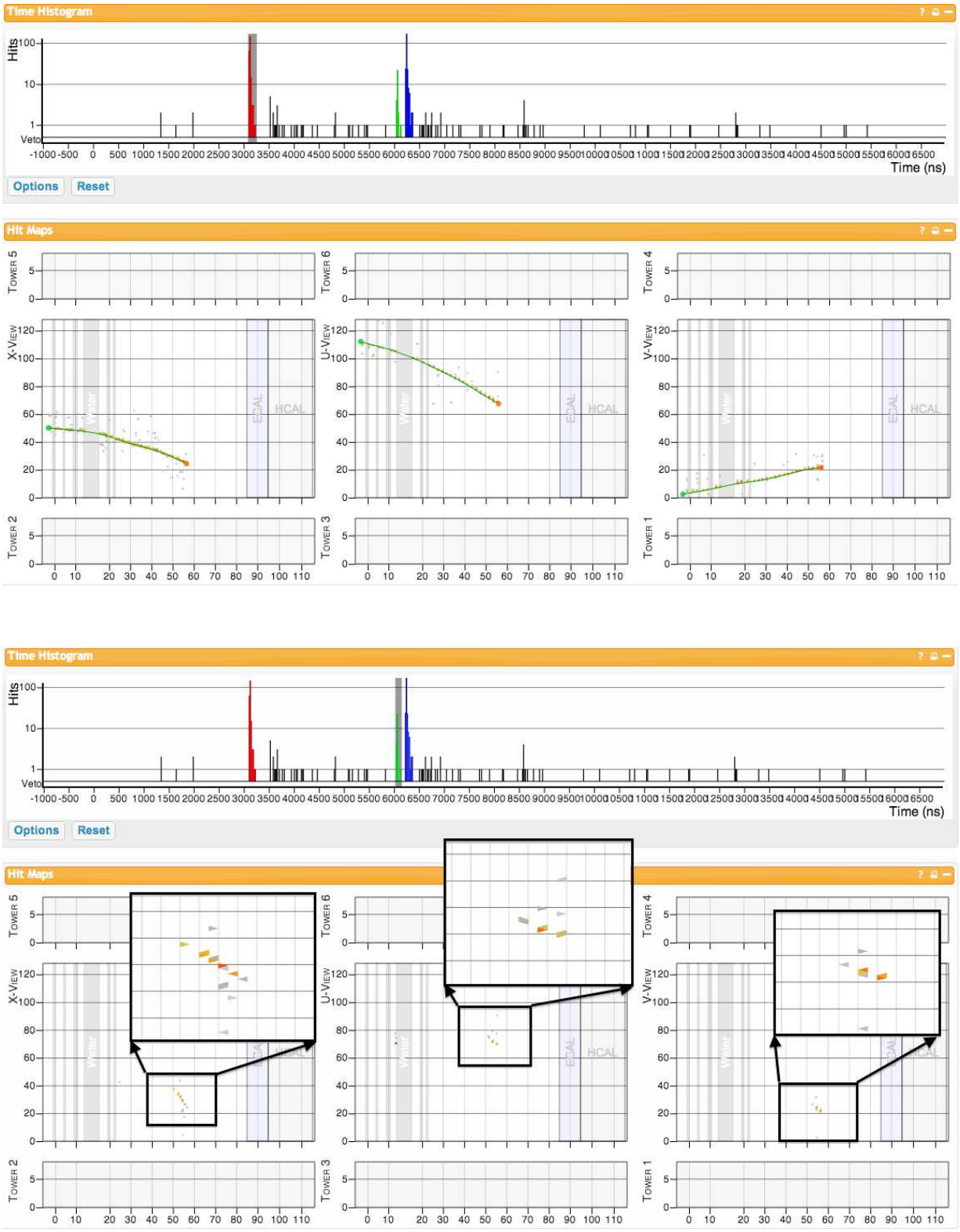

FIG. 5.16: An example of a ThreeView Michel electron in Run 2000, Subrun 1, Gate 80. The upper plot shows a muon track stopping in fiducial in timeslice 1. The lower plot shows the ThreeView Michel electron found in all three views in timeslice 2.

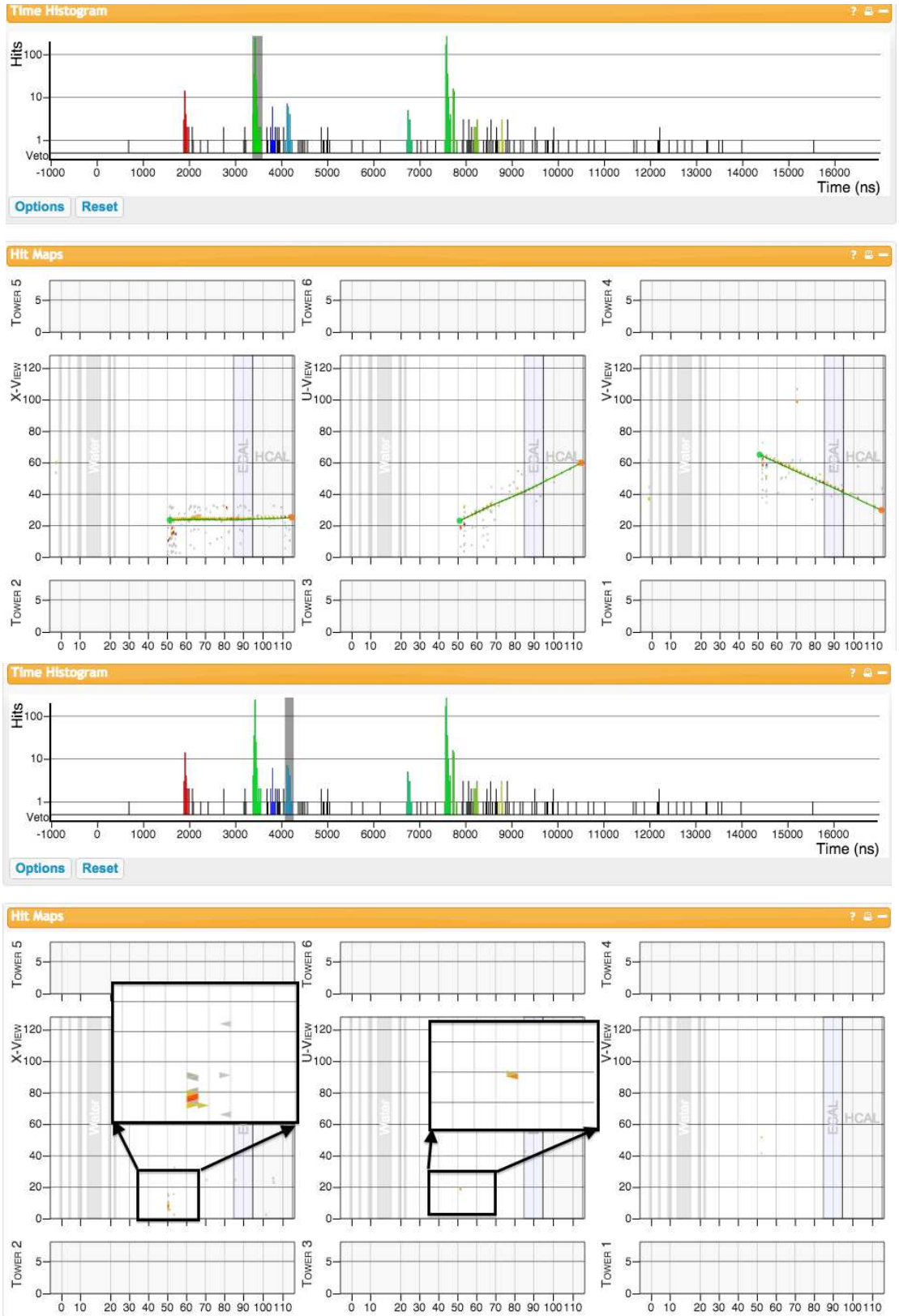

FIG. 5.17: An example of a vertex Michel electron in Run 2003, Subrun 8, Gate 127. The upper plot shows a CCQE-like event candidates with the interaction vertex in fiducial in timeslice 2. The lower plot shows the vertex Michel electron found in X and U view in timeslice 4.

5.2.3.2 Michel Electron Distributions from Rock Muons

Various distributions of Michel electrons are shown in this section. Michel electrons are found in the samples of rock muons. In the following plots (Fig. 5.18 — Fig. 5.22), black dots represent entries from data files and the red line represents entries from simulation samples. The four sub-plots in each figure are in the following order: the top left is OneView Michel electrons; the top right is TwoView Michel electrons; the bottom left is ThreeView Michel electrons; the bottom right is all Michel electrons. Also, Fig. 5.23 — Fig. 5.26 are two dimensional distributions of Michel electrons found in the rock muon samples.

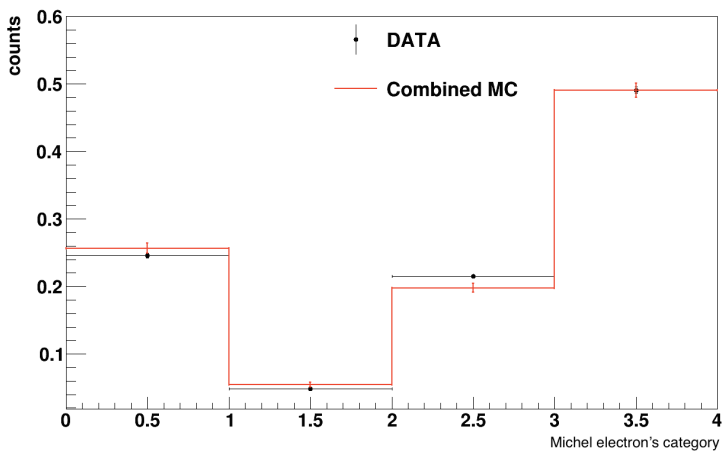

FIG. 5.18: Category Distribution of Michel electrons in the data and combined simulation. 0 means no Michel electron was found. 1, 2, and 3 represent OneView, TwoView, and ThreeView Michel electrons, respectively. The plot is normalized to the number of stopping rock muon tracks.

Michel Electrons — Energy Distributions

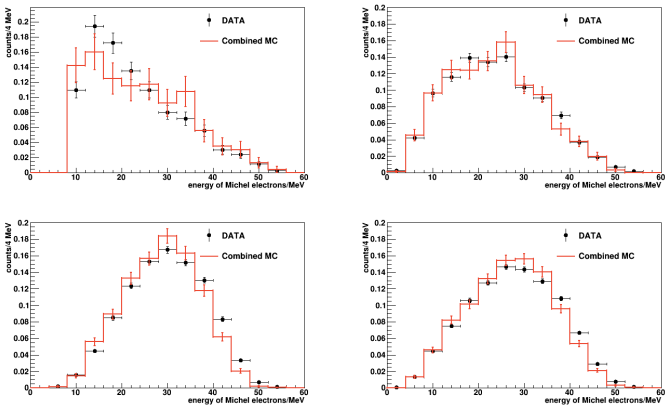

FIG. 5.19: Visible energy distributions of different categories of Michel electrons in the data and combined simulation. Distributions of OneView, TwoView, ThreeView, and all Michel electrons are shown in the top left, top right, bottom left, and bottom right plot, respectively.

Michel Electrons — Time Distributions

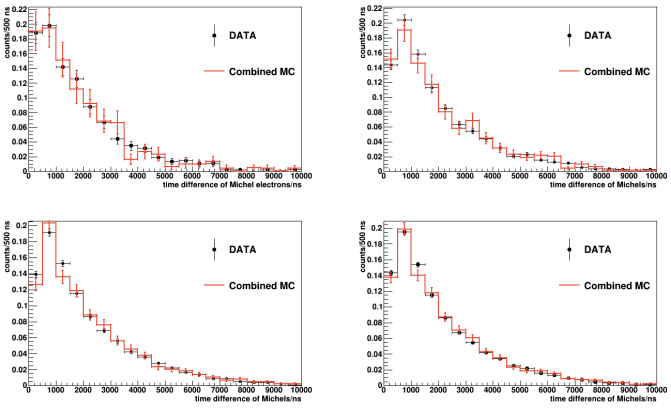

FIG. 5.20: Decay time distributions of different categories of Michel electrons in the data and combined simulation. Distributions of OneView, TwoView, ThreeView, and all Michel electrons are shown in the top left, top right, bottom left, and bottom right plot, respectively.

Michel Electrons — Number of Digits Distributions

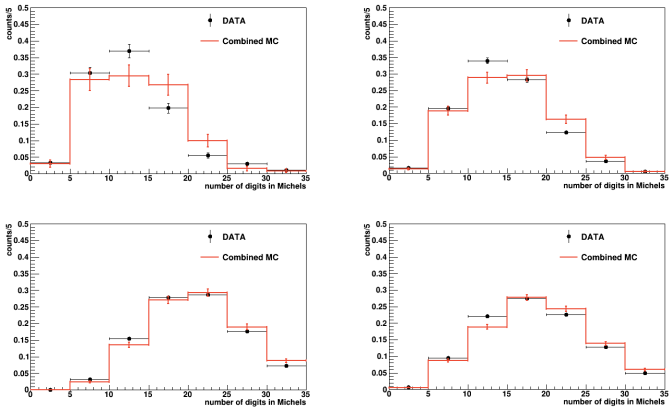

FIG. 5.21: Number of digits distributions of different categories of Michel electrons in the data and combined simulation. Distributions of OneView, TwoView, ThreeView, and all Michel electrons are shown in the top left, top right, bottom left, and bottom right plot, respectively.

Michel Electrons — Distance Distributions

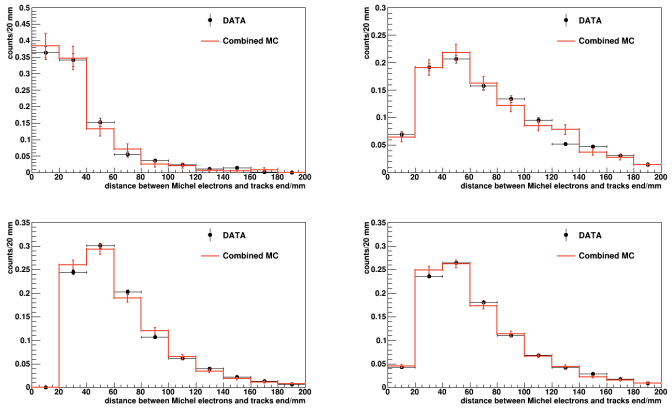

FIG. 5.22: Distance distributions of different categories of Michel electrons in the data and combined simulation. The top left plot shows distributions of OneView Michel electrons. Distributions of OneView, TwoView, ThreeView, and all Michel electrons are shown in the top left, top right, bottom left, and bottom right plot, respectively.

Michel Electrons — Energy vs Time Distributions

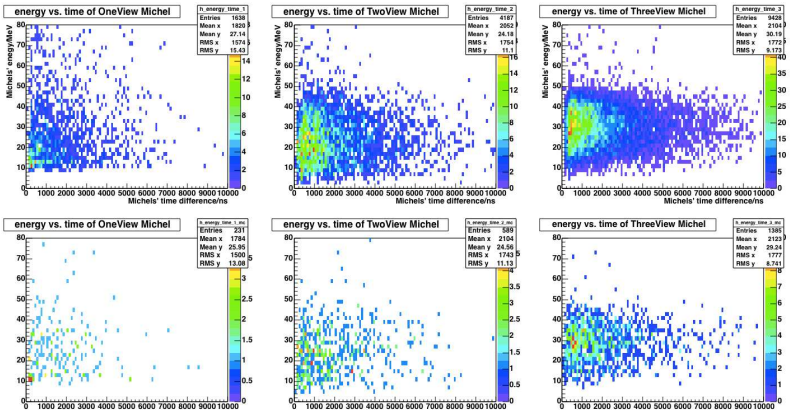

FIG. 5.23: Energy versus time 2D distributions of different categories of Michel electrons in the data and simulation which combines negative muon sample and positive muon sample. Upper plots are distributions from data. Lower plots are distributions from simulation. From left to right are OneView, TwoView, and ThreeView Michel electrons.

Michel Electrons — Distance vs Time Distributions

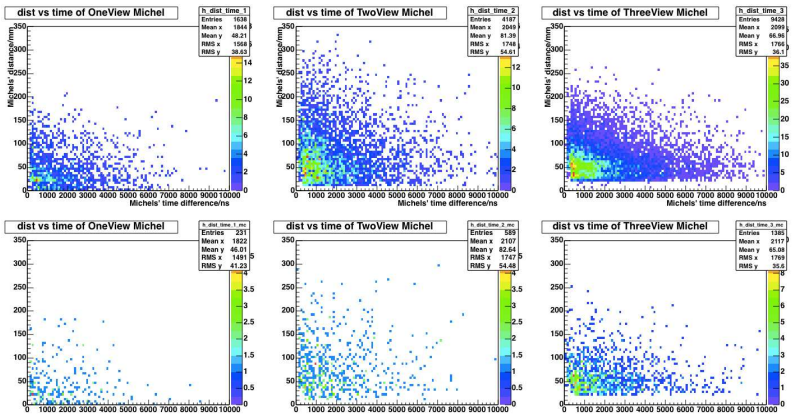

FIG. 5.24: Distance versus time 2D distributions of different categories of Michel electrons in the data and simulation which combines negative muon sample and positive muon sample. Upper plots are distributions from data. Lower plots are distributions from simulation. From left to right: OneView, TwoView, and ThreeView Michel electrons.

Michel Electrons — Distance vs Energy Distributions

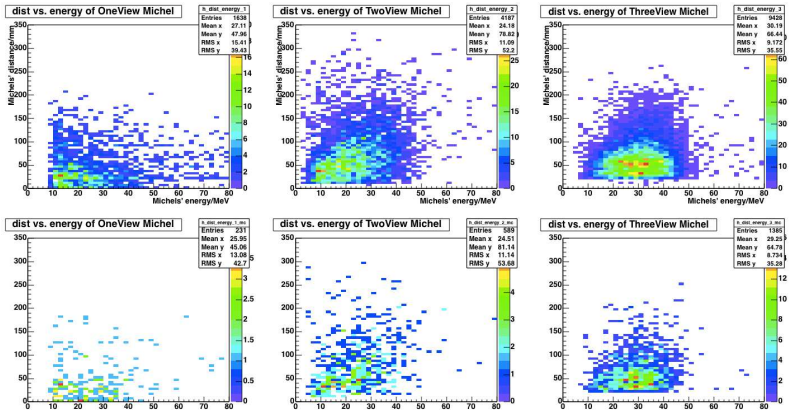

FIG. 5.25: Distance versus energy 2D distributions of different categories of Michel electrons in the data and simulation which combines negative muon sample and positive muon sample. Upper plots are distributions from data. Lower plots are distributions from simulation. From left to right: OneView, TwoView, and ThreeView Michel electrons.

Michel Electrons — Number of Digits vs Energy Distributions

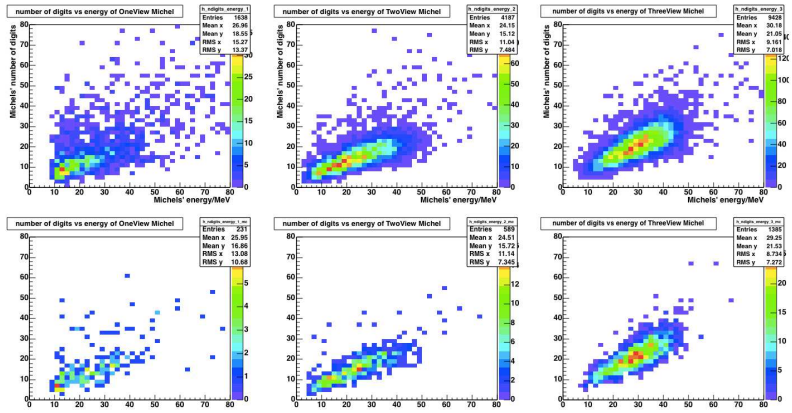

FIG. 5.26: Number of digits versus energy 2D distributions of different categories of Michel electrons in the data and simulation which combines negative muon sample and positive muon sample. Upper plots are distributions from data. Lower plots are distributions from simulation. From left to right: OneView, TwoView, and ThreeView Michel electrons.

5.3 Tool Performance Monitoring

A study of the tool's efficiency and purity has been done using the same set of data files that were used in plotting the Michel electron distributions (Fig. 5.18 — Fig. 5.26). A data-driven simulation samples of rock muons (similar to the ones used to plot Michel electrons distributions) was also used. Additional simulated samples were used to study the effects of overlaying strategies on simulating the background to Michel electrons.

There are three types of simulation samples using different data overlay strategies. **Simulated samples with no data overlay** contain purely rock muons, simulated using the data-driven procedure described earlier. **Simulated samples with regular data overlay** contain simulated rock muons and some activities from data chosen from random gates. The digits from the data are within a time window that is 50 ns before and 200 ns after the rock muon time in simulation. This is the default simulation strategy for most analyses. **Simulated samples with long data overlay** contain simulated rock muons and some activities from data chosen from random gates. The digits from data are within a time window that is 50 ns before the rock muon time in simulation and until the end of that gate. In principle, this is the best simulation.

The goal of overlaying Monte Carlo files with randomly picked data gates is to mimic some unsimulated activities in the data. This is crucial to the Michel electron study because part of the background to Michel electrons is not explicitly simulated in the Monte Carlo. Examples of unsimulated background are hits due to PMT afterpulsing and energy deposited by neutrons that were created outside the detector. It is necessary to introduce the background of Michel electrons by overlaying the randomly picked data onto Monte Carlo, especially when there is no later activity.

5.3.1 Characterizing Rock Muon Samples Used in the Study

Here again, Michel electrons tagged near the endpoint of rock muon tracks are used. Rock muon tracks are selected using the same criteria that were used to make Fig. 5.18 — Fig. 5.26 (Sec. 5.2.3). In this subsection, different distributions of rock muons are shown in both data and simulation. The distributions include those of the position of beginning and endpoint of rock muons in X/Y/Z as well as the two-dimensional in XY plane. The distribution of energy and timing of rock muons are also shown. Plots of the data (Fig. 5.27, 5.28, and 5.29) are shown first, followed by the plots from the long overlay simulation (Fig. 5.30, 5.31, and 5.32).

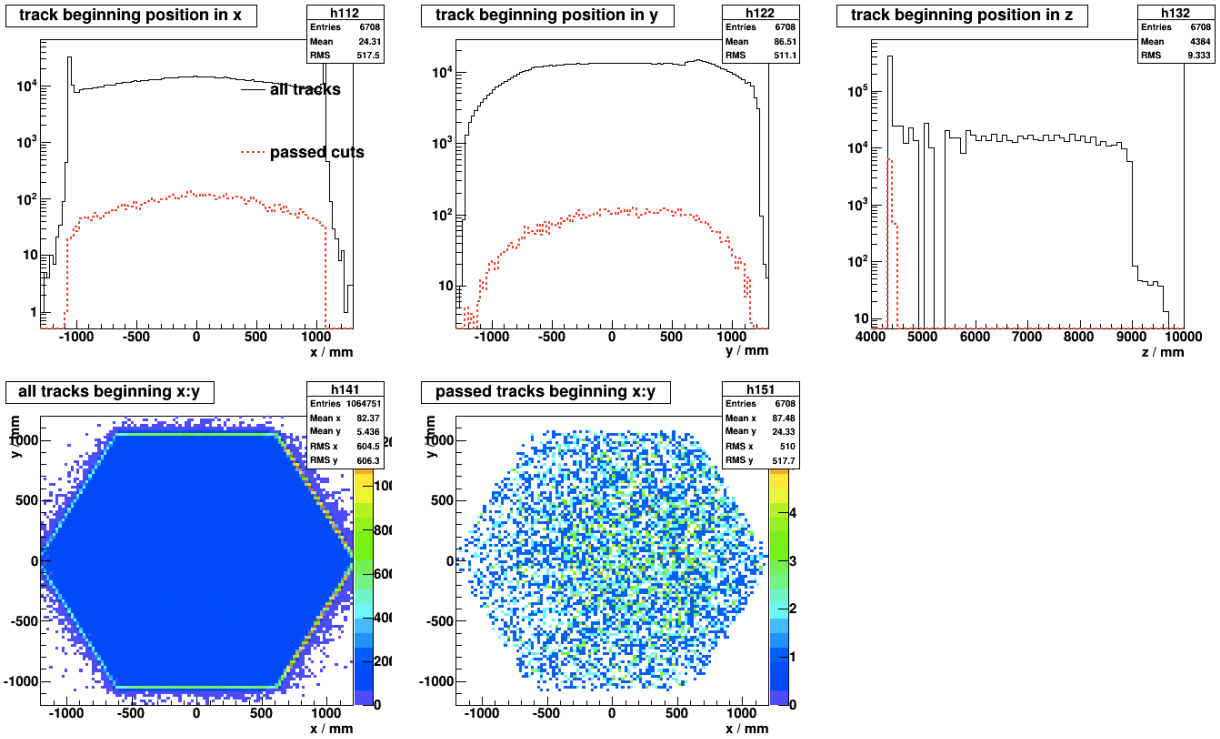

FIG. 5.27: The X,Y,Z positions of the **beginning** of rock muon tracks in data. The three top distributions, from left to right, are the distributions of X,Y,Z position of the tracks beginning point. The black solid line is for all tracks. The red dotted line is for tracks passing the rock muon selection. The bottom distributions are the 2D distributions of XY position of the tracks beginning point. The left is for all tracks and the right is for selected tracks.

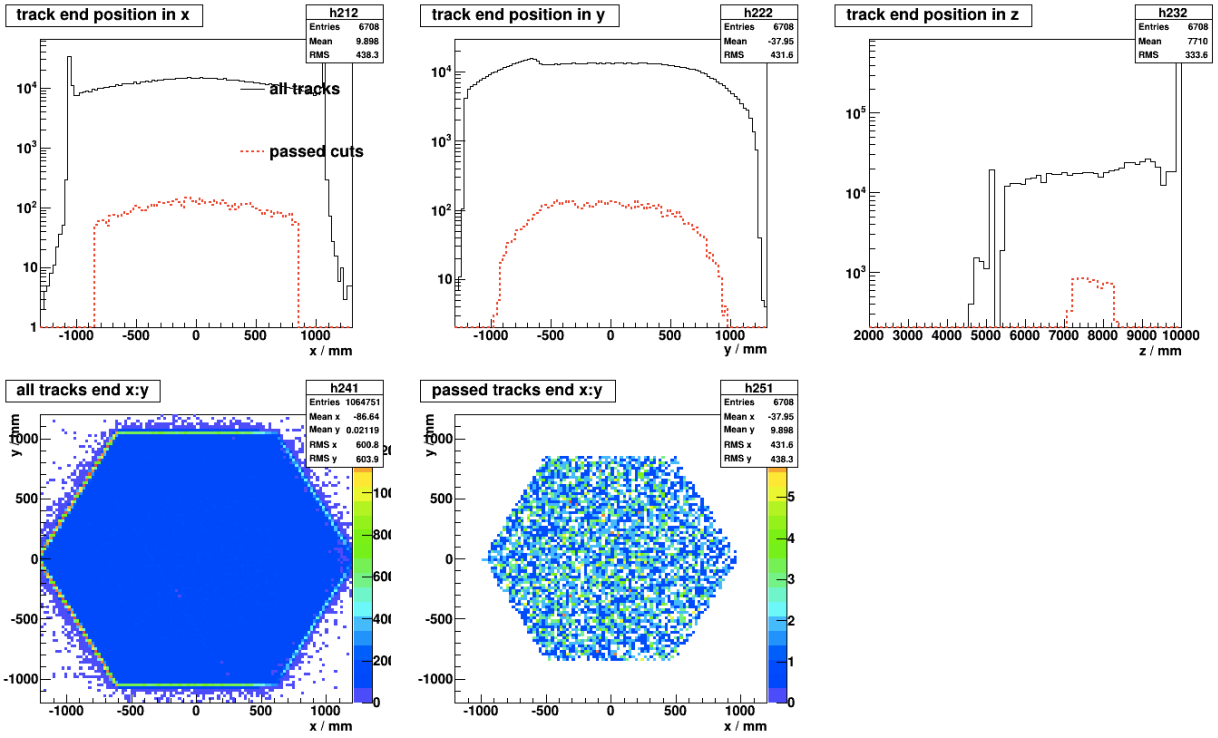

FIG. 5.28: The X,Y,Z positions of the **end** of rock muon tracks in data. Three top distributions, from left to right, are the distributions of X,Y,Z position of the track end point. The black solid line is for all tracks. The red dotted line is for tracks passing the rock muon selection. The bottom distributions are the 2D distributions of the XY position of track end point. The left is for all tracks and the right is for selected tracks.

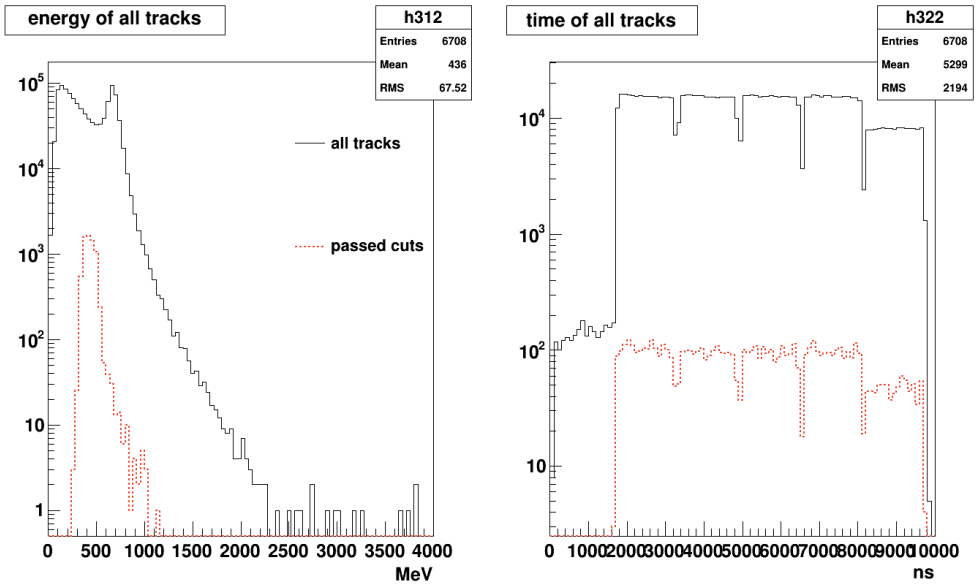

FIG. 5.29: The energy and time of rock muon tracks in data

Plots of rock muons in long overlay simulation samples

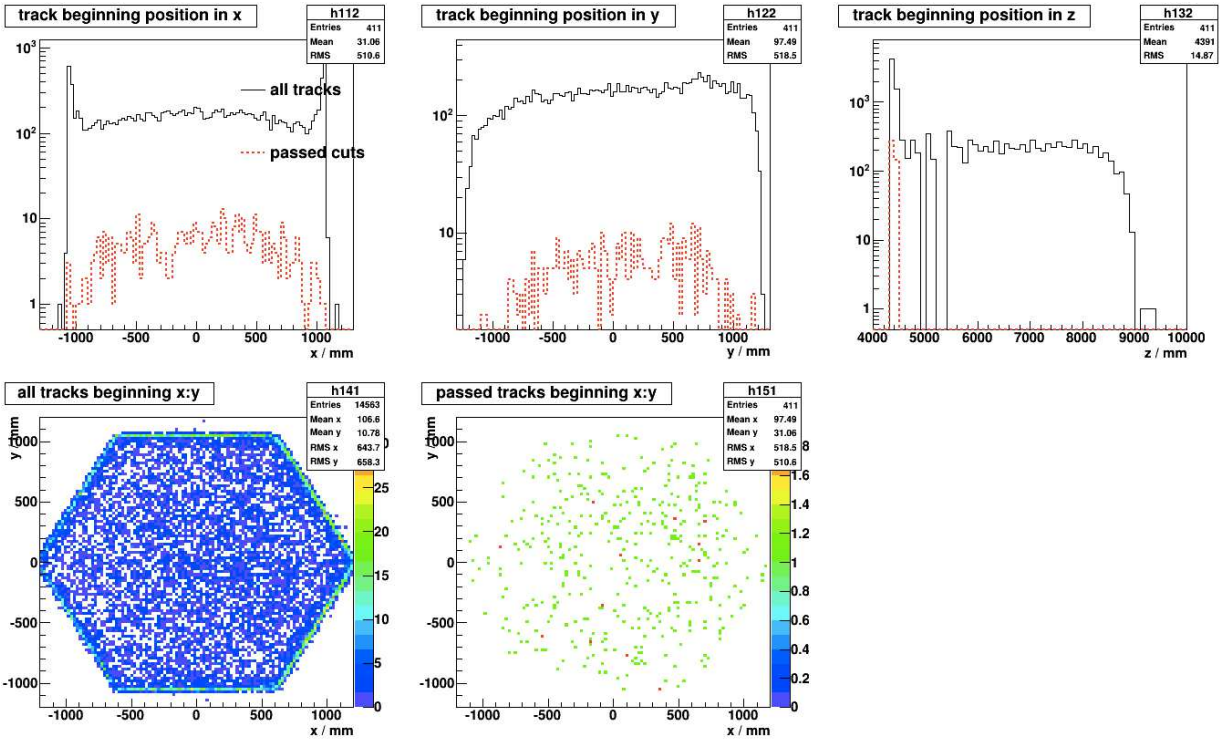

FIG. 5.30: The X,Y,Z positions of beginning of rock muon tracks in the long overlay Muon minus sample. The three top distributions, from left to right, are the distributions of X,Y,Z position of the track beginning point. The black solid line is for all tracks. The red dotted line is for tracks passing the rock muon selection. The bottom distributions are the 2D distributions of the XY position of track beginning point. The left is for all tracks and the right is for selected tracks.

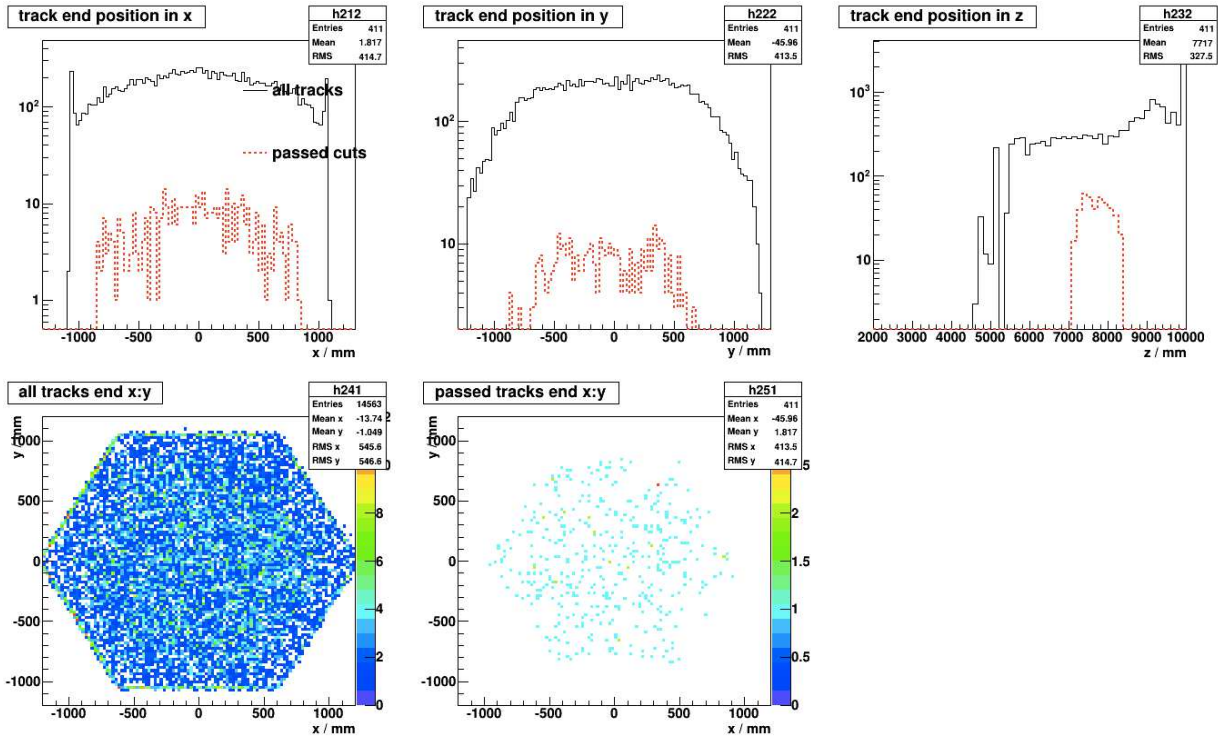

FIG. 5.31: The X,Y,Z positions of end of rock Muon tracks in the long overlay muon minus sample. The three top distributions, from left to right, are the distributions of X,Y,Z position of the track end point. The black solid line is for all tracks. The red dotted line is for tracks passing the rock muon selection. The bottom distributions are the 2D distributions of the XY position of track end point. The left is for all tracks and the right is for selected tracks.

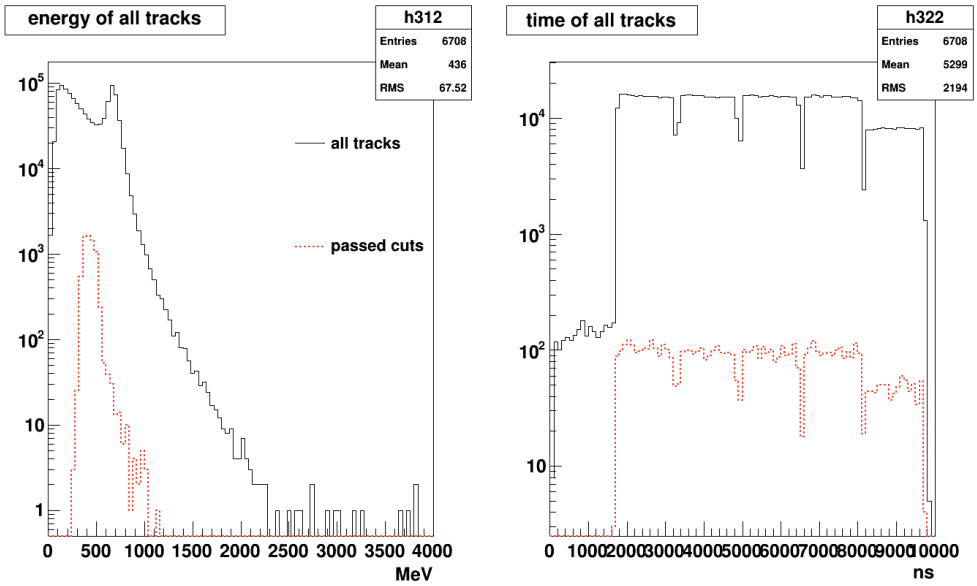

FIG. 5.32: Distributions of energy (left) and time (right) of rock muon tracks in the long overlay muon minus sample.

The selections were applied to selected rock muon candidates sequentially. The number and ratio of rock muons passing the selection are listed in Tab. 5.1. These numbers are the foundation used to calculate the tool's efficiency, purity, and uncertainty. Details of the calculation are discussed in the following section.

TABLE 5.1: Number of Rock Muons Passing Sequential Selections

Samples	Stop in Fiducial	Single Track	ddead==0	$N(E > 1\text{MeV}) < 3$
Data	40778(100%)	35274(86.5%)	32205(79.0%)	19661(48.2%)
μ^- no overlay	5984(100%)	5922(99.0%)	5474(91.5%)	4957(82.8%)
μ^- regular overlay	5900(100%)	5390(91.4%)	5002(84.8%)	3986(67.6%)
μ^- long overlay	5920(100%)	5404(91.3%)	5008(84.6%)	3987(67.3%)
μ^+ no overlay	6002(100%)	5933(98.9%)	5461(91.0%)	4901(81.7%)
μ^+ regular overlay	5957(100%)	5449(91.5%)	5026(84.4%)	3977(66.8%)
μ^+ long overlay	5966(100%)	5453(91.4%)	5026(84.2%)	4004(67.1%)

5.3.2 Efficiency and Purity

There are two kinds of efficiencies: one is the efficiency to tag Michel electrons when there are true Michel electrons, and the other one is called the tagging probability, which is measurable in both data and MC. Purity is defined as the fraction of true Michel electrons in the sample tagged by the `MichelTool`. In the simulated samples, true Michel trajectories are electron trajectories with parent trajectories that are negative muon and GEANT4 process *MuonCaptureAtRest*, or positron trajectories with parent trajectories that are positive muon and GEANT4 process *decay*.

To demonstrate the calculations of the efficiencies, tagging probabilities, and purities, three examples are described here and a table of efficiencies in all samples is listed at the end of this section. The three examples are a data sample and a negative/positive muon sample with long data overlay.

The first example is to calculate efficiency in data. A total of 19661 tracks passed rock muon selection and 15041 of those were tagged by the `MichelTool`. Therefore, the tagging probability is 15041 / 19661 = 76.5%.

The second example is to calculate efficiencies in the negative muon sample with long data overlay. A total of 3987 tracks passed rock muon selection: 3634 of those had true Michel electron trajectories and the remaining 353 did not. Among those with true Michel electron trajectories, 2966 tracks were tagged by the `MichelTool` and the remaining 668 did not have Michel electron tags. Among those without true Michel trajectories, 17 tracks had Michel electron tags and the remaining 336 did not have. Therefore, the efficiency to tag Michel electrons is the portion of true Michel electrons tagged by the `MichelTool` successfully, which is 81.6% (2966/3634). Purity is the portion of true Michel electrons in the tagged Michel electrons, which is 99.4% (2966/2983). The tagging probability is 74.8% (2983/3987).

The last example is to calculate efficiencies in the positive muon sample with long data overlay. In total, there were 4004 tracks passing rock muon selection and all of them had true Michel electron trajectories. Of those, 3257 tracks were tagged by the `MichelTool` and 747 were not. Therefore, the efficiency to tag Michel electrons is the same as the tagging probability of stopping muon tracks, which is 81.3% (3257/4004), and the purity is 100%.

Tab. 5.2 shows the summary of the tool's efficiency in data and different simulated samples.

TABLE 5.2: The `MichelTool`'s Efficiency and Purity in Different Samples

Samples	Efficiency (%) (tag Michels)	Purity(%)	Probability (%) (tag muon tracks)
Data	-	-	76.5
μ^- no overlay	90.0	99.4	82.6
μ^- regular overlay	82.3	99.6	75.4
μ^- long overlay	81.6	99.4	75.4
μ^+ no overlay	90.0	100	90.0
μ^+ regular overlay	81.3	100	81.3
μ^+ long overlay	81.3	100	81.3

5.3.3 Uncertainty

A combined simulation sample, similar to the one used in plotting Michel electron distributions, was constructed to mimic the data. Tab. 5.2 shows that the tagging probability of Michel electrons around the rock muon endpoints in the data (76.5%) represents the combined tagging probability of the negative Muon long overlay sample (75.5%) and the positive Muon long overlay sample (81.3%). Considering the measured ratio between positive muons and negative muons, 0.09 ± 0.04, and propagating all uncertainties to the final efficiency, the tagging probability on the mixed simulation samples is

$\epsilon_{prediction} = 75.4\% \pm 0.7\%$ compared to the probability on the data $\epsilon_{data} = 76.5\% \pm 0.3\%$. The difference between the probabilities on the simulation and data is adopted as the uncertainty on the tagging efficiency of the `MichelTool`, which is 1.1%.

5.3.4 Tagging Probability and Efficiency Stability Check

In this section, the stability of the tagging probability and efficiency is discussed. A short conclusion of this study is that all of these plots show the high stability of the `MichelTool`'s tagging probability and efficiency. Different checks done on various parameters include:

- **Data run numbers**
- **Michel electrons' true energy** —the energy of true Michel electrons trajectories in simulation
- **Michel electrons' true time difference** —the time difference between true Michel electrons trajectories and their parent muon trajectories in simulation
- **Rock muons' energy** —the energy of true muon trajectories in simulation
- **Rock muons' time** —the time of true muon trajectories in simulation
- **Rock muons'** θ —the angle between true muon trajectories in simulation and the Z direction of the MINERνA detector
- **Rock muons'** ϕ —the cosine of the angle of true muon trajectories in simulation in XY plane
- **Rock muons' track length** —the length of true muon trajectories in simulation
- **Rock muons' endpoint z position** —the position of true muon trajectories' end in simulation in the Z direction

- **Rock muons' radius** —true muon trajectories' endpoint radial coordinate in the XY plane with respect to the center of plane

The MichelTool tagging probability vs run number in data

To assure that the `MichelTool` performs stably, the `MichelTool` efficiency is calculated in different runs of data samples. Fig. 5.33 shows that the tool's efficiency is quite similar in different data runs.

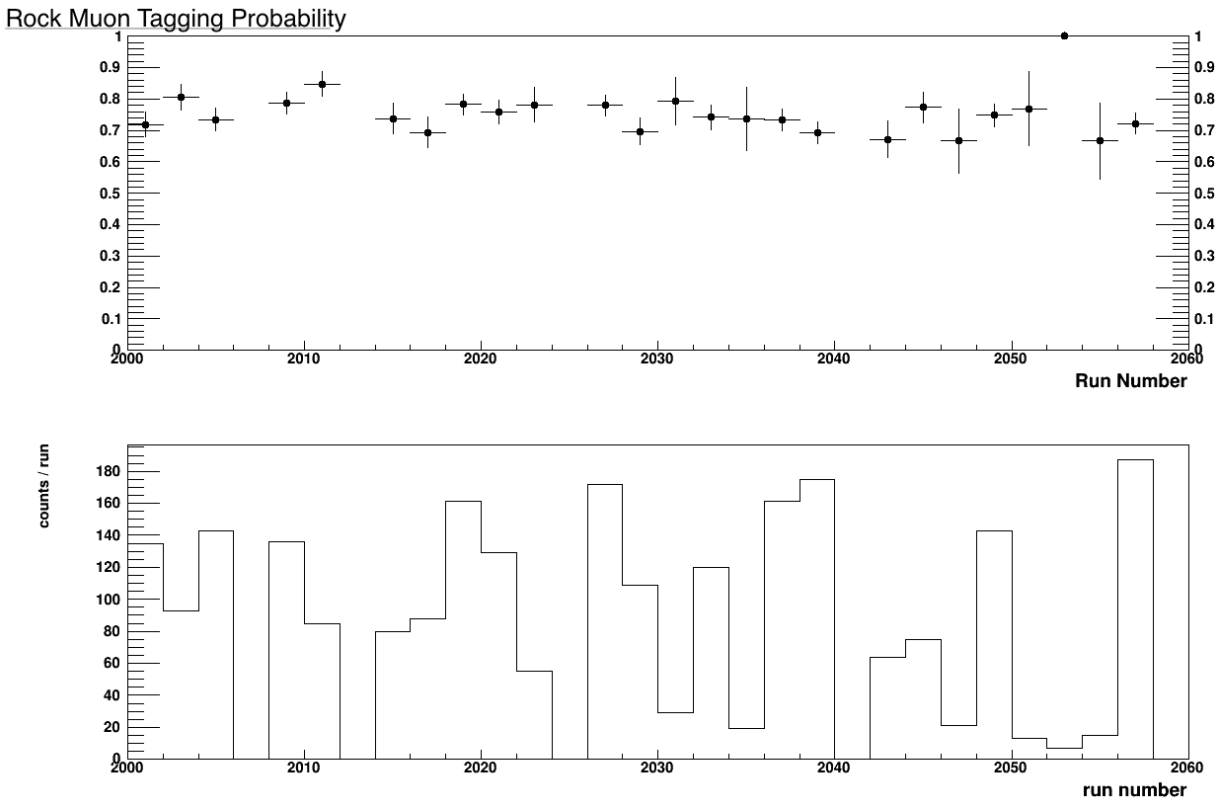

FIG. 5.33: Efficiency of the `MichelTool` vs different runs (top). Numbers of Michel electrons in every two runs (bottom).

The MichelTool efficiency vs Michel electrons true energy

Fig. 5.34 shows the tool's performance on Michel electrons with different energies. It is expected that the tool does not perform as well on low energy Michel electrons as on Michel electrons with fairly high energy. The reason is simple — low energy Michel electrons tend to deposit less energy into the strips in the MINERνA detector and less energy deposition has a higher possibility of failing the selection selections.

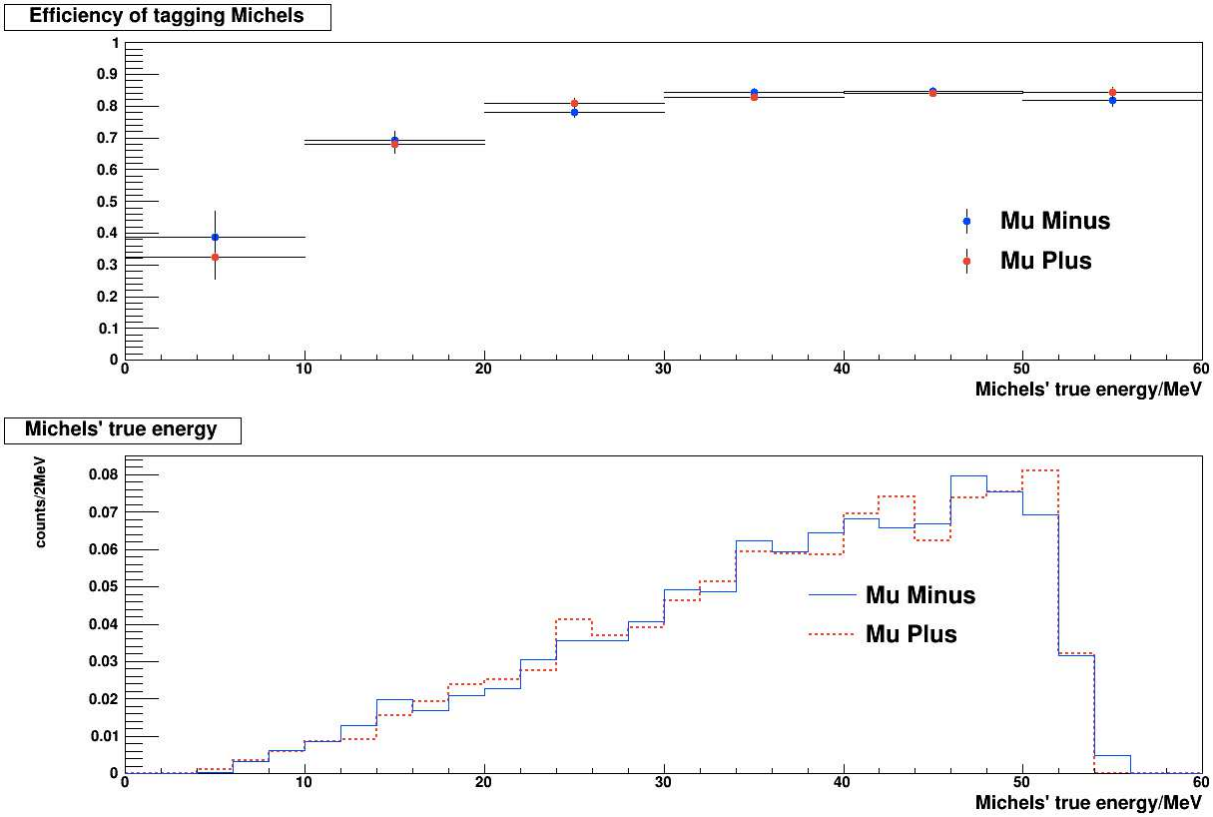

FIG. 5.34: Efficiency of the `MichelTool` vs true energy of Michel electrons. The top plot is the efficiency distribution as a function of the energy of true Michel electrons. The bottom plot is the distribution of the energy of true Michel electrons.

The MichelTool efficiency vs Michel electrons true time

The true time of a Michel electron is calculated as the time difference between the electron's trajectory and the parent muon trajectory. Fig. 5.35 shows that efficiency is not dependent on that time gap for times less than around 6000 ns. As the time gap increases, the tool's efficiency decreases because the detector goes dead 188 ns after the end of the beam spill.

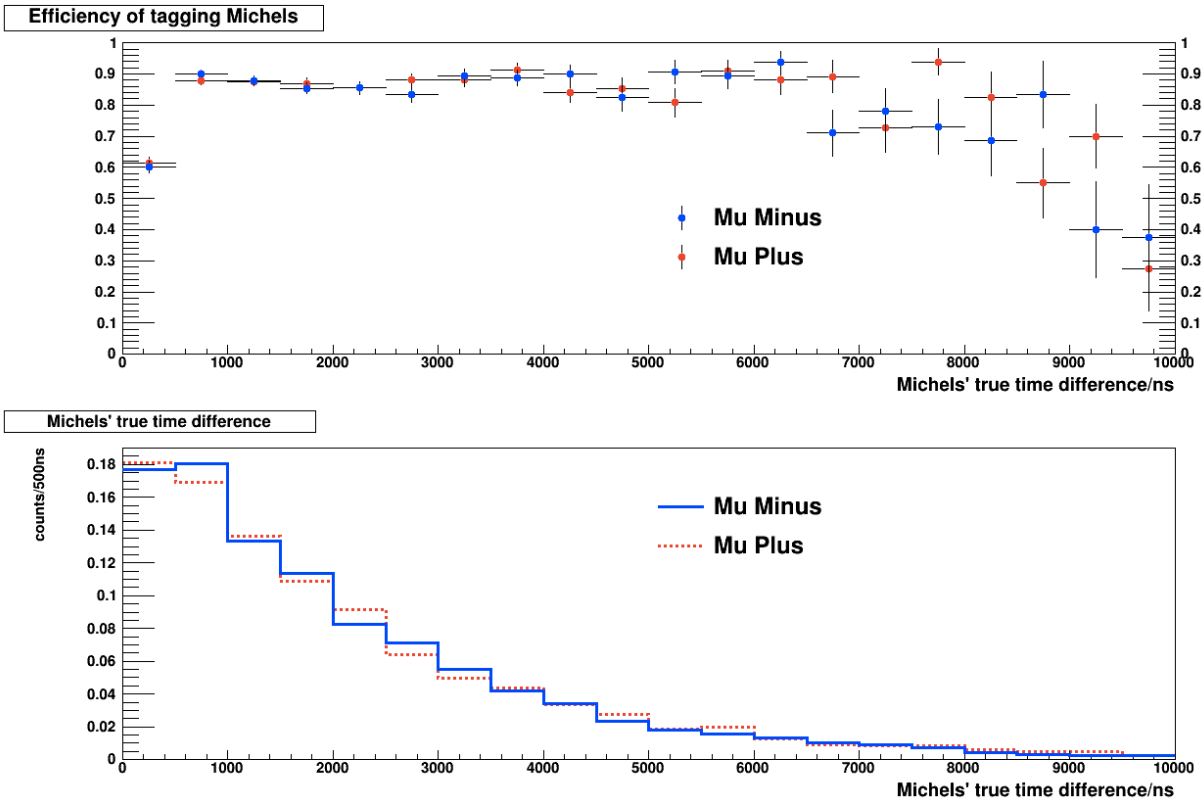

FIG. 5.35: Efficiency of the `MichelTool` VS the time difference between Michel electrons and rock Muons. The top plot is the efficiency distribution as a function of the time difference of true Michel electrons. The bottom plot is the distribution of the time difference of true Michel electrons.

The MichelTool tagging probability vs rock muon energy

The energy of a rock muon is the energy extracted from real data and injected into the GEANT simulation (Sec. 5.3). The `MichelTool` efficiency should not depend on any parameters of rock muons, such as the energy.

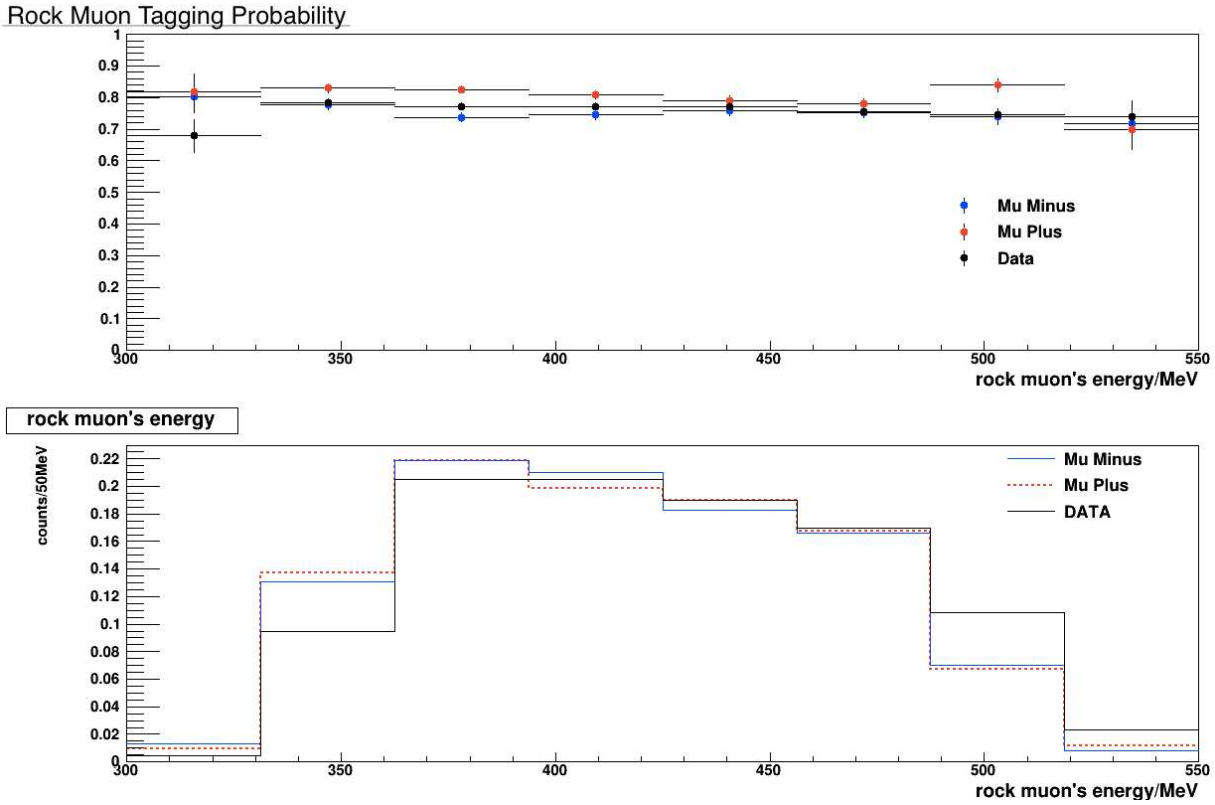

FIG. 5.36: Efficiency of the MichelTool vs the energy of rock muons. The top plot is the efficiency distribution as a function of the energy of true rock muons. The bottom plot is the distribution of the energy of true rock muons.

The MichelTool tagging probability vs rock muon time

Similar to the other parameters of the rock muon, the time when the rock muon enters the MINERνA detector should not affect the tool's efficiency (Fig. 5.37).

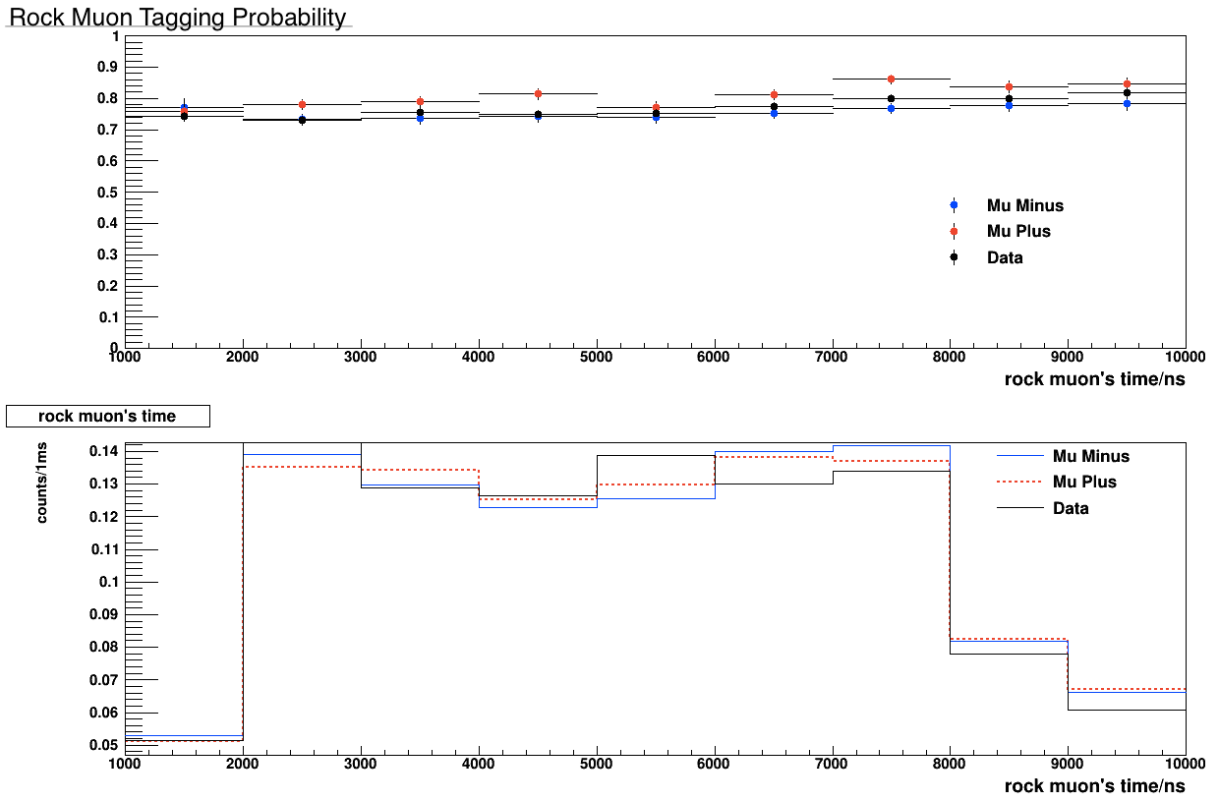

FIG. 5.37: Efficiency of the MichelTool vs the time of rock Muons. The top plot is the efficiency distribution as a function of the time of true rock muons. The bottom plot is the distribution of the time of true rock muons.

The MichelTool tagging probability vs rock muon angle ϕ

Here, angle ϕ is the angle between the rock muon tracks projection in the XY plane and the detector's X direction. Again, the rock muon angle should not affect the tool's efficiency. Recall that the neutrino beam travels downside from the Earth's surface to the MINERνA detector, which is 100 m deep in the Earth. The bottom plot shows more rock muons entering the MINERνA detector downside (Fig. 2.12).

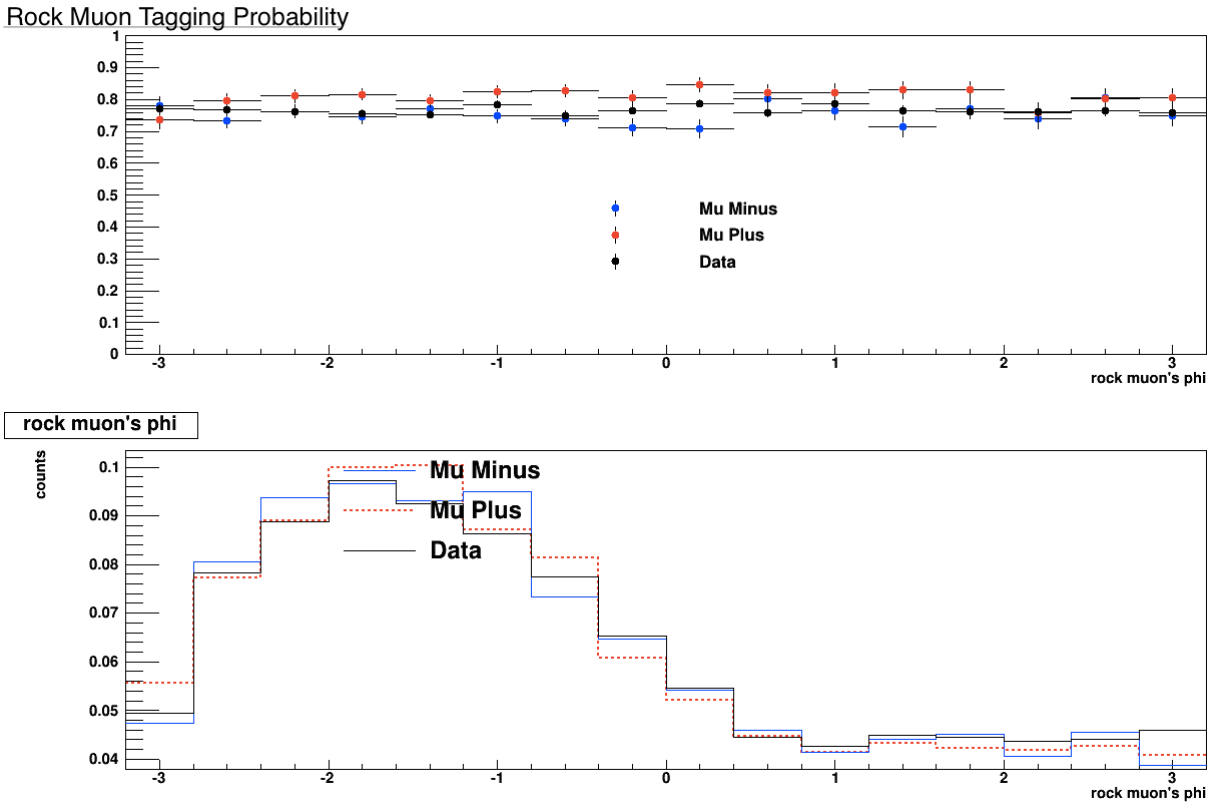

FIG. 5.38: Efficiency of the MichelTool vs phi of rock muons. The top plot is the efficiency distribution as a function of cosine phi of true rock muons. The bottom plot is the distribution of phi of true rock muons.

The MichelTool tagging probability vs rock muon angle θ

Here, angle θ is the angle between rock muon tracks and the detector's Z direction. The larger this angle, the higher possibility that the rock muon exits the side of the MINERνA detector. This tendency is indicated in the bottom plot.

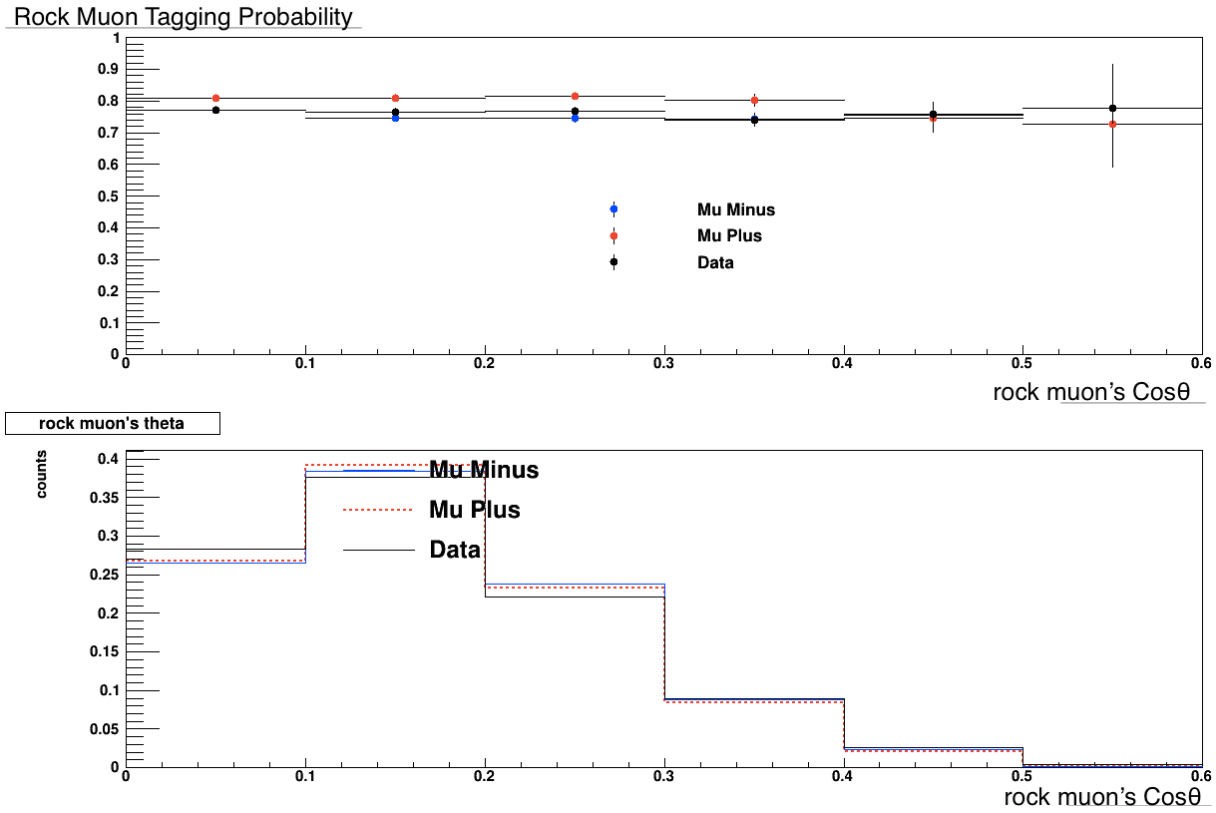

FIG. 5.39: Efficiency of the MichelTool vs theta of rock muons. The top plot is the efficiency distribution as a function of cosine theta of true rock muons. The bottom plot is the distribution of cosine theta of true rock muons.

The MichelTool tagging probability vs rock muon endpoint

The rock muon endpoint Z positions have no effect on the tool's efficiency. Fewer entries in the last bin of bottom plot is due to the selection edge of the endpoints.

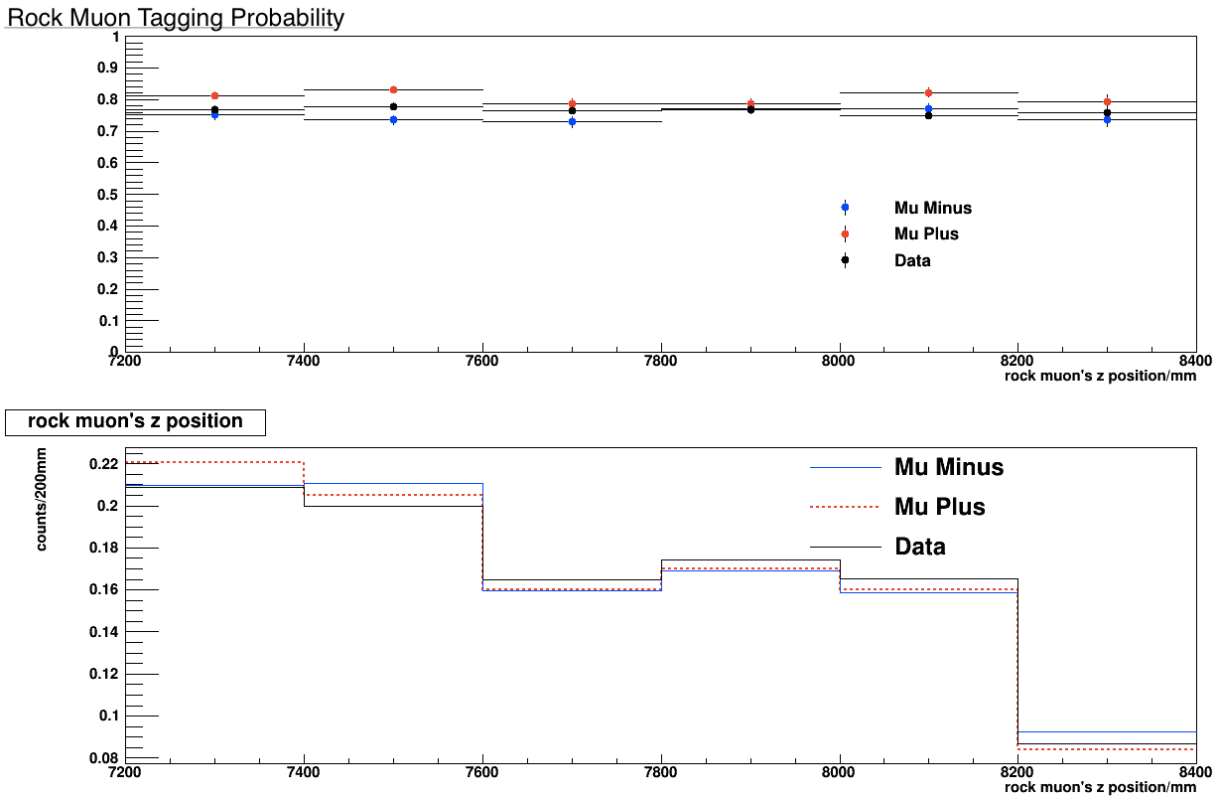

FIG. 5.40: Efficiency of the the MichelTool vs the z position of rock muon track ends. The top plot is the efficiency distribution as a function of the Z position of true rock muons. The bottom plot is the distribution of the Z position of true rock muons.

The MichelTool tagging probability vs rock muon radius of endpoint

As long as the rock muon stops in the fiducial volume, the distance between the endpoint and the central line of the detector should not affect the tool's efficiency. The distribution slope in the bottom plot is due to the increasing area as the radius increases.

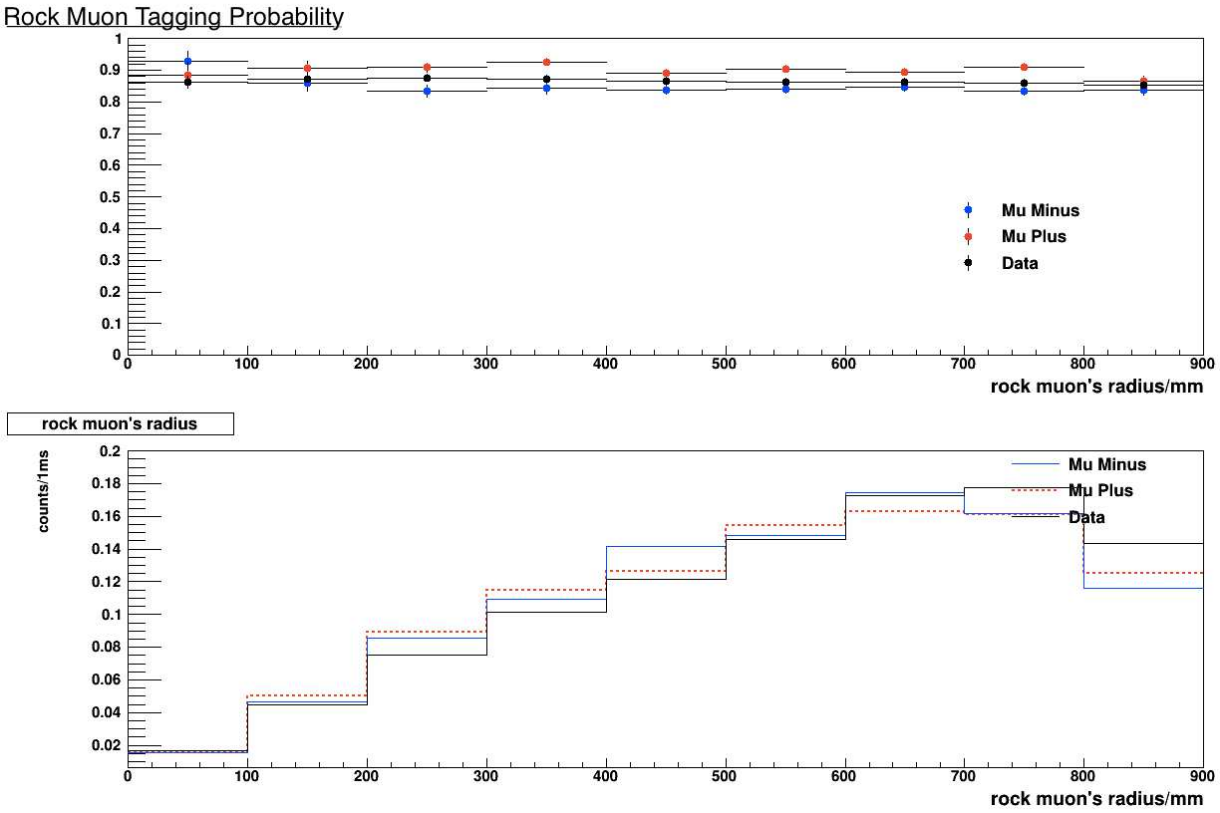

FIG. 5.41: Efficiency of the MichelTool vs the radius of rock muons. The top plot is the efficiency distribution as a function of radius of true rock muons. The bottom plot is the distribution of radius of true rock muons.

5.3.5 Discussion on the Efficiency of the MichelTool

Certain factors limit the MichelTool's tagging probability:

1. Negative muons can be absorbed by carbon. In such cases, Michel electrons coming from the muons decay are not expected. The absorption rate is about 4%.

2. When the MichelTool looks for the qualified clusters, the lower limit of the Qualified Clusters' energy is 1 MeV. Therefore, if all clusters in a Michel electron prong have visible energy less than 1 MeV, it will not be tagged by the MichelTool.

3. The `MichelTool` starts to look for Qualified Clusters from the later timeslice rather than the parent timeslice. If a Michel electron is produced quickly and appears in the same timeslices as the parent activities, the tool is not able to identify this type of Michel electrons, which is named as prompt Michel electrons. The typical length of a readout window is 150 ns.

4. The MINERνA detector has limitations. Combining the readout window length and the dead time, the portion of Michel electrons that are not in the tool's searching window is calculated as:

   - A negative muon has a life time of 2196 ns
   - the decay probability is $f(t) = e^{-t/\tau}/\tau$
   - the readout window is 150 ns and the deadtime window following it is 188 ns. the probability of prompt Michel electrons plus the probability of Michel electrons that disappear in the deadtime window is $1 - e^{-338/2196} = 14.27\%$.

Due to these factors, the MichelTool's efficiency to tag negative muons is not expected to be higher than 1 - 4% - 14.27% or 81.63%. For positive muons, since no capture is expected, the efficiency is no higher than 1 - 14.27% or 85.63%.

This simple calculation ignores several effects in the real world. For example, rock muons can come in near the end of readout windows. The length of readout windows are not always 150 ns, and can be shorter. Sometimes, dead time is not really dead and the detector is able to record the data.

5.4 Michel Electrons Background Study

The previous section shows that the `MichelTool` has a 75.4% probability to tag rock muon tracks, with good agreement between the data and simulation. In this section the procedure to estimate the background to the Michel sample is described and several extra selections are developed to clean the sample. MINERνA data and the rock muon simulation samples using six different overlay strategies are used in this background study, using the same data and simulation as used in the efficiency study.

5.4.1 Methodology

Given a random position and a random time for every gate, the `MichelTool` is executed on the data and different simulation samples to look for Michel electrons. Thus, no Michel electrons are expected at random positions and random times. The possibility of finding Michel candidates at random positions and random times is the background misidentification rate and these Michel candidates are termed as fake Michel electrons. The random position is a 3D vector with a uniform distribution in X,Y, and Z. After it is retrieved, passing the fiducial volume check is also required. A list of rock muon times within the gate were used to simulate rock muon samples and this list is used here to provide the random time. The time provided to the `MichelTool` to look for Michel electron candidates is not the same as the time used to simulate rock muons. Instead, the time is randomly picked from the list to mimic the timing structure of the beam spill.

Note that the `MichelTool` is executed on all the gates in the data, not only the gates with rock muons, while the simulation has rock muons in all gates. It is not ideal to compare the neutrino interaction data to the rock muon samples but the rock muon simulations were the only available samples using the special overlay strategy at that time. Although the uncertainty is overestimated, the systematic uncertainty due to the Michel tagging efficiency is not sensitive to this misidentification uncertainty. Furthermore, the Michel tagging systematic uncertain contributes a little to the total systematic uncertainty.

The following distributions (Fig. 5.42 — Fig. 5.45) show the data and the random variables simulated in this background study.

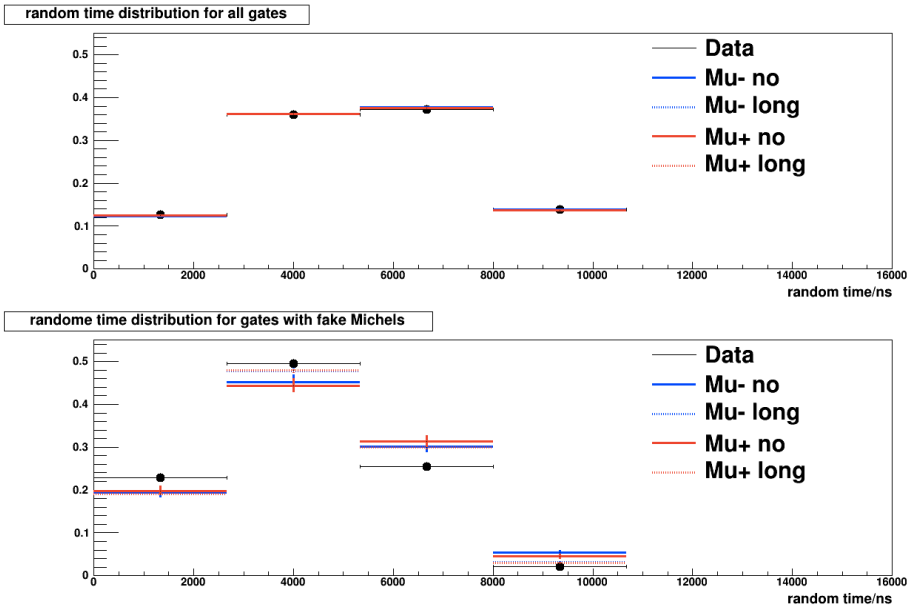

FIG. 5.42: The distribution of randomly picked track time.

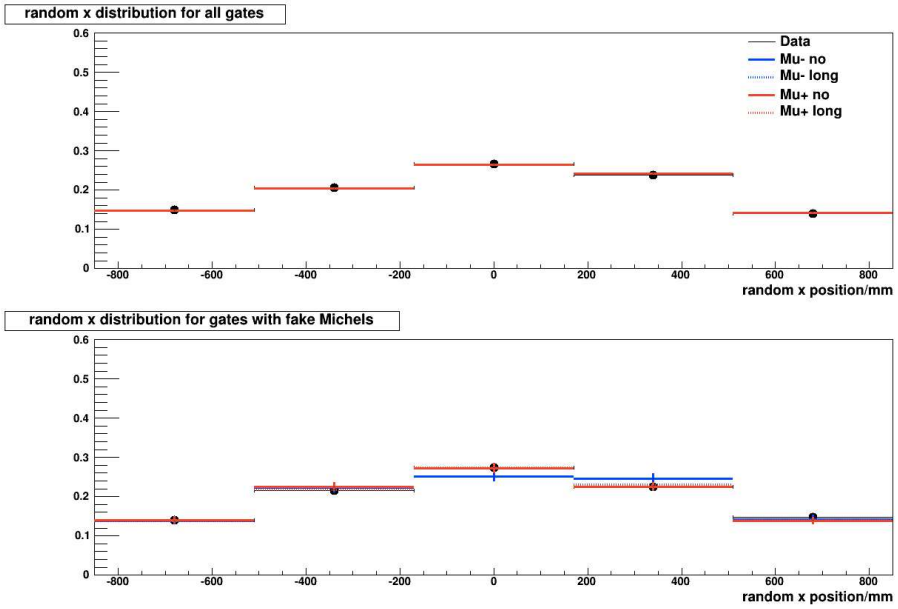

FIG. 5.43: The distribution of randomly picked position in x.

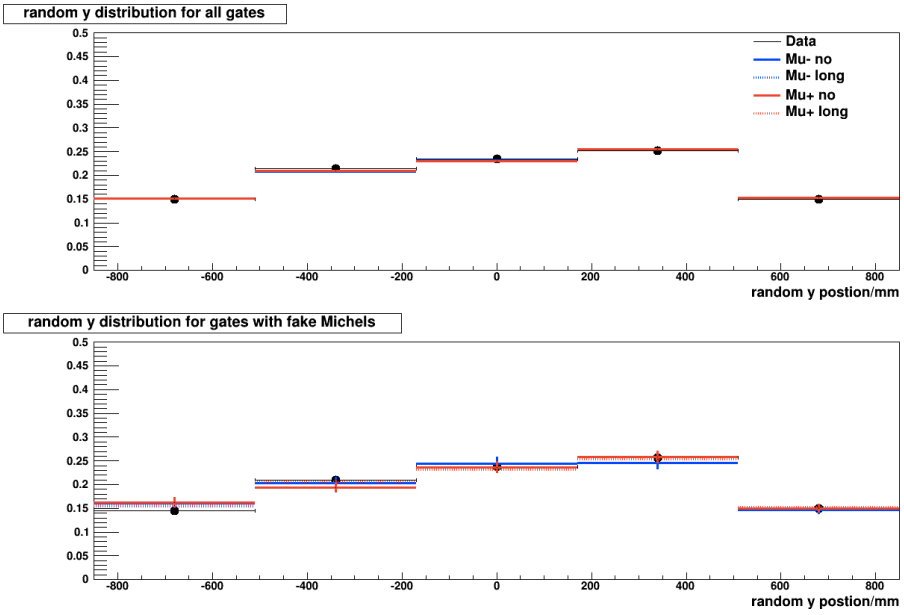

FIG. 5.44: The distribution of randomly picked position in y.

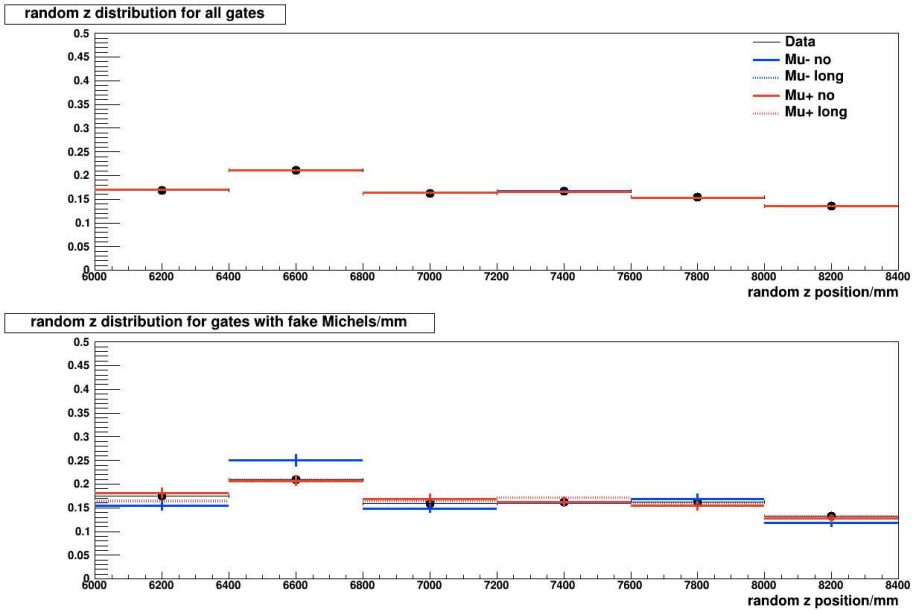

FIG. 5.45: The distribution of randomly picked position in z.

5.4.2 Misidentification Rate and Uncertainty

Recall that in the Michel electrons tagging efficiency study various simulation samples were utilized. In the study of misidentification rate and uncertainty estimation, a similar strategy is used. Tab. 5.3 shows the misidentification rates in data and each simulation sample.

TABLE 5.3: The MichelTool's Misidentification Rates

Samples	Gates	Fake Michel Electrons	Misidentification Rates(%)
Data	2,380,829	26,297	1.01 ± 0.01
μ^- no overlay	133,020	987	0.74 ± 0.02
μ^- regular overlay	133,020	1,138	0.86 ± 0.03
μ^- long overlay	133,020	2,101	1.58 ± 0.03
μ^+ no overlay	133,283	1,091	0.82 ± 0.02
μ^+ regular overlay	133,283	1,351	1.01 ± 0.03
μ^+ long overlay	133,283	2,179	1.63 ± 0.03

It is possible that the so called "fake Michel" are real Michel electrons, but just not associated with the random event that is used to look for Michel electrons. By comparing the rates in the data (1.1% ± 0.01%) and the long overlay simulation samples (1.58% ± 0.03% and 1.63% ± 0.03%), the misidentification rate of the MichelTool is estimated to be 1.1%, with 50% uncertainty.

5.4.3 Cleaning Selections on Michel Electrons

The cleaning selections are part of the reconstruction stage in the `MichelTool` (Sec. 5.2.2). The cleaning selections were developed in the background study by comparing the fake Michel electrons to the real Michel electrons, where the real Michel electrons are the TwoView and ThreeView Michel electrons tagged near the end of rock muon tracks in the data, and the fake Michel electrons are the ones tagged by the `MichelTool` in the data

with random positions and times.

First of all, there is one cleaning selection on the visible energy of time slices:

$$E_{slice} < 100 \text{ MeV},$$

which was chosen to remove Michel electrons that are in the same time slice as other activities. Additional selections are on the energy and number of digits of Michel electrons.

Cleaning selection on energy

Fig. 5.46 shows visible energy distributions of fake Michel electrons and real Michel electrons. The right plot is the first two bins of the left one. The distribution in the dashed line indicates a selection on the visible energy to reject the fake Michel electrons,

$$E_{Michel} < 55 \text{ MeV}$$

.

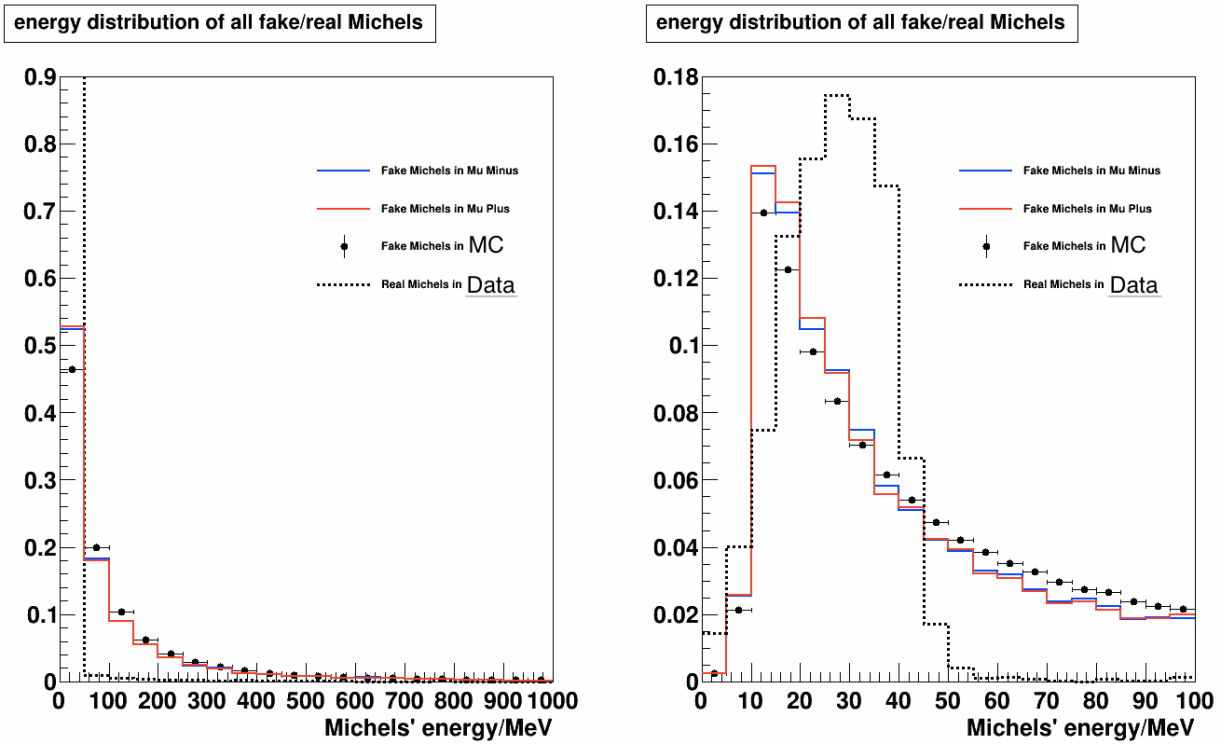

FIG. 5.46: The energy distributions of fake Michel electrons and Michel electrons. The left is the distribution between 0 GeV and 1 GeV. The right is the first 2 bins in left. The solid lines are fake Michel electrons from different simulation samples. The dashed line is the real Michel electrons, which are the TwoView and ThreeView Michel electrons tagged at the endpoint of rock muon tracks in the data.

Cleaning selection on number of digits

Fig. 5.47 shows distributions of the number of digits of fake Michel electrons and real Michel electrons. The right plot is the first four bins of the left one. The distribution in the dashed line indicates a selection on the number of digits to reject the fake Michel electrons, $N_{digits} < 35$.

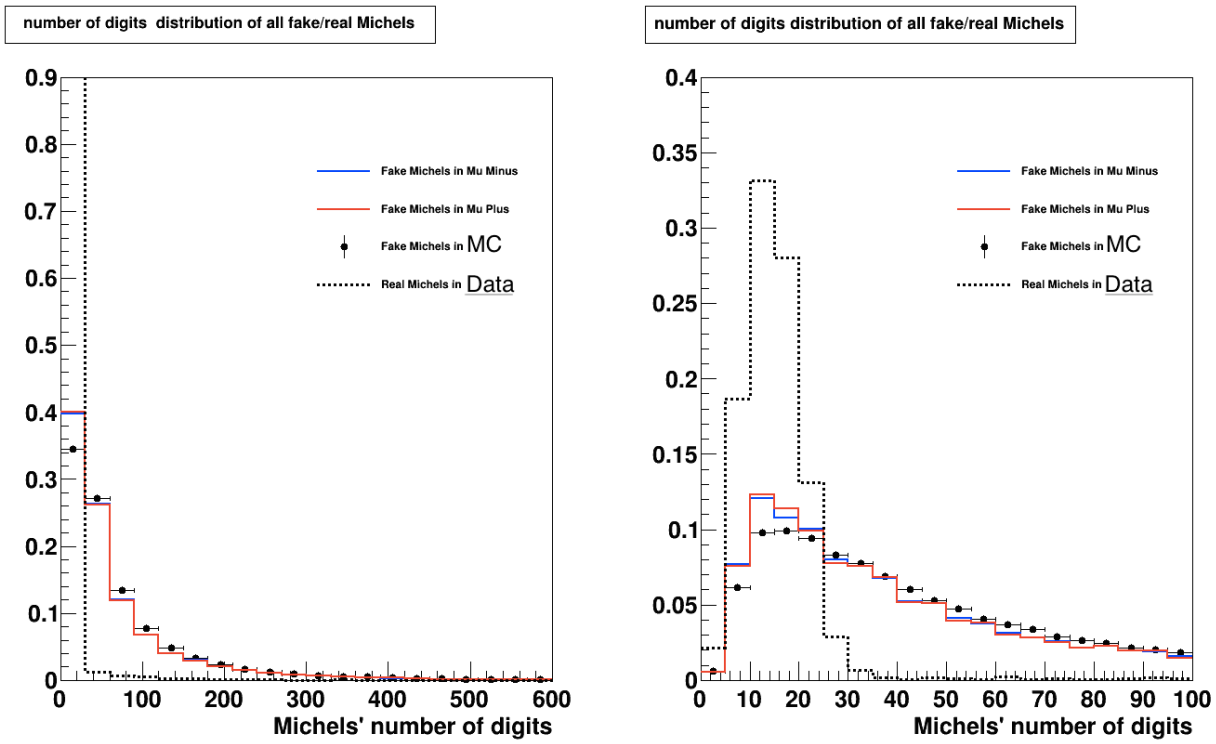

FIG. 5.47: The number of digits distributions of fake Michel electrons and Michel electrons. The left is the distribution between 0 and 600 digits. The right is the first 4 bins in left plot. The solid lines are fake Michel electrons from different simulation samples. The dashed line is the real Michel electrons, which are the TwoView and ThreeView Michel electrons tagged at the endpoint of rock muon tracks in the data.

Cleaning selection on energy and number of digits

Fig. 5.48 shows the number of digits vs energy for OneView (left), TwoView (middle) and ThreeView (right) Michel electrons. Red dots are the entries from real Michel electrons and blue dots represent the fake Michel electrons.

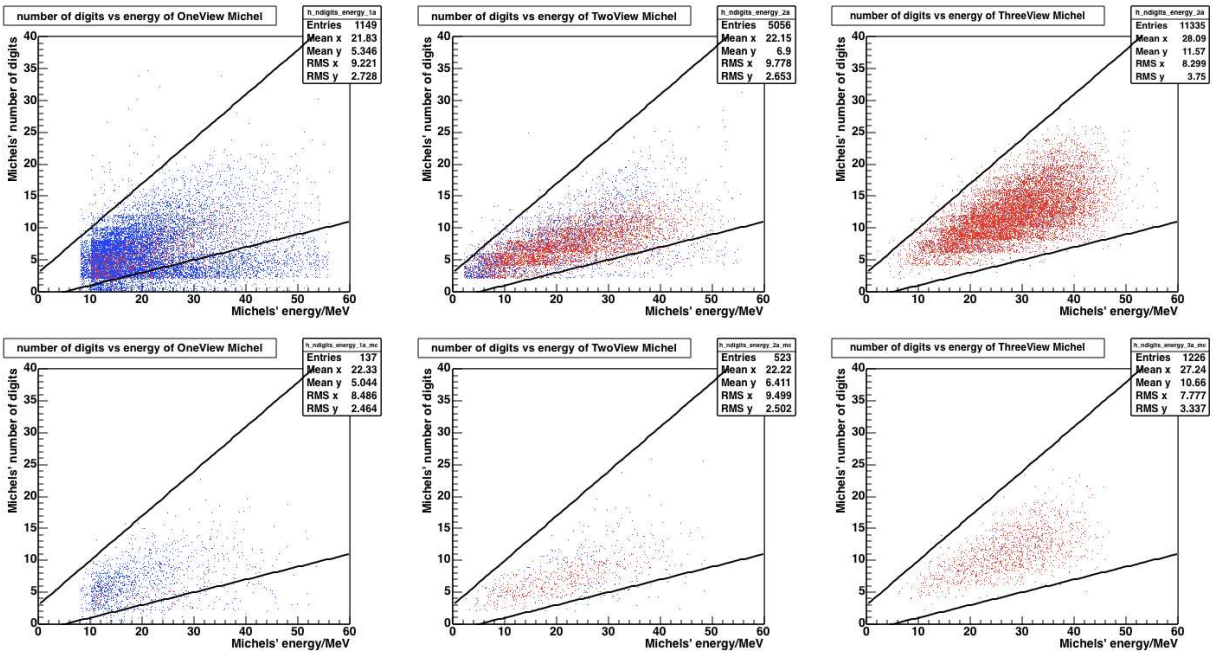

FIG. 5.48: 2D distributions of energy vs number of digits of Michel electrons. The three top plots are from data and the three bottom plotss are from the simulation. In each plot, the red dots are Michel electrons tagged by the MichelTool and the blue dots are fake Michel electrons. The two solid black lines in each plots are the cleaning selections which keep 98.5% of TwoView and ThreeView true Michels in Monte Carlo.

The main sources of the background to Michel electrons are afterpulsing, cross-talk, and clusters with fairly large energy due to muons and protons. Two selections on number of digits vs energy are introduced here. The upper cut, $N_{digits} < 0.7 \times E_{Michel} + 3$, is used to exclude the background due to afterpulsing or cross-talk, which have less energy and a greater number of digits. The lower cut, $N_{digits} > 0.2 \times E_{Michel} - 1$, is to exclude the background due to large energy deposition from muons or protons.

Summary: Cleaning Selections

All cleaning selections on Michel electron candidates are listed here:

- $E_{slice} < 100$ MeV
- $E_{Michel} < 55$ MeV
- $N_{digits} < 35$
- $N_{digits} < 0.7 \times E_{Michel} + 3$
- $N_{digits} > 0.2 \times E_{Michel} - 1.$

The study shows that after applying cleaning selections, for fake Michel electrons, there are 11.4% (14206/124221) of them remaining in the sample. For real Michel electrons, 89.5% (1428/1595) of them survived the clean selections. A similar study to measure the power of the cleaning selection on the Michel candidates in CCQE candidates shows that, before applying cleaning selections, 7.8% (2019/25791) of Michel candidates tagging from CCQE candidates are fake Michel electrons, and after applying the cleaning selections, the fraction of fake Michel electrons in the Michel candidates tagging from CCQE candidates is reduced to 4.8% (890/18687).

CHAPTER 6

Analysis

6.1 Analysis Overview

This chapter describes the measurement of the muon neutrino charged-current quasi-elastic-like (CCQE-like) differential cross-section $\frac{d\sigma}{dQ^2}$ on polystyrene scintillator (CH). Two closely related reactions are considered in this analysis, CCQE and CCQE-like. CCQE neutrino scattering is the scattering of the neutrino from a nucleon embedded in carbon (C) or on free proton (H), exchanging a vector boson $W^{\pm}$, and producing a muon as well as a nucleon. This reaction is defined at the level of the generator and does not account for final state interactions. CCQE-like is a definition on the final states of neutrino interactions in the MINERνA detector. Neutrinos interact with carbon nucleus and the interaction can occur with multiple nucleons. CCQE is more sensitive to the models in the simulation. The signal channel for CCQE on a neutron in carbon is $\nu_\mu n \to \mu^- p$, which requires each event candidate has one muon, no mesons, and possible light activities due to the proton. This kind of topology is defined as CCQE. CCQE-like has the same topology, which means the selection of CCQE and CCQE-like candidates are the same. The

measurement on CCQE-like is presented in this chapter. In addition, a similar study on CCQE channel has also been performed. The results are shown in this chapter and the details are presented in App. A.

This chapter is organized in the following order. The first part of this chapter discusses the event selection and the step by step calculation of the differential cross section, including background subtraction, sample unfolding, efficiency correction, and normalizations using flux and target numbers. The second part of this chapter describes the systematic uncertainties on the cross-section result.

6.2 Event Candidates Selection

The ν_μ CCQE-like events have a simple topology, which is a muon prong and no other heavy activity. CCQE-like event candidates are selected by first isolating a sample of charged-current (CC) muon neutrino interactions by identifying the muon track in the final state. Then, from the CC sample, candidates are selected by applying a variety of cuts on the final state topology.

6.2.1 Muon Selection

Muons are the only particles that regularly leave the MINERνA detector and enter the MINOS detector, creating hits in it. So selecting muons is as simple as requiring a track originating in the fiducial volume of the MINERνA detector and matching to either a track or a stub in the MINOS detector. Here the fiducial volume is defined as:

- The z vertex position of the muon track is between 5980 mm and 8422 mm,
- The transverse (x, y) position is within a hexagonal apothem of 850 mm.

ν_μ CCQE-like events have muons with negative charges in the final states. MINOS is able to determine the charge signs of muons by examining their curvature.

Event reconstruction may be impacted by the deadtime. Here the term "deadtime" represents the time after each event during which the MINERνA detector is not able to record another event. The channels experiencing deadtime can not record energy depositions. Thus, a rock muon can mimic a muon having a vertex within the fiducial volume when the upstream strips of the reconstructed vertex experience deadtime. To remove the low quality reconstructed events, and veto rock muon events, an additional cut on the deadtime is necessary. This analysis requires there are no more than 2 dead strips (approximately 3 cm) upstream of the vertex of a muon track. It is performed by projecting the muon two modules upstream and examining whether the Trip-t chips servicing the strips in the muon's path underwent deadtime.

6.2.2 CCQE-like Selection

The remaining cuts are a recoil cut and a Michel veto. These two cuts are utilized to select the CCQE-like channel candidates.

Removing Events with Heavy Activity

Pion production events and deep inelastic (DIS) events are the main background events in this analysis. Pions and other hadrons in the interaction can induce heavy activities in the MINERνA detector. In order to reject such background events with heavy activities, the recoil system is introduced and utilized to develop cuts. The recommended recoil system consists of all unused clusters in the Tracker and ECAL regions, whose distance to the interaction vertex is greater than 30 cm [1]. The clusters inside the 30 cm

[1] Protons with energy up to 218 MeV range out in 30 cm

radius sphere are not added to the recoil system because it is sensitive to the GENIE's mis-modeling of the multi-nucleon contribution to the ν_μ CCQE-like cross section. Events with heavy activities lead to high recoil energies. The recoil energy is calculated as the sum of the energy of unused clusters in the recoil system. Note that unused clusters that are identified as low activity or crosstalk are not added to the recoil system. Fig. 6.1 and Fig. 6.2 show distributions of recoil energy for CCQE-like event candidates before and after applying the cut on recoil energy when applying all cuts mentioned previously. The rejected events in the fat tail of the distribution are mostly non QE-like event candidates.

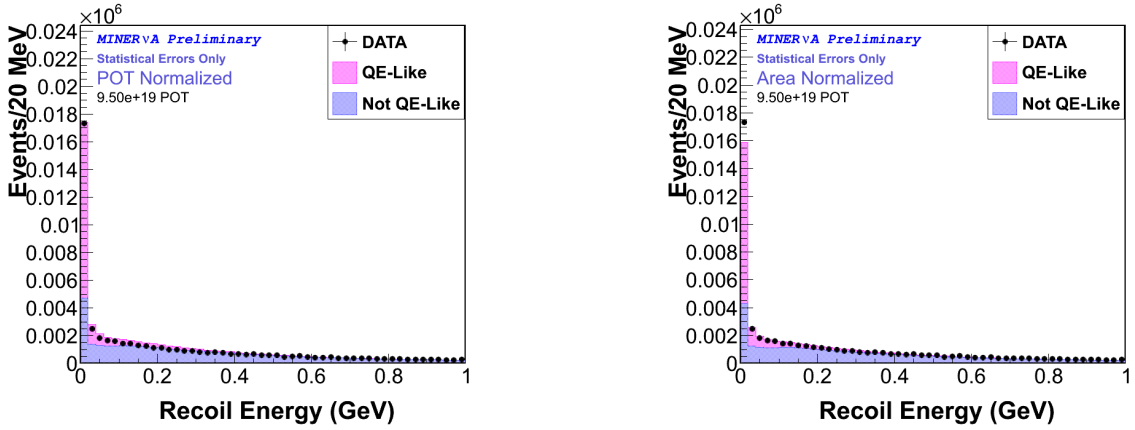

FIG. 6.1: Recoil energy distributions for CCQE-like candidates after applying all previous mentioned cuts. The left plot is POT normalized. The right plot is area normalized.

For Quasi-elastic events on a nucleon at rest, $Q^2 = 2m\nu x$ with $x = 1$. The higher Q^2 the events have, the higher the momentum transferred. This general relation holds for carbon, even though the relation between Q^2 and x is smeared by the nuclear environment. Because events with higher Q^2_{QE} have larger amounts of energy transferred to the nucleus, and sequently deposit more energy in the detector, the cut on recoil energy should be dependent on the Q^2_{QE} of an event. The three-segment selection function is defined as follows:

- $E_{recoil} < 0.05$ GeV when $Q^2 > 0.166$ GeV^2,

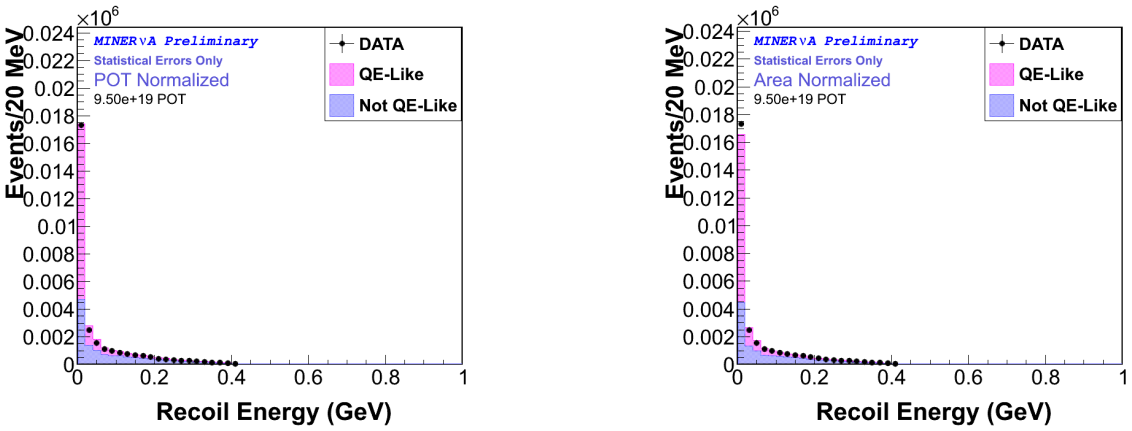

FIG. 6.2: Recoil energy distributions for CCQE-like candidates after applying all previous mentioned cuts plus the cut on recoil energy. The left plot is POT normalized. The right plot is area normalized.

- $E_{recoil} < -0.05 + 0.64 \times Q^2 - 0.22 \times (Q^2)^2$ GeV when 0.166 GeV$^2 \leq Q^2 < 1.297$ GeV^2,
- $E_{recoil} < 0.41$ GeV when $Q^2 \geq 1.297$ GeV^2.

Fig. 6.3 illustrates the cut on recoil energy as a function of Q^2_{QE}.

Here the Q^2 is calculated using Eq. 6.1

$$Q^2 = -m_\mu^2 + 2E_\nu^{QE}(E_\mu - \sqrt{E_\mu^2 - m_\mu^2}cos\theta_\mu). \tag{6.1}$$

The neutrino energy E_ν^{QE} using Eq. 6.2

$$E_\nu^{QE} = \frac{2(M_n - E_B)E_\mu - [(M_n - E_B)^2 + m_\mu^2 - M_p^2]}{2[M_n - E_B - E_\mu - p_\mu cos\theta_\mu]}, \tag{6.2}$$

where M_n, M_p and M_μ are the masses of the neutron, proton and muon, respectively, and E_B is the binding energy. For neutrinos, the default binding energy is 34 MeV and for antineutrinos, the default value is 30 MeV. The results are used in previous studies in MINERνA [1] [58] and calculated based on electron scattering data [59] [60]. E_μ, p_μ and θ_μ are the muon energy, momentum, and angle with respect to the beam.

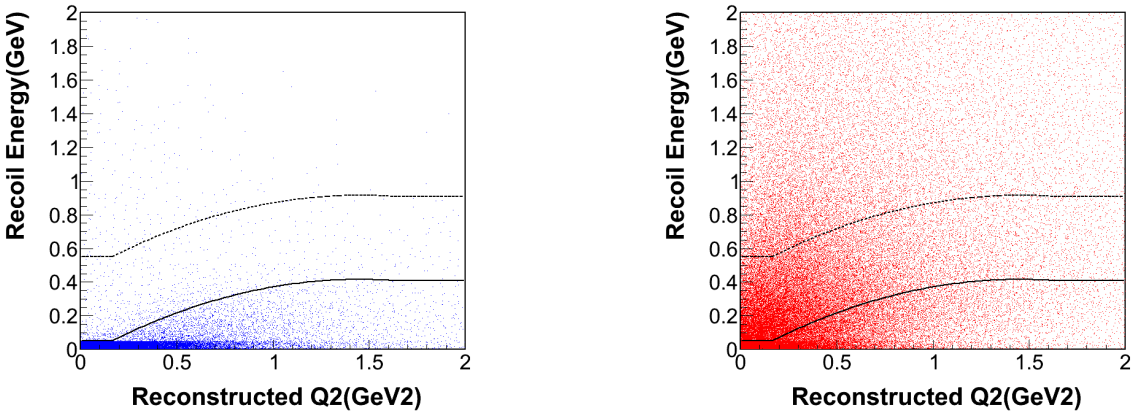

FIG. 6.3: 2D distributions of recoil energy vs reconstructed Q^2. The left plot is for CCQE-like events (blue dots). The right plot is for CCQE-like not events (red dots). The solid curve in the plot represents the 2D cut described above. The area between the dashed line and the solid line is the region where the side band is selected.

Removing Events with Michel Electrons

Background events of pion production, such as $\nu_\mu n \to n\mu\pi^+$ and $\nu_\mu p \to p\mu\pi^+$, can also be rejected by the Michel veto. Charged pions decay with the decay constant 2.6×10^{-8}s and the decay product Michel electrons can be utilized to reject background events where pions were produced with low energy and decay into Michel electrons close to the primary vertex. A cut on the presence of Michel electrons is applied to veto events with soft pions. Michel electrons are identified using the MichelTool discussed in Chap. 5, by searching around the interaction vertex in all events. Fig. 6.4 shows the distributions of event candidates with and without Michel tagging. Most candidates with Michel tagging are not QE-like events.

This cut was not utilized in the previous analysis and applying it reduces the background rate significantly. Take Q^2 for example: the left (right) plot in Fig. 6.5 shows the distributions of Q^2 of CCQE-like event candidates without (with) cutting on Michel electrons,. Here the CCQE-like event candidates are selected by applying all cuts described in this section. In the Monte Carlo, after applying the recoil cut, 31.4% background events

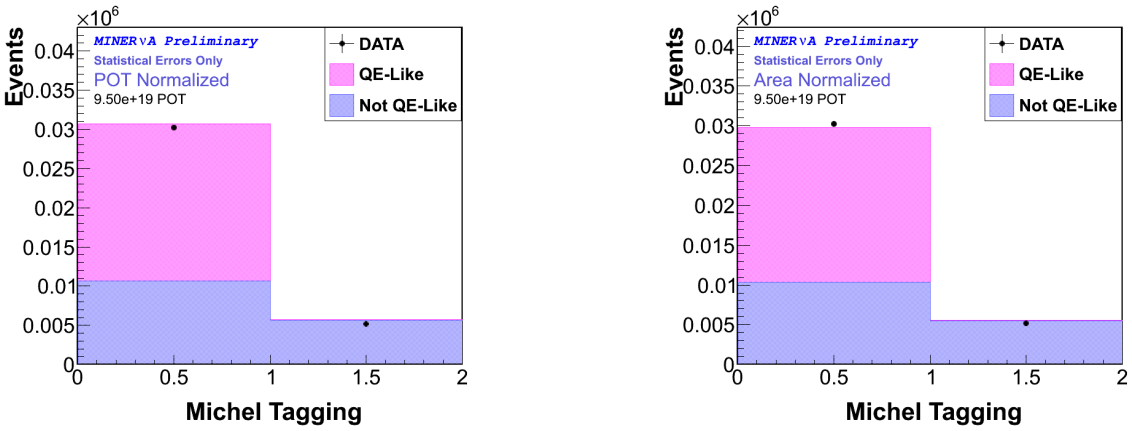

FIG. 6.4: Vertex Michel electrons presence distributions. 0 means no vertex Michel electron is found. 1 means this event has a vertex Michel electron. The left plot is POT normalized and the right plot is normalized by area.

are rejected by the Michel veto while only 0.58% signal events are rejected. Details are listed in Tab. 6.1.

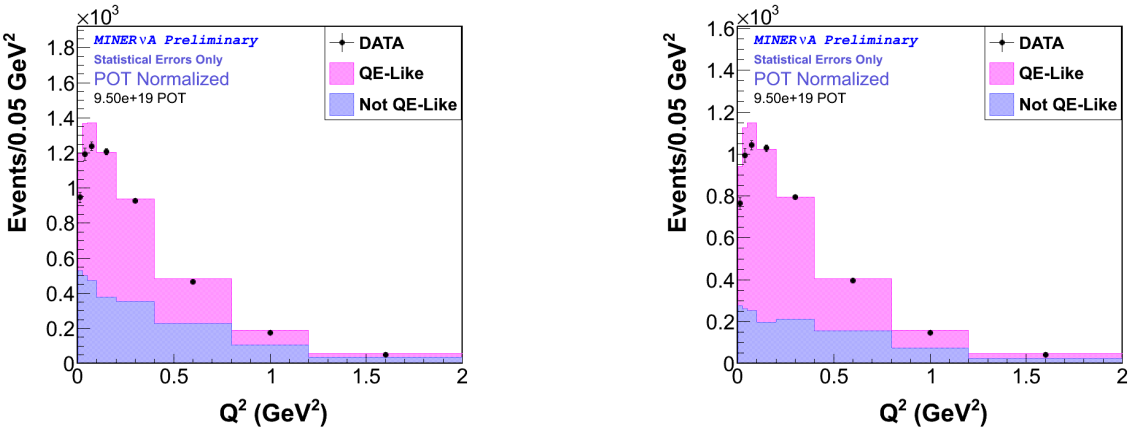

FIG. 6.5: Q^2 distributions of CCQE-like event candidates. The left plot shows the distribution from candidates without applying Michel veto. The right plot shows the distribution from candidates after vetoing Michel electrons.

TABLE 6.1: The number of CCQE-like candidates before and after applying Michel veto. The recoil cut has been applied.

Samples	Entries (No Michel Veto)	Entries (Michel Veto)	Fraction Rejected
Data	17332	14114	18.6%
MC QE like	34988.8	34785.2	0.58%
MC QE like not	29308.2	20101.9	31.4%

6.2.3 Selected CCQE-like Event Candidates

In this section, three examples of selected signal events are shown. Fig. 6.6 is a CCQE-like event candidate passing all selection cuts. This candidate has one muon track and other light activity. Fig. 6.7 shows a CCQE like candidate who has one reconstructed muon track and one proton trajectory. This proton trajectory has not been reconstructed as a track. Fig. 6.8 is an example of two-track candidate, which has one reconstructed muon track, exiting the back of the MINERνA detector, and one short proton track.

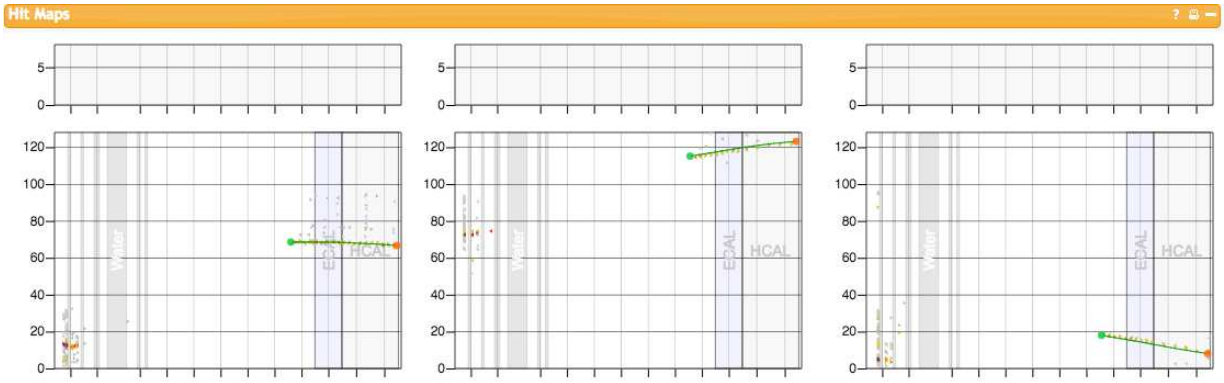

FIG. 6.6: Example 1: CCQE-like candidate, run 2027, subrun 12, gate 203, slice 1. In the final state, there is one muon track and on other heavy activities.

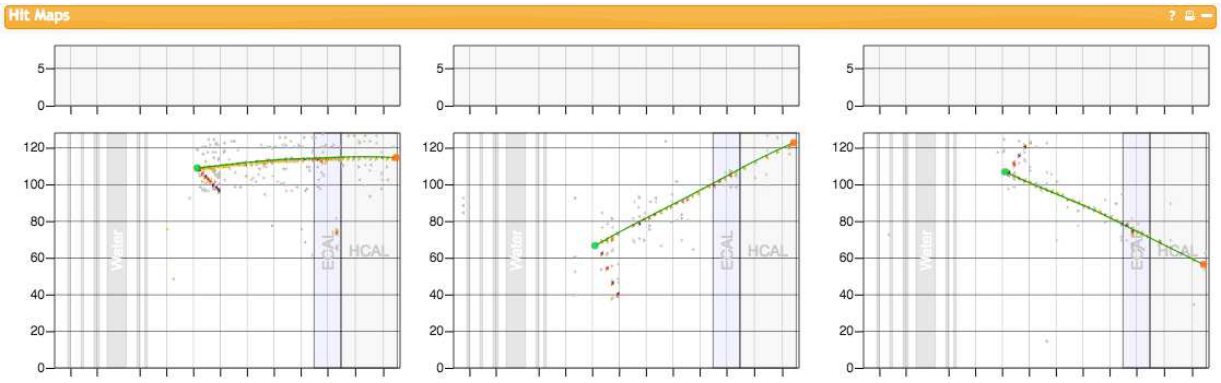

FIG. 6.7: Example 2: CCQE-like candidate, run 2027, subrun 12, gate 262, slice 11. In the final state, there is one muon track and light activities caused by the proton.

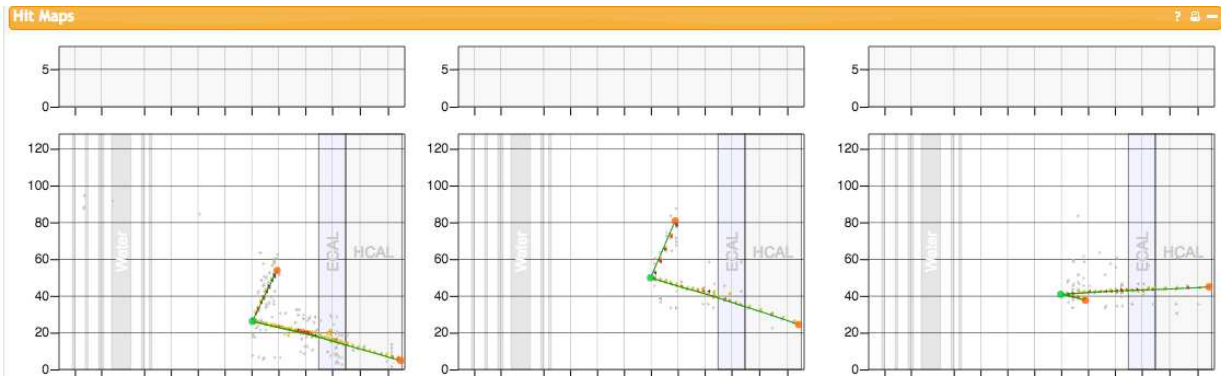

FIG. 6.8: Example 3: CCQE-like candidate, run 2027, subrun 12, gate 215, slice 8. In the final state, there is one muon track and one proton track.

In addition, various distributions of the selected sample of CCQE-like event candidates are shown including **Muon Energy** (Fig. 6.9), **Muon Angle** (Fig. 6.10), **Neutrino Energy** (Fig. 6.11), **Minos Face X** (Fig. 6.12), and **Minos Face Y** (Fig. 6.13). The good agreement of these quantities between data and the simulation enhances some confidence on the Monte Carlo modeling.

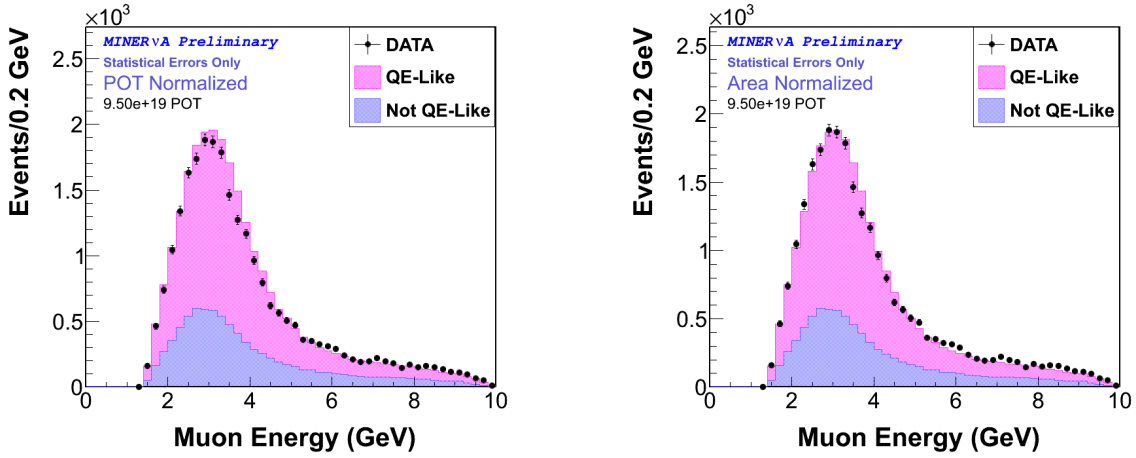

FIG. 6.9: Distributions of muon energy in CCQE-like candidates after applying all cuts. The left plot is normalized by POT. The right plot is normalized by area.

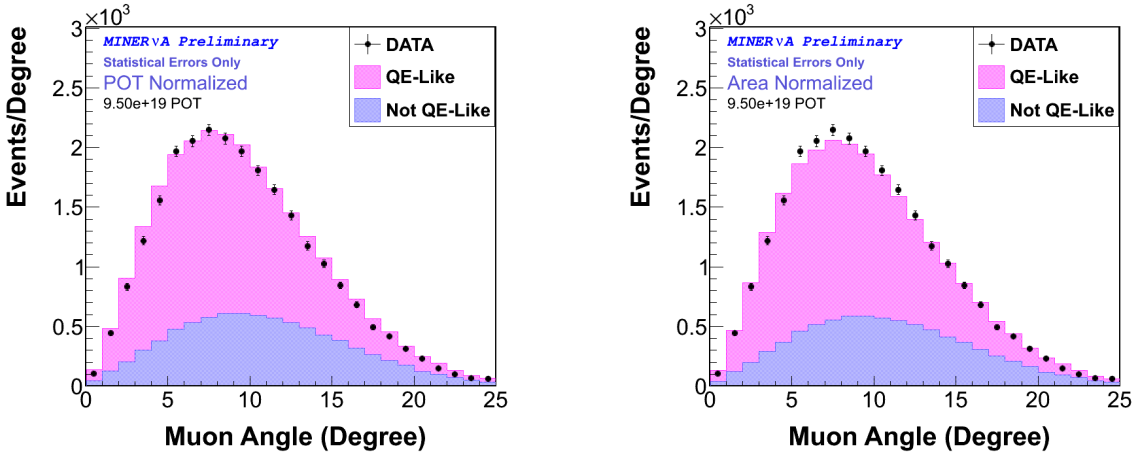

FIG. 6.10: Distributions of muon angle in CCQE-like candidates after applying all cuts. The left plot is normalized by POT. The right plot is normalized by area.

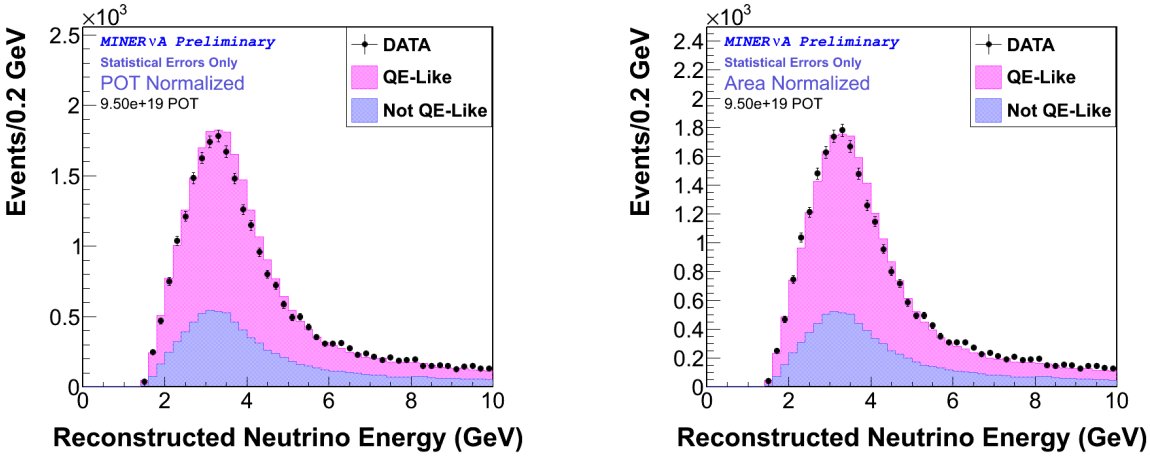

FIG. 6.11: Distributions of neutrino energy in CCQE-like candidates after applying all cuts. The left plot is normalized by POT. The right plot is normalized by area.

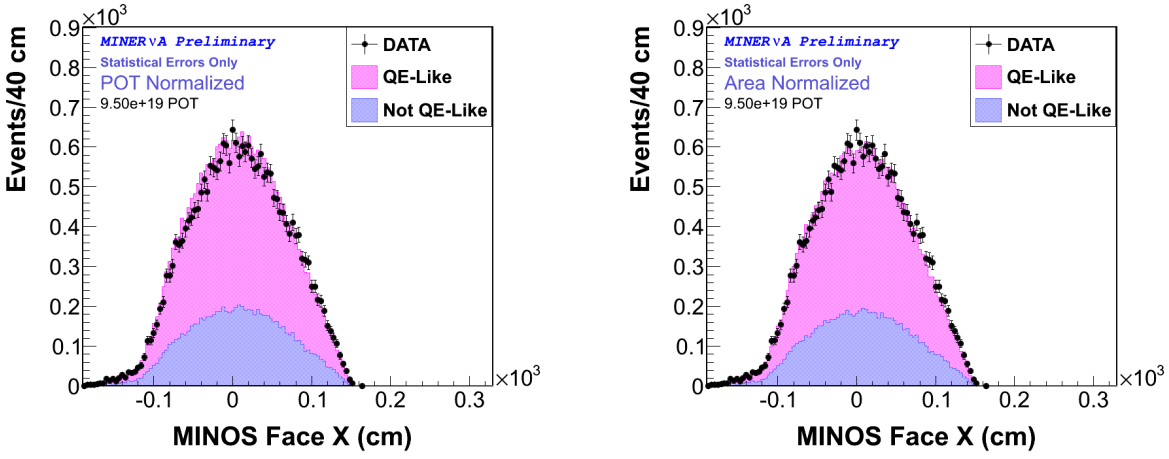

FIG. 6.12: Distributions of minos face X in CCQE-like candidates after applying all cuts. The left plot is normalized by POT. The right plot is normalized by area.

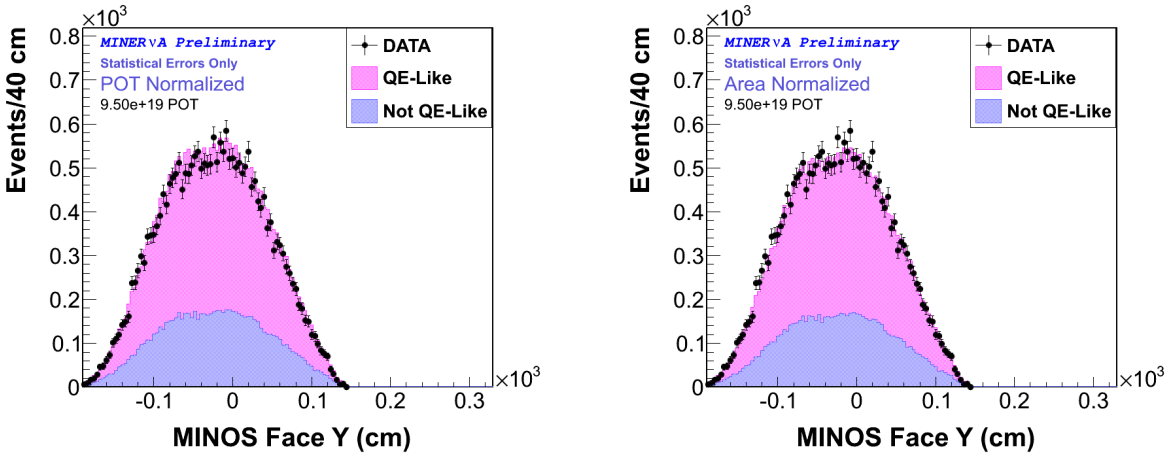

FIG. 6.13: Distributions of minos face Y in CCQE-like candidates after applying all cuts. The left plot is normalized by POT. The right plot is normalized by area.

6.3 Cross-Section Extraction

After selecting the quasi-elastic-like sample, the cross-section is extracted using a multistep procedure described in this section. First of all, the formula to calculate the differential cross-section $\frac{d\sigma}{dQ^2}$ per Q^2 bin i, is given by

$$\left(\frac{d\sigma}{dQ^2_{QELike}}\right)_i = \frac{1}{\phi T} \cdot \frac{\sum_j U_{ij}(N_{data,j} - N^{bkgd}_{data,j})}{\epsilon_i \Delta Q^2_{QELike,i}} \tag{6.3}$$

where U is the migration matrix from the reconstructed Q^2 to the simulated Q^2, $N_{data,j}$ is the number of data events in the j-th Q^2 bin, $N^{bkgd}_{data,j}$ is the estimated number of background data events in the j-th Q^2 bin, ϵ_i is the efficiency in the i-th Q^2 bin to reconstruct the CCQE-like candidates, ϕ is the integrated flux, and T is the target number. The binning is chosen as 0 GeV^2, 0.025 GeV^2, 0.05 GeV^2, 0.1 GeV^2, 0.2 GeV^2, 0.4 GeV^2, 0.8 GeV^2, 1.2 GeV^2, and 2.0 GeV^2.

This analysis aims to extract the differential cross-section as the function of Q^2. There-

fore, the foundation is the distribution of event candidates in each Q^2 bin in both the data and simulation samples as shown in Fig. 6.14.

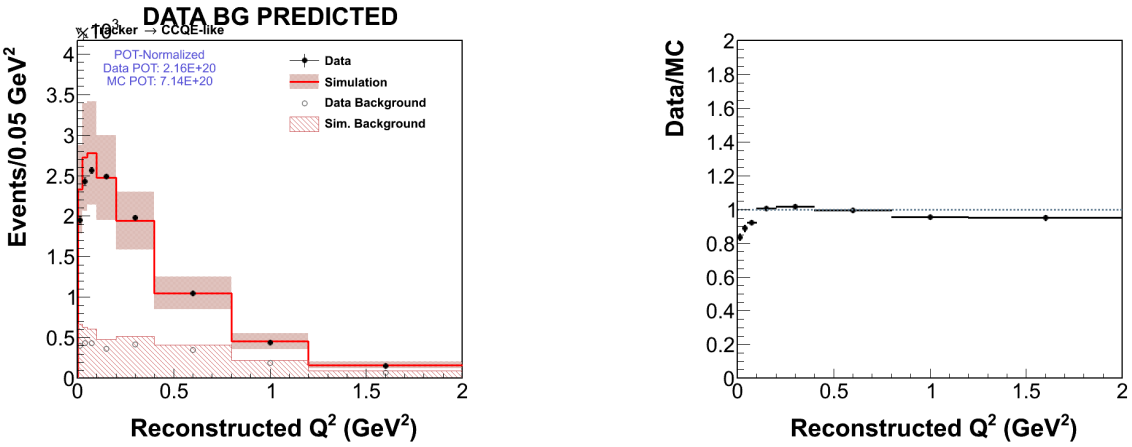

FIG. 6.14: Left: Q^2 distribution for CCQE-like candidates after all cuts described above in data and simulation, with predicted background events in shaded area. Right: ratio of Q^2 distribution for CCQE-like candidates after all cuts described above between data and simulation

The cross-section extraction procedure is divided into four steps. In the **background subtraction step**, the rate of background events are estimated using MC samples and the estimated backgrounds are subtracted from the data. In the **unfolding step**, the reconstructed Q^2_{QElike} distribution is converted to an estimate of the true Q^2_{QElike} distribution. In the **efficiency correction step**, the Monte Carlo as well as the background subtracted and unfolded data are utilized to estimate the number of QE events that actually occurred in each Q^2 bin. This corrects for the imperfect performance of the detector and reconstruction algorithms. In the **normalization step**, the efficiency corrected event yields are normalized by the neutrino flux and the number of targets to produce the differential cross-section. The following sub-sections describe the detailed calculations in each step, in sequential order.

6.3.1 Background Subtraction

In Eq. 6.3, the calculation begins with counting the number of signal events in each Q^2 bin, $N^{data} - N^{bkgd}$. The possible background channels include rock muon events, neutrino interactions occurring outside the fiducial volume, and the non-CCQE-like neutrino interactions, such as the pion productions and DIS interactions. By an eye-scanning procedure, the background from rock muons and neutrino interactions outside the fiducial volume was found to be less than 0.1% and is therefore negligible [7]. Thus, in this analysis, only background due to non CCQE-like neutrino interactions is subtracted by a data-driven technique, which utilizes a combination of MC along with the distributions of recoil energy in each Q^2 bin. Fig. 6.17 shows distributions of the recoil energy for event candidates and it tells the background (shadowed area) tends to be at larger E_{recoil}.

The distributions at high recoil energies are used to constrain the fraction of background events in the low-recoil signal region. This mitigates systematic uncertainties affecting the overall background level in each Q^2 bin. The MC is used to predict the shape of the recoil energy distributions for the signal and background event samples. In later part of this chapter, uncertainties on those shapes caused by uncertainties in the cross-section model and detector response are evaluated.

The recoil energy distributions in MC are utilized to define shape templates for signal and background. The normalizations of these templates are varied to match the corresponding recoil distributions from data for the same Q^2 bin. The fitting algorithm is a maximum likelihood technique using Poisson statistics described in Ref. [61]. In the given Q^2 bin, the scale factor (weights), denoted as $f_{fit,i}$ for bin i, is the result of the template fit, which forces the data and Monte Carlo event rates to be equal.

The factors are utilized to estimate the number of signal events in data, given as

$$N_{data,i}^{signal} = \left(1 - f_{fit,i}\frac{N_{MC,i}^{bkgd}}{N_{MC,i}}\right) N_{data,i}, \tag{6.4}$$

where $N_{MC,i}$ is the number of total event in simulation in bin i, $N_{MC,i}^{bkgd}$ is the subset of those events that are background, and $N_{data,i}$ is the number of events in data in bin i.

From the template fit, the scale factors, the term $f_{fit,i}$ in Eq. 6.4 in each Q^2 bin as a function of Q^2 are shown in Fig. 6.15. The Q^2_{QElike} distribution after subtracting the estimated background is shown in Fig. 6.16.

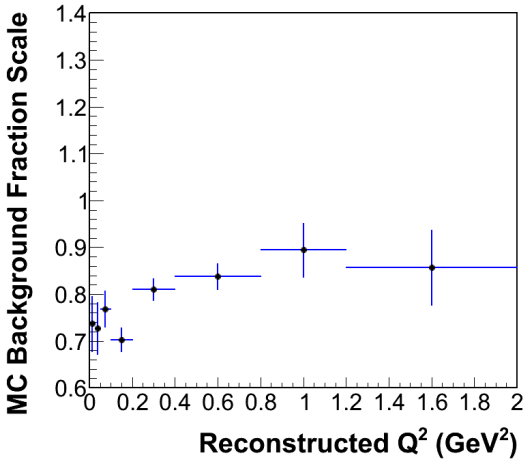

FIG. 6.15: The fit results in each Q^2 bin, the same binning as Q^2.

Distributions of recoil energy before and after fits in each Q^2 bin are shown in Fig. 6.17 (distributions of recoil energy in Q^2 bin 1, 2, 3, and 4 before the template 4), Fig. 6.18 (distributions of recoil energy in Q^2 bin 5, 6, 7, and 8 before the template 4), Fig. 6.19 (distributions of recoil energy in Q^2 bin 1, 2, 3, and 4 after the template 4), and Fig. 6.20 (distributions of recoil energy in Q^2 bin 5, 6, 7, and 8 after the template 4).

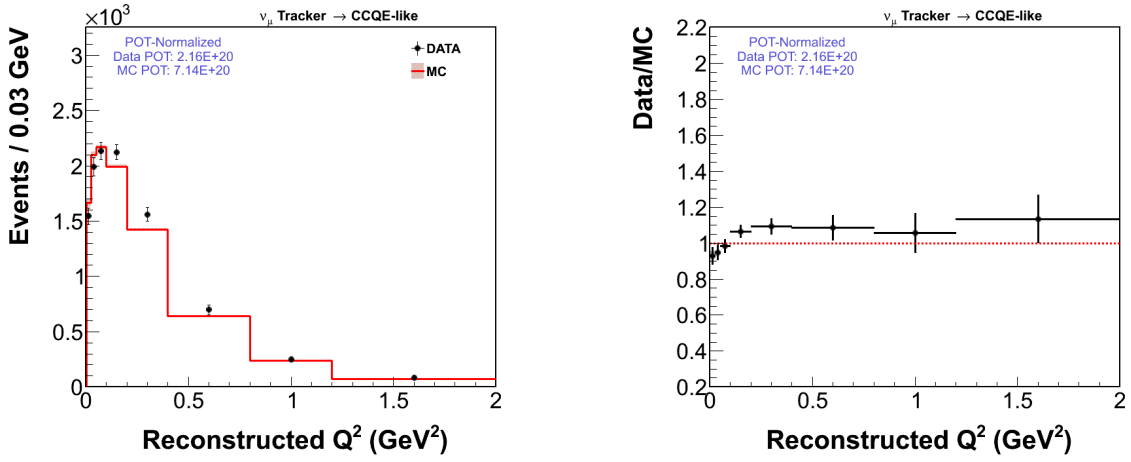

FIG. 6.16: The left plot is Q^2 distribution for CCQE-like candidates after subtracting estimating background in data and simulation. The right plot is the ratio plot.

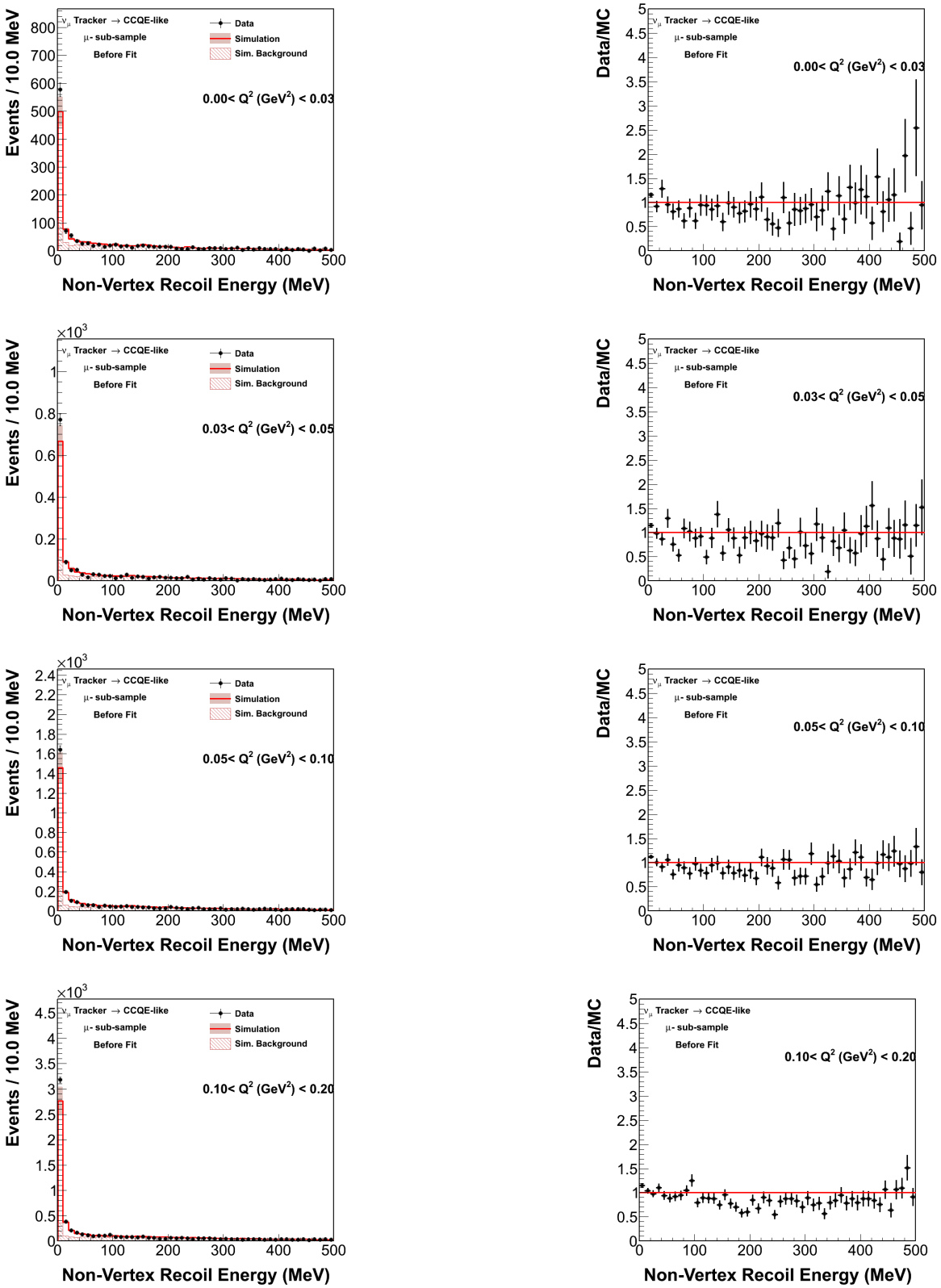

FIG. 6.17: Area normalized data/MC overlays and ratios for the first four of eight Q^2 bins of recoil energy before the template fit. From top to bottom, the plots are for bin 1, bin 2, bin 3, and bin 4, respectively. The right plots are the ratio distributions between data and Monte Carlo.

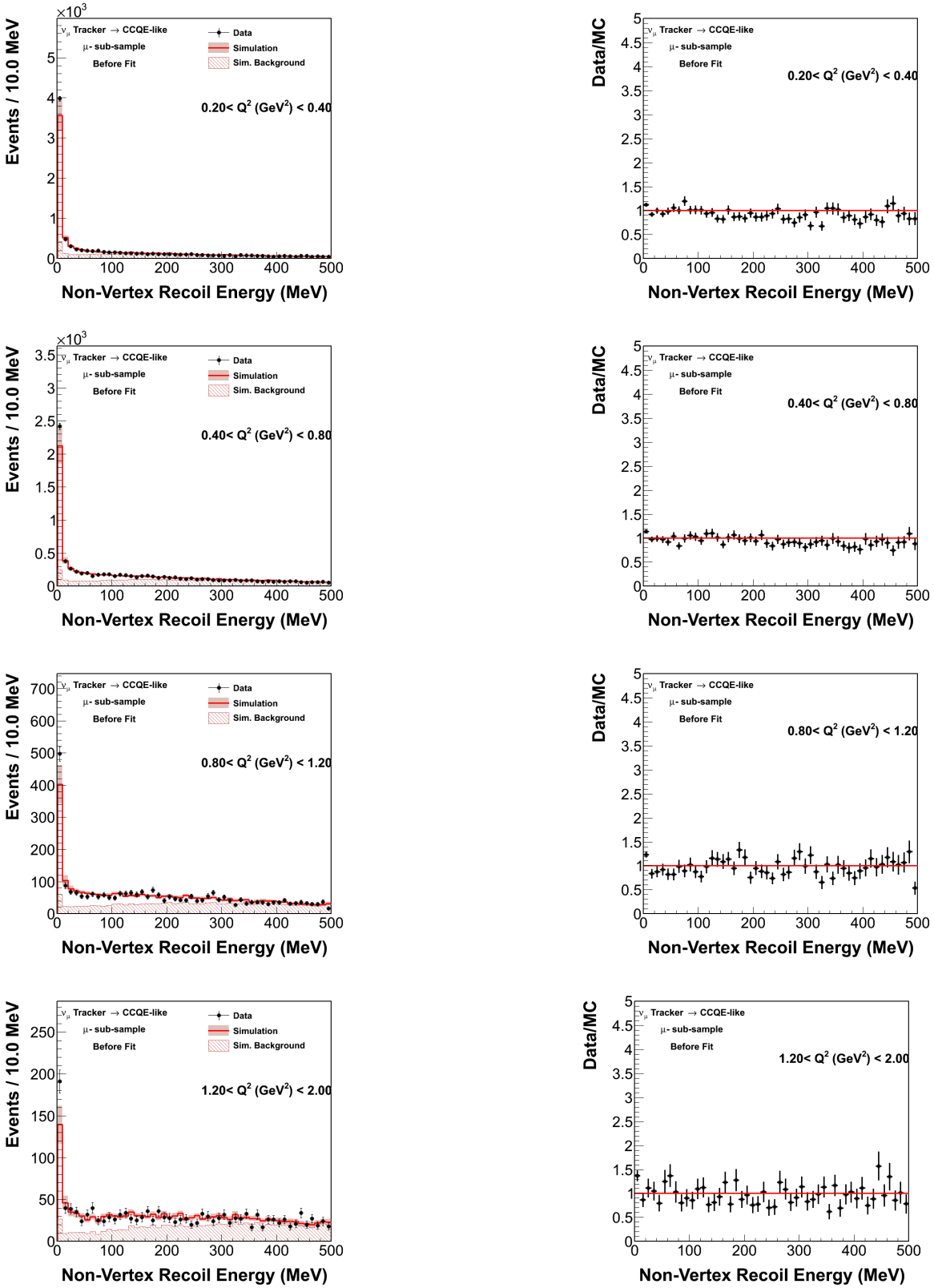

FIG. 6.18: Continued. Area normalized data/MC overlays and ratios for the last four of eight Q^2 bins of recoil energy before the template fit. From top to bottom, the plots are for bin 5, bin 6, bin 7, and bin 8, respectively. The right plots are the ratio distributions between data and Monte Carlo.

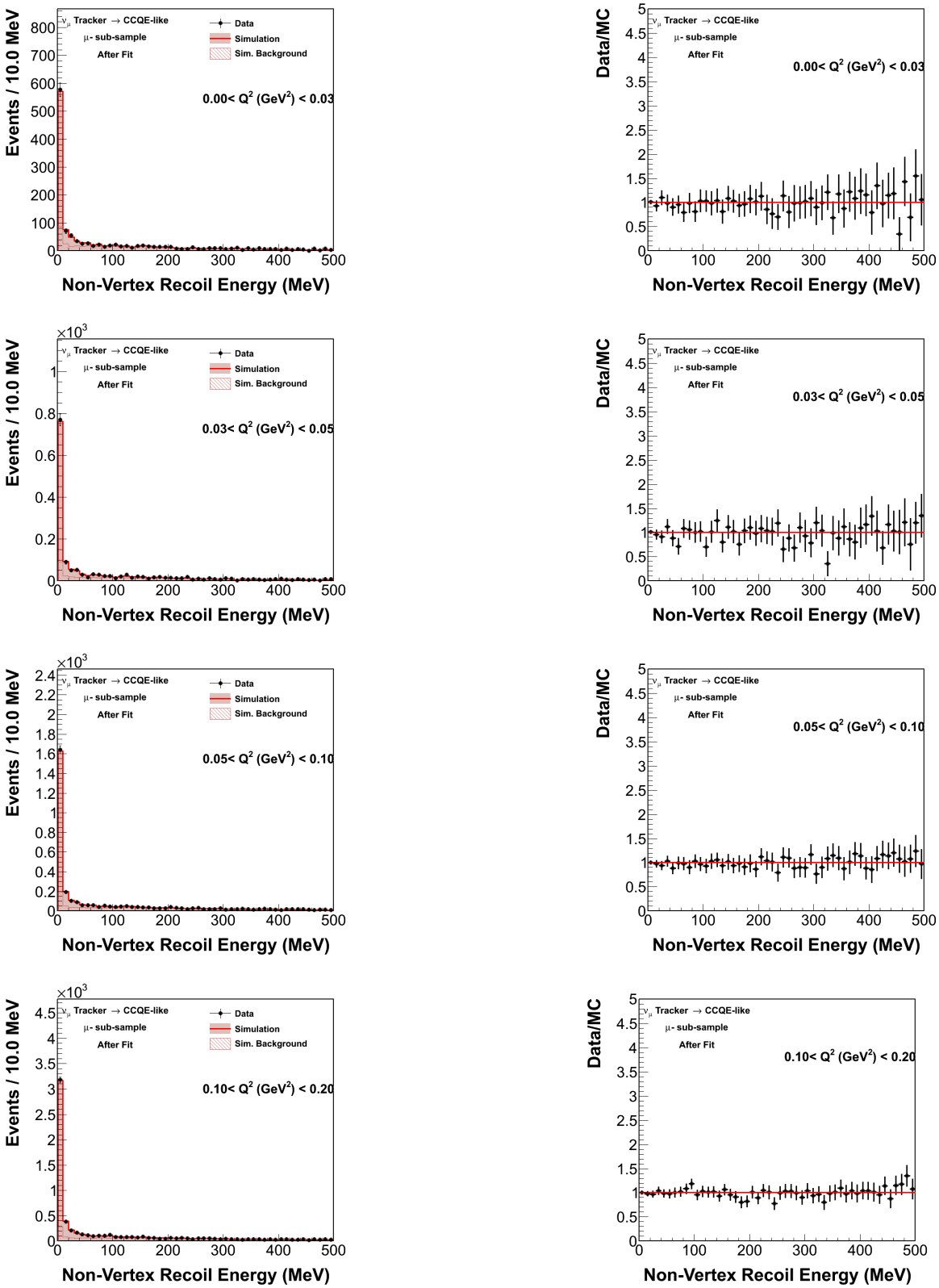

FIG. 6.19: Area normalized data/MC overlays and ratios for the first four of eight Q^2 bins of recoil energy after the template fit. From top to bottom, the plots are for bin 1, bin 2, bin 3, and bin 4, respectively. The right plots are the ratio distributions between data and Monte Carlo.

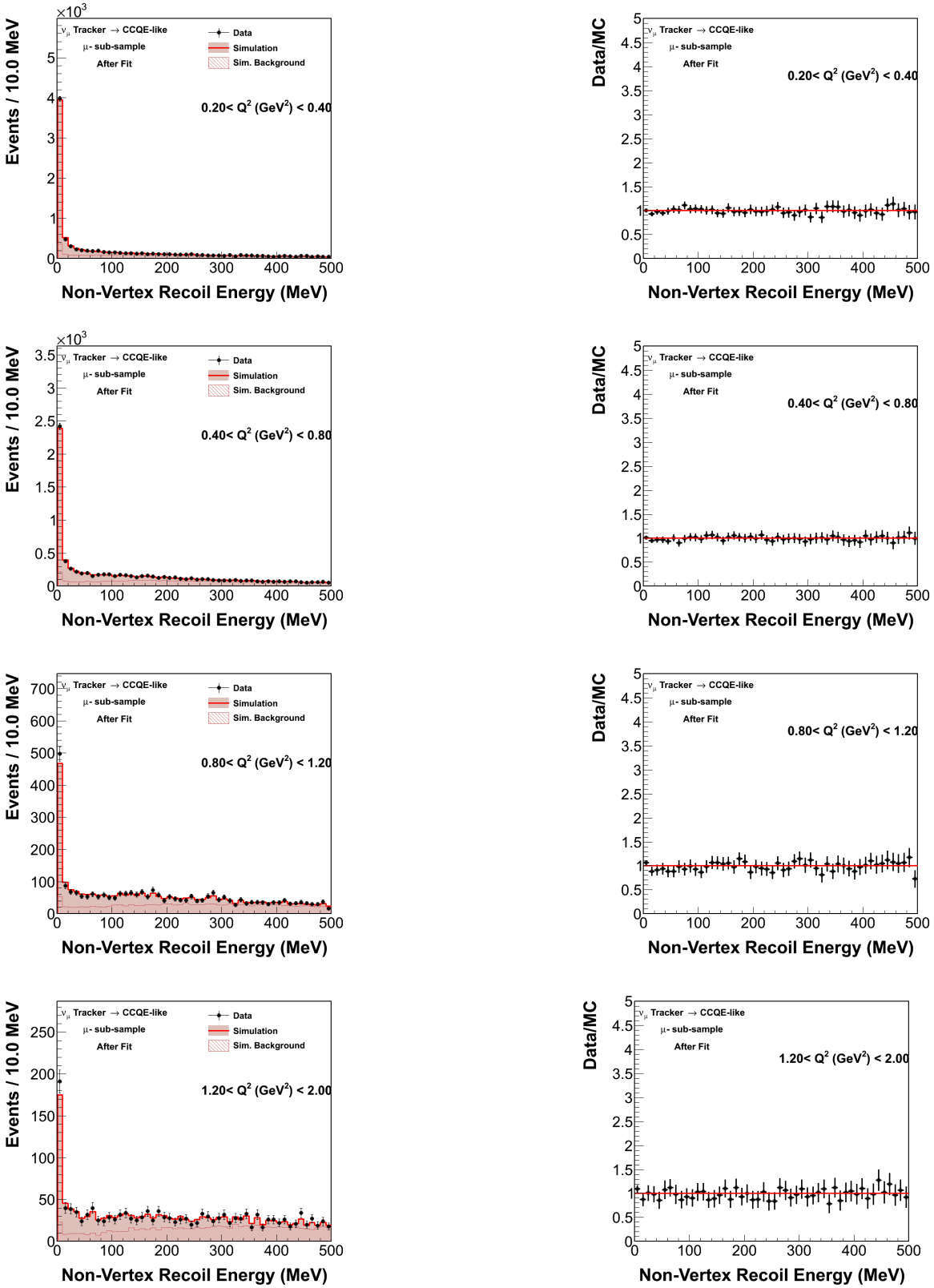

FIG. 6.20: Area normalized data/MC overlays and ratios for the last four of eight Q^2 bins of recoil energy after the template fit. From top to bottom, the plots are for bin 5, bin 6, bin 7, and bin 8, respectively. The right plots are the ratio distributions between data and Monte Carlo.

6.3.2 Bin Migration and Unfolding

After the estimated backgrounds have been subtracted, the reconstructed Q^2 distribution is unfolded to mimic the true Q^2 distribution. This unfolding procedure accounts for the detector smearing effects, such as the resolution effects and reconstruction basis. For example, the muon energy and angle are not measured with perfect resolution. The smearing effects cause events to migrate from bin to bin.

The unfolding procedure starts by constructing the smearing matrix, which is determined from the Monte Carlo truth information and is given by

$$U_{ij} = \frac{N^{reco,i}_{true,j}}{N^{reco}_{true,j}}, \tag{6.5}$$

where $N^{reco}_{true,j}$ is the number of events with truth information located in bin j and $N^{reco,i}_{true,j}$ is a subset of those events that are reconstructed in bin i. The next step is to invert the smearing matrix and unfold the reconstructed distribution to the truth distribution. The step is demonstrated in the following equation:

$$N^{true}_{data,i} = \sum_j N^{reco}_{data,j} U_{ij}. \tag{6.6}$$

The migration matrix, shown in Fig. 6.21, converts the number of reconstructed events in bin j to the number of true events in bin i.

The Q^2_{QElike} distribution after unfolding is shown in Fig. 6.22.

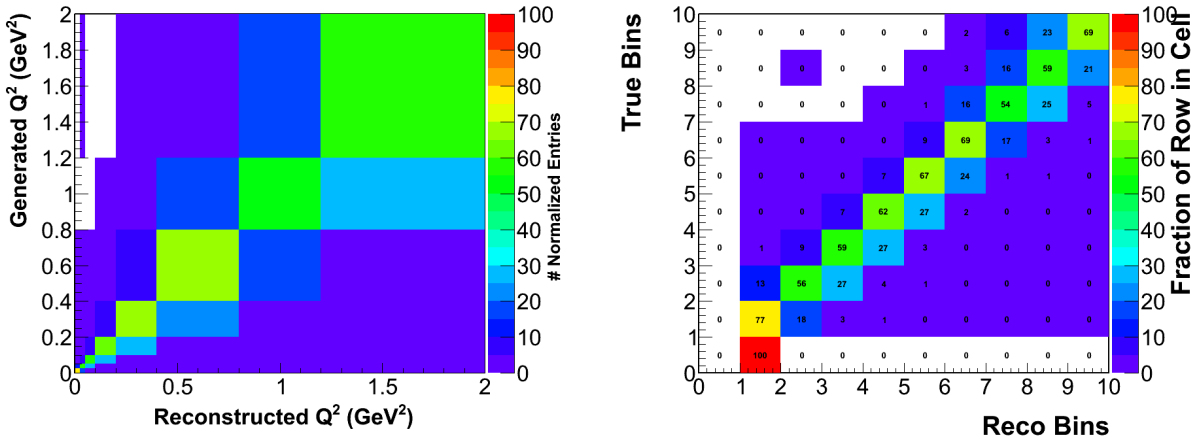

FIG. 6.21: migration matrix

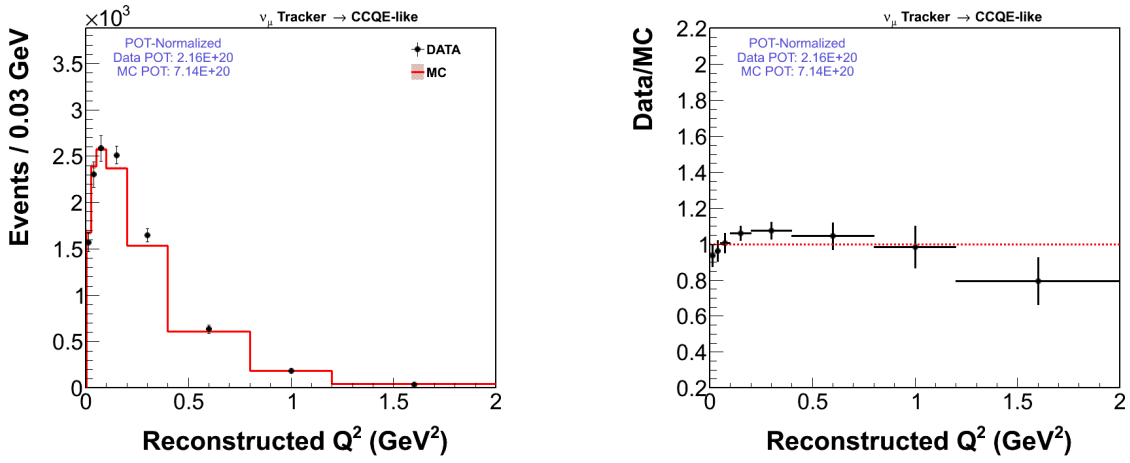

FIG. 6.22: The left plot is Q^2 distribution for CCQE-like candidates after unfolding in data and simulation. The right plot is the ratio plot.

6.3.3 Efficiency and Acceptance Corrections

It is expected that some of the observed ν_μ CCQE-like events fail to enter the final selected sample due to the detector and reconstruction inefficiencies, and some signal events are rejected by the cuts. For example, larger angle muon tracks have lower possibilities matching to a track in MINOS. Therefore, an overall bin by bin correction must be conducted. The efficiency of observing CCQE-like events is estimated using the simulation as:

$$\epsilon_i = \frac{N^{rec}_{gen,i}}{N_{gen,fid,i}}, \tag{6.7}$$

where $N^{rec}_{gen,i}$ is the number of MC signal events that pass reconstruction cuts and that are located in Q^2 bin i.$N_{gen,fid,i}$ is the number of signal events generated in bin i that have true vertices in the fiducial volume.

The plot of efficiency as a function of Q^2 and the purity plot are shown in Fig. 6.23. The efficiency and purity are not uniformly distributed. The cut on the recoil energy removes more events in high Q^2 than in low Q^2 bins. The efficiency is also reduced due to several other effects, including deadtime, and muons that are mis-reconstructed in MINERνA or do not lead to tracks in MINOS. The efficiency corrected true Q^2 distribution is shown in Fig. 6.24.

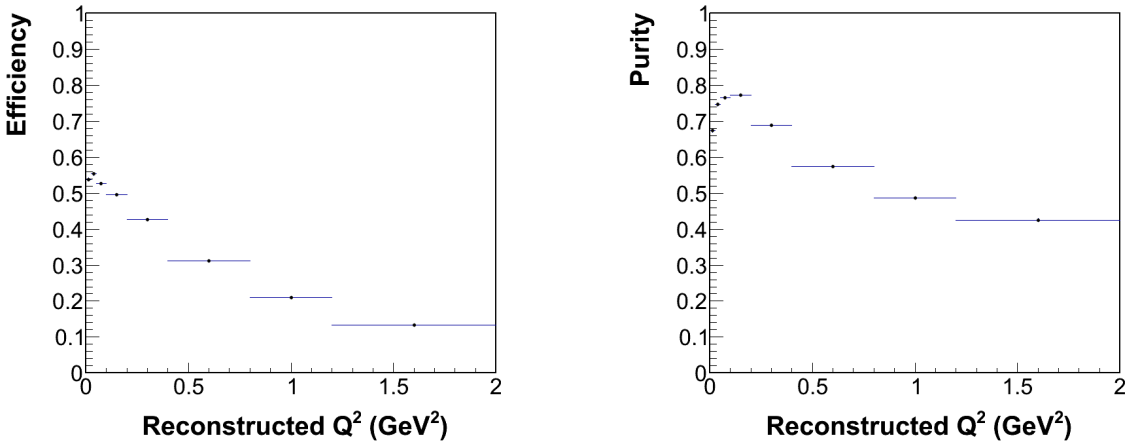

FIG. 6.23: Efficiency distribution (right) and purity distribution (left) of CCQE-like candidates reconstruction as a function of Q^2.

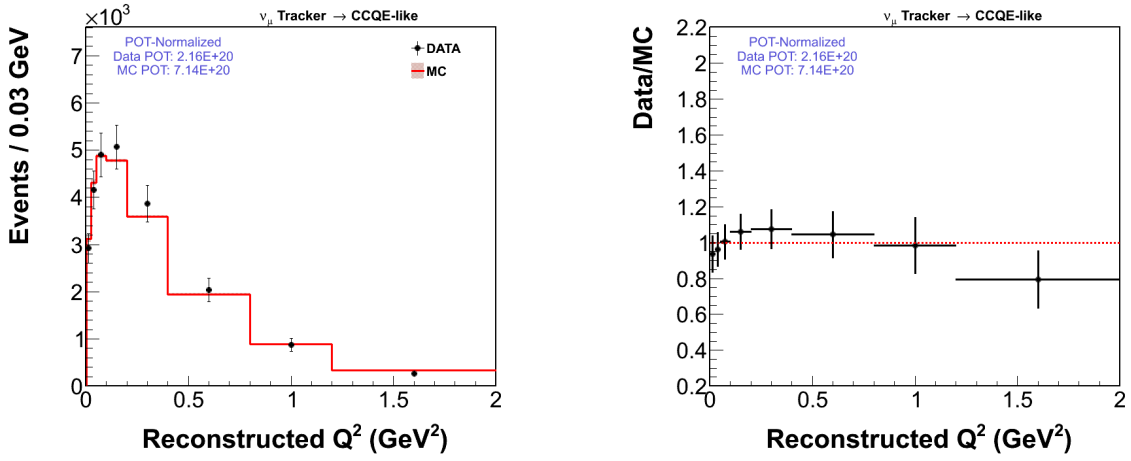

FIG. 6.24: The left plot is Q^2 distribution for CCQE-like candidates after efficiency correction in data and simulation. The right plot is the ratio plot.

6.3.4 Normalization

Normalization includes two factors: one is neutrino flux and the other is the number of nucleons in the detector target. The Gen0 muon neutrino flux used as a normalization factor in this analysis is shown in Fig. 6.25. The flux integrated over the entire spectrum, $0 < E_\nu < 100$ GeV, is $2.90561 \times 10^{-8}/cm^2/POT$.

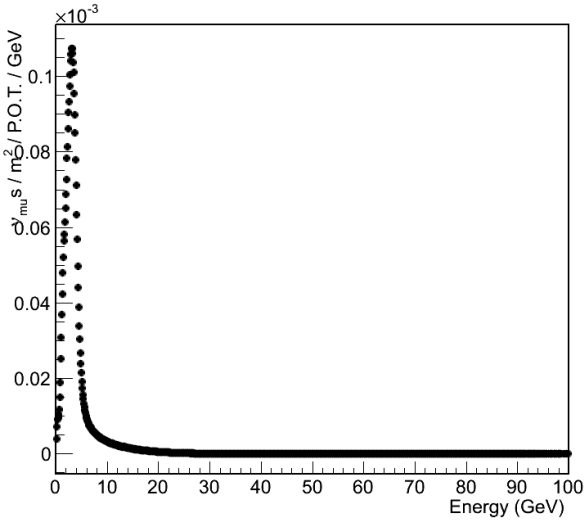

FIG. 6.25: The NuMI flux at MINERνA in neutrino mode as a function of neutrino energy, extracted from Monte Carlo.

Although the fiducial volume for this analysis is composed primarily of polystyrene scintillator, other elements are also present. Details can be found in Chap. 2. In total, the number of targets within in the MINERνA fiducial volume is calculated to be 1.51596×10^{30} neutrons.

6.3.5 Final Differential Cross-section Results of CCQE-like Analysis

After normalization, the differential cross-section $d\sigma/dQ^2_{QElike}$ for CCQE-like one track analysis is shown in Fig. 6.26. Tab. 6.2 lists the cross-section measurement for each bin.

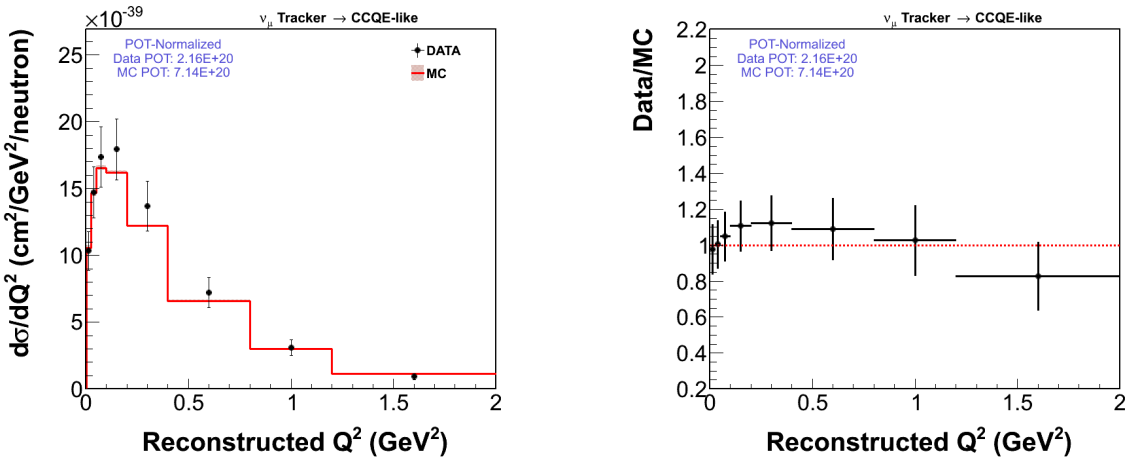

FIG. 6.26: The left plot shows the differential cross section distribution as function of Q^2 for CCQE-like candidates in data and simulation. The right plot is the ratio between data and simulation.

TABLE 6.2: Flux-integrated $d\sigma/dQ^2_{QE-like}$ summary. Both the statistical (first) and absolute systematic (second) errors are presented in each bin.

$Q^2_{QE-like}$(GeV^2)	Cross Section (10^{-38}cm^2/GeV^2/nucleon)
0.0 - 0.025	1.033 ± 0.025 ± 0.142
0.025 - 0.05	1.471 ± 0.025 ± 0.192
0.05 - 0.1	1.734 ± 0.021 ± 0.224
0.1 - 0.2	1.793 ± 0.016 ± 0.229
0.2 - 0.4	1.368 ± 0.012 ± 0.186
0.4 - 0.8	0.720 ± 0.009 ± 0.112
0.8 - 1.2	0.310 ± 0.007 ± 0.058
1.2 - 2.0	0.093 ± 0.004 ± 0.021

The Differential Cross-section of CCQE Channel

Fig.6.27 shows the distribution of the differential cross-section for the CCQE channel, including both statistical and systematic errors.

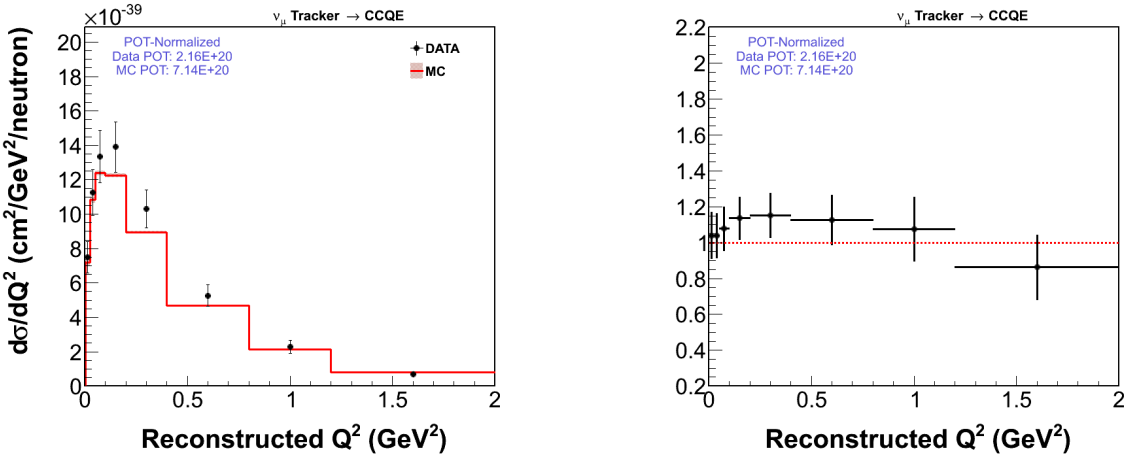

FIG. 6.27: The left plot shows the differential cross section distribution as function of Q^2 for CCQE candidates in data and simulation. The right plot is the ratio between data and simulation.

TABLE 6.3: Flux-integrated $d\sigma/dQ^2_{QE}$ summary. Both the statistical (first) and absolute systematic (second) errors are presented in each bin.

Q^2_{QE}(GeV^2)	Cross Section (10^{-38}cm^2/GeV^2/nucleon)
0.0 - 0.025	0.748 ± 0.021 ± 0.088
0.025 - 0.05	1.126 ± 0.021 ± 0.131
0.05 - 0.1	1.335 ± 0.018 ± 0.150
0.1 - 0.2	1.390 ± 0.014 ± 0.145
0.2 - 0.4	1.029 ± 0.010 ± 0.110
0.4 - 0.8	0.527 ± 0.008 ± 0.064
0.8 - 1.2	0.229 ± 0.007 ± 0.037
1.2 - 2.0	0.070 ± 0.003 ± 0.014

6.3.6 Comparing to the Previous Published Result

As mentioned in Chapter 1, part of the motivation of this analysis is to improve the measurement of the previous published result. Two major changes have been made in this analysis comparing to the previous published analysis:

- expand the energy range of incoming neutrino flux from 1.5-10 GeV to 0-100 GeV;
- implement the application of Michel veto.

In order to compare to the previous result, results from intermedia stage analysis are shown in this section, each of which restores back one major change sequentially. This thesis focuses on the measurement of $d\sigma/dQ^2_{QE}$ for E_ν at 0-100 GeV using Michel veto. The intermedia stage analysis include: **intermedia stage 1**, the measurement made for E_ν at 1.5-10 GeV using Michel veto, and **intermedia stage 2**, the measurement made for E_ν at 1.5-10 GeV not using Michel veto. The second analysis uses the same settings and is comparable to the previous analysis.

The differential cross-section differences between each stage and previous stage analysis in each Q^2 bin are calculated as well as the overall changes between stages. At the end, an apple-to-apple comparison is made between stage 2 analysis and previous published analysis.

6.3.6.1 Intermedia Stage 1: $d\sigma/dQ^2_{QE}$ for E_ν at 1.5-10 GeV with Michel Veto

Fig.6.28 shows the distribution of the differential cross-section for the CCQE channel from the intermedia stage 1 analysis. Comparing to the main analysis, the first major change is restored, which is the neutrino energy range from 0-100 GeV (my analysis) to 1.5-10 GeV (previous published analysis). Tab. 6.4 shows the differential cross section difference between the main analysis and the intermedia stage 1 analysis. Overall, the $d\sigma/dQ^2_{QE}$ in the intermedia stage 1 analysis is 2.8% lower.

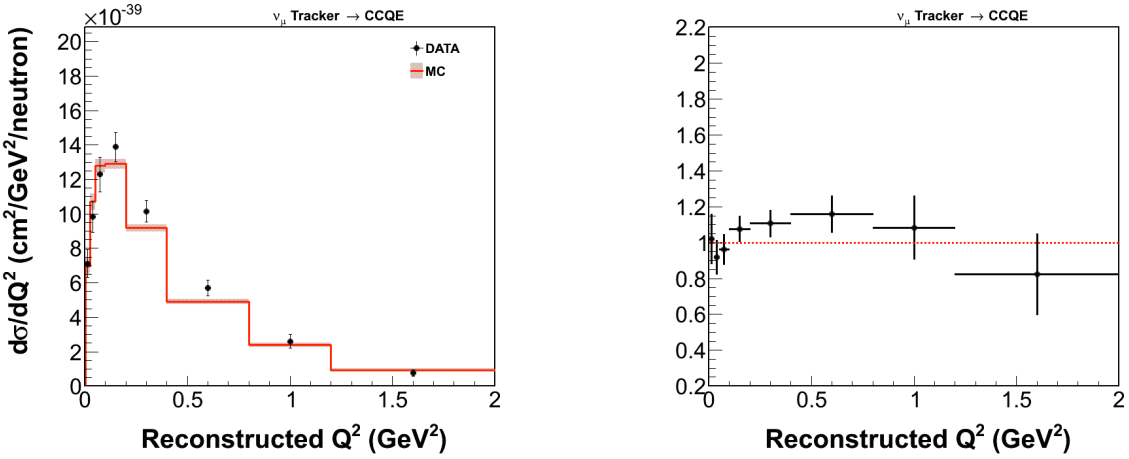

FIG. 6.28: The left plot shows $d\sigma/dQ^2_{QE}$ from the intermedia stage 1 analysis. The ratio plot is on the right.

TABLE 6.4: Summary of the difference between $d\sigma/dQ^2_{QE}$ measurements on neutrino energy range 0-100 GeV and 1.5-10 GeV. Overall the new result is 2.8% lower.

Q^2_{QE} (GeV^2)	Main Analysis Cross-section (10^{-38}cm^2/GeV^2/nucleon)	Intermedia Stage 1 Cross-section (10^{-38}cm^2/GeV^2/nucleon)	Difference (%)
0.0 - 0.025	0.748	0.720	-2.70
0.025 - 0.05	1.126	0.997	-11.46
0.05 - 0.1	1.335	1.240	-7.12
0.1 - 0.2	1.390	1.396	0.43
0.2 - 0.4	1.029	1.014	-1.46
0.4 - 0.8	0.527	0.578	9.68
0.8 - 1.2	0.229	0.247	7.86
1.2 - 2.0	0.070	0.081	15.71

6.3.6.2 Intermedia Stage 2: $d\sigma/dQ^2_{QE}$ for E_ν at 1.5-10 GeV without Michel Veto

Furthermore, the Michel veto is removed in the intermedia stage 2 analysis in order to mimic the published analysis. Both major changes are restored. Fig.6.29 shows the distribution of the differential cross-section for the CCQE channel from the intermedia stage 2 analysis, including both statistical and systematic errors, shown in Tab. 6.5 as well as central values in each bin. Tab. 6.6 shows the differential cross section difference between the intermedia stage 1 and 2 analysis. Overall, the $d\sigma/dQ^2_{QE}$ in the intermedia stage 2 analysis is 3.86% higher comparing to the stage 1 analysis.

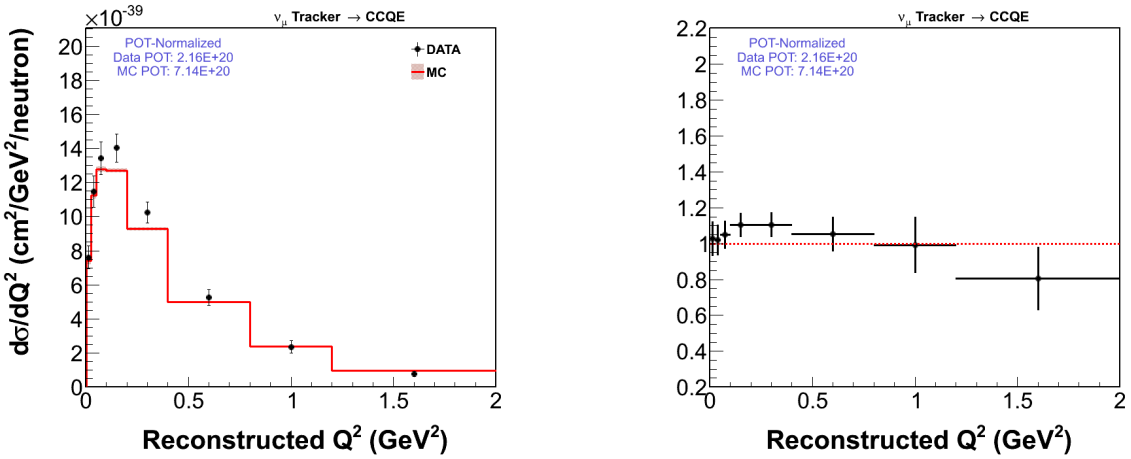

FIG. 6.29: The left plot shows the differential cross section distribution as function of Q^2 for CCQE candidates in data and simulation. The right plot is the ratio between data and simulation. This analysis is for neutrino energy range 1.5-10 GeV without Michel veto.

TABLE 6.5: Stage 2 flux-averaged $d\sigma/dQ^2_{QE}$ summary. In each measurement, the first error is statistical and the second is systematic.

Q^2_{QE} (GeV^2)	Cross Section $(10^{-38} cm^2/GeV^2/\text{nucleon})(\%)$
0.0 - 0.025	0.761 ± 0.026 ± 0.061
0.025 - 0.05	1.148 ± 0.024 ± 0.089
0.05 - 0.1	1.342 ± 0.019 ± 0.095
0.1 - 0.2	1.402 ± 0.015 ± 0.080
0.2 - 0.4	1.024 ± 0.011 ± 0.061
0.4 - 0.8	0.525 ± 0.009 ± 0.046
0.8 - 1.2	0.236 ± 0.009 ± 0.036
1.2 - 2.0	0.077 ± 0.005 ± 0.016

TABLE 6.6: Summary of the difference between $d\sigma/dQ^2_{QE}$ measurement with and without Michel veto. Overall the new result is 3.86% higher.

Q^2_{QE} (GeV^2)	Intermedia Stage 1 Cross-section (10^{-38}cm^2/GeV^2/nucleon)	Intermedia Stage 2 Cross-section (10^{-38}cm^2/GeV^2/nucleon)	Difference (%)
0.0 - 0.025	0.720	0.761	5.69
0.025 - 0.05	0.997	1.148	15.15
0.05 - 0.1	1.240	1.342	8.23
0.1 - 0.2	1.396	1.402	0.43
0.2 - 0.4	1.014	1.024	0.99
0.4 - 0.8	0.578	0.525	-9.17
0.8 - 1.2	0.247	0.236	-4.45
1.2 - 2.0	0.081	0.077	-4.94

6.3.6.3 The Previous Published Result

Fig. 6.30 shows the previous published results: the differential cross-section as a function of Q^2 for CCQE channel, including statistical errors only, reprinted from [23]. Tab. 6.7 lists the central values and errors in each Q^2 bin [1].

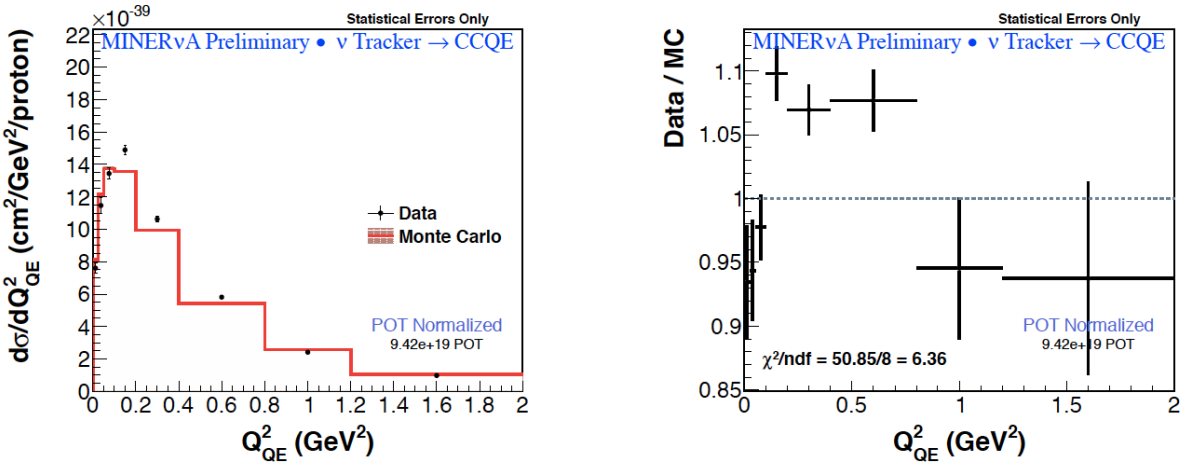

FIG. 6.30: Previous results of differential cross-section with respect to Q^2. Reprinted from [23].

TABLE 6.7: Previous flux-averaged $d\sigma/dQ^2_{QE}$ summary. In each measurement, the first error is statistical and the second is systematic. Reprinted from [1].

Q^2_{QE} (GeV^2)	Cross Section $(10^{-38}cm^2/GeV^2/\text{nucleon})(\%)$
0.0 - 0.025	0.761 ± 0.035 ± 0.097
0.025 - 0.05	1.146 ± 0.047 ± 0.137
0.05 - 0.1	1.343 ± 0.034 ± 0.156
0.1 - 0.2	1.490 ± 0.028 ± 0.170
0.2 - 0.4	1.063 ± 0.019 ± 0.120
0.4 - 0.8	0.582 ± 0.013 ± 0.074
0.8 - 1.2	0.242 ± 0.014 ± 0.053
1.2 - 2.0	0.097 ± 0.008 ± 0.024

Tab. 6.8 shows the differential cross section difference between the intermedia stage 2 analysis and the previous published analysis. The two analysis have the same neutrino energy range and neither of the analysis has applied Michel veto. Thus, they are comparable analysis. Overall, the $d\sigma/dQ^2_{QE}$ in the intermedia stage 2 analysis is 3.10% lower than the published result. Besides the two major changes, some other changes are also accomplished in my analysis, such as 230% more data are used, decreasing the statistical errors, and the updated error estimation reduced the systematic uncertainties, which is covered in the Sec. 6.4.

TABLE 6.8: Summary of the difference between $d\sigma/dQ^2_{QE}$ measurements from intermedia stage 2 and the previous published analysis. Overall the new result is 3.10% lower.

Q^2_{QE} (GeV^2)	Previous Published Cross-section (10^{-38}cm^2/GeV^2/nucleon)	Intermedia Stage 2 Cross-section (10^{-38}cm^2/GeV^2/nucleon)	Difference (%)
0.0 - 0.025	0.761	0.761	0.0
0.025 - 0.05	1.146	1.148	1.37
0.05 - 0.1	1.343	1.342	-0.07
0.1 - 0.2	1.490	1.402	-5.90
0.2 - 0.4	1.063	1.024	-3.67
0.4 - 0.8	0.582	0.525	-9.79
0.8 - 1.2	0.242	0.236	-2.48
1.2 - 2.0	0.097	0.077	-20.62

6.3.7 CCQE/CCQE-like Analyses Using the New Flux

Similar analyses using a newer prediction of the neutrino flux prediction have been performed as well. Details of the studies are discussed in this section.

Different from the Gen0 flux used to normalize the differential cross-sections in the CCQE-like and CCQE analysis described in the previous section, the newer prediction of the flux includes corrections on the horn geometry and it is termed as the Gen2-thin flux. Fig. 6.31 shows the new neutrino flux (top) and the ratio between the new flux and the Gen0 flux (bottom). The new flux is integrated to be 2.88996×10^{-8}/cm^2/POT from 0 GeV to 20 GeV. Note that, these studies consider central values only because the systematic uncertainties on the new flux have not been estimated.

There are two places where the new flux affects these analyses. First, when assigning weights to MC events, a correction from the new flux was introduced and applied. Second, when normalizing the differential cross-section with the neutrino flux, the newer prediction of the neutrino flux was used. Step by step calculation on the final cross-section is shown. Results of the CCQE-like analysis are shown first, followed by results of the CCQE analysis.

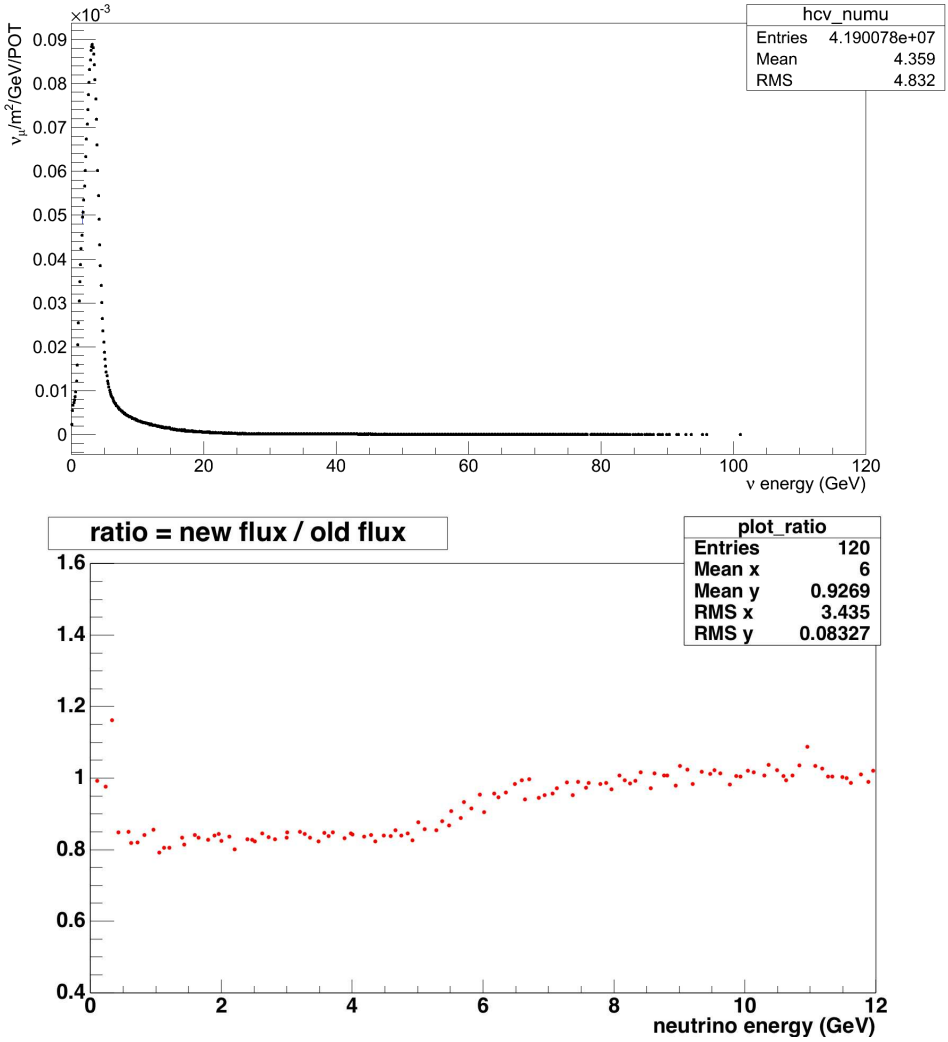

FIG. 6.31: The new NuMI flux at MINERνA in neutrino mode as a function of neutrino energy (upper). The distribution of ratio between the new flux and the old flux (lower).

6.3.7.1 The CCQE-like Analysis Using the New Flux

Event Candidates Selection

Fig. 6.32 shows that data distributions are the same in two analysis using the old flux and the new flux, and the simulation sample predicts fewer events using the new flux than the one using the old flux.

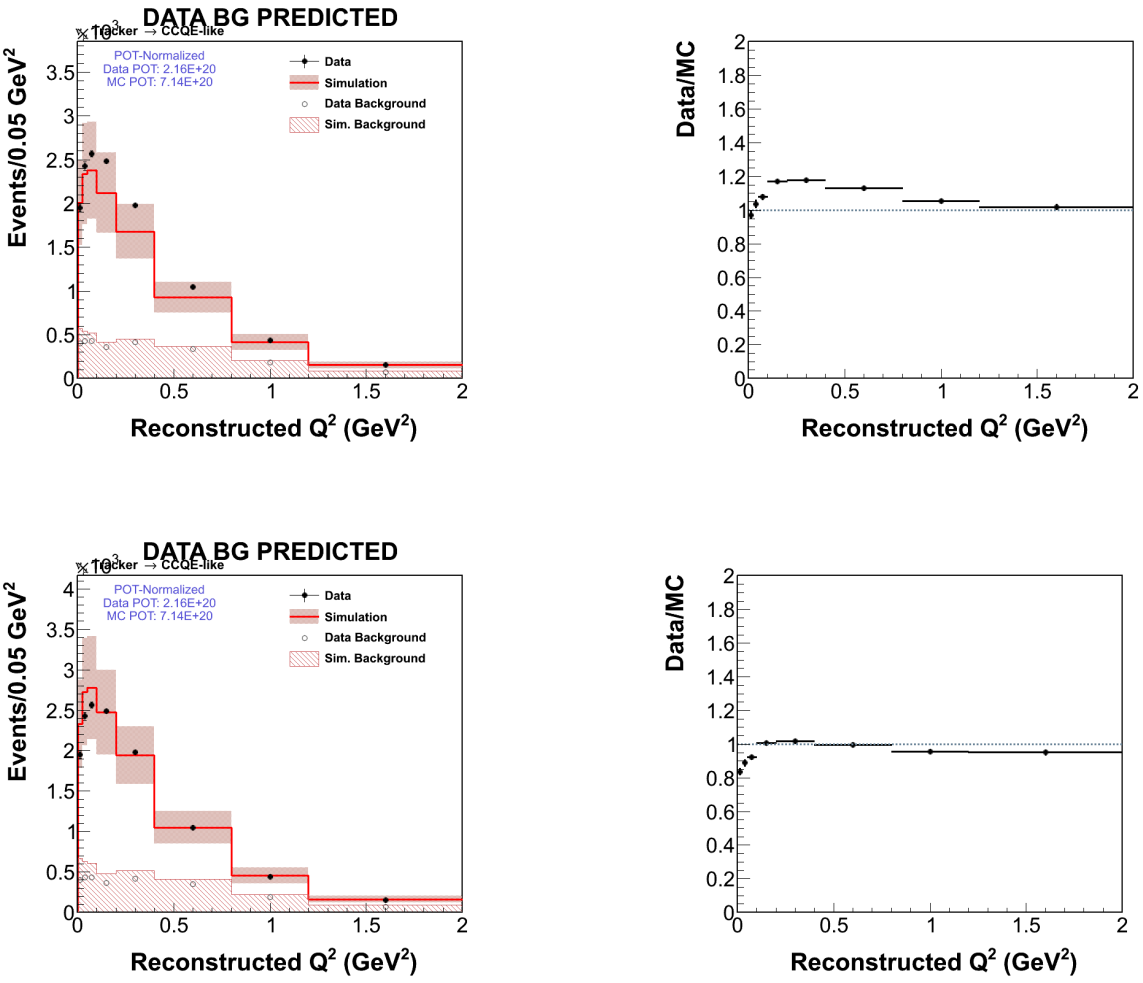

FIG. 6.32: Number of event candidates in each Q^2 bin from the data and the simulation. Right plots are the ratio between the data and simulation. Top plots are from the analysis using the new flux. Bottom plots are from the analysis using the old flux.

Background Subtraction

Fig. 6.33 shows the background scale factors in the left and ratio between factors in the analysis using the new and old flux. After subtracting the predicted background, the data distribution in the analysis using the new flux is higher than the distribution in the analysis using the old flux (Fig. 6.34). The reason is the simulation using the new flux predicts fewer signal/background events.

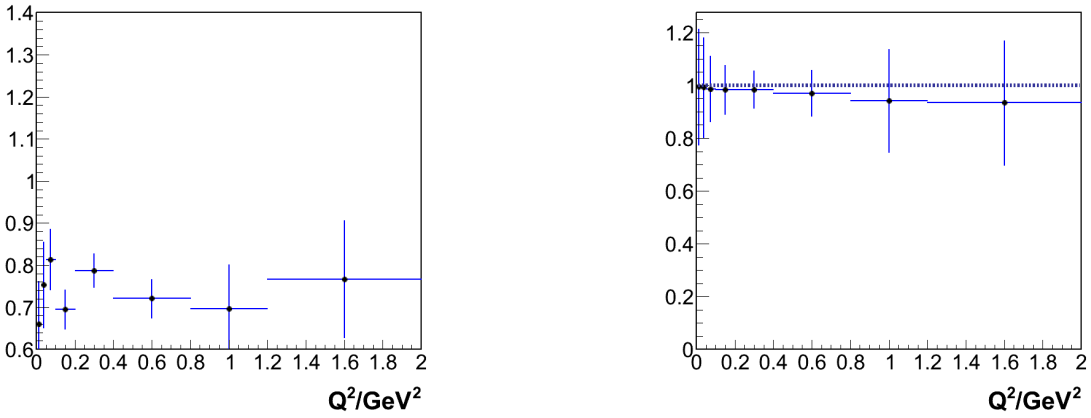

FIG. 6.33: Background fraction scales in the simulation (left). The right plot is the ratio between scale factors from the analysis using the new flux and the ones from the analysis using the old flux.

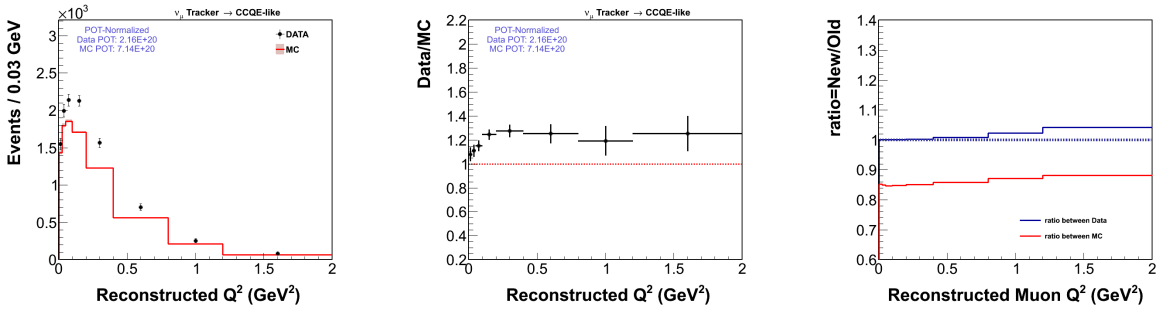

FIG. 6.34: The left plot is the distribution of event candidates after subtracting the background. The middle plot is the data/MC ratio. The right plot shows the ratio between the analysis using the new flux and the analysis using the old flux.

Unfolding

Fig. 6.35 shows the migration matrix in the CCQE-like analysis using the new flux. Fig. 6.36 shows the event entries in the data and simulation after unfolding. The left plot is the ratio between entries in the analysis using the new and old flux.

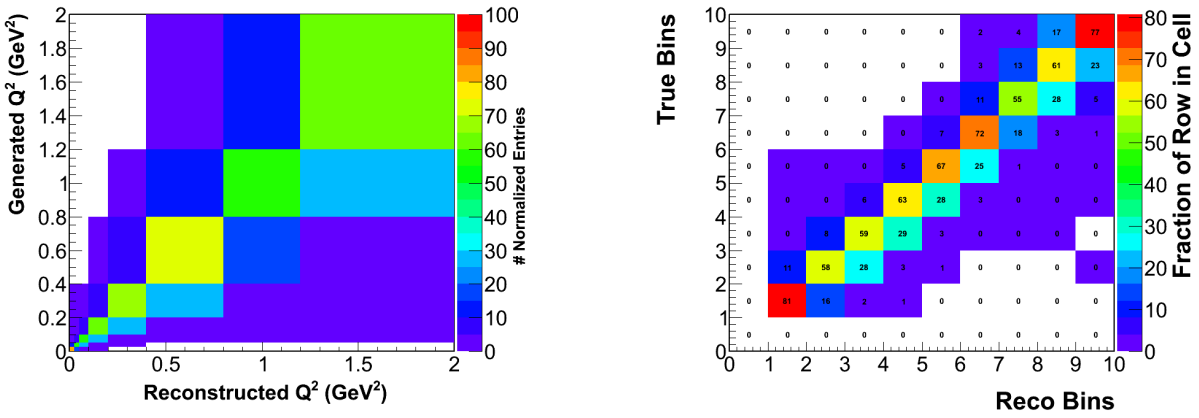

FIG. 6.35: The migration matrix.

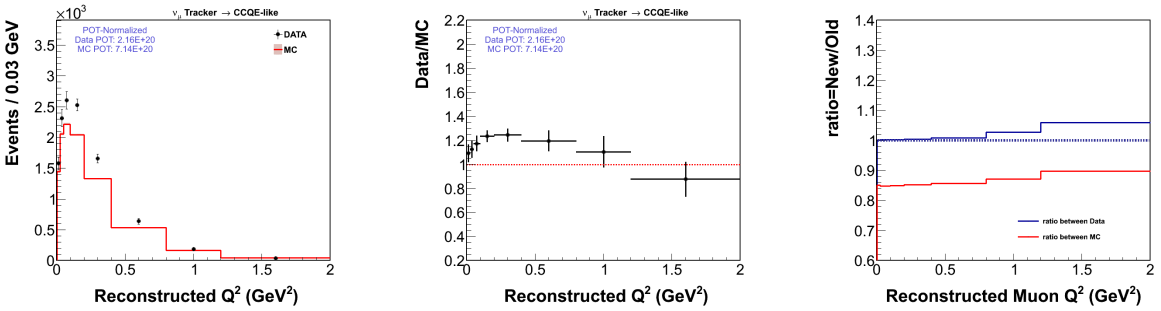

FIG. 6.36: The left plot is the distribution of event candidates after unfolding. The middle plot is the data/MC ratio. The right plot shows the ratio between the analysis using the new flux and the analysis using the old flux.

Efficiency Correction

Fig. 6.37 shows the efficiency of selecting CCQE-like candidates (left) and the ratio between efficiencies in the analysis using the new and old flux. After correcting the efficiency of selection the CCQE-like candidates in the simulation, the data distribution looks almost the same in the analyses using the new flux and the old flux (Fig. 6.38).

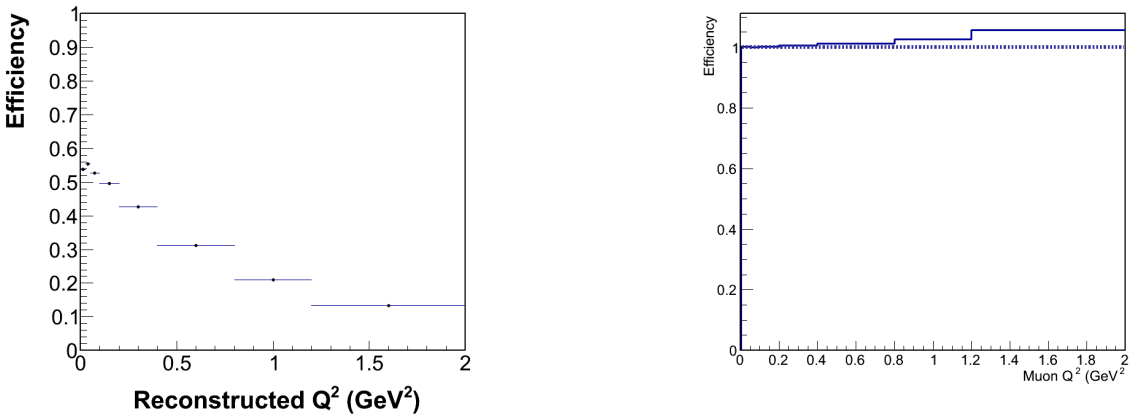

FIG. 6.37: The distribution of efficiency as a function of Q^2 in the simulation (left). The right plot is the ratio between efficiencies from the analysis using the new flux and the ones from the analysis using the old flux.

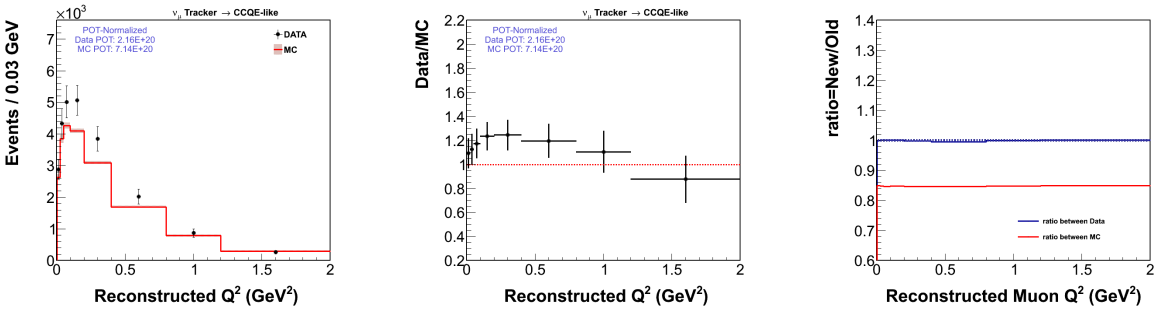

FIG. 6.38: The left plot is the distribution of event candidates after efficiency correction. The middle plot is the data/MC ratio. The right plot shows the ratio between the analysis using the new flux and the analysis using the old flux.

Final Cross-section After Normalization

After normalizing with the new flux, Fig. 6.39 shows the distribution of the differential cross-section for CCQE-like as a function of Q^2_{QElike}. When normalizing with the new prediction of the neutrino flux which is less intense than the old (Gen0) flux, GENIE produces the same cross-sections in old and new analyses. A similar study on the CCQE channel using the new flux is shown in Fig. 6.40.

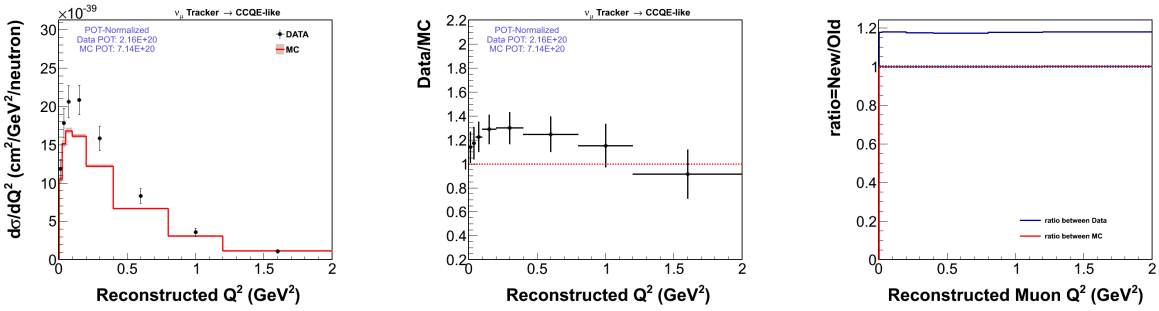

FIG. 6.39: The left plot is the distribution of the differential cross-section for CCQE-like. The middle plot is the data/MC ratio. The right plot shows the ratio between the analysis using the new flux and the analysis using the old flux.

The CCQE Analysis Using the New Flux

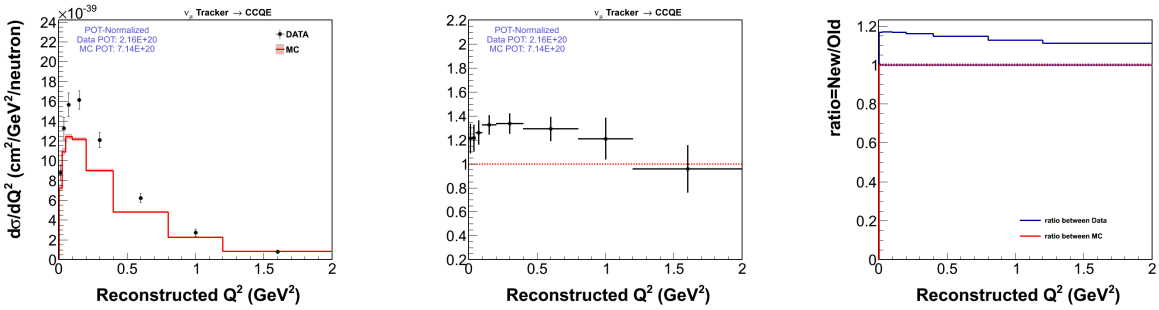

FIG. 6.40: The left plot is the distribution of the differential cross-section for CCQE. The middle plot is the data/MC ratio. The right plot shows the ratio between the analysis using the new flux and the analysis using the old flux.

6.4 Systematic Uncertainties

The different components that were used to produce the $\frac{d\sigma}{dQ^2}$ have been presented throughout this dissertation. These components, which include the incoming neutrino flux, the neutrino interactions in the scintillator, and the particle propagation through the detector, were modeled by simulations that are known to be imperfect. In general, correctly estimating and propagating systematic uncertainties is vital for the CCQE/CCQE-like analysis. For example, the GENIE generator has model parameters that have uncertainties that could effect the normalization and shape of the background and the fraction of events that pass various selections. The detector response and energy reconstruction is also not known perfectly and uncertainties there would likely effect the shape of kinematic distributions, the fraction of events passing selections, and the migration between bins.

A procedure called "many universes" is used to propagate systematic uncertainties from their source (e.g. GENIE) to the differential cross-section $\frac{d\sigma}{dQ^2}$. The general procedure is to shift an amount (denoted as σ) in simulation or reconstruction to approximate the uncertainty on a particular effect and re-extract the cross-section within the complete analysis procedure. This variation is commonly referred as a universe, which represents the shift deviation from the central value. In most cases, the shifted amount on parameters is $\pm 1\sigma$, which leads to the cases with 2 universes. In some other cases, the error on the systematic effect has been reproduced using 100 variations (aka. 100 universes), where the shifted values are randomly drawn from sampling a Gaussian distribution with a width of 1 σ. For example, 100 universe technique was used in estimating the systematic errors caused by the incoming neutrino flux. Part of the purpose for using 100 universes is to minimize the statistical uncertainties on the systematic uncertainties. Furthermore, in contrast to other parameters that are uncorrelated, flux data points are correlated and

there are a few hundred points, so it is not correct to vary each individual parameter randomly by $\pm 1\sigma$.

A covariance matrix is computed for each systematic and the total covariance matrix is the sum of the matrices for each source of systematic error. The construction of the covariance matrix depends on the number of universes, 2 or 100 universes.

- For the case with one variation, the covariance matrix is given by

$$C_{ij} = \Delta\left(\frac{d\sigma}{dQ^2_{QELike}}\right)_i \Delta\left(\frac{d\sigma}{dQ^2_{QELike}}\right)_j, \tag{6.8}$$

  where $\Delta\left(\frac{d\sigma}{dQ^2_{Q}ELike}\right)_i$ is the difference between the $\frac{d\sigma}{dQ^2_{QELike}}$ value measured in the i-th bin using the varied parameter and the central nominal value.

- For all other cases, the covariance matrix is calculated as,

$$C_{ij} = \frac{1}{N}\sum_N \Delta\left(\frac{d\sigma}{dQ^2_{Q}E}\right)^N_i \Delta\left(\frac{d\sigma}{dQ^2_{QE}}\right)^N_j, \tag{6.9}$$

  where N is the number of universes and the superscript N refers to a particular shifted universe, i and j indicate the bin number of the measured differential cross-section.

In general, there are two categories of systematic errors, vertical and lateral. The difference lays in how the shifted universes are produced. Vertical systematic errors are the uncertainties on the probability that an event occurs. Vertical shifted universes are produced by weighting candidate events according to the ratio $w = \frac{P_{shifted}}{P_{CV}}$, where $P_{shifted}$ is the probability of observing a certain event in the shifted universe and P_{CV} is the probability of observing the certain event in its central value.

Lateral systematic errors vary the value of an observed quantity, which can move an event candidate from one measured bin to another and change whether an event candidate

passes an analysis cut or not. In this analysis, two shifted universes are used in evaluating lateral systematic errors and they are produced by shifting affected quantities by $\pm 1\sigma$.

All systematic error sources are divided into six groups: flux, primary interaction, hadron interactions, muon reconstruction, recoil reconstruction, and "other". The rest of this section describes how each systematic error source is computed.

6.4.1 Neutrino Flux

Predicting neutrino flux is one of the biggest challenges for the MINERνA experiment. The MINERνA detector is exposed to a tertiary neutrino beam which is the final product of proton-carbon collisions in the NuMI target. Therefore, the flux systematic errors are mainly derived from uncertainties in hadron production models, beamline modeling, and the data constraint technique described in Chap. 4.1. These three sources are mutually uncorrelated. The detail of each individual source is discussed and Fig. 6.41 shows the three systematic errors on the final cross-section in the group of flux for both CCQE-like and CCQE analyses.

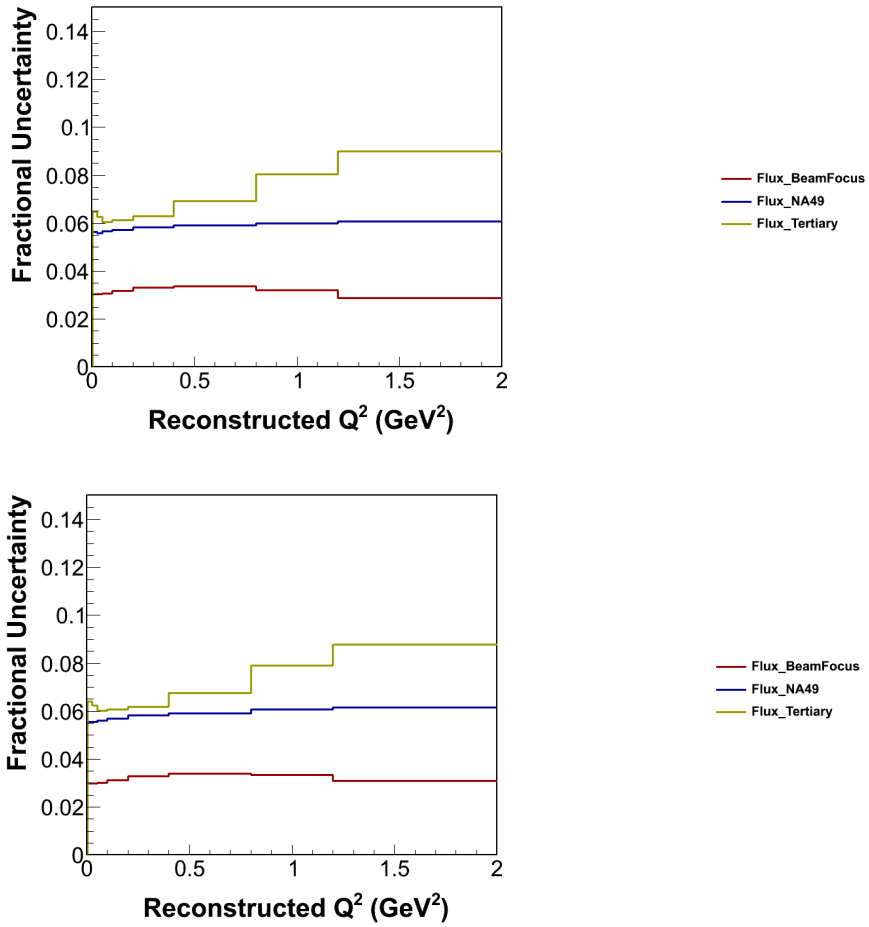

FIG. 6.41: Systematic errors on the differential cross-section for the ν_μ CCQE-like (top) and CCQE (bottom) analysis, with unstacked contributions from the Flux group. The systematic uncertainties propagated from the neutrino flux are almost identical in CCQE-like and CCQE analyses since the same prediction of the neutrino flux were used in both analyses.

Flux NA49 The data constraint (Sec. 4.1) uncertainty rises from the experimental error of the NA49 measurement which uses a 158 GeV proton beam to identify charged hadrons and neutral strange particles. The measurement is related to NuMI beam (120 GeV) through Feynman scaling [62]. The correction at 120 GeV is very small for typical p_T values but can be up 10% when the incident proton's energy goes down to 12 GeV [24]. The systematic uncertainty on the constrained hadron production has an additional negligible contribution [63] from the scaling procedure.

TABLE 6.9: Summary of NA49 systematic errors. The statistical error is 1 3% in the focusing region. Reprinted from Ref. [43].

Normalization	2.5%
Tracking efficiency	0.5%
Trigger bias	1%
Feed-down	1-2.5%
Detector absorption	
Pion decay $\pi \rightarrow \mu + \nu_\mu$	0.5%
Re-interaction in the target	
Binning	0.5%
Total(upper limit)	7.5%
Total(quadratic sum)	3.8%

Flux Tertiary The hadron production model uncertainty covers the uncertainty on the production of hadrons from the NuMI target for particles which are not constrained by data. Three models are used to evaluate the uncertainty: FTFP BERT and QGSP BERT in Geant4, and Fluka [24]. The hadron production model uncertainty is the maximum spread between these three models.

Flux BeamFocus The beamline uncertainty is evaluated by MINOS with contributions from magnetic horns and target density. All details are listed in Tab. 6.10.

TABLE 6.10: Systematic uncertainties on various sources of the NuMI beamline. Reprinted from Reference [27], Copyright 2008.

Sources	Uncertainty
Number of proton on target	2.0%
Horn transverse mis-alignment	1.0 mm
Horn tilt	0.2 mrad
Horn current mis-calibration	1.0%
Horn current distribution	$\delta = 6$ mm $/\delta = \infty$
Baffle scrapting	0.25%
Mis-alignment of shielding blocks	1.0 cm
Target density	2.0%

6.4.2 Event Generator Uncertainties

Neutrino interactions are simulated by GENIE and the measurement of the differential cross-section is potentially sensitive to the GENIE physics model. For example, in the background subtraction step, a data-driven procedure is implemented for tuning the non QE-Like background. The procedure assumes GENIE correctly predicts the event rate for each neutrino interaction process in each of the sidebands in the high recoil energy regime. Another example is the reconstruction of muons, which depend on GENIE modeling of the final state interaction (FSI) effects. Also in the efficiency correction step, the efficiency to select CCQE-like events in each Q^2 bin is dependent on the event rate of the GENIE model. Therefore, uncertainties on the GENIE model parameters indeed propagate to the final measurement, and they are evaluated by shifting model parameters by $\pm 1\sigma$ using GENIE reweighting tools. The most significant contributors from GENIE systematic are listed in Tab. 6.11 showing the $\pm 1\sigma$ uncertainties. The uncertainties are recommended by GENIE developers [64].

A few other parameters in the GENIE model cannot be reweighted, such as the ones that control the effective size of the nucleus and quark hadronization time. They are

TABLE 6.11: Systematic uncertainties on various parameters for GENIE models. Reprinted from Reference [46], Copyright 2010.

GENIE Model Parameters	GENIE Knob Name	1σ
Cross Section Models		
M_A for CCQE Scattering	MaCCQE	$\pm 10\%$
M_A for Resonance	MaRES	$\pm 20\%$
$M_V$for Resonance	MvRES	$\pm 10\%$
CCQE Normalization	NormCCQE	$+20\% - 15\%$
CC Resonance Normalization	NormCCRES	$\pm 20\%$
1π Production from ν_μp non-resonant	Rvp1pi	$\pm 50\%$
1π Production from $\bar{\nu}_\mu$n non-resonant	Rvn1pi	$\pm 50\%$
2π Production from ν_μp non-resonant	Rvp2pi	$\pm 50\%$
2π Production from $\bar{\nu}_\mu$n non-resonant	Rvn2pi	$\pm 50\%$
IntraNuclear Cascade Models		
Nucleon Elastic Scattering	FrElasN	$\pm 30\%$
π Elastic Scattering	FrElaspi	$\pm 10\%$
Nucleon Inelastic Scattering	FrInelN	$\pm 40\%$
π Inelastic Scattering	FrInelpi	$\pm 40\%$
Nucleon Absorption	FrAbsN	$\pm 20\%$
π Absorption	FrAbspi	$\pm 30\%$
Nucleon Mean Free Path	MFPN	$\pm 20\%$
π Mean Free Path	MFPpi	$\pm 20\%$

studied by simulating independent samples, one for each change of a non-reweightable parameter, using a procedure similar to one used by MINOS [65]. The results show that none of these uncertainties is added to the measurement because they are all within the simulation's statistical uncertainty.

Two groups that contain systematic errors from GENIE are the primary interaction group and the hadron interaction group.

6.4.2.1 Primary Interaction

All systematic errors in the primary interaction group are listed. Fig. 6.42 shows all systematic errors on the final cross-section in this group for both CCQE-like and CCQE analyses.

AhtBY represents the uncertainty on Bodek-Yang parameter A_{HT}, that is estimated by tweaking the Bodek-Yang model parameter $A_{HT} - incl$ by $\pm 25\%$. It affects both shape and normalization.

BhtBY represents the uncertainty on Bodek-Yang parameter B_{HT}, which is estimated by tweaking the Bodek-Yang model parameter $B_{HT} - incl$ by $\pm 25\%$. it affects both shape and normalization.

The Bodek-Yang model is a method to extend the continuum neutrino nucleon scattering cross-section that is well understood in high energy region to the low energy region where the scattering process is poorly understood. Parameters A and B come from corrections on ξ_ω, given as

$$\xi_\omega = \frac{2x(Q^2 + M_f^2 + B)}{Q^2(1 + \sqrt{(}1 + (2Mx)^2/Q^2)) + 2Ax}. \tag{6.10}$$

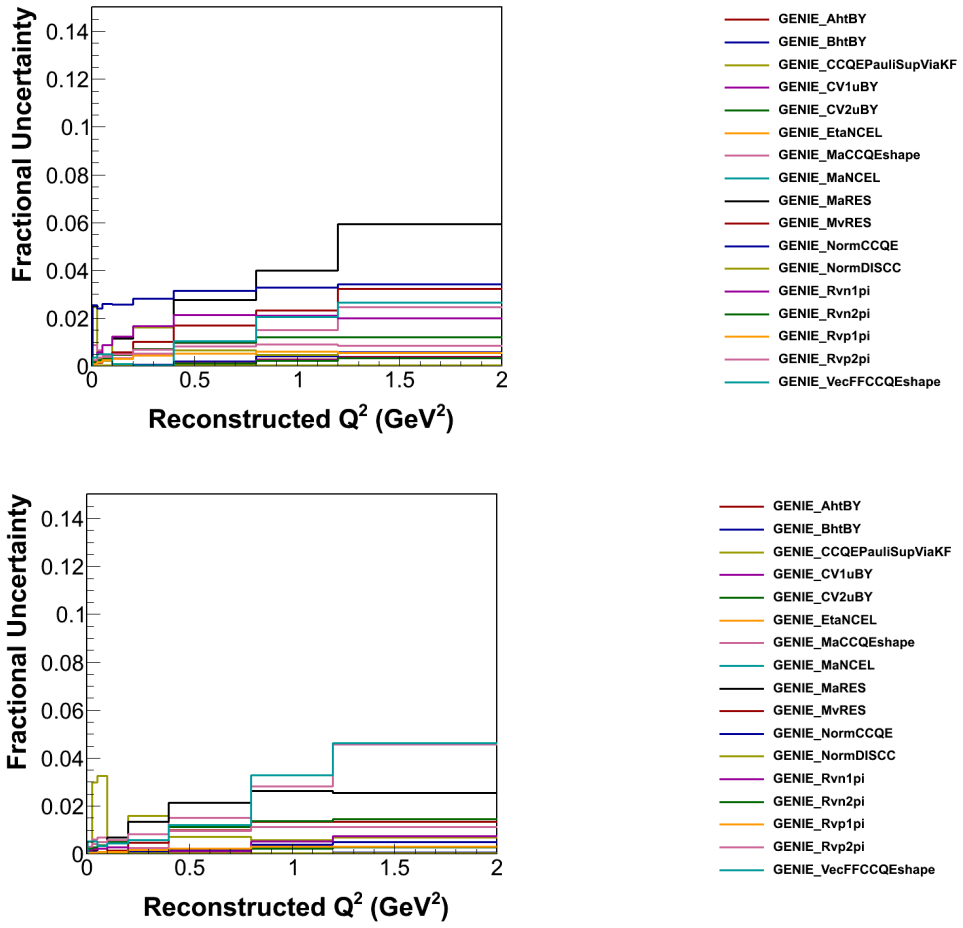

FIG. 6.42: Systematic errors on the differential cross-section for the ν_μ CCQE-like (top) and CCQE (bottom) analysis, with unstacked contributions from the Primary Interaction group. The significant difference on the MaRES uncertainty in CCQE-like/CCQE analysis indicates that resonances play more important roles in the CCQE-like analysis than in the CCQE analysis. Also, the uncertainty due to the CCQE normalization is higher in the CCQE-like analysis than in the CCQE analysis.

Parameter A corrects the effects of initial binding and target mass plus higher order terms. Parameter B corrects final state mass m_f^2, Δm^2, and photo production.

CCQEPauliSupViaKF represents the uncertainty on the model of Pauli blocking (CCQE) at low Q^2, that is estimated by varying Pauli blocking momentum cutoff by $\pm 30\%$.

CV1uBY represents the uncertainty on Bodek-Yang parameter C_{V1u}, that is estimated by tweaking the Bodek-Yang model parameter $CV1u - incl$ by $\pm 30\%$. It affects both shape and normalization effect.

CV2uBY represents the uncertainty on Bodek-Yang parameter C_{V2u}, that is estimated by tweaking the Bodek-Yang model parameter $CV2u - incl$ by $\pm 40\%$. It affects both shape and normalization effect.

EtaNCEL represents the uncertainty on the strange axial form factor (η) for neutral current elastic scattering, that is estimated by varying η by $\pm 30\%$.

MaCCQEshape represents the uncertainty on M_A for CCQE Scattering (shape only), that is estimated by varying M_A in Llewellyn-Smith cross-section by $\pm 10\%$. It affects shape only.

NormCCQE represents the uncertainty on CCQE normalization, that is estimated by varying the normalization by $+25\%/-15\%$.

MaNCEL represents the uncertainty on M_A for elastic Scattering, that is estimated by varying M_A in elastic scattering cross section by $\pm 25\%$.

MaRES represents the uncertainty on M_A for resonance production, that is estimated by varying M_A in Rein-Sehgal cross section by $\pm 20\%$. It affects both shape and normalization.

MvRES represents the uncertainty on M_V for resonance production, that is estimated by varying M_V in Rein-Sehgal cross section by $\pm 10\%$. It affects both shape and normalization.

NormDISCC represents the uncertainty on DIS CC normalization, that is estimated by adjusting the overall normalization of the non-resonance inclusive cross section.

Rvn1pi represents the uncertainty on 1π production from $\nu n/\bar{\nu}p$ non-resonant interactions, affecting NC and CC production of single pion final states from non-resonant inelastic (i.e. Bodek-Yang) scattering, $\nu n/\bar{\nu}p$ initial states, that is estimated by varying the production by $\pm 50\%$.

Rvn2pi represents the uncertainty on 2π productionfrom $\nu n/\bar{\nu}p$ non-resonant interactions, affecting NCand CC production of two pion final states from non-resonant inelastic (i.e.Bodek-Yang) scattering, $\nu n/\bar{\nu}p$ initial states, that is estimated by varying the production by $\pm 50\%$.

Rvp1pi represents the uncertainty on 1π productionfrom $\nu p/\bar{\nu}n$ non-resonant interactions, affecting NC and CC production of single pion final states from non-resonant inelastic (i.e.Bodek-Yang) scattering, $\nu p/\bar{\nu}n$ initial states, that is estimated by varying the production by $\pm 50\%$.

Rvp2pi represents the uncertainty on 2π productionfrom $\nu p/\bar{\nu}n$ non-resonant interactions, affecting NC and CC production of two pion final states from non-resonant inelastic (i.e.Bodek-Yang) scattering, $\nu p/\bar{\nu}n$ initial states, that is estimated by varying the production by $\pm 50\%$.

VecffCCQEshape represents the uncertainty on CCQE vector form factor model, that is estimated by changing from BBBA to dipole. It affects shape only.

6.4.2.2 Hadron Interactions

All of systematic uncertainties in the hadronic interactions inside the struct nucleus. Fig. 6.43 shows the effect that these uncertainties have on the final differential cross-section for both CCQE-like and CCQE analyses.

AGKYxF1pi represents the uncertainty on the pion Feynman x (x_F) in AGKY hadronization model, that is estimated by tweaking x_F distribution for low multiplicity (N+π) DIS f/s produced by AGKY.

FrAbs N represents the uncertainty on the final state interactions of nucleons inside the target nucleus, that is estimated by tweaking absorption probability for nucelons by $\pm$20%, for given total rescattering probability.

FrAbs π represents the uncertainty on the final state interactions of pions inside the target nucleus, that is estimated by tweaking absorption probability for pions by $\pm$30%, for given total rescattering probability.

FrCEx N represents the uncertainty on the charge exchange interaction of nucleons, that is estimated by tweaking charge exchange probability for nucleons by $\pm$50%, for given total rescattering probability.

FrCEx π represents the uncertainty on the charge exchange of pions, that is estimated by tweaking charge exchange probability for pions by $\pm$50%, for given total rescattering probability.

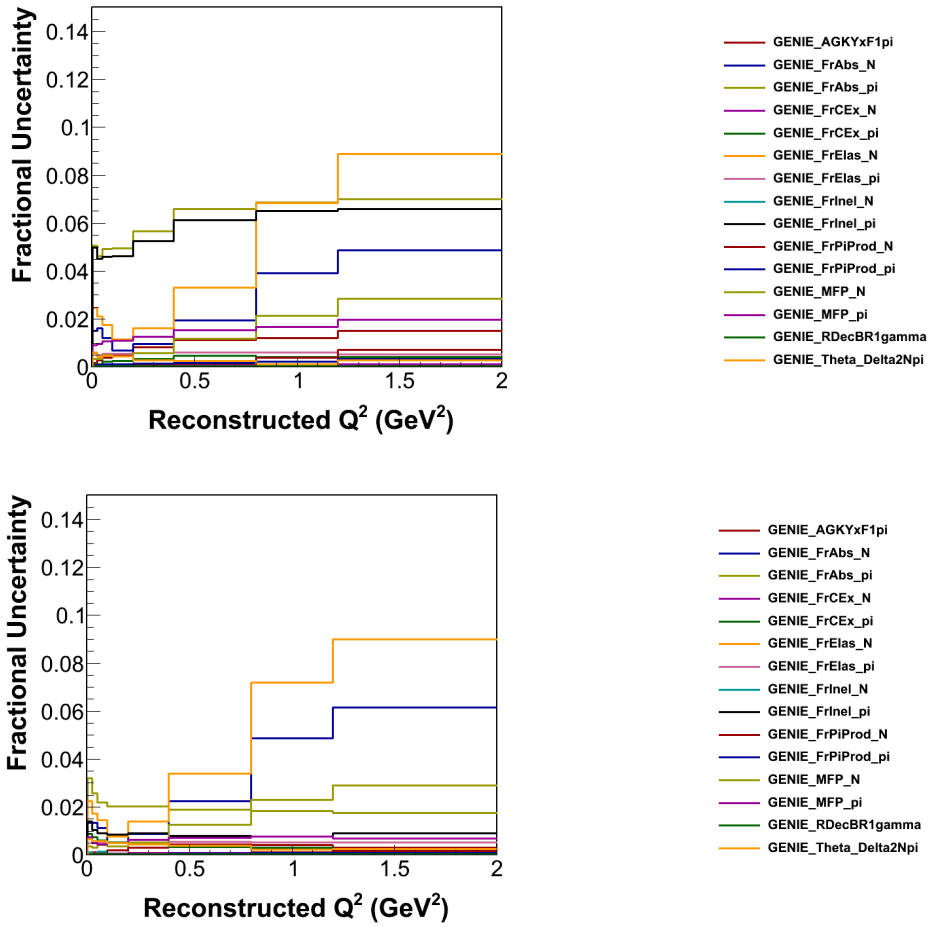

FIG. 6.43: Systematic errors on the differential cross-section for the ν_μ CCQE-like (top) and CCQE (bottom) analysis, with unstacked contributions from the Hadron Interaction group. The uncertainty on the pion inelastic scattering and pion absorption is much higher in the CCQE-like analysis than in the CCQE analysis. The nucleon elastic scattering propagates nearly the same uncertainty to the final cross-section in both analysis.

FrElas N represents the uncertainty on the elastic scattering of nucleons, that is estimated by tweaking elastic probability for nulceons by ±30%, for given total rescattering probability.

FrElas π represents the uncertainty on the elastic scattering of pions, that is estimated by tweaking elastic probability for pions by ±10%, for given total rescattering probability.

FrInel N represents the uncertainty on the inelastic scattering of nucleons, that is estimated by tweaking inelastic probability for nucleons by ±40%, for given total rescattering probability.

FrInel π represents the uncertainty on the inelastic scattering of pions, that is estimated by tweaking inelastic probability for pions by ±40%, for given total rescattering probability.

FrPiProd N represents the uncertainty on the pion production of nucleons, that is estimated by tweaking pion production probability for nucleons by ±20%, for given total rescattering probability.

FrPiProd π represents the uncertainty on the pion production of pions, that is estimated by tweaking pion production probability for pions by ±20%, for given total rescattering probability.

Mean Free Path N represents the uncertainty on nucleon mean free path, the length between two interactions, that is estimated by varying the length by ±20%.

Mean Free Path π represents the uncertainty on pion mean free path, the length between two interactions, that is estimated by varying the length by ±20%.

RDecBR1gamma represents the uncertainty on resonance decay branching ratio to photon, that is estimated by tweaking the resonance → X + gamma branching ratio, e.g.

$\Delta^{+}_{(1232)} \to p + \gamma$, by $\pm 50\%$.

Theta Delta 2Nπ represents the uncertainty on the Delta decay angular distribution, that is estimated by changing between isotropic and anisotropic decays.

6.4.3 Detector Response Uncertainties

Understanding and propagating uncertainties on the response of the MINERνA and MINOS detectors is critically important for two main reasons. First, hits in MINERνA and MINOS are combined to reconstruct muons and measure their charge, momentum, and angle with respect to the neutrino direction. The momentum and angle measurements are used to compute Q^2 as show in Eq. 6.1. Second, when selecting CCQE/CCQE-like event candidates, the energy of the recoil system is required to be below a Q^2 dependent threshold, as discussed in Sec. 6.2.2. In addition, the background inside the selected region is constrained by fitting the recoil energy distribution to the data in bins of Q^2. In this section, the response uncertainties are described and their impact is discussed. Generally speaking, the uncertainties are propagated by shifting the reconstructed quantities up or down in the Monte Carlo and repeating the analysis. Events that enter or leave the selected sample during this process are accounted carefully.

Two groups of systematics errors are related to the uncertainties rising from GEANT4, the group of muon reconstruction and recoil reconstruction.

6.4.3.1 Muon Reconstruction

Systematic errors in the group of muon reconstruction are described individually, followed by a summary plot of group errors on the final cross-section for both CCQE-like and CCQE analyses (Fig. 6.44).

Muon Energy Muon energy uncertainty is estimated in three components: MINOS

range uncertainty, MINOS curvature uncertainty, and MINERνA energy loss uncertainty, listed in Tab. 6.12. These three components are independent and added in quadrature.

TABLE 6.12: Uncertainties on muon energy reconstruction

Error Source	1σ
MINOS Range	2.0%
MINOS Curvature($p_u < 1$ GeV/c)	2.5%
MINOS Curvature($p_u > 1$ GeV/c)	0.6%
MINERνA dE/dx (scintillator events)	30 MeV
MINERνA dE/dx (C, Fe, Pb events)	40 MeV
MINERνA mass (scintillator events)	11 MeV
MINERνA mass (C,Fe, Pb events)	17 MeV

- MINOS Range Uncertainty

  The uncertainty on measuring the muon energy in MINOS comes from several components, such as the detector mass and geometry uncertainties, and the dE/dx model uncertainty. MINOS has estimated the uncertainty to be 2%, which is applicable to all muons that are reconstructed in MINOS [66].

- MINOS Curvature Uncertainty

  MINOS has determined the additional uncertainty on MINOS curvature to be 2.5% for a muon with less than 1 GeV/c and 0.6% for a muon with more than 1 GeV/c. This uncertainty is estimated by comparing the residual on the inverse muon momentum in data and simulation, where the residual means the difference in inverse

muon momentum found using range and curvature.

$$\delta\kappa = \frac{1}{p_{curv}} - \frac{1}{p_{range}}$$

The residual distribution is fit to a Gaussian and the difference between the mean of the Gaussian fits in data and simulation is the uncertainty on reconstruction by curvature, $\mu_{data} - \mu_{MC}$.

Note that this method utilizes the MINOS range reconstruction to form the residual, so when computing the total uncertainty on MINOS curvature, the uncertainty on MINOS range should be added. The total uncertainty on muon energy reconstructed by curvature is estimated to be 3.1% for a muon with less than 1 GeV/c and 2.1% for a muon with more than 1 GeV/c.

- MINERνA Energy Loss Model

  The energy loss model uses the dE/dx algorithm implementing the Bethe-Bloch formula to identify particles and reconstruct energies. By comparing the Bethe-Bloch calculation to Groom's muon energy range table, the uncertainty on the energy loss model is estimated to be approximately 1% for pure materials and 3% for mixtures. This uncertainty contributes 30 MeV to the muon energy on average.

Muon Theta The muon scattering angle is measured by a Kalman filter that is used to fit track trajectories. The uncertainty on the muon scattering angle is estimated by a study of rock muons that enter the front of MINERνA and are matched in MINOS. The method breaks the track at its midpoint and refits each half independently. The two fits measure the scattering angle at the broken point for each half track. The uncertainty on the muon theta is defined as the difference between the two measured angles in data and simulation, which is 1 mrad in the XZ plane and 0.9 mrad in the YZ plane. This

has less than a 1% effect on the total systematic uncertainty.

Normalization Correction All distributions from simulation need to be normalized to the corresponding distributions from data. This causes an uncertainty on the normalization, which is a flat correction applied to distributions from simulation. It is 3.5%.

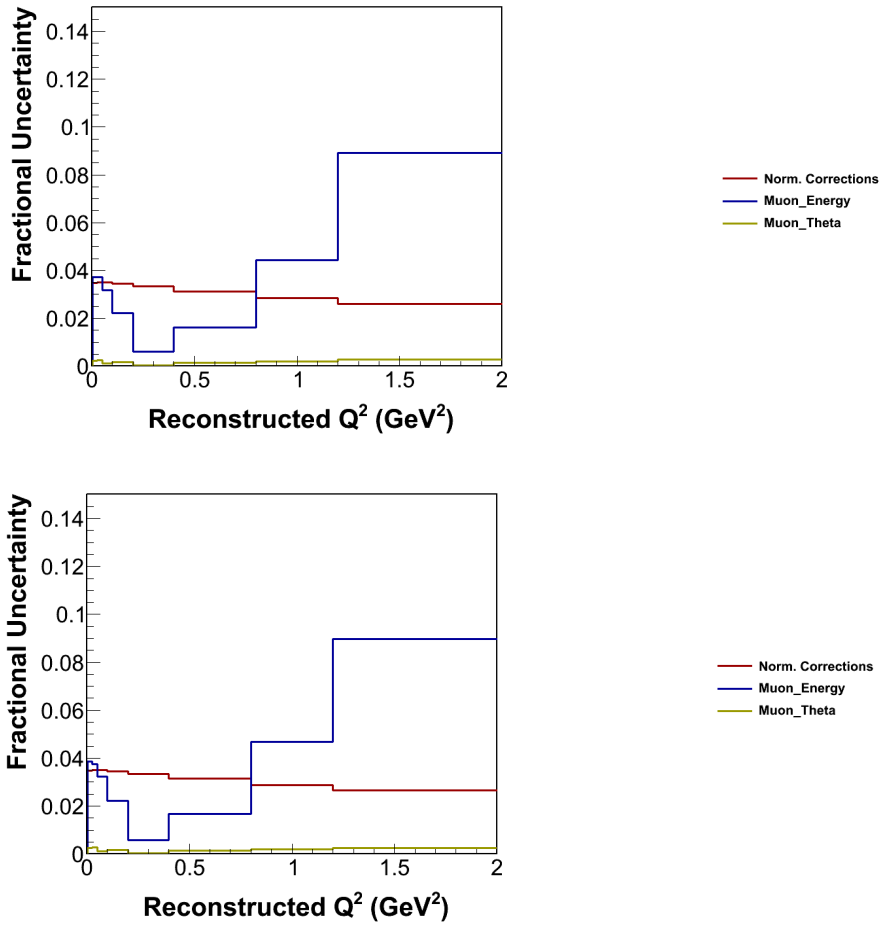

FIG. 6.44: Systematic errors on the differential cross-section for the ν_μ CCQE-like (top) and CCQE (bottom) analysis, with unstacked contributions from the Muon Reconstruction group. Uncertainties in the muon reconstruction group are nearly identical in both analyses.

6.4.3.2 Recoil Reconstruction

Recoil energy (unattached visible energy) is utilized to select QE-like candidates, and this cut is sensitive to the measured energy of particles that produce hits in the detector as a part of the recoil energy. The uncertainty on recoil reconstruction is estimated for each component particle in this energy system. First each particle-specified component is identified by the Monte Carlo. Then the energy of the simulated hit is shifted by the

particle's response uncertainty, given in Tab. 6.13. The difference between the nominal and shifted energy is the systematic uncertainty on the specific particle. Each contribution to the systematic uncertainty on recoil reconstruction is described one by one. At the end, Fig. 6.49 shows all systematic errors in the recoil reconstruction group.

TABLE 6.13: The $E^{vis}_{unattached}$ Uncertainties on Recoil Energy Reconstruction to different sources of light.

Particle Sources	Uncertainty
proton	3.5%
neutron(E_{kin} <50 MeV)	25%
neutron(50 MeV <E_{kin} <150 MeV)	10%
neutron(E_{kin} >150 MeV)	20%
muon	2.4%
$\gamma, \pi^0, e^{\pm}$	3%
$\pi^{\pm}$,Kaon	5%
optical cross talk	20%
other	20%

CrossTalk Cross talk remains in the unattached visible energy because it is not removed with 100% efficiency. It is simulated by determining a likelihood that cross talk will be produced by a energy deposition in a neighboring channel. The uncertainty due to cross talk is estimated by comparing two independent measurements of optical cross talk. One of the measurement is done by injecting light onto PMTs on a test stand. The other measurement is an *situ* procedure which looks at visible energy near rock muon tracks. These two measurements disagree at the 20% level, which is assigned as the uncertainty on recoil reconstruction due to cross talk.

EM Response The uncertainty on electromagnetic showers is estimated by comparing the energy spectrum of Michel electrons in data and simulation. A Michel electron is the decay product of an anti muon $\mu^+ \rightarrow \bar{\nu}_\mu + \nu_e + e^+$. The energy spectrum of

Michel electrons is well known, which makes them an important calibration source. A Michel electron sample was obtained by selecting candidates with small isolated energy deposition only. The comparison shows that the difference between data and simulation samples is 3%. That is assigned as the uncertainty due to electromagnetic showers. Fig. 6.45 shows the energy distributions of Michel electrons in data and simulation.

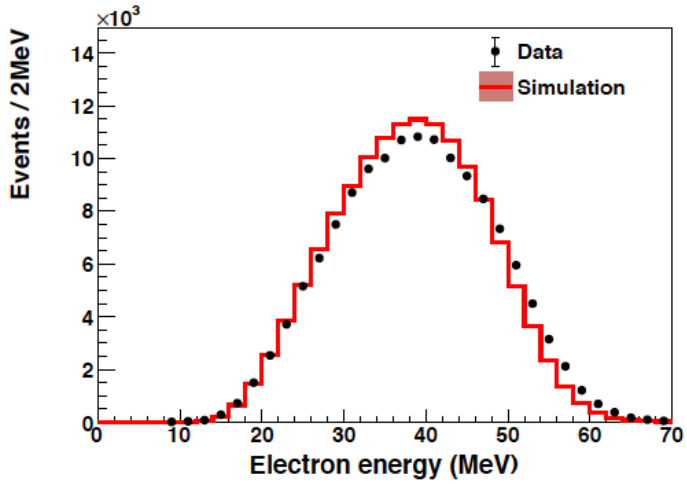

FIG. 6.45: Michel electron energy distribution, data and simulation comparison. The mean of the difference is 3%.

High Neutron Response

Mid Neutron Response

Low Neutron Response The uncertainty on the detector's response to neutrons is estimated by comparing the cross-section of $nA \rightarrow pX$ in data and simulation. This process is the only important source of uncertainty because that neutrons only deposit energy in the detector when they scatter and produce charged particles. The discrepancy between data and simulation is dependent on the neutron kinetic energy. The uncertainty is assigned as 25% for the neutrons with the kinematic energy less than 50 MeV, 10% for the neutrons with the kinematic energy between 50 MeV and 150 MeV,

and 20% for the neutrons with the kinematic energy greater than 150 MeV. Fig. 6.46 shows the discrepancy as a function of neutron's kinematic energy.

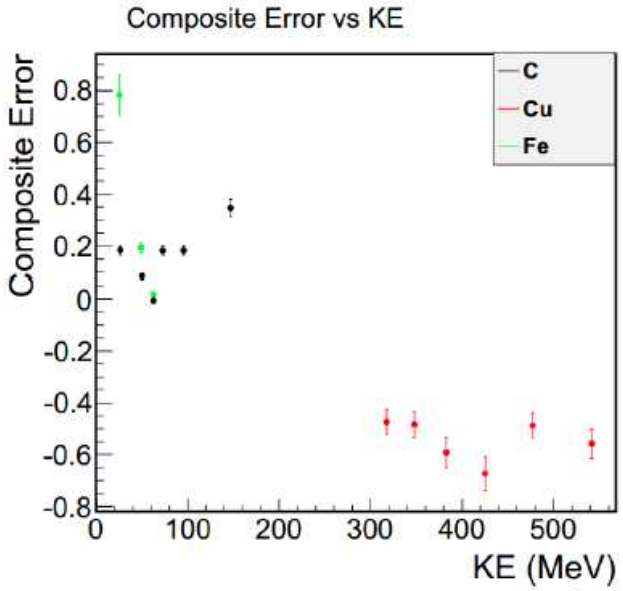

FIG. 6.46: Discrepancy between data and simulation in the $nA \to pX$ cross section as a function of neutron kinematic energy. The fractional error on neutron response is half this discrepancy, that is 25% for energies below 50 MeV, 10% between 50 MeV and 150 MeV, 20% above 150 MeV. Reprinted from Ref. [67].

Muon Response The uncertainty on the detector's response to muons is estimated by comparing the absolute muon energy scale between the data and MC. It comes from two components. One is from the minimum-ionizing energy unit (MEU) which depends on the accuracy of the simulation. The MEU study utilizes a rock muon sample that is matched in MINOS. By comparing the energy of one or two strip hits of muon tracks in data and simulation, the uncertainty on MEU is determined to be 2%. The other component is from the Bethe-Bloche process which simulates the energy deposited by a muon. The uncertainty on the Bethe-Bloche compatation is determined as 1%. Therefore, these two uncertainties added in quadrature give a total uncertainty on muon response of 2.4%.

Pion The uncertainty on the detector's response to pions is estimated by comparing test beam measurements of the available energy that is observed in the detector in the data and simulation [68]. The available energy observed in the test beam detector is the sum of all hits in the detector corrected for the passive material traversed. After accounting for known systematic uncertainties, an additional 5% error is necessary to cover the residual discrepancy between the data and the MC. This 5% is assigned as the uncertainty due to charged pions. Fig. 6.47 shows the result of this pion study.

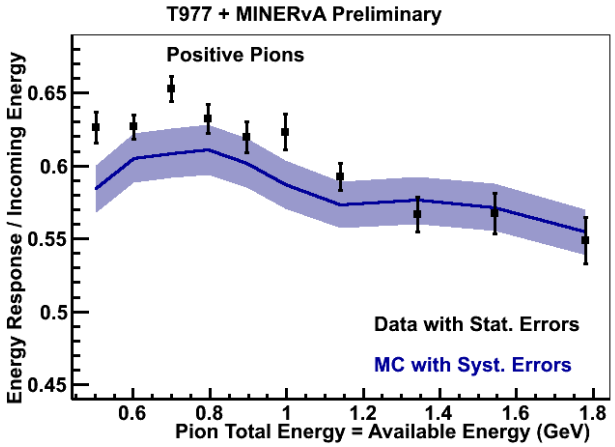

FIG. 6.47: Fraction of pion energy observed in the test beam detector vs. pion energy in data and simulation. The shaded simulation blue band shows the systematic errors. An additional error of 5% is needed to cover the difference in data and simulation. This figure is from Ref. [68].

A 5% uncertainty is also applied to kaons since there are not enough charged kaons in the test beam data to repeat a similar study as the one on charged pions and it is assumed that the uncertainty due to kaons is the same as that due to charged pions.

Proton The uncertainty on the detector's response to protons is estimated through a test beam measurement of protons kinetic energy reconstruction [31] [69]. This study was accomplished with the Fermilab Meson Test Facility beamline that reconstructs the momentum of charged particles precisely by curvature. The difference of kinetic energy

of protons stopping in the test beam detector between data and simulation (Fig. 6.48) is assigned as the uncertainty, which is about 3.5%.

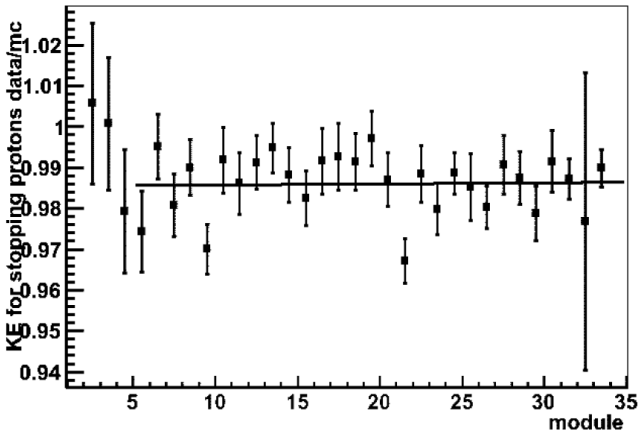

FIG. 6.48: Distribution of the ratio of beamline kinetic energy to range of protons in MINERνA test beam between data and simulation as the function of the module number in which the proton stops. The discrepancy determined a 3.5% error on proton repsonse.

Other Response There are some rare cases that a particle is not assigned an uncertainty by any of the procedures discussed above. In these cases, a default 10% uncertainty is assigned.

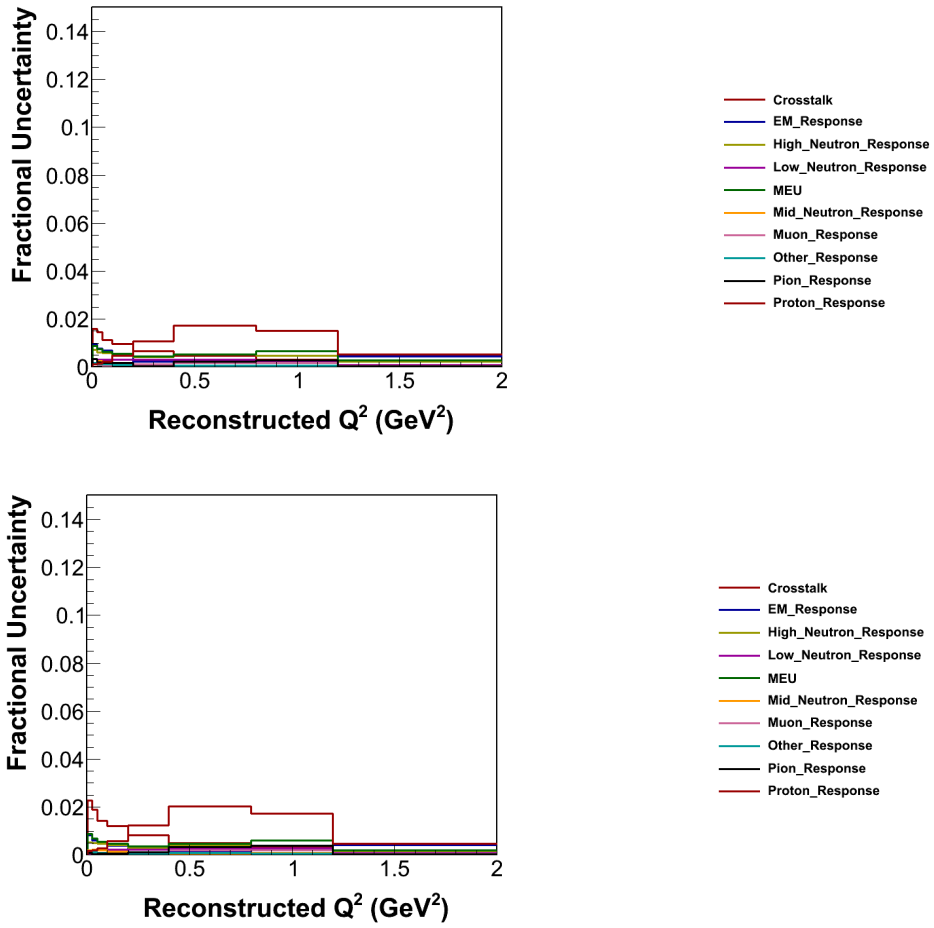

FIG. 6.49: Systematic errors on the differential cross-section for the ν_μ CCQE-like analysis, with unstacked contributions from the Recoil Reconstruction group. Uncertainties in the recoil reconstruction group are not significantly different in the CCQE-like/CCQE analyses.

6.4.4 Other Systematic Uncertainties

The systematic errors that do not fall into the groups described above are in the group of "other", including the errors due to Michel tagging efficiency, pion reweighting procedure, target mass, and the binding energy. Fig. 6.50 shows uncertainties in this group for both CCQE-like and CCQE analyses.

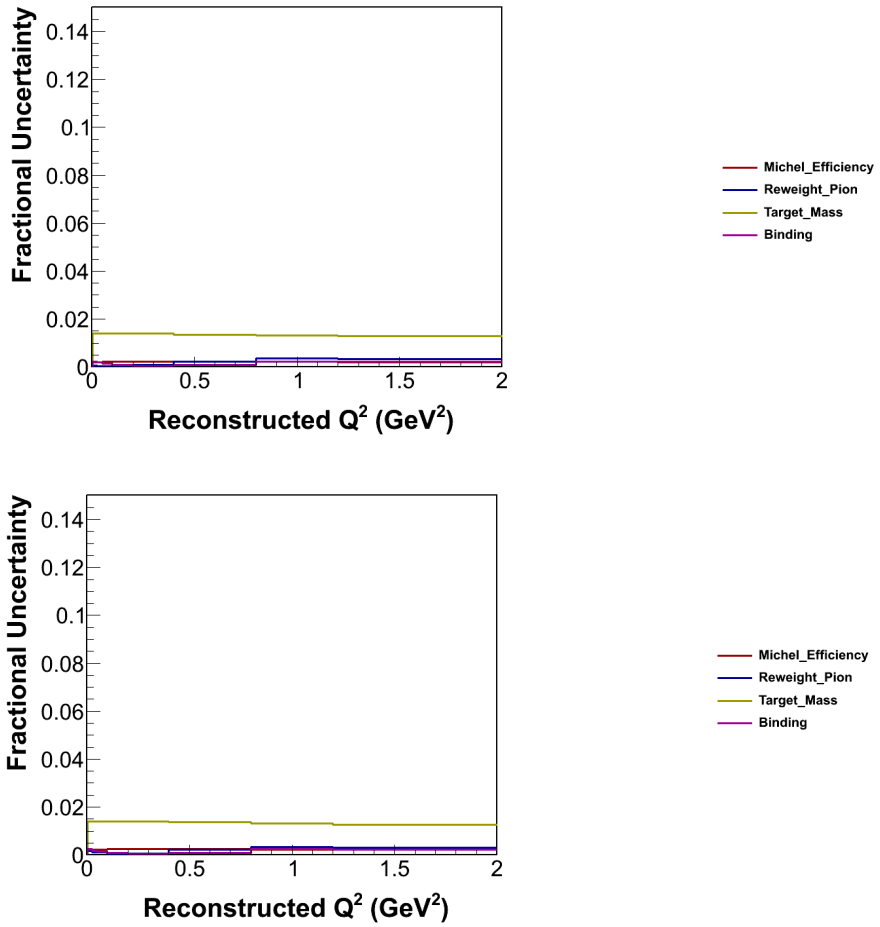

FIG. 6.50: Systematic errors on the differential cross-section for the ν_μ CCQE-like (top) and CCQE (bottom) analysis, with unstacked contributions from the Other group. The leading uncertainty in this group is the one due to the target mass, which should be identical in both analyses.

Michel Efficiency The Michel veto is newly added to the CCQE-like analysis aiming

to reject background events with one or more soft pions produced near the interaction vertex. The veto is utilized not only in the event candidates selection but also in the step of extracting the background scale factors. Therefore, the uncertainty on Michel tagging efficiency contributes to the final measurement.

In the previous chapter, a rock muon study was described, which compared the Michel tagging rate in the MC with that observed using the data. This study determined that the Michel tagging rate was 70.0% ± 1.1%. A different study looked for Michel electrons at random positions and determined that the misidentification rate was 1.0% ± 0.5%.

In the sample used in this analysis, there are 249,457 Monte Carlo entries (N) passing all CCQE cuts but the Michel veto. 40,286 (T) of these entries are tagged by MichelTool while 209,171 (U) have no Michel tag. 53,538 (N_m) of these entries have true Michel electrons while 195,919 (N_b) of these entries do not have true Michel electrons.

$$T \approx \epsilon_m \times N_m + \epsilon_b \times N_b$$

The uncertainty due to Michel tagging efficiency on the total systematic uncertainty is estimated by shifting the Michel tagging efficiency up and down by 1σ, and reweighting the candidates with Michel electrons by the ratios between T^+ and T^-. It is a small and nearly flat correction to the total systematic uncertainty.

$$T^+ = (\epsilon_m + \delta\epsilon_m) \times N_m + (\epsilon_b - \delta\epsilon_b) \times N_b$$

$$T^- = (\epsilon_m - \delta\epsilon_m) \times N_m + (\epsilon_b + \delta\epsilon_b) \times N_b$$

where the tagging efficiency and the misidentification rate are fully negatively corre-

lated.

Pion Reweight The pion reweight uncertainty is one of the uncertainties attributed to Geant4 and is newly added to this analysis. This uncertainty on the Geant4 particles interaction model is estimated by shifting the pion total inelastic cross-section by $\pm 10\%$ and shifting the ratio of the pion disappearance to pion scattering cross section by $\pm 10\%$. The 10% error is determined by comparing Geant4 cross-section predictions to data, and the cross section is shifted using a reweighting technique [70]. This systematic is largest at high Q^2, about 0.5% and smallest at low Q^2, about 0.1%.

Target Mass The mass of the detector introduces an uncertainty on the final measurement in several parts of this analysis including the dE/dx particle identification algorithm, the muon and pion energy reconstruction, and the calculation of the number of target nucleons. To estimate its effect on dE/dx particle identification, the uncertainty is propagated into the calculation of the best fit energy loss for each hadron track candidate individually. To estimate its effect on muon energy reconstruction, the muon energy loss is recalculated by shifting the detector mass within the uncertainties. It is determined to be 11 MeV on average for muons originating in the tracker and exiting the back of MINERνA. The uncertainty on the number of target nucleons is equivalent to 1.4% of the scintillator plane mass. This is applied as a constant uncertainty in all Q^2 bins.

Binding Energy Binding energy is utilized in the neutrino energy reconstruction. Therefore it introduces an uncertainty on the total systematic when calculating the energy of neutrinos and sequentially in the calculation of Q^2.

The neutrino energy is reconstructed from the muon's kinematics as:

$$E_{\nu}^{QE} = \frac{2(M_n - E_B)E_{\mu} - [(M_n - E_B)^2 + m_{\mu}^2 - M_p^2]}{2[M_n - E_B - E_{\mu} - p_{\mu}cos\theta_{\mu}]}$$

where M_n and M_p are the masses of the neutron and proton, and E_B is the binding energy. The square of the transferred four-momentum is reconstructed as:

$$Q^2 = -m_{\mu}^2 + 2E_{\nu}^{QE}(E_{\mu} - \sqrt{E_{\mu}^2 - m_{\mu}^2}cos\theta_{\mu})$$

For neutrinos, the default binding energy is 34 MeV and for anti neutrinos, the default value is 30 MeV. In this analysis, this uncertainty is estimated by shifting the default binding energy by ± 5 MeV and it turns to be insignificant to the total systematic uncertainty.

6.5 Systematic Errors Summary

The results of estimating systematic errors in the CCQE-like and CCQE analyses are listed in this section. The first part shows the plots of total systematic errors as well as systematic errors in each group described in the previous section. The second part tabulates the total systematic error and presents secondary tables that contain systematic errors for each step in the calculation of the differential cross-section.

6.5.1 Systematic Errors Summary Plots

In this section, the systematic error summary plots on CCQE-like cross-section are shown as well as each individual group summary plots for all 6 groups: flux, hadron interaction, muon reconstruction, other group, primary interaction, and recoil reconstruction. Uncertainties are estimated at four stags: background subtraction, unfolding, efficiency

correction, and normalization to produce the final results. In addition, the similar summary plots at each stage towards calculating the CCQE cross-section are shown as well.

All Systematic Uncertainties at Four Stages for the CCQE-like Analysis

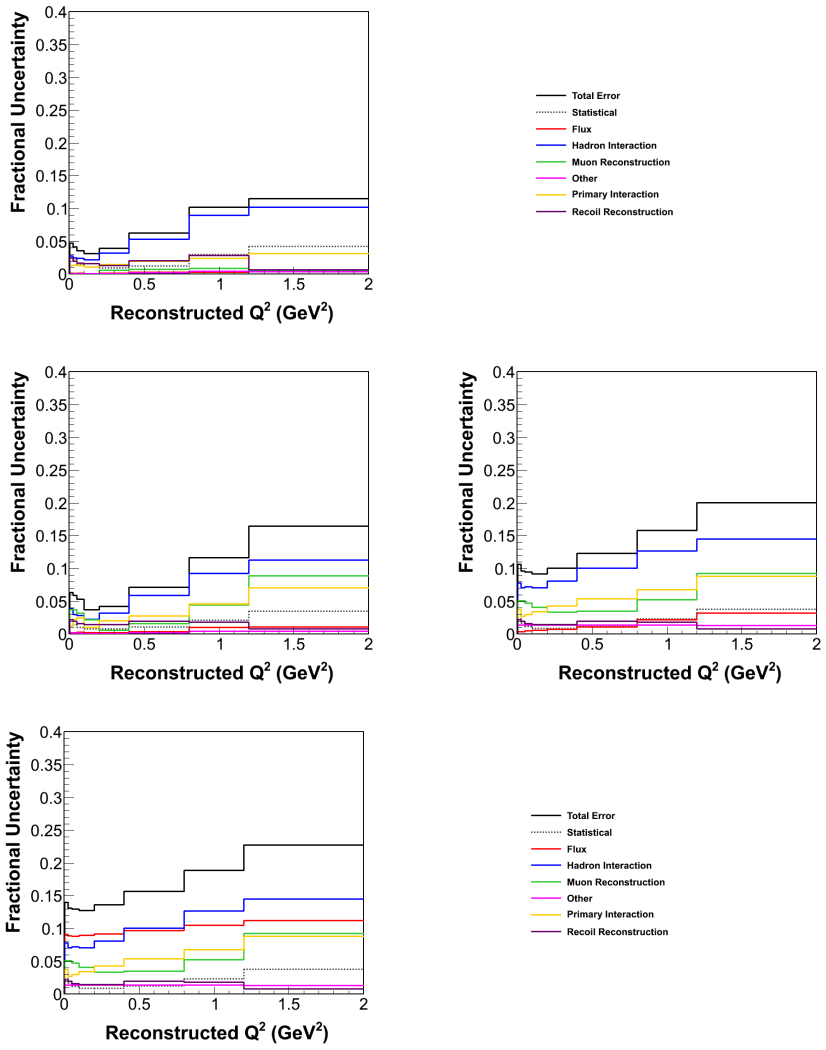

FIG. 6.51: Total systematic errors for the neutrino mode CCQE-like one track analysis, with unstacked contributions from all six groups. Top: background subtraction stage. Middle left: unfolding stage. Middle right: efficiency correction stage. Bottom: final stage, all systematic errors on the double differential cross section.

Systematic Uncertainties in the Flux Group at Four Stages for the CCQE-like Analysis

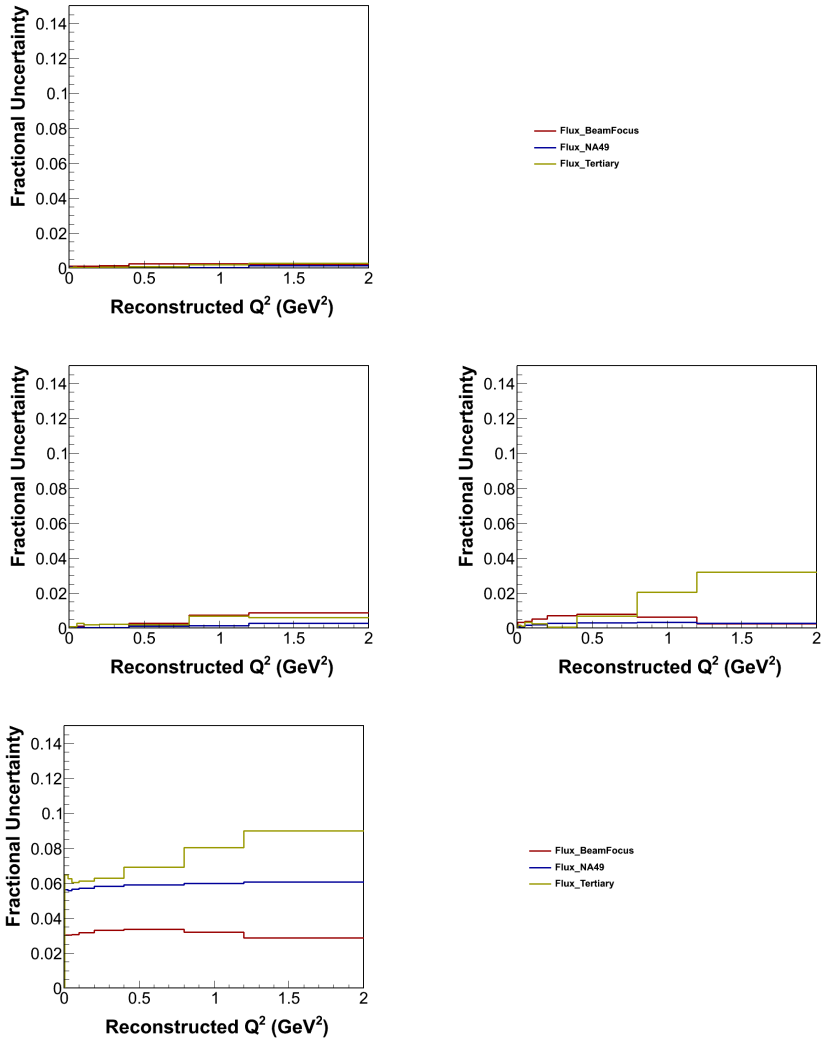

FIG. 6.52: Systematic errors in **Group Flux** for the neutrino mode CCQE-like one track analysis. Top: background subtraction stage. Middle left: unfolding stage. Middle right: efficiency correction stage. Bottom: final stage, systematic errors in **Group Flux** on the double differential cross section.

Systematic Uncertainties in the Primary Interaction Group at Four Stages for the CCQE-like Analysis

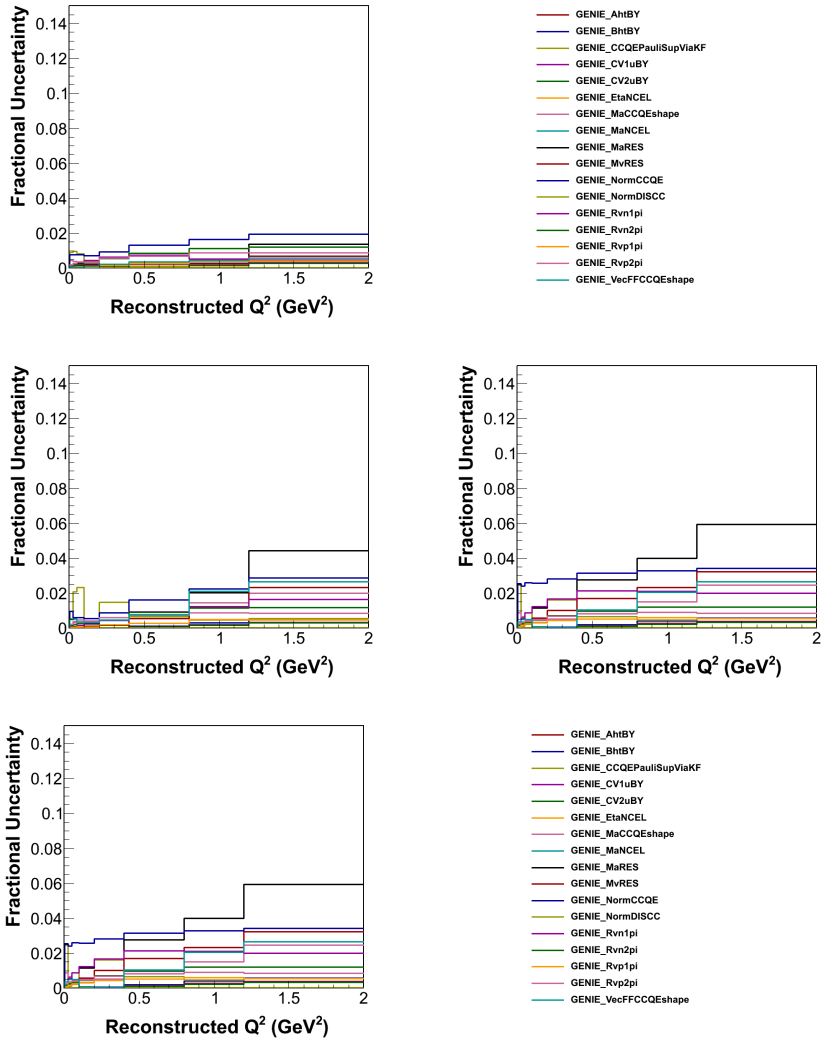

FIG. 6.53: Systematic errors in **Group Primary Interaction** for the neutrino mode CCQE-like one track analysis. Top: background subtraction stage. Middle left: unfolding stage. Middle right: efficiency correction stage. Bottom: final stage, systematic errors in **Group Primary Interaction** on the double differential cross section.

Systematic Uncertainties in the Hadron Interaction Group at Four Stages for the CCQE-like Analysis

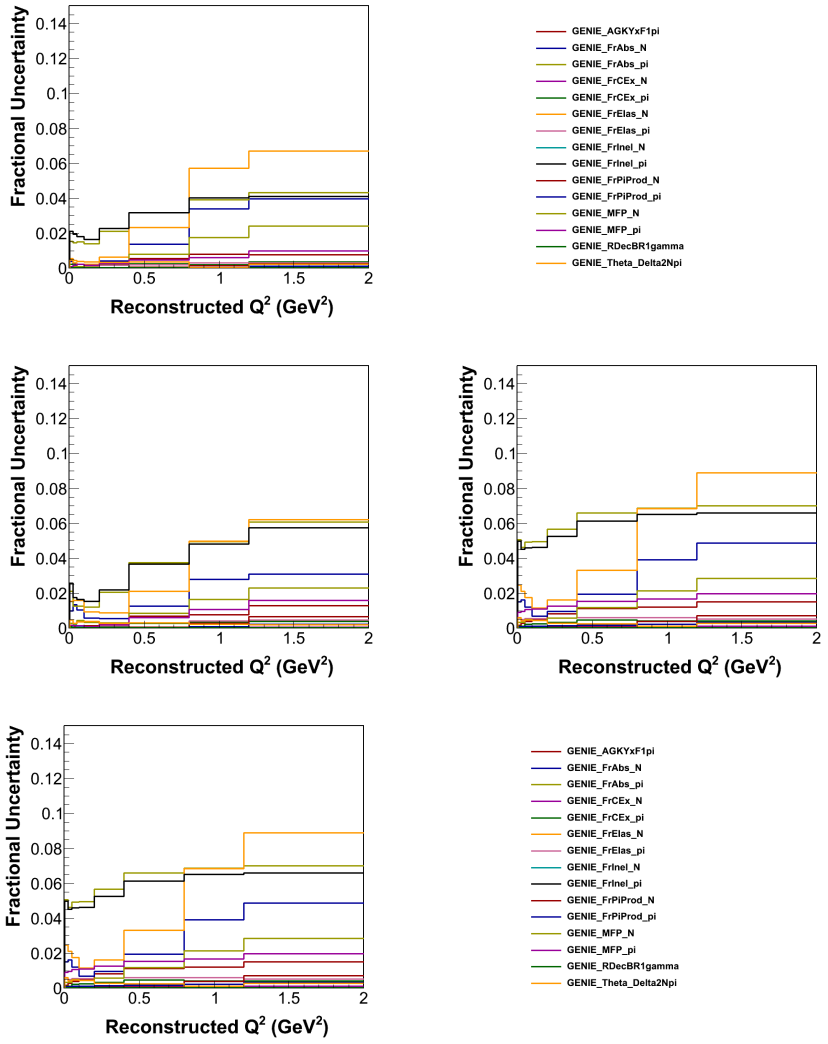

FIG. 6.54: Systematic errors in **Group Hadron Interactions** for the neutrino mode CCQE-like one track analysis. Top: background subtraction stage. Middle left: unfolding stage. Middle right: efficiency correction stage. Bottom: final stage, systematic errors in **Group Hadron Interactions** on the double differential cross section.

Systematic Uncertainties in the Muon Reconstruction Group at Four Stages for the CCQE-like Analysis

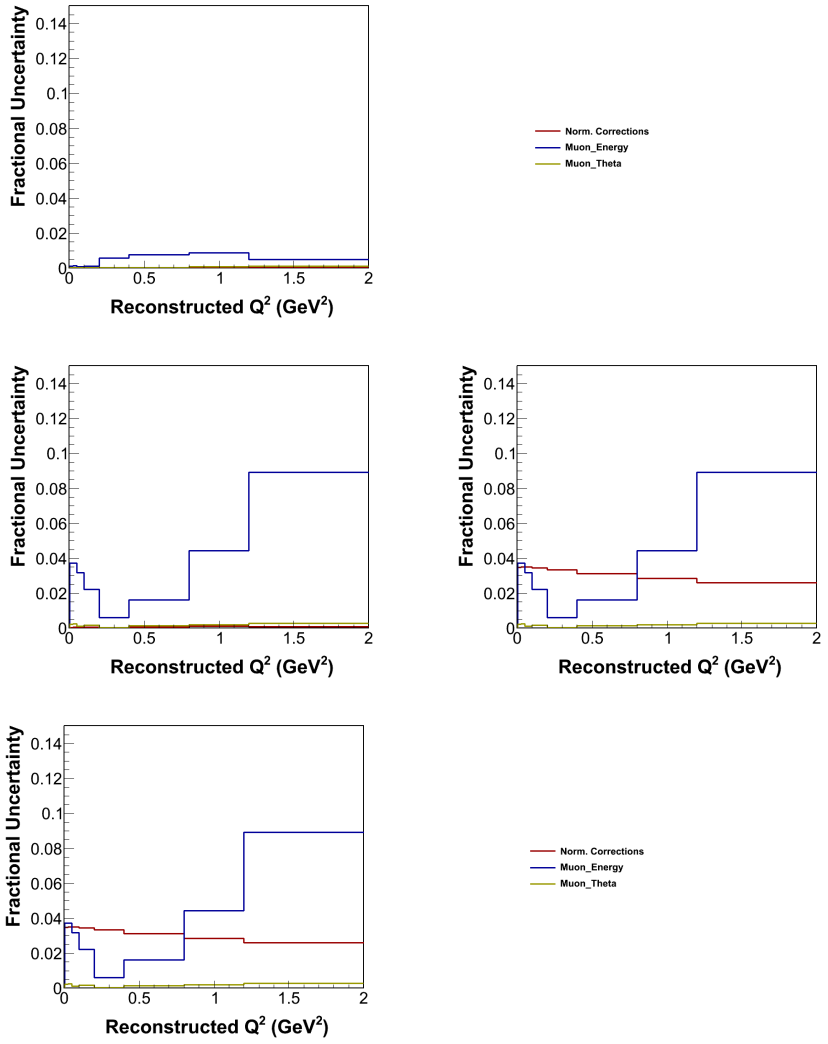

FIG. 6.55: Systematic errors in **Group Muon Reconstruction** for the neutrino mode CCQE-like one track analysis. Top: background subtraction stage. Middle left: unfolding stage. Middle right: efficiency correction stage. Bottom: final stage, systematic errors in **Group Muon Reconstruction** on the double differential cross section.

Systematic Uncertainties in the Recoil Construction Group at Four Stages for the CCQE-like Analysis

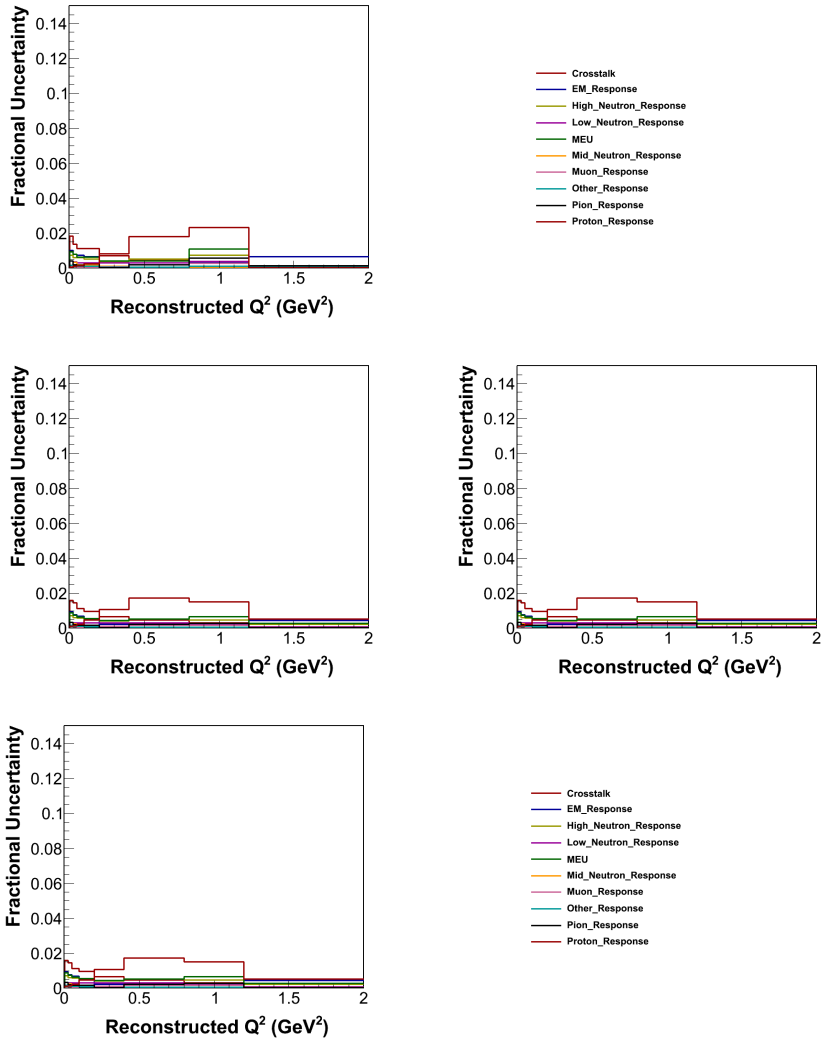

FIG. 6.56: Systematic errors in **Group Recoil Reconstruction** for the neutrino mode CCQE-like one track analysis. Top: background subtraction stage. Middle left: unfolding stage. Middle right: efficiency correction stage. Bottom: final stage, systematic errors in **Group Recoil Reconstruction** on the double differential cross section.

Systematic Uncertainties in the Other Group at Four Stages for the CCQE-like Analysis

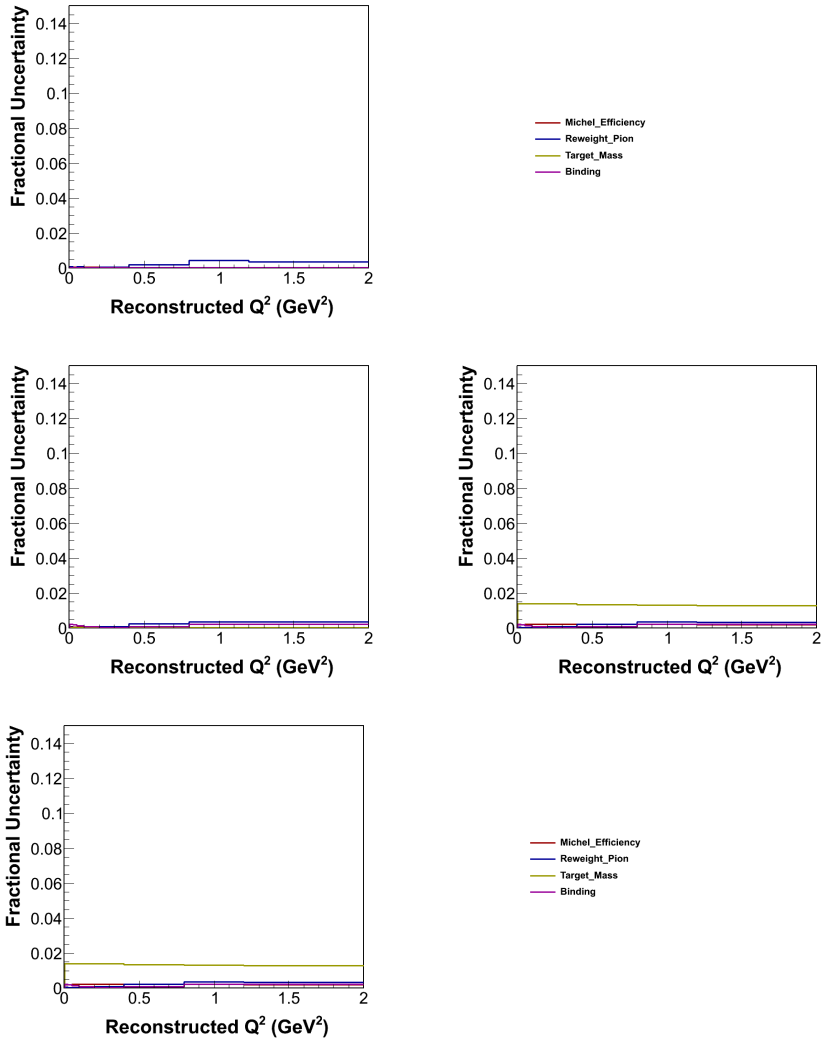

FIG. 6.57: Systematic errors in **Group Other** for the neutrino mode CCQE-like one track analysis. Top: background subtraction stage. Middle left: unfolding stage. Middle right: efficiency correction stage. Bottom: final stage, systematic errors in **Group Other** on the double differential cross section.

All Systematic Uncertainties at Four Stages for the CCQE Analysis

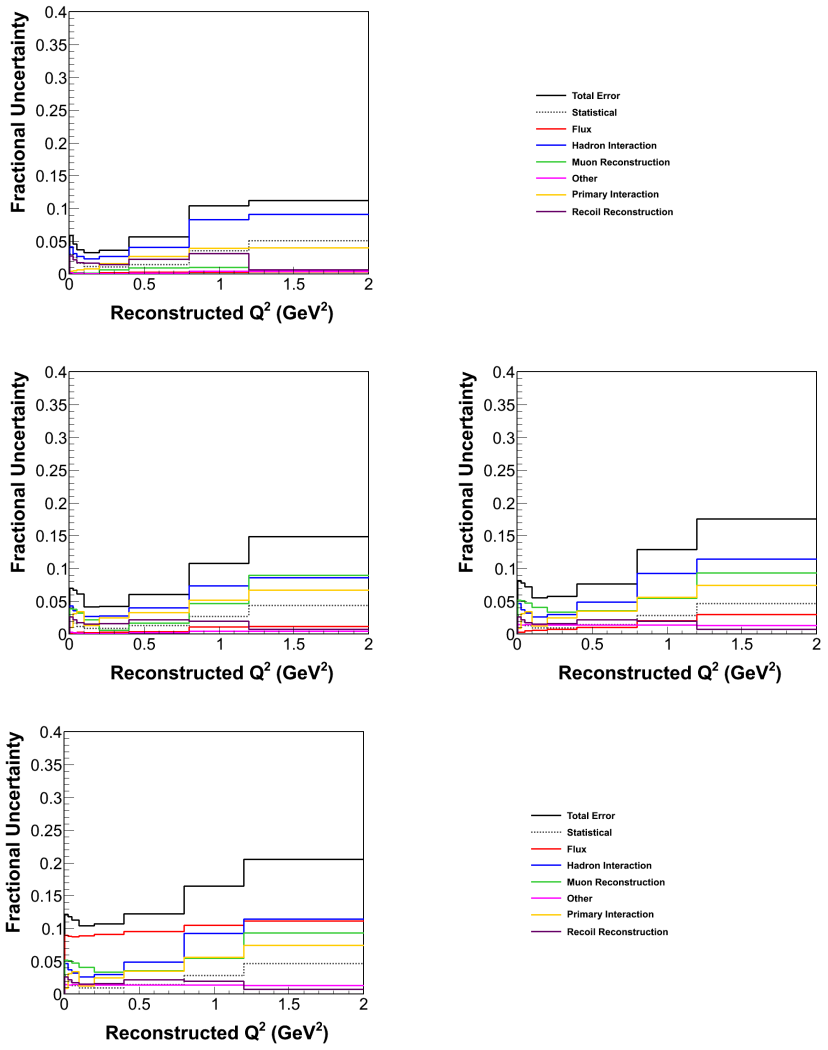

FIG. 6.58: Total systematic errors for the neutrino mode CCQE one track analysis, with unstacked contributions from all six groups. Top: background subtraction stage. Middle left: unfolding stage. Middle right: efficiency correction stage. Bottom: final stage, all systematic errors on the double differential cross section.

Systematic Uncertainties in the Flux Group at Four Stages for the CCQE Analysis

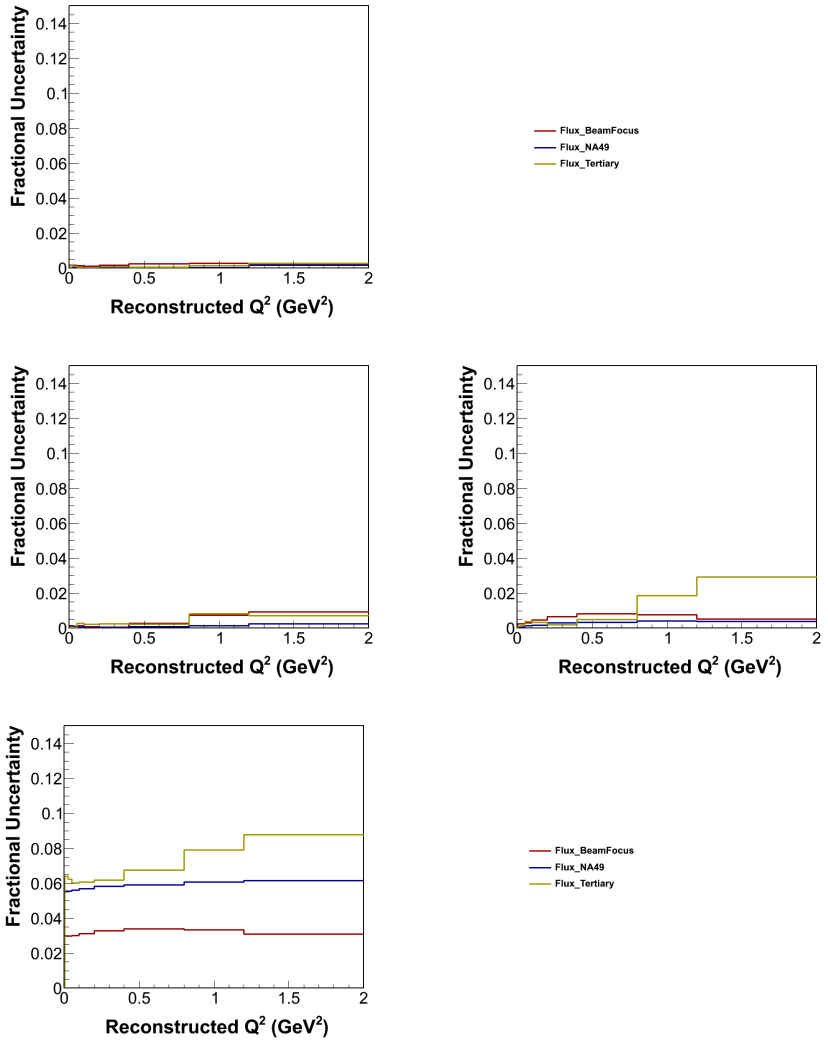

FIG. 6.59: Systematic errors in **Group Flux** for the neutrino mode CCQE one track analysis. Top: background subtraction stage. Middle left: unfolding stage. Middle right: efficiency correction stage. Bottom: final stage, systematic errors in **Group Flux** on the double differential cross section.

Systematic Uncertainties in the Primary Interaction Group at Four Stages for the CCQE Analysis

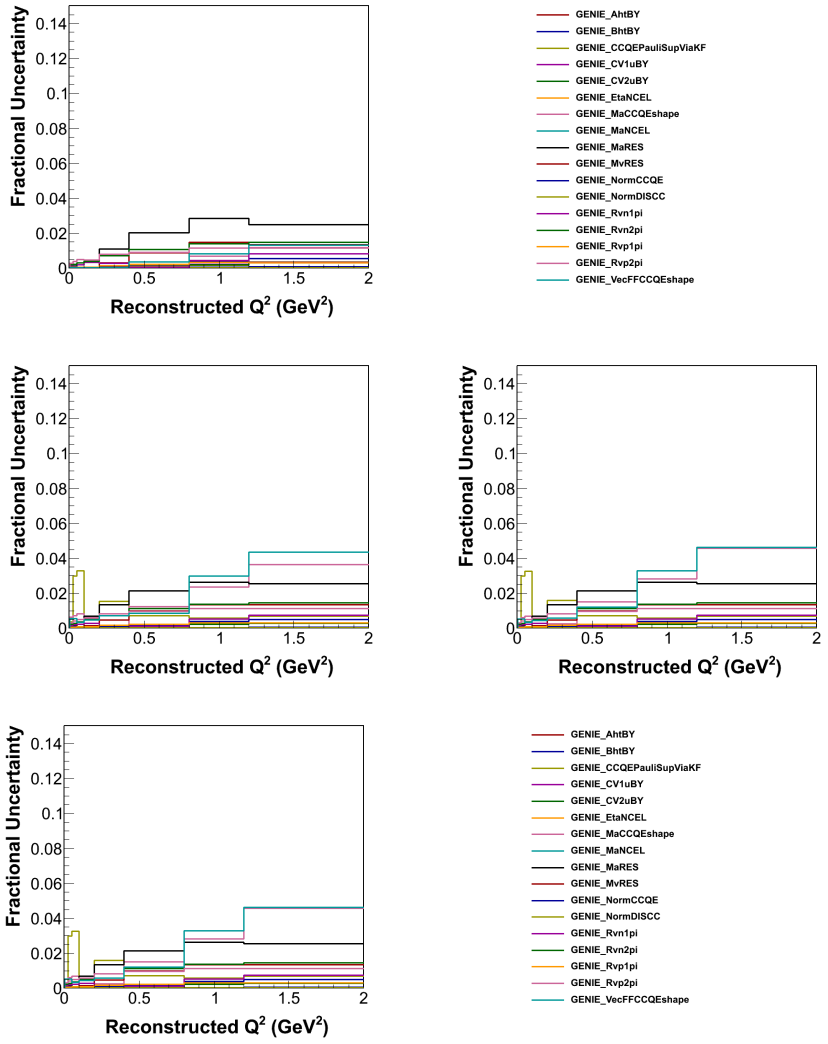

FIG. 6.60: Systematic errors in **Group Primary Interaction** for the neutrino mode CCQE one track analysis. Top: background subtraction stage. Middle left: unfolding stage. Middle right: efficiency correction stage. Bottom: final stage, systematic errors in **Group Primary Interaction** on the double differential cross section.

Systematic Uncertainties in the Hadron Interaction Group at Four Stages for the CCQE Analysis

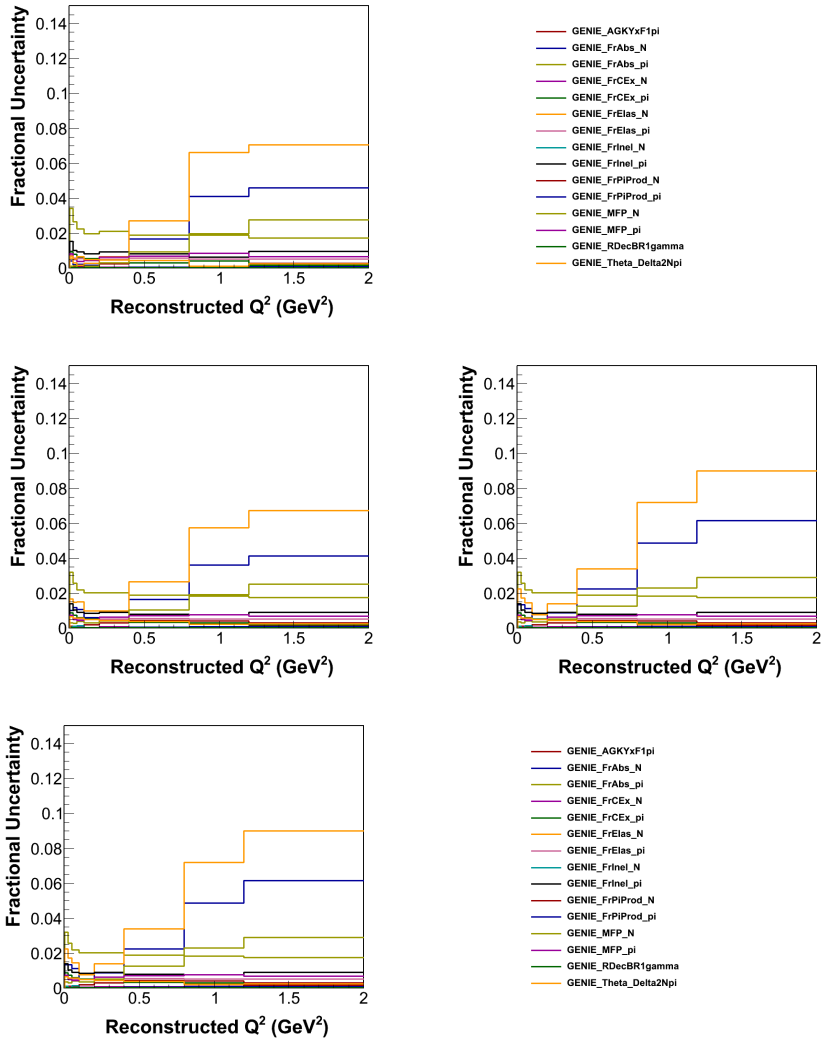

FIG. 6.61: Systematic errors in **Group Hadron Interactions** for the neutrino mode CCQE one track analysis. Top: background subtraction stage. Middle left: unfolding stage. Middle right: efficiency correction stage. Bottom: final stage, systematic errors in **Group Hadron Interactions** on the double differential cross section.

Systematic Uncertainties in the Muon Reconstruction Group at Four Stages for the CCQE Analysis

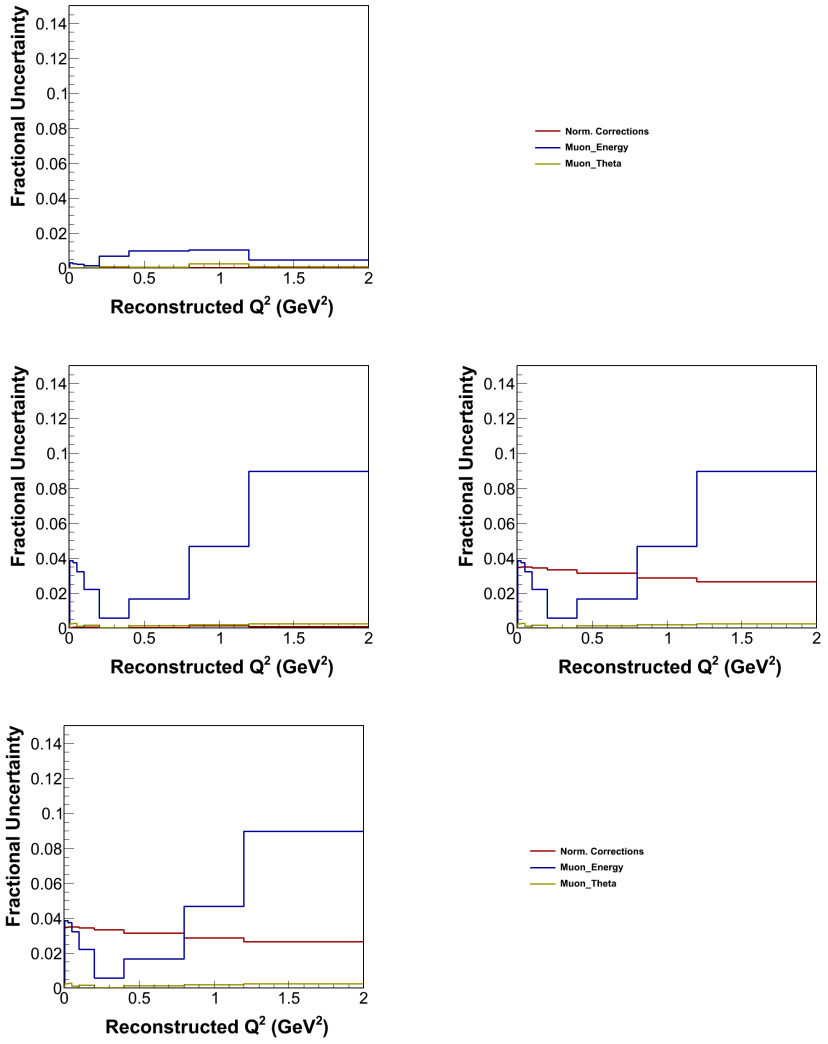

FIG. 6.62: Systematic errors in **Group Muon Reconstruction** for the neutrino mode CCQE one track analysis. Top: background subtraction stage. Middle left: unfolding stage. Middle right: efficiency correction stage. Bottom: final stage, systematic errors in **Group Muon Reconstruction** on the double differential cross section.

Systematic Uncertainties in the Recoil Construction Group at Four Stages for the CCQE Analysis

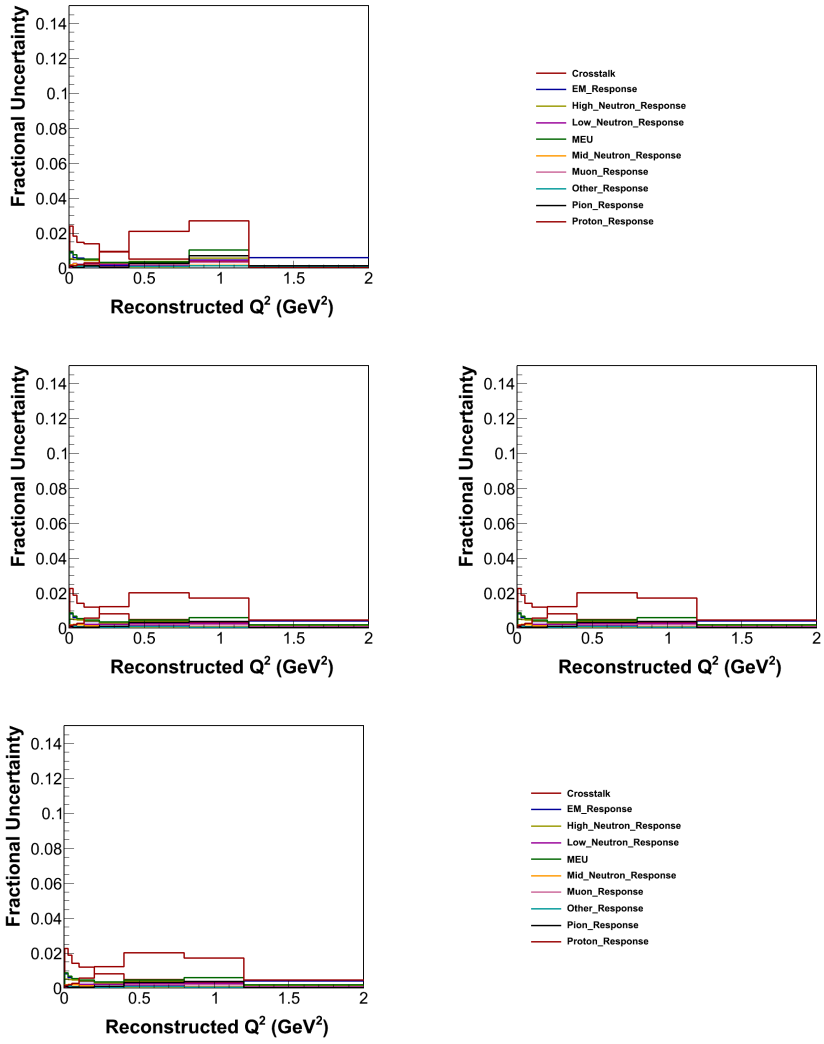

FIG. 6.63: Systematic errors in **Group Recoil Reconstruction** for the neutrino mode CCQE one track analysis. Top: background subtraction stage. Middle left: unfolding stage. Middle right: efficiency correction stage. Bottom: final stage, systematic errors in **Group Recoil Reconstruction** on the double differential cross section.

Systematic Uncertainties in the Other Group at Four Stages for the CCQE Analysis

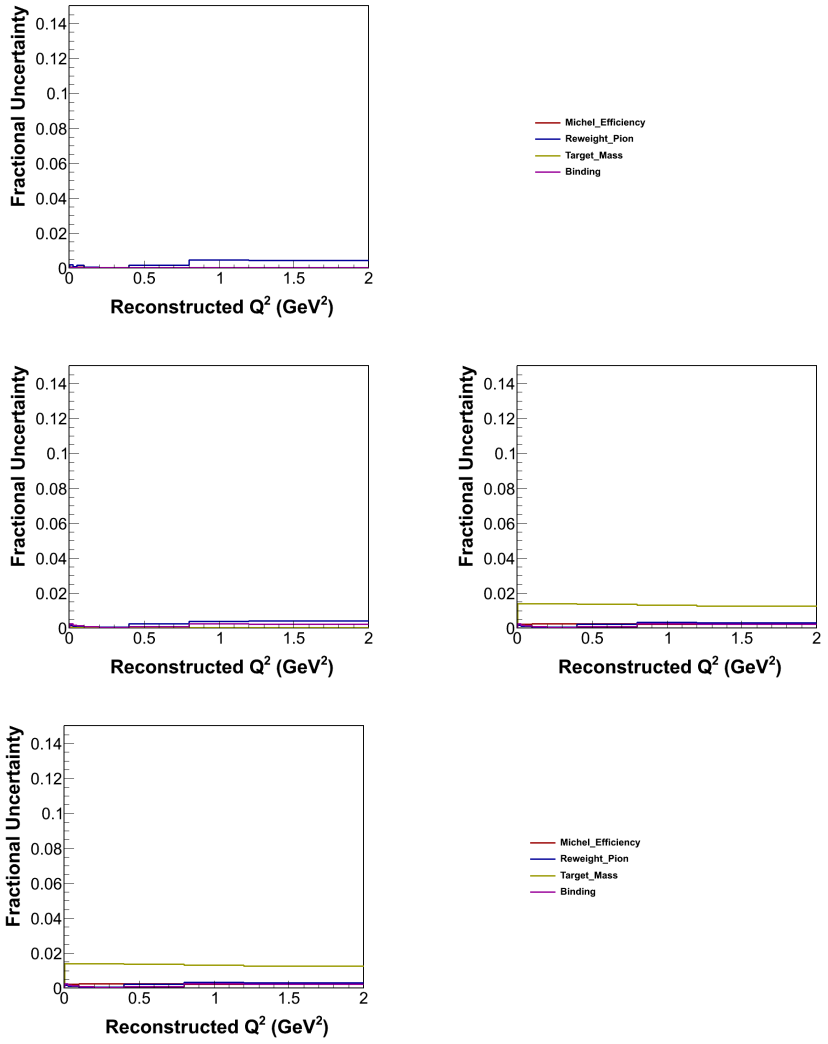

FIG. 6.64: Systematic errors in **Group Other** for the neutrino mode CCQE-like one track analysis. Top: background subtraction stage. Middle left: unfolding stage. Middle right: efficiency correction stage. Bottom: final stage, systematic errors in **Group Other** on the double differential cross section.

6.5.2 Systematic Error Summary Tables

The fractional systematic error in each Q^2 bin for each systematic uncertainty are shown in Tab. 6.14 (the CCQE-like channel) and Tab. 6.15 (the CCQE channel).

TABLE 6.14: Total fractional systematic errors on the ν_μ differential cross-sections $d\sigma/dQ^2_{QELike}$ and their correlation matrix.

$Q^2_{QELike}(GeV^2)$	[0,0.025)	[0.025,0.05)	[0.05,0.1)	[0.1,0.2)	[0.2,0.4)	[0.4,0.8)	[0.8,1.2)	[1.2,2.0)	[2.0,∞)
σ_{sys}	0.14	0.13	0.13	0.13	0.14	0.16	0.19	0.23	0.28
$[0, 0.025)$	1.00	0.99	0.98	0.97	0.94	0.86	0.77	0.64	0.54
$[0.025, 0.05)$		1.00	0.99	0.98	0.94	0.87	0.77	0.64	0.54
$[0.05, 0.1)$			1.00	0.99	0.96	0.90	0.79	0.66	0.58
$[0.1, 0.2)$				1.00	0.99	0.93	0.82	0.69	0.63
$[0.2, 0.4)$					1.00	0.97	0.89	0.78	0.73
$[0.4, 0.8)$						1.00	0.97	0.89	0.86
$[0.8, 1.2)$							1.00	0.97	0.94
$[1.2, 2.0)$								1.00	0.98
$[2.0, \infty)$									1.00

TABLE 6.15: Total fractional systematic errors on the ν_μ differential cross-sections $d\sigma/dQ^2_{QE}$ and their correlation matrix.

$Q^2_{QE}(GeV^2)$	[0,0.025)	[0.025,0.05)	[0.05,0.1)	[0.1,0.2)	[0.2,0.4)	[0.4,0.8)	[0.8,1.2)	[1.2,2.0)	[2.0,∞)
σ_{sys}	0.12	0.12	0.11	0.11	0.11	0.12	0.16	0.20	0.23
$[0, 0.025)$	1.00	0.97	0.95	0.96	0.90	0.80	0.63	0.48	0.34
$[0.025, 0.05)$		1.00	1.00	0.94	0.85	0.76	0.60	0.45	0.31
$[0.05, 0.1)$			1.00	0.95	0.85	0.77	0.60	0.45	0.32
$[0.1, 0.2)$				1.00	0.96	0.85	0.65	0.50	0.39
$[0.2, 0.4)$					1.00	0.93	0.77	0.64	0.55
$[0.4, 0.8)$						1.00	0.94	0.86	0.78
$[0.8, 1.2)$							1.00	0.97	0.90
$[1.2, 2.0)$								1.00	0.96
$[2.0, \infty)$									1.00

In addition, the uncertainties at each stage of the cross-section calculation are tabulated in the following order: the background subtraction stage, the unfolding stage, the efficiency correction stage, and the normalization to get the final cross-section stage.

TABLE 6.16: ν_μ fractional systematic uncertainties on $d\sigma/dQ^2_{QELike}$ after background subtraction.

$Q^2_{QELike}(GeV^2)$	[0,0.025)	[0.025,0.05)	[0.05,0.1)	[0.1,0.2)	[0.2,0.4)	[0.4,0.8)	[0.8,1.2)	[1.2,2.0)	[2.0,∞)	total
Muon Reconstruction										
Muon Energy	0.001	0.001	0.001	0.001	0.006	0.008	0.009	0.005	0.000	0.004
Muon Theta	0.000	0.000	0.000	0.000	0.000	0.000	0.001	0.001	0.000	0.000
Norm.Correction	0.000	0.000	0.000	0.000	0.000	0.000	0.000	0.000	0.000	0.001
Group Total	0.001	0.001	0.001	0.001	0.006	0.008	0.009	0.005	0.000	0.004
Recoil Reconstruction										
CrossTalk	0.018	0.014	0.011	0.011	0.007	0.005	0.004	0.001	0.000	0.009
EM Response	0.010	0.008	0.007	0.007	0.003	0.001	0.004	0.007	0.000	0.006
High Neutron Response	0.007	0.006	0.006	0.005	0.004	0.005	0.007	0.001	0.000	0.005
Mid Neutron Response	0.001	0.003	0.002	0.002	0.001	0.000	0.000	0.000	0.000	0.001
Low Neutron Response	0.001	0.004	0.003	0.003	0.003	0.003	0.004	0.000	0.000	0.003
MEU	0.009	0.008	0.006	0.006	0.004	0.004	0.011	0.001	0.000	0.006
Muon Response	0.001	0.001	0.001	0.001	0.001	0.002	0.003	0.000	0.000	0.001
Other Response	0.002	0.001	0.001	0.001	0.000	0.001	0.001	0.001	0.000	0.001
Pion Response	0.004	0.002	0.002	0.002	0.000	0.002	0.006	0.002	0.000	0.002
Proton Response	0.001	0.001	0.001	0.002	0.008	0.018	0.023	0.000	0.000	0.007
Group Total	0.025	0.020	0.017	0.016	0.013	0.020	0.028	0.007	0.000	0.018
Primary Interaction Models										
AhtBY	0.000	0.000	0.000	0.000	0.000	0.000	0.002	0.003	0.000	0.001
BhtBY	0.000	0.000	0.000	0.000	0.000	0.001	0.003	0.005	0.000	0.001
CCQEPauliSupViaKF	0.009	0.010	0.008	0.004	0.002	0.001	0.002	0.003	0.000	0.005
CV1uBY	0.000	0.000	0.000	0.000	0.000	0.000	0.002	0.003	0.000	0.001
CV2uBY	0.000	0.000	0.000	0.000	0.000	0.000	0.002	0.003	0.000	0.001
EtaNCEL	0.000	0.000	0.000	0.000	0.000	0.000	0.000	0.000	0.000	0.000
MaCCQEshape	0.004	0.004	0.003	0.002	0.002	0.002	0.002	0.004	0.000	0.003
MaNCEL	0.000	0.000	0.000	0.000	0.000	0.000	0.000	0.000	0.000	0.000
MaRES	0.002	0.003	0.002	0.002	0.001	0.003	0.004	0.014	0.000	0.004
MvRES	0.001	0.001	0.001	0.002	0.002	0.003	0.003	0.007	0.000	0.002
NormCCQE	0.008	0.008	0.008	0.007	0.009	0.013	0.017	0.019	0.000	0.011
NormDISCC	0.000	0.000	0.000	0.000	0.000	0.000	0.000	0.000	0.000	0.000
Rvn1pi	0.002	0.003	0.003	0.004	0.006	0.008	0.005	0.005	0.000	0.004
Rvn2pi	0.001	0.002	0.002	0.003	0.005	0.009	0.011	0.012	0.000	0.006
Rvp1pi	0.000	0.001	0.001	0.001	0.001	0.003	0.004	0.004	0.000	0.002
Rvp2pi	0.002	0.003	0.004	0.003	0.006	0.007	0.009	0.009	0.000	0.005
VecffCCQEshape	0.001	0.000	0.001	0.001	0.002	0.004	0.004	0.006	0.000	0.002
Group Total	0.013	0.014	0.013	0.011	0.015	0.020	0.024	0.031	0.000	0.018
Final State Interactions										
AGKYxF1pi	0.001	0.001	0.001	0.001	0.003	0.006	0.008	0.008	0.000	0.003
FrAbs N	0.004	0.003	0.002	0.002	0.004	0.014	0.034	0.040	0.000	0.013
FrAbs π	0.015	0.014	0.015	0.014	0.021	0.032	0.039	0.043	0.000	0.024
FrCEx N	0.000	0.000	0.000	0.000	0.000	0.000	0.000	0.000	0.000	0.000
FrCEx π	0.002	0.002	0.001	0.001	0.000	0.002	0.002	0.004	0.000	0.002
FrElas N	0.006	0.003	0.002	0.002	0.006	0.023	0.057	0.067	0.000	0.021
FrElas π	0.001	0.001	0.001	0.001	0.002	0.002	0.003	0.003	0.000	0.002
FrInel N	0.000	0.000	0.000	0.000	0.000	0.000	0.000	0.000	0.000	0.000
FrInel π	0.021	0.019	0.018	0.017	0.023	0.032	0.040	0.041	0.000	0.026
FrPiProd N	0.000	0.000	0.000	0.000	0.000	0.001	0.002	0.002	0.000	0.001
FrPiProd π	0.000	0.000	0.000	0.000	0.000	0.000	0.000	0.001	0.000	0.000
Mean Free Path N	0.001	0.001	0.001	0.001	0.002	0.008	0.018	0.024	0.000	0.007
Mean Free Path π	0.001	0.002	0.002	0.002	0.002	0.005	0.006	0.010	0.000	0.004
RDecBR1gamma	0.000	0.000	0.000	0.000	0.000	0.000	0.000	0.000	0.000	0.000
Theta Delta 2Nπ	0.005	0.005	0.004	0.003	0.003	0.004	0.000	0.002	0.000	0.003
Group Total	0.028	0.025	0.024	0.022	0.032	0.054	0.089	0.102	0.000	0.047
Flux										
Flux BeamFocus	0.001	0.001	0.001	0.001	0.002	0.002	0.003	0.002	0.000	0.002
Flux Tertiary	0.000	0.001	0.000	0.000	0.001	0.001	0.002	0.003	0.000	0.001
Flux NA49	0.001	0.000	0.000	0.000	0.000	0.001	0.000	0.001	0.000	0.001
Group Total	0.001	0.001	0.001	0.001	0.002	0.003	0.003	0.004	0.000	0.002
Michel Efficiency	0.001	0.001	0.001	0.001	0.001	0.000	0.000	0.000	0.000	0.001
Pion Reweight	0.001	0.000	0.001	0.000	0.000	0.002	0.004	0.004	0.000	0.002
Target Mass	0.000	0.000	0.000	0.000	0.000	0.000	0.000	0.000	0.000	0.000
Binding Energy	0.000	0.000	0.000	0.000	0.000	0.000	0.000	0.000	0.000	0.000
Group Total	0.001	0.001	0.001	0.001	0.001	0.002	0.004	0.004	0.000	0.002
Total Systematic	0.039	0.035	0.032	0.030	0.038	0.061	0.098	0.107	0.000	0.055
Statistical	0.027	0.023	0.016	0.011	0.010	0.013	0.030	0.042	0.000	0.021
Total	0.047	0.042	0.036	0.032	0.040	0.063	0.102	0.115	0.000	0.060

TABLE 6.17: ν_μ fractional systematic uncertainties on $d\sigma/dQ^2_{QELike}$ after unfolding.

$Q^2_{QELike}(GeV^2)$	[0,0.025)	[0.025,0.05)	[0.05,0.1)	[0.1,0.2)	[0.2,0.4)	[0.4,0.8)	[0.8,1.2)	[1.2,2.0)	[2.0,∞)	total
Muon Reconstruction										
Muon Energy	0.037	0.037	0.032	0.022	0.006	0.016	0.044	0.089	0.139	0.036
Muon Theta	0.002	0.003	0.001	0.002	0.000	0.001	0.002	0.003	0.006	0.002
Norm.Correction	0.000	0.001	0.001	0.001	0.000	0.000	0.001	0.001	0.000	0.002
Group Total	0.037	0.037	0.032	0.022	0.006	0.016	0.044	0.089	0.139	0.036
Recoil Reconstruction										
CrossTalk	0.016	0.014	0.011	0.009	0.007	0.005	0.003	0.003	0.001	0.009
EM Response	0.009	0.008	0.007	0.005	0.002	0.000	0.000	0.004	0.005	0.005
High Neutron Response	0.007	0.006	0.006	0.005	0.004	0.005	0.005	0.002	0.001	0.005
Mid Neutron Response	0.002	0.002	0.002	0.002	0.001	0.000	0.000	0.000	0.000	0.001
Low Neutron Response	0.002	0.003	0.003	0.003	0.003	0.003	0.003	0.001	0.001	0.003
MEU	0.009	0.007	0.006	0.006	0.004	0.005	0.007	0.003	0.002	0.006
Muon Response	0.001	0.001	0.001	0.001	0.001	0.002	0.002	0.001	0.001	0.001
Other Response	0.002	0.001	0.001	0.001	0.000	0.001	0.000	0.000	0.000	0.001
Pion Response	0.003	0.002	0.002	0.002	0.000	0.002	0.003	0.000	0.000	0.002
Proton Response	0.001	0.002	0.002	0.005	0.011	0.017	0.015	0.005	0.005	0.007
Group Total	0.022	0.020	0.016	0.015	0.015	0.020	0.018	0.008	0.007	0.017
Primary Interaction Models										
AhtBY	0.000	0.000	0.000	0.000	0.000	0.001	0.002	0.003	0.007	0.001
BhtBY	0.000	0.000	0.000	0.000	0.000	0.001	0.003	0.005	0.009	0.001
CCQEPauliSupViaKF	0.005	0.021	0.023	0.002	0.015	0.007	0.005	0.005	0.005	0.010
CV1uBY	0.000	0.000	0.000	0.000	0.000	0.001	0.002	0.003	0.006	0.001
CV2uBY	0.000	0.000	0.000	0.000	0.000	0.001	0.002	0.003	0.005	0.001
EtaNCEL	0.000	0.000	0.000	0.000	0.000	0.000	0.000	0.000	0.000	0.000
MaCCQEshape	0.001	0.004	0.005	0.004	0.002	0.009	0.015	0.020	0.018	0.007
MaNCEL	0.000	0.000	0.000	0.000	0.000	0.000	0.000	0.000	0.000	0.000
MaRES	0.002	0.001	0.001	0.003	0.002	0.007	0.020	0.044	0.091	0.010
MvRES	0.001	0.001	0.001	0.001	0.000	0.005	0.012	0.023	0.043	0.006
NormCCQE	0.010	0.006	0.006	0.005	0.009	0.016	0.022	0.029	0.063	0.013
NormDISCC	0.000	0.000	0.000	0.000	0.000	0.000	0.000	0.000	0.000	0.000
Rvn1pi	0.000	0.002	0.002	0.003	0.004	0.009	0.012	0.017	0.058	0.006
Rvn2pi	0.002	0.002	0.003	0.004	0.006	0.009	0.011	0.012	0.019	0.006
Rvp1pi	0.000	0.001	0.001	0.001	0.002	0.003	0.005	0.005	0.001	0.002
Rvp2pi	0.002	0.003	0.003	0.004	0.006	0.007	0.009	0.009	0.008	0.005
VecffCCQEshape	0.005	0.005	0.004	0.003	0.005	0.008	0.021	0.027	0.015	0.010
Group Total	0.013	0.023	0.025	0.010	0.021	0.028	0.046	0.071	0.137	0.030
Final State Interactions										
AGKYxF1pi	0.001	0.001	0.001	0.001	0.003	0.007	0.008	0.013	0.026	0.004
FrAbs N	0.010	0.013	0.011	0.006	0.006	0.013	0.028	0.031	0.037	0.015
FrAbs π	0.021	0.013	0.013	0.012	0.021	0.037	0.050	0.061	0.124	0.028
FrCEx N	0.000	0.000	0.001	0.000	0.001	0.000	0.000	0.001	0.002	0.000
FrCEx π	0.001	0.002	0.001	0.001	0.001	0.003	0.003	0.004	0.007	0.002
FrElas N	0.015	0.016	0.016	0.009	0.009	0.021	0.050	0.062	0.079	0.025
FrElas π	0.002	0.000	0.000	0.000	0.001	0.003	0.004	0.005	0.011	0.002
FrInel N	0.000	0.002	0.001	0.000	0.000	0.000	0.000	0.000	0.001	0.000
FrInel π	0.026	0.018	0.016	0.015	0.022	0.037	0.048	0.058	0.112	0.030
FrPiProd N	0.000	0.000	0.000	0.000	0.000	0.000	0.003	0.007	0.010	0.001
FrPiProd π	0.000	0.000	0.000	0.000	0.000	0.000	0.001	0.002	0.007	0.000
Mean Free Path N	0.003	0.002	0.004	0.003	0.003	0.009	0.016	0.023	0.034	0.008
Mean Free Path π	0.002	0.001	0.001	0.001	0.002	0.006	0.011	0.016	0.042	0.005
RDecBR1gamma	0.000	0.000	0.000	0.000	0.000	0.000	0.000	0.000	0.000	0.000
Theta Delta 2Nπ	0.005	0.003	0.004	0.004	0.003	0.003	0.002	0.002	0.001	0.003
Group Total	0.039	0.030	0.029	0.023	0.032	0.059	0.092	0.113	0.199	0.052
Flux										
Flux BeamFocus	0.001	0.001	0.001	0.000	0.000	0.003	0.007	0.009	0.007	0.003
Flux Tertiary	0.001	0.001	0.003	0.002	0.002	0.002	0.007	0.006	0.031	0.003
Flux NA49	0.000	0.001	0.001	0.000	0.000	0.001	0.001	0.003	0.004	0.001
Group Total	0.001	0.001	0.003	0.002	0.002	0.004	0.010	0.011	0.032	0.004
Michel Efficiency	0.001	0.001	0.001	0.001	0.000	0.000	0.000	0.000	0.000	0.001
Pion Reweight	0.001	0.000	0.000	0.000	0.001	0.002	0.004	0.004	0.004	0.002
Target Mass	0.000	0.000	0.000	0.000	0.000	0.000	0.000	0.000	0.000	0.000
Binding Energy	0.002	0.002	0.002	0.001	0.000	0.001	0.002	0.002	0.003	0.001
Group Total	0.001	0.001	0.001	0.001	0.001	0.002	0.004	0.004	0.004	0.002
Total Systematic	0.059	0.057	0.053	0.037	0.042	0.071	0.114	0.161	0.280	0.074
Statistical	0.022	0.015	0.011	0.008	0.008	0.011	0.021	0.035	0.067	0.016
Total	0.064	0.059	0.054	0.038	0.042	0.071	0.116	0.165	0.288	0.076

TABLE 6.18: ν_μ fractional systematic uncertainties on $d\sigma/dQ^2_{QELike}$ after efficiency correction.

$Q^2_{QELike}(GeV^2)$	[0,0.025)	[0.025,0.05)	[0.05,0.1)	[0.1,0.2)	[0.2,0.4)	[0.4,0.8)	[0.8,1.2)	[1.2,2.0)	[2.0,∞)	total
Muon Reconstruction										
Muon Energy	0.037	0.037	0.032	0.022	0.006	0.016	0.044	0.089	0.139	0.036
Muon Theta	0.002	0.003	0.001	0.002	0.000	0.001	0.002	0.003	0.006	0.002
Norm.Correction	0.035	0.036	0.035	0.035	0.034	0.032	0.029	0.027	0.024	0.035
Group Total	0.051	0.052	0.048	0.041	0.035	0.036	0.053	0.093	0.141	0.051
Recoil Reconstruction										
CrossTalk	0.016	0.014	0.011	0.009	0.007	0.005	0.003	0.003	0.001	0.009
EM Response	0.009	0.008	0.007	0.005	0.002	0.000	0.000	0.004	0.005	0.005
High Neutron Response	0.007	0.006	0.006	0.005	0.004	0.005	0.005	0.002	0.001	0.005
Mid Neutron Response	0.002	0.002	0.002	0.002	0.001	0.000	0.000	0.000	0.000	0.001
Low Neutron Response	0.002	0.003	0.003	0.003	0.003	0.003	0.003	0.001	0.001	0.003
MEU	0.009	0.007	0.006	0.006	0.004	0.005	0.007	0.003	0.002	0.006
Muon Response	0.001	0.001	0.001	0.001	0.001	0.002	0.002	0.001	0.001	0.001
Other Response	0.002	0.001	0.001	0.001	0.000	0.001	0.000	0.000	0.000	0.001
Pion Response	0.003	0.002	0.002	0.002	0.000	0.002	0.003	0.000	0.000	0.002
Proton Response	0.001	0.002	0.002	0.005	0.011	0.017	0.015	0.005	0.005	0.007
Group Total	0.022	0.020	0.016	0.015	0.015	0.020	0.018	0.008	0.007	0.017
Primary Interaction Models										
AhtBY	0.000	0.000	0.000	0.000	0.000	0.001	0.003	0.004	0.005	0.001
BhtBY	0.000	0.000	0.000	0.000	0.001	0.002	0.004	0.006	0.008	0.002
CCQEPauliSupViaKF	0.023	0.003	0.002	0.013	0.016	0.007	0.005	0.005	0.005	0.009
CV1uBY	0.000	0.000	0.000	0.000	0.000	0.001	0.003	0.003	0.005	0.001
CV2uBY	0.000	0.000	0.000	0.000	0.000	0.001	0.002	0.003	0.004	0.001
EtaNCEL	0.000	0.000	0.000	0.000	0.000	0.000	0.000	0.000	0.000	0.000
MaCCQEshape	0.007	0.005	0.004	0.003	0.004	0.009	0.014	0.025	0.041	0.009
MaNCEL	0.000	0.000	0.000	0.000	0.000	0.000	0.000	0.000	0.000	0.000
MaRES	0.000	0.005	0.008	0.012	0.019	0.032	0.046	0.063	0.082	0.023
MvRES	0.000	0.001	0.003	0.006	0.011	0.020	0.027	0.035	0.043	0.013
NormCCQE	0.024	0.024	0.027	0.027	0.031	0.035	0.035	0.035	0.051	0.030
NormDISCC	0.000	0.000	0.000	0.000	0.000	0.000	0.000	0.000	0.000	0.000
Rvn1pi	0.002	0.006	0.009	0.013	0.019	0.024	0.023	0.020	0.041	0.014
Rvn2pi	0.002	0.002	0.003	0.005	0.007	0.010	0.012	0.012	0.017	0.007
Rvp1pi	0.001	0.002	0.003	0.003	0.005	0.006	0.006	0.005	0.001	0.004
Rvp2pi	0.003	0.004	0.004	0.005	0.007	0.008	0.009	0.009	0.006	0.006
VecffCCQEshape	0.004	0.005	0.005	0.000	0.000	0.010	0.020	0.026	0.016	0.009
Group Total	0.034	0.027	0.031	0.036	0.047	0.060	0.074	0.092	0.124	0.050
Final State Interactions										
AGKYxF1pi	0.002	0.003	0.004	0.005	0.009	0.012	0.013	0.015	0.021	0.008
FrAbs N	0.015	0.016	0.011	0.008	0.010	0.020	0.039	0.048	0.048	0.021
FrAbs π	0.052	0.046	0.050	0.052	0.061	0.072	0.073	0.071	0.101	0.060
FrCEx N	0.000	0.001	0.000	0.000	0.001	0.001	0.001	0.001	0.001	0.001
FrCEx π	0.001	0.001	0.002	0.003	0.004	0.005	0.005	0.004	0.005	0.003
FrElas N	0.025	0.021	0.016	0.012	0.017	0.034	0.069	0.089	0.098	0.035
FrElas π	0.006	0.005	0.006	0.006	0.006	0.007	0.007	0.005	0.008	0.006
FrInel N	0.001	0.001	0.001	0.000	0.000	0.000	0.000	0.000	0.002	0.001
FrInel π	0.051	0.045	0.047	0.049	0.056	0.066	0.069	0.067	0.094	0.056
FrPiProd N	0.000	0.000	0.000	0.000	0.001	0.001	0.004	0.007	0.010	0.002
FrPiProd π	0.001	0.001	0.001	0.001	0.002	0.002	0.002	0.003	0.007	0.002
Mean Free Path N	0.004	0.004	0.005	0.004	0.006	0.012	0.021	0.028	0.032	0.011
Mean Free Path π	0.009	0.010	0.011	0.012	0.014	0.017	0.018	0.020	0.034	0.014
RDecBR1gamma	0.000	0.000	0.000	0.000	0.000	0.000	0.000	0.000	0.000	0.000
Theta Delta 2Nπ	0.007	0.004	0.005	0.004	0.003	0.002	0.001	0.003	0.002	0.004
Group Total	0.080	0.071	0.073	0.075	0.088	0.108	0.132	0.146	0.184	0.096
Flux										
Flux BeamFocus	0.001	0.001	0.001	0.002	0.004	0.005	0.005	0.002	0.004	0.003
Flux Tertiary	0.013	0.006	0.004	0.005	0.006	0.013	0.025	0.038	0.030	0.014
Flux NA49	0.000	0.000	0.001	0.001	0.002	0.003	0.003	0.003	0.008	0.002
Group Total	0.013	0.006	0.004	0.005	0.008	0.014	0.026	0.038	0.031	0.014
Michel Efficiency	0.002	0.002	0.002	0.002	0.002	0.002	0.002	0.002	0.002	0.002
Pion Reweight	0.001	0.000	0.000	0.000	0.001	0.002	0.003	0.003	0.003	0.001
Target Mass	0.013	0.014	0.014	0.014	0.014	0.013	0.013	0.013	0.013	0.013
Binding Energy	0.002	0.002	0.002	0.001	0.000	0.001	0.002	0.002	0.003	0.001
Group Total	0.014	0.014	0.014	0.014	0.014	0.014	0.014	0.013	0.014	0.014
Total Systematic	0.105	0.095	0.095	0.095	0.107	0.132	0.164	0.200	0.265	0.124
Statistical	0.024	0.016	0.012	0.009	0.009	0.012	0.023	0.038	0.074	0.018
Total	0.107	0.096	0.096	0.095	0.108	0.132	0.166	0.204	0.275	0.126

TABLE 6.19: ν_μ fractional systematic uncertainties on $d\sigma/dQ^2_{QELike}$.

$Q^2_{QELike}(GeV^2)$	[0,0.025)	[0.025,0.05)	[0.05,0.1)	[0.1,0.2)	[0.2,0.4)	[0.4,0.8)	[0.8,1.2)	[1.2,2.0)	[2.0,∞)	total
Muon Reconstruction										
Muon Energy	0.037	0.037	0.032	0.022	0.006	0.016	0.044	0.089	0.139	0.036
Muon Theta	0.002	0.003	0.001	0.002	0.000	0.001	0.002	0.003	0.006	0.002
Norm.Correction	0.035	0.036	0.035	0.035	0.034	0.032	0.029	0.027	0.024	0.035
Group Total	0.051	0.052	0.048	0.041	0.035	0.036	0.053	0.093	0.141	0.051
Recoil Reconstruction										
CrossTalk	0.016	0.014	0.011	0.009	0.007	0.005	0.003	0.003	0.001	0.009
EM Response	0.009	0.008	0.007	0.005	0.002	0.000	0.000	0.004	0.005	0.005
High Neutron Response	0.007	0.006	0.006	0.005	0.004	0.005	0.005	0.002	0.001	0.005
Mid Neutron Response	0.002	0.002	0.002	0.002	0.001	0.000	0.000	0.000	0.000	0.001
Low Neutron Response	0.002	0.003	0.003	0.003	0.003	0.003	0.003	0.001	0.001	0.003
MEU	0.009	0.007	0.006	0.006	0.004	0.005	0.007	0.003	0.002	0.006
Muon Response	0.001	0.001	0.001	0.001	0.001	0.002	0.002	0.001	0.001	0.001
Other Response	0.002	0.001	0.001	0.001	0.000	0.001	0.000	0.000	0.000	0.001
Pion Response	0.003	0.002	0.002	0.002	0.000	0.002	0.003	0.000	0.000	0.002
Proton Response	0.001	0.002	0.002	0.005	0.011	0.017	0.015	0.005	0.005	0.007
Group Total	0.022	0.020	0.016	0.015	0.015	0.020	0.018	0.008	0.007	0.017
Primary Interaction Models										
AhtBY	0.000	0.000	0.000	0.000	0.000	0.001	0.003	0.004	0.005	0.001
BhtBY	0.000	0.000	0.000	0.000	0.001	0.002	0.004	0.006	0.008	0.002
CCQEPauliSupViaKF	0.023	0.003	0.002	0.013	0.016	0.007	0.005	0.005	0.005	0.009
CV1uBY	0.000	0.000	0.000	0.000	0.000	0.001	0.003	0.003	0.005	0.001
CV2uBY	0.000	0.000	0.000	0.000	0.000	0.001	0.002	0.003	0.004	0.001
EtaNCEL	0.000	0.000	0.000	0.000	0.000	0.000	0.000	0.000	0.000	0.000
MaCCQEshape	0.007	0.005	0.004	0.003	0.004	0.009	0.014	0.025	0.041	0.009
MaNCEL	0.000	0.000	0.000	0.000	0.000	0.000	0.000	0.000	0.000	0.000
MaRES	0.000	0.005	0.008	0.012	0.019	0.032	0.046	0.063	0.082	0.023
MvRES	0.000	0.001	0.003	0.006	0.011	0.020	0.027	0.035	0.043	0.013
NormCCQE	0.024	0.024	0.027	0.027	0.031	0.035	0.035	0.035	0.051	0.030
NormDISCC	0.000	0.000	0.000	0.000	0.000	0.000	0.000	0.000	0.000	0.000
Rvn1pi	0.002	0.006	0.009	0.013	0.019	0.024	0.023	0.020	0.041	0.014
Rvn2pi	0.002	0.002	0.003	0.005	0.007	0.010	0.012	0.012	0.017	0.007
Rvp1pi	0.001	0.002	0.003	0.003	0.005	0.006	0.006	0.005	0.001	0.004
Rvp2pi	0.003	0.004	0.004	0.005	0.007	0.008	0.009	0.009	0.006	0.006
VecffCCQEshape	0.004	0.005	0.005	0.000	0.000	0.010	0.020	0.026	0.016	0.009
Group Total	0.034	0.027	0.031	0.036	0.047	0.060	0.074	0.092	0.124	0.050
Final State Interactions										
AGKYxF1pi	0.002	0.003	0.004	0.005	0.009	0.012	0.013	0.015	0.021	0.008
FrAbs N	0.015	0.016	0.011	0.008	0.010	0.020	0.039	0.048	0.048	0.021
FrAbs π	0.052	0.046	0.050	0.052	0.061	0.072	0.073	0.071	0.101	0.060
FrCEx N	0.000	0.001	0.000	0.000	0.001	0.001	0.001	0.001	0.001	0.001
FrCEx π	0.001	0.001	0.002	0.003	0.004	0.005	0.005	0.004	0.005	0.003
FrElas N	0.025	0.021	0.016	0.012	0.017	0.034	0.069	0.089	0.098	0.035
FrElas π	0.006	0.005	0.006	0.006	0.006	0.007	0.007	0.005	0.008	0.006
FrInel N	0.001	0.001	0.001	0.000	0.000	0.000	0.000	0.000	0.002	0.001
FrInel π	0.051	0.045	0.047	0.049	0.056	0.066	0.069	0.067	0.094	0.056
FrPiProd N	0.000	0.000	0.000	0.000	0.001	0.001	0.004	0.007	0.010	0.002
FrPiProd π	0.001	0.001	0.001	0.001	0.002	0.002	0.002	0.003	0.007	0.002
Mean Free Path N	0.004	0.004	0.005	0.004	0.006	0.012	0.021	0.028	0.032	0.011
Mean Free Path π	0.009	0.010	0.011	0.012	0.014	0.017	0.018	0.020	0.034	0.014
RDecBR1gamma	0.000	0.000	0.000	0.000	0.000	0.000	0.000	0.000	0.000	0.000
Theta Delta 2Nπ	0.007	0.004	0.005	0.004	0.003	0.002	0.001	0.003	0.002	0.004
Group Total	0.080	0.071	0.073	0.075	0.088	0.108	0.132	0.146	0.184	0.096
Flux										
Flux BeamFocus	0.030	0.030	0.031	0.032	0.033	0.035	0.034	0.031	0.028	0.032
Flux Tertiary	0.069	0.063	0.061	0.062	0.063	0.069	0.079	0.090	0.083	0.069
Flux NA49	0.056	0.056	0.057	0.057	0.059	0.060	0.061	0.062	0.065	0.058
Group Total	0.094	0.090	0.089	0.090	0.092	0.097	0.105	0.113	0.109	0.096
Michel Efficiency	0.002	0.002	0.002	0.002	0.002	0.002	0.002	0.002	0.002	0.002
Pion Reweight	0.001	0.000	0.000	0.000	0.001	0.002	0.003	0.003	0.003	0.001
Target Mass	0.013	0.014	0.014	0.014	0.014	0.013	0.013	0.013	0.013	0.013
Binding Energy	0.002	0.002	0.002	0.001	0.000	0.001	0.002	0.002	0.003	0.001
Group Total	0.014	0.014	0.014	0.014	0.014	0.014	0.014	0.013	0.014	0.014
Total Systematic	0.140	0.130	0.130	0.131	0.141	0.163	0.193	0.227	0.285	0.157
Statistical	0.024	0.016	0.012	0.009	0.009	0.012	0.023	0.038	0.074	0.018
Total	0.142	0.132	0.131	0.131	0.142	0.163	0.195	0.230	0.294	0.158

TABLE 6.20: ν_μ fractional systematic uncertainties on $d\sigma/dQ^2_{QE}$ after background subtraction.

$Q^2_{QE}(GeV^2)$	[0,0.025)	[0.025,0.05)	[0.05,0.1)	[0.1,0.2)	[0.2,0.4)	[0.4,0.8)	[0.8,1.2)	[1.2,2.0)	[2.0,∞)	total
Muon Reconstruction										
Muon Energy	0.003	0.003	0.002	0.001	0.007	0.010	0.010	0.005	0.000	0.005
Muon Theta	0.000	0.000	0.000	0.000	0.001	0.001	0.002	0.001	0.000	0.001
Norm.Correction	0.000	0.000	0.000	0.000	0.000	0.000	0.000	0.000	0.000	0.001
Group Total	0.003	0.003	0.002	0.001	0.007	0.010	0.011	0.005	0.000	0.005
Recoil Reconstruction										
CrossTalk	0.024	0.018	0.015	0.014	0.009	0.005	0.004	0.001	0.000	0.011
EM Response	0.009	0.006	0.006	0.005	0.002	0.002	0.005	0.006	0.000	0.005
High Neutron Response	0.005	0.005	0.005	0.005	0.003	0.004	0.006	0.001	0.000	0.004
Mid Neutron Response	0.002	0.003	0.002	0.002	0.001	0.000	0.002	0.000	0.000	0.001
Low Neutron Response	0.000	0.003	0.002	0.002	0.002	0.003	0.004	0.000	0.000	0.002
MEU	0.009	0.008	0.005	0.005	0.003	0.004	0.010	0.000	0.000	0.006
Muon Response	0.002	0.001	0.001	0.000	0.001	0.002	0.003	0.000	0.000	0.001
Other Response	0.002	0.001	0.001	0.001	0.000	0.001	0.001	0.001	0.000	0.001
Pion Response	0.001	0.000	0.000	0.001	0.001	0.003	0.007	0.001	0.000	0.002
Proton Response	0.002	0.001	0.002	0.003	0.010	0.021	0.027	0.000	0.000	0.008
Group Total	0.028	0.022	0.018	0.017	0.014	0.023	0.032	0.006	0.000	0.020
Primary Interaction Models										
AhtBY	0.000	0.000	0.000	0.000	0.000	0.000	0.002	0.004	0.000	0.001
BhtBY	0.000	0.000	0.000	0.000	0.000	0.001	0.003	0.005	0.000	0.001
CCQEPauliSupViaKF	0.001	0.001	0.000	0.000	0.001	0.001	0.002	0.004	0.000	0.001
CV1uBY	0.000	0.000	0.000	0.000	0.000	0.000	0.002	0.003	0.000	0.001
CV2uBY	0.000	0.000	0.000	0.000	0.000	0.000	0.002	0.003	0.000	0.001
EtaNCEL	0.000	0.000	0.000	0.000	0.000	0.000	0.000	0.000	0.000	0.000
MaCCQEshape	0.001	0.001	0.000	0.000	0.001	0.004	0.007	0.012	0.000	0.003
MaNCEL	0.000	0.000	0.000	0.000	0.000	0.000	0.000	0.000	0.000	0.000
MaRES	0.000	0.000	0.002	0.004	0.011	0.020	0.029	0.025	0.000	0.011
MvRES	0.000	0.001	0.001	0.000	0.003	0.009	0.015	0.013	0.000	0.005
NormCCQE	0.001	0.001	0.001	0.000	0.001	0.002	0.001	0.001	0.000	0.001
NormDISCC	0.000	0.000	0.000	0.000	0.000	0.000	0.000	0.000	0.000	0.000
Rvn1pi	0.002	0.002	0.002	0.003	0.003	0.000	0.005	0.008	0.000	0.003
Rvn2pi	0.002	0.002	0.003	0.004	0.007	0.011	0.014	0.015	0.000	0.007
Rvp1pi	0.001	0.001	0.001	0.001	0.001	0.002	0.003	0.003	0.000	0.002
Rvp2pi	0.003	0.004	0.005	0.005	0.008	0.009	0.012	0.011	0.000	0.007
VecffCCQEshape	0.000	0.000	0.000	0.000	0.000	0.004	0.008	0.013	0.000	0.003
Group Total	0.004	0.005	0.007	0.008	0.016	0.027	0.039	0.040	0.000	0.018
Final State Interactions										
AGKYxF1pi	0.001	0.001	0.001	0.002	0.002	0.004	0.005	0.003	0.000	0.002
FrAbs N	0.004	0.002	0.002	0.002	0.005	0.017	0.041	0.046	0.000	0.015
FrAbs π	0.034	0.027	0.022	0.020	0.021	0.019	0.019	0.017	0.000	0.022
FrCEx N	0.000	0.000	0.001	0.000	0.001	0.000	0.000	0.000	0.000	0.000
FrCEx π	0.009	0.008	0.006	0.005	0.005	0.003	0.004	0.002	0.000	0.005
FrElas N	0.006	0.003	0.002	0.003	0.007	0.027	0.066	0.071	0.000	0.023
FrElas π	0.007	0.006	0.006	0.005	0.005	0.006	0.005	0.005	0.000	0.006
FrInel N	0.001	0.000	0.000	0.000	0.000	0.000	0.000	0.001	0.000	0.000
FrInel π	0.015	0.010	0.009	0.008	0.009	0.008	0.006	0.010	0.000	0.010
FrPiProd N	0.000	0.000	0.000	0.000	0.000	0.000	0.001	0.000	0.000	0.000
FrPiProd π	0.000	0.000	0.000	0.000	0.000	0.001	0.001	0.001	0.000	0.000
Mean Free Path N	0.001	0.001	0.000	0.001	0.003	0.009	0.020	0.028	0.000	0.008
Mean Free Path π	0.008	0.005	0.004	0.004	0.006	0.007	0.009	0.007	0.000	0.006
RDecBR1gamma	0.000	0.000	0.000	0.000	0.000	0.000	0.000	0.000	0.000	0.000
Theta Delta 2Nπ	0.007	0.005	0.007	0.005	0.005	0.004	0.001	0.003	0.000	0.005
Group Total	0.041	0.031	0.027	0.024	0.027	0.041	0.084	0.091	0.000	0.046
Flux										
Flux BeamFocus	0.002	0.002	0.001	0.001	0.002	0.003	0.003	0.002	0.000	0.002
Flux Tertiary	0.002	0.001	0.001	0.000	0.001	0.001	0.002	0.003	0.000	0.001
Flux NA49	0.001	0.000	0.000	0.000	0.000	0.001	0.000	0.002	0.000	0.001
Group Total	0.003	0.002	0.002	0.001	0.002	0.003	0.003	0.004	0.000	0.002
Michel Efficiency	0.001	0.001	0.001	0.000	0.000	0.000	0.000	0.000	0.000	0.000
Pion Reweight	0.002	0.001	0.002	0.001	0.000	0.002	0.005	0.004	0.000	0.002
Target Mass	0.000	0.000	0.000	0.000	0.000	0.000	0.000	0.000	0.000	0.000
Binding Energy	0.000	0.000	0.000	0.000	0.000	0.000	0.000	0.000	0.000	0.000
Group Total	0.002	0.001	0.002	0.001	0.000	0.002	0.005	0.004	0.000	0.002
Total Systematic	0.050	0.039	0.033	0.030	0.035	0.055	0.098	0.100	0.000	0.055
Statistical	0.031	0.025	0.017	0.012	0.011	0.015	0.036	0.051	0.000	0.025
Total	0.059	0.046	0.037	0.033	0.037	0.057	0.105	0.112	0.000	0.061

TABLE 6.21: ν_μ fractional systematic uncertainties on $d\sigma/dQ^2_{QE}$ after unfolding.

$Q^2_{QE}(GeV^2)$	[0,0.025)	[0.025,0.05)	[0.05,0.1)	[0.1,0.2)	[0.2,0.4)	[0.4,0.8)	[0.8,1.2)	[1.2,2.0)	[2.0,∞)	total
Muon Reconstruction										
Muon Energy	0.038	0.038	0.032	0.022	0.006	0.017	0.047	0.090	0.144	0.036
Muon Theta	0.002	0.003	0.001	0.002	0.000	0.001	0.002	0.002	0.003	0.002
Norm.Correction	0.000	0.001	0.001	0.001	0.000	0.000	0.001	0.001	0.001	0.002
Group Total	0.039	0.038	0.032	0.022	0.006	0.017	0.047	0.090	0.144	0.036
Recoil Reconstruction										
CrossTalk	0.023	0.019	0.014	0.012	0.008	0.005	0.003	0.002	0.003	0.011
EM Response	0.008	0.006	0.005	0.004	0.001	0.002	0.001	0.004	0.004	0.004
High Neutron Response	0.005	0.005	0.005	0.004	0.003	0.004	0.004	0.002	0.002	0.004
Mid Neutron Response	0.002	0.002	0.002	0.001	0.001	0.000	0.001	0.000	0.000	0.001
Low Neutron Response	0.000	0.002	0.002	0.002	0.002	0.003	0.003	0.001	0.001	0.002
MEU	0.009	0.007	0.005	0.005	0.004	0.005	0.006	0.002	0.002	0.005
Muon Response	0.001	0.001	0.001	0.001	0.001	0.002	0.002	0.001	0.001	0.001
Other Response	0.001	0.001	0.001	0.001	0.000	0.001	0.001	0.000	0.000	0.001
Pion Response	0.001	0.000	0.000	0.000	0.001	0.003	0.004	0.000	0.000	0.001
Proton Response	0.002	0.002	0.003	0.006	0.012	0.020	0.017	0.005	0.006	0.008
Group Total	0.027	0.022	0.017	0.015	0.016	0.022	0.020	0.007	0.008	0.018
Primary Interaction Models										
AhtBY	0.000	0.000	0.000	0.000	0.000	0.001	0.002	0.003	0.003	0.001
BhtBY	0.000	0.000	0.000	0.000	0.000	0.001	0.004	0.005	0.005	0.001
CCQEPauliSupViaKF	0.004	0.030	0.033	0.001	0.015	0.007	0.006	0.007	0.007	0.013
CV1uBY	0.000	0.000	0.000	0.000	0.000	0.001	0.002	0.003	0.003	0.001
CV2uBY	0.000	0.000	0.000	0.000	0.000	0.001	0.002	0.003	0.003	0.001
EtaNCEL	0.000	0.000	0.000	0.000	0.000	0.000	0.000	0.000	0.000	0.000
MaCCQEshape	0.006	0.007	0.008	0.006	0.001	0.012	0.023	0.036	0.057	0.013
MaNCEL	0.000	0.000	0.000	0.000	0.000	0.000	0.000	0.000	0.000	0.000
MaRES	0.000	0.001	0.003	0.007	0.014	0.021	0.026	0.025	0.025	0.012
MvRES	0.000	0.000	0.000	0.001	0.005	0.010	0.013	0.013	0.013	0.005
NormCCQE	0.001	0.001	0.001	0.001	0.001	0.002	0.000	0.001	0.000	0.001
NormDISCC	0.000	0.000	0.000	0.000	0.000	0.000	0.000	0.000	0.000	0.000
Rvn1pi	0.002	0.002	0.002	0.003	0.002	0.001	0.005	0.007	0.007	0.003
Rvn2pi	0.002	0.003	0.004	0.005	0.008	0.011	0.014	0.014	0.014	0.008
Rvp1pi	0.001	0.001	0.001	0.001	0.002	0.002	0.003	0.003	0.003	0.002
Rvp2pi	0.003	0.004	0.005	0.006	0.008	0.010	0.011	0.011	0.011	0.007
VecffCCQEshape	0.006	0.006	0.003	0.005	0.007	0.009	0.030	0.044	0.046	0.014
Group Total	0.010	0.032	0.035	0.013	0.025	0.033	0.052	0.067	0.082	0.033
Final State Interactions										
AGKYxF1pi	0.001	0.001	0.001	0.002	0.003	0.004	0.004	0.003	0.003	0.003
FrAbs N	0.010	0.012	0.011	0.006	0.006	0.016	0.036	0.041	0.027	0.017
FrAbs π	0.032	0.026	0.022	0.020	0.020	0.019	0.018	0.018	0.018	0.022
FrCEx N	0.000	0.000	0.001	0.000	0.001	0.000	0.001	0.001	0.000	0.000
FrCEx π	0.009	0.007	0.006	0.005	0.005	0.003	0.003	0.002	0.002	0.005
FrElas N	0.017	0.015	0.015	0.010	0.010	0.027	0.057	0.067	0.052	0.027
FrElas π	0.007	0.006	0.005	0.005	0.005	0.006	0.005	0.005	0.005	0.006
FrInel N	0.001	0.001	0.001	0.000	0.000	0.000	0.000	0.000	0.001	0.001
FrInel π	0.014	0.010	0.009	0.009	0.009	0.008	0.008	0.009	0.009	0.010
FrPiProd N	0.000	0.000	0.000	0.000	0.000	0.000	0.001	0.001	0.002	0.000
FrPiProd π	0.000	0.000	0.000	0.000	0.000	0.001	0.001	0.001	0.001	0.000
Mean Free Path N	0.003	0.003	0.004	0.003	0.004	0.010	0.019	0.025	0.030	0.009
Mean Free Path π	0.007	0.005	0.004	0.005	0.006	0.007	0.008	0.007	0.007	0.006
RDecBR1gamma	0.000	0.000	0.000	0.000	0.000	0.000	0.000	0.000	0.000	0.000
Theta Delta 2Nπ	0.007	0.006	0.006	0.005	0.005	0.004	0.002	0.002	0.003	0.005
Group Total	0.043	0.036	0.032	0.027	0.028	0.040	0.074	0.086	0.070	0.046
Flux										
Flux BeamFocus	0.001	0.001	0.001	0.001	0.001	0.003	0.007	0.009	0.006	0.003
Flux Tertiary	0.001	0.000	0.003	0.002	0.003	0.002	0.008	0.007	0.004	0.003
Flux NA49	0.001	0.001	0.001	0.000	0.000	0.001	0.001	0.003	0.006	0.001
Group Total	0.002	0.002	0.003	0.002	0.003	0.004	0.011	0.012	0.009	0.005
Michel Efficiency	0.001	0.001	0.001	0.000	0.000	0.000	0.000	0.000	0.000	0.000
Pion Reweight	0.002	0.001	0.001	0.000	0.001	0.002	0.004	0.004	0.006	0.002
Target Mass	0.000	0.000	0.000	0.000	0.000	0.000	0.000	0.000	0.000	0.000
Binding Energy	0.002	0.002	0.001	0.001	0.000	0.001	0.002	0.002	0.002	0.002
Group Total	0.002	0.001	0.001	0.001	0.001	0.002	0.004	0.004	0.006	0.002
Total Systematic	0.064	0.065	0.060	0.041	0.041	0.059	0.105	0.142	0.180	0.072
Statistical	0.027	0.017	0.012	0.009	0.009	0.013	0.027	0.044	0.089	0.020
Total	0.070	0.067	0.061	0.042	0.042	0.061	0.108	0.149	0.201	0.075

TABLE 6.22: ν fractional systematic uncertainties on $d\sigma/dQ^2_{QE}$ after efficiency correction.

$Q^2_{QE}(GeV^2)$	[0,0.025)	[0.025,0.05)	[0.05,0.1)	[0.1,0.2)	[0.2,0.4)	[0.4,0.8)	[0.8,1.2)	[1.2,2.0)	[2.0,∞)	total
Muon Reconstruction										
Muon Energy	0.038	0.038	0.032	0.022	0.006	0.017	0.047	0.090	0.144	0.036
Muon Theta	0.002	0.003	0.001	0.002	0.000	0.001	0.002	0.002	0.003	0.002
Norm.Correction	0.035	0.035	0.035	0.035	0.034	0.032	0.029	0.027	0.024	0.035
Group Total	0.052	0.052	0.048	0.041	0.034	0.036	0.055	0.094	0.146	0.052
Recoil Reconstruction										
CrossTalk	0.023	0.019	0.014	0.012	0.008	0.005	0.003	0.002	0.003	0.011
EM Response	0.008	0.006	0.005	0.004	0.001	0.002	0.001	0.004	0.004	0.004
High Neutron Response	0.005	0.005	0.005	0.004	0.003	0.004	0.004	0.002	0.002	0.004
Mid Neutron Response	0.002	0.002	0.002	0.001	0.001	0.000	0.001	0.000	0.000	0.001
Low Neutron Response	0.000	0.002	0.002	0.002	0.002	0.003	0.003	0.001	0.001	0.002
MEU	0.009	0.007	0.005	0.005	0.004	0.005	0.006	0.002	0.002	0.005
Muon Response	0.001	0.001	0.001	0.001	0.001	0.002	0.002	0.001	0.001	0.001
Other Response	0.001	0.001	0.001	0.001	0.000	0.001	0.001	0.000	0.000	0.001
Pion Response	0.001	0.000	0.000	0.000	0.001	0.003	0.004	0.000	0.000	0.001
Proton Response	0.002	0.002	0.003	0.006	0.012	0.020	0.017	0.005	0.006	0.008
Group Total	0.027	0.022	0.017	0.015	0.016	0.022	0.020	0.007	0.008	0.018
Primary Interaction Models										
AhtBY	0.000	0.000	0.000	0.000	0.000	0.001	0.002	0.003	0.003	0.001
BhtBY	0.000	0.000	0.000	0.000	0.000	0.001	0.004	0.005	0.005	0.001
CCQEPauliSupViaKF	0.002	0.030	0.033	0.000	0.016	0.007	0.006	0.007	0.007	0.013
CV1uBY	0.000	0.000	0.000	0.000	0.000	0.001	0.002	0.003	0.003	0.001
CV2uBY	0.000	0.000	0.000	0.000	0.000	0.001	0.002	0.003	0.003	0.001
EtaNCEL	0.000	0.000	0.000	0.000	0.000	0.000	0.000	0.000	0.000	0.000
MaCCQEshape	0.007	0.008	0.009	0.006	0.001	0.014	0.028	0.046	0.079	0.015
MaNCEL	0.000	0.000	0.000	0.000	0.000	0.000	0.000	0.000	0.000	0.000
MaRES	0.000	0.001	0.003	0.007	0.014	0.021	0.026	0.025	0.025	0.012
MvRES	0.000	0.000	0.000	0.001	0.005	0.010	0.013	0.013	0.013	0.005
NormCCQE	0.001	0.001	0.001	0.001	0.001	0.002	0.000	0.001	0.000	0.001
NormDISCC	0.000	0.000	0.000	0.000	0.000	0.000	0.000	0.000	0.000	0.000
Rvn1pi	0.002	0.002	0.002	0.003	0.002	0.001	0.005	0.007	0.007	0.003
Rvn2pi	0.002	0.003	0.004	0.005	0.008	0.011	0.014	0.014	0.014	0.008
Rvp1pi	0.001	0.001	0.001	0.001	0.002	0.002	0.003	0.003	0.003	0.002
Rvp2pi	0.003	0.004	0.005	0.006	0.008	0.010	0.011	0.011	0.011	0.007
VecffCCQEshape	0.005	0.005	0.003	0.005	0.007	0.011	0.033	0.046	0.042	0.014
Group Total	0.010	0.032	0.035	0.014	0.026	0.034	0.056	0.075	0.097	0.035
Final State Interactions										
AGKYxF1pi	0.001	0.001	0.001	0.002	0.003	0.004	0.004	0.003	0.003	0.003
FrAbs N	0.013	0.013	0.010	0.006	0.009	0.022	0.049	0.062	0.046	0.023
FrAbs π	0.032	0.026	0.022	0.020	0.020	0.019	0.018	0.018	0.018	0.022
FrCEx N	0.001	0.001	0.000	0.001	0.001	0.001	0.001	0.001	0.000	0.001
FrCEx π	0.009	0.007	0.006	0.005	0.005	0.003	0.003	0.002	0.002	0.005
FrElas N	0.023	0.017	0.013	0.008	0.014	0.034	0.072	0.090	0.074	0.034
FrElas π	0.007	0.006	0.005	0.005	0.005	0.006	0.005	0.005	0.005	0.006
FrInel N	0.001	0.001	0.002	0.000	0.000	0.000	0.000	0.000	0.002	0.001
FrInel π	0.014	0.010	0.009	0.009	0.009	0.008	0.008	0.009	0.009	0.010
FrPiProd N	0.000	0.000	0.000	0.000	0.000	0.000	0.001	0.002	0.002	0.000
FrPiProd π	0.000	0.000	0.000	0.000	0.000	0.001	0.001	0.001	0.001	0.000
Mean Free Path N	0.003	0.004	0.004	0.003	0.006	0.013	0.023	0.029	0.035	0.011
Mean Free Path π	0.007	0.005	0.004	0.005	0.006	0.007	0.008	0.007	0.007	0.006
RDecBR1gamma	0.000	0.000	0.000	0.000	0.000	0.000	0.000	0.000	0.000	0.000
Theta Delta 2Nπ	0.007	0.006	0.006	0.005	0.005	0.004	0.002	0.002	0.003	0.005
Group Total	0.046	0.038	0.031	0.027	0.031	0.049	0.093	0.115	0.096	0.054
Flux										
Flux BeamFocus	0.002	0.001	0.001	0.001	0.003	0.005	0.006	0.005	0.003	0.003
Flux Tertiary	0.009	0.006	0.004	0.004	0.005	0.011	0.023	0.034	0.044	0.012
Flux NA49	0.001	0.000	0.000	0.001	0.002	0.003	0.003	0.004	0.010	0.002
Group Total	0.009	0.007	0.004	0.005	0.006	0.013	0.024	0.034	0.046	0.013
Michel Efficiency	0.002	0.002	0.002	0.002	0.002	0.002	0.002	0.002	0.002	0.002
Pion Reweight	0.002	0.001	0.001	0.000	0.001	0.002	0.003	0.003	0.005	0.002
Target Mass	0.014	0.014	0.014	0.014	0.014	0.013	0.013	0.012	0.013	0.013
Binding Energy	0.002	0.002	0.001	0.001	0.000	0.001	0.002	0.002	0.002	0.002
Group Total	0.014	0.014	0.014	0.014	0.014	0.014	0.014	0.013	0.014	0.014
Total Systematic	0.077	0.076	0.071	0.055	0.057	0.075	0.126	0.170	0.206	0.089
Statistical	0.028	0.018	0.013	0.010	0.010	0.014	0.029	0.047	0.096	0.021
Total	0.082	0.078	0.072	0.056	0.058	0.077	0.129	0.176	0.227	0.091

TABLE 6.23: ν_μ fractional systematic uncertainties on $d\sigma/dQ^2_{QE}$.

$Q^2_{QE}(GeV^2)$	[0,0.025)	[0.025,0.05)	[0.05,0.1)	[0.1,0.2)	[0.2,0.4)	[0.4,0.8)	[0.8,1.2)	[1.2,2.0)	[2.0,∞)	total
Muon Reconstruction										
Muon Energy	0.038	0.038	0.032	0.022	0.006	0.017	0.047	0.090	0.144	0.036
Muon Theta	0.002	0.003	0.001	0.002	0.000	0.001	0.002	0.002	0.003	0.002
Norm.Correction	0.035	0.035	0.035	0.035	0.034	0.032	0.029	0.027	0.024	0.035
Group Total	0.052	0.052	0.048	0.041	0.034	0.036	0.055	0.094	0.146	0.052
Recoil Reconstruction										
CrossTalk	0.023	0.019	0.014	0.012	0.008	0.005	0.003	0.002	0.003	0.011
EM Response	0.008	0.006	0.005	0.004	0.001	0.002	0.001	0.004	0.004	0.004
High Neutron Response	0.005	0.005	0.005	0.004	0.003	0.004	0.004	0.002	0.002	0.004
Mid Neutron Response	0.002	0.002	0.002	0.001	0.001	0.000	0.001	0.000	0.000	0.001
Low Neutron Response	0.000	0.002	0.002	0.002	0.002	0.003	0.003	0.001	0.001	0.002
MEU	0.009	0.007	0.005	0.005	0.004	0.005	0.006	0.002	0.002	0.005
Muon Response	0.001	0.001	0.001	0.001	0.001	0.002	0.002	0.001	0.001	0.001
Other Response	0.001	0.001	0.001	0.001	0.000	0.001	0.001	0.000	0.000	0.001
Pion Response	0.001	0.000	0.000	0.000	0.001	0.003	0.004	0.000	0.000	0.001
Proton Response	0.002	0.002	0.003	0.006	0.012	0.020	0.017	0.005	0.006	0.008
Group Total	0.027	0.022	0.017	0.015	0.016	0.022	0.020	0.007	0.008	0.018
Primary Interaction Models										
AhtBY	0.000	0.000	0.000	0.000	0.000	0.001	0.002	0.003	0.003	0.001
BhtBY	0.000	0.000	0.000	0.000	0.000	0.001	0.004	0.005	0.005	0.001
CCQEPauliSupViaKF	0.002	0.030	0.033	0.000	0.016	0.007	0.006	0.007	0.007	0.013
CV1uBY	0.000	0.000	0.000	0.000	0.000	0.001	0.002	0.003	0.003	0.001
CV2uBY	0.000	0.000	0.000	0.000	0.000	0.001	0.002	0.003	0.003	0.001
EtaNCEL	0.000	0.000	0.000	0.000	0.000	0.000	0.000	0.000	0.000	0.000
MaCCQEshape	0.007	0.008	0.009	0.006	0.001	0.014	0.028	0.046	0.079	0.015
MaNCEL	0.000	0.000	0.000	0.000	0.000	0.000	0.000	0.000	0.000	0.000
MaRES	0.000	0.001	0.003	0.007	0.014	0.021	0.026	0.025	0.025	0.012
MvRES	0.000	0.000	0.000	0.001	0.005	0.010	0.013	0.013	0.013	0.005
NormCCQE	0.001	0.001	0.001	0.001	0.001	0.002	0.000	0.001	0.000	0.001
NormDISCC	0.000	0.000	0.000	0.000	0.000	0.000	0.000	0.000	0.000	0.000
Rvn1pi	0.002	0.002	0.002	0.003	0.002	0.001	0.005	0.007	0.007	0.003
Rvn2pi	0.002	0.003	0.004	0.005	0.008	0.011	0.014	0.014	0.014	0.008
Rvp1pi	0.001	0.001	0.001	0.001	0.002	0.002	0.003	0.003	0.003	0.002
Rvp2pi	0.003	0.004	0.005	0.006	0.008	0.010	0.011	0.011	0.011	0.007
VecffCCQEshape	0.005	0.005	0.003	0.005	0.007	0.011	0.033	0.046	0.042	0.014
Group Total	0.010	0.032	0.035	0.014	0.026	0.034	0.056	0.075	0.097	0.035
Final State Interactions										
AGKYxF1pi	0.001	0.001	0.001	0.002	0.003	0.004	0.004	0.003	0.003	0.003
FrAbs N	0.013	0.013	0.010	0.006	0.009	0.022	0.049	0.062	0.046	0.023
FrAbs π	0.032	0.026	0.022	0.020	0.020	0.019	0.018	0.018	0.018	0.022
FrCEx N	0.001	0.001	0.000	0.001	0.001	0.001	0.001	0.001	0.000	0.001
FrCEx π	0.009	0.007	0.006	0.005	0.005	0.003	0.003	0.002	0.002	0.005
FrElas N	0.023	0.017	0.013	0.008	0.014	0.034	0.072	0.090	0.074	0.034
FrElas π	0.007	0.006	0.005	0.005	0.005	0.006	0.005	0.005	0.005	0.006
FrInel N	0.001	0.001	0.002	0.000	0.000	0.000	0.000	0.000	0.002	0.001
FrInel π	0.014	0.010	0.009	0.009	0.009	0.008	0.008	0.009	0.009	0.010
FrPiProd N	0.000	0.000	0.000	0.000	0.000	0.000	0.001	0.002	0.002	0.000
FrPiProd π	0.000	0.000	0.000	0.000	0.000	0.001	0.001	0.001	0.001	0.000
Mean Free Path N	0.003	0.004	0.004	0.003	0.006	0.013	0.023	0.029	0.035	0.011
Mean Free Path π	0.007	0.005	0.004	0.005	0.006	0.007	0.008	0.007	0.007	0.006
RDecBR1gamma	0.000	0.000	0.000	0.000	0.000	0.000	0.000	0.000	0.000	0.000
Theta Delta 2Nπ	0.007	0.006	0.006	0.005	0.005	0.004	0.002	0.002	0.003	0.005
Group Total	0.046	0.038	0.031	0.027	0.031	0.049	0.093	0.115	0.096	0.054
Flux										
Flux BeamFocus	0.002	0.001	0.001	0.001	0.003	0.005	0.006	0.005	0.003	0.003
Flux Tertiary	0.009	0.006	0.004	0.004	0.005	0.011	0.023	0.034	0.044	0.012
Flux NA49	0.001	0.000	0.000	0.001	0.002	0.003	0.003	0.004	0.010	0.002
Group Total	0.009	0.007	0.004	0.005	0.006	0.013	0.024	0.034	0.046	0.013
Michel Efficiency	0.002	0.002	0.002	0.002	0.002	0.002	0.002	0.002	0.002	0.002
Pion Reweight	0.002	0.001	0.001	0.000	0.001	0.002	0.003	0.003	0.005	0.002
Target Mass	0.014	0.014	0.014	0.014	0.014	0.013	0.013	0.012	0.013	0.013
Binding Energy	0.002	0.002	0.001	0.001	0.000	0.001	0.002	0.002	0.002	0.002
Group Total	0.014	0.014	0.014	0.014	0.014	0.014	0.014	0.013	0.014	0.014
Total Systematic	0.077	0.076	0.071	0.055	0.057	0.075	0.126	0.170	0.206	0.089
Statistical	0.028	0.018	0.013	0.010	0.010	0.014	0.029	0.047	0.096	0.021
Total	0.082	0.078	0.072	0.056	0.058	0.077	0.129	0.176	0.227	0.091

CHAPTER 7

Conclusions

7.1 Model Comparisons of the Differential Cross-sections

The differential cross-section $d\sigma/dQ^2_{QE-like}$ ($d\sigma/dQ^2_{QE}$) data has been compared to predictions using the Wroclaw Neutrino Event Generator (NuWro) [71], provided by J.Sobczyk. One significant difference between NuWro and GENIE is that NuWro has a simulation of the nucleus that includes MEC or spectral functions while GENIE does not includes these models.

NuWro simulates the QE process by the standard formalism of Llewellyn-Smith. Neutrino scattering in this model is described by the plane wave impulse approximation. Nuclear dynamics modeling in NuWro implements the Meson Exchange Currents (MEC) [71], Transverse Enhancement Model (TEM) [71], and Random Phase Approximation (RPA) [21]. In addition, NuWro also predicts the CCQE cross-section with $M_A = 1.35$ GeV, which was measured by MiniBooNE.

Various configurations of NuWro simulation are utilized in this study including:

- **NuWro Relativistic Fermi Gas (RFG), M_A=1.35 GeV**

- **NuWro RFG, M_A=0.99 GeV**
- **NuWro RFG, M_A=0.99 GeV + MEC**
- **NuWro RFG, M_A=0.99 GeV + TEM**
- **NuWro RFG, M_A=0.99 GeV + MEC + RPA**
- **NuWro RFG, M_A=0.99 GeV + TEM + RPA**
- **NuWro Spectral Functions, M_A=0.99 GeV** .

Two types of χ^2 are calculated to check the agreement between data and various predictions. The smaller the χ^2 is, the better agreement two distributions have. The calculation of the first χ^2 takes the correlation between entries in all bins into account. The second type of χ^2 is calculated using the central value and errors in each bin only and there is no consideration of the correlations between bins. Since the non-diagonal elements in the covariance matrix are not utilized in calculating the second type of χ^2, it is named as diagonal χ^2, donated as $D\chi^2$ in the plots.

Figure 7.1 shows a comparison of various NuWro predictions and GENIE simulation as well as he measured $d\sigma/dQ^2_{QElike}$ on CH in MINERνA for CCQE-like channel. The NuWro predictions were produced using the Gen2-thin + ν_e flux. The GENIE simulation was generated using Gen0 flux and reweighted event by event with $\frac{Gen2-thin+\nu_e flux}{Gen1 flux}$ for every 0.5 GeV neutrino energy bin, and then reweighted overall by $\frac{Gen1 flux}{Gen0 flux}$, which is 0.9501 for the neutrino energy region (0-20 GeV). I used the Monte Carlo simulation reweighted as above to analyze the data (1.38331×10^{19} POT) and extract the cross-section that was normalized by the Gen2-thin + ν_e flux. The integrated Gen2-thin + ν_e flux is $2.85887 \times 10^{-8}/cm^2/POT$ for 0-100 GeV and $2.80841 \times 10^{-8}/cm^2/POT$ for 0-20 GeV.

The comparison shows that the reweighted GENIE simulation under predicts neutrino events. Among all NuWro predictions, the prediction made by MEC and RPA model has the least χ^2 and agrees with data the best. NuWro prediction with TEM model also agrees with data very well. The NuWro prediction with TEM and RPA model is not as good as the one with TEM only, which indicates that the TEM and RPA model may double count the nuclear effect. Also notice that the good agreement between the GENIE prediction and the NuWro prediction using RFG model with $M_A = 0.99$. A short conclusion is that the χ^2 comparison indicates that the data distribution favors the prediction made by NuWro with a value of M_A of 0.99 GeV including MEC and RPA model for the CCQE-like analysis.

Data/GENIE/NuWro Comparisons for CCQE-like Channel

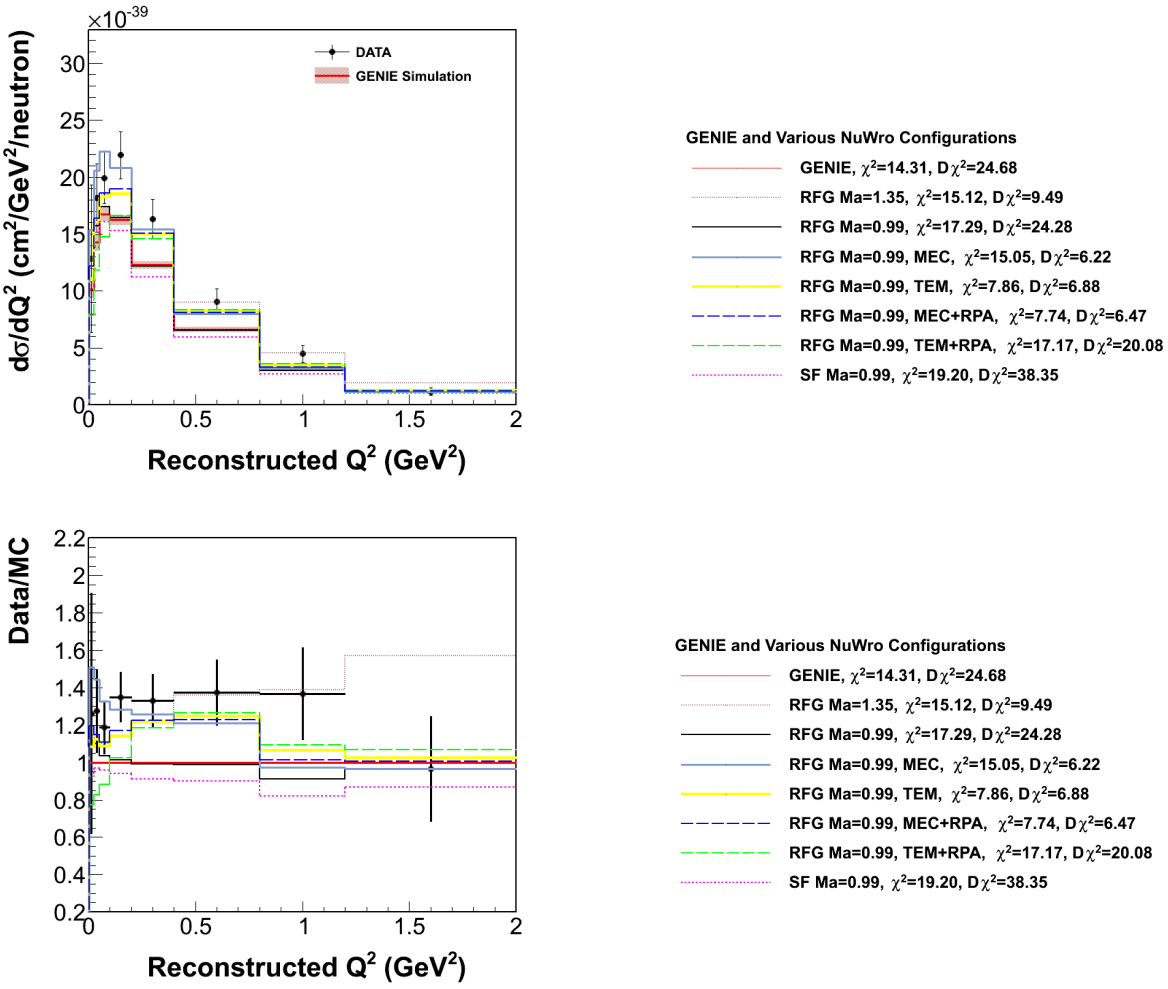

FIG. 7.1: A comparison of the CCQE like differential cross-section extracted in MINERνA on CH with various predictions made using the NuWro neutrino simulation (upper plot) and the ratios between cross-sections (lower plot).

TABLE 7.1: Gen2-thin plus ν_e constraint flux-integrated $d\sigma/dQ^2_{QE-like}$ summary. Both the statistical (first) and absolute systematic (second) errors are presented in each bin.

$Q^2_{QE-like}(\mathrm{GeV}^2)$	Cross Section ($10^{-38}\mathrm{cm}^2/\mathrm{GeV}^2$/nucleon)
0.0 - 0.025	$1.284 \pm 0.118 \pm 0.635$
0.025 - 0.05	$1.816 \pm 0.124 \pm 0.275$
0.05 - 0.1	$1.993 \pm 0.093 \pm 0.206$
0.1 - 0.2	$2.193 \pm 0.078 \pm 0.189$
0.2 - 0.4	$1.634 \pm 0.055 \pm 0.160$
0.4 - 0.8	$0.908 \pm 0.041 \pm 0.104$
0.8 - 1.2	$0.448 \pm 0.039 \pm 0.066$
1.2 - 2.0	$0.118 \pm 0.018 \pm 0.027$

A similar comparison has been made for CCQE analysis as well, shown in Fig. 7.2.

First of all, similar to the CCQE-like analysis, the distribution of reweighted GENIE simulation is lower than data. The GENIE prediction is lower than the NuWro prediction using $M_A = 0.99$ for CCQE channel while the previous comparison shows that the GENIE prediction agrees with the NuWro prediction using $M_A = 0.99$ for CCQE-like channel. This indicates difference in modeling the FSI between NuWro and GENIE. Same as the CCQE-like analysis, the NuWro prediction with the MEC model only is not as good as the one with the MEC and RPA models because the RPA model suppresses activities in the low Q^2 region. Also, the NuWro prediction using TEM and RPA models does not agrees with data as well as the NuWro prediction using TEM model only. Among all NuWro predictions, the one with the TEM model agrees with the data distribution best.

Data/GENIE/NuWro Comparisons for CCQE Channel

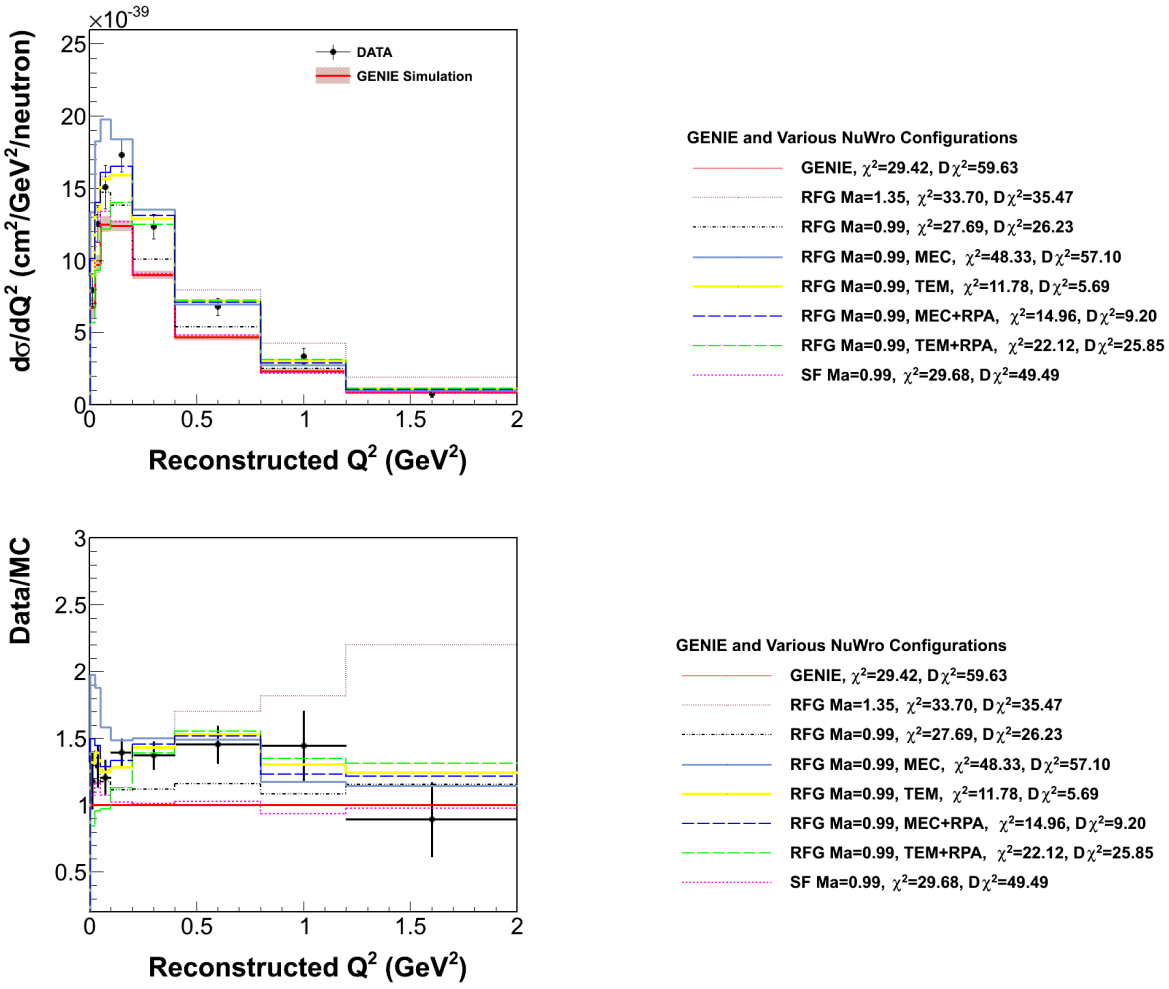

FIG. 7.2: A comparison of the CCQE differential cross-section extracted in MINERνA on CH with various predictions made using the NuWro neutrino simulation (upper plot) and the ratios between cross-sections (lower plot).

TABLE 7.2: Gen2-thin plus ν_e constraint flux-integrated $d\sigma/dQ^2_{QE}$ summary. Both the statistical (first) and absolute systematic (second) errors are presented in each bin.

Q^2_{QE}(GeV^2)	Cross Section (10^{-38}cm^2/GeV^2/nucleon)
0.0 - 0.025	0.796 ± 0.094 ± 0.066
0.025 - 0.05	1.254 ± 0.097 ± 0.081
0.05 - 0.1	1.510 ± 0.077 ± 0.130
0.1 - 0.2	1.729 ± 0.065 ± 0.095
0.2 - 0.4	1.237 ± 0.047 ± 0.070
0.4 - 0.8	0.680 ± 0.037 ± 0.046
0.8 - 1.2	0.338 ± 0.036 ± 0.042
1.2 - 2.0	0.077 ± 0.016 ± 0.016

7.2 Conclusions

The improved measurement of the neutrino mode charge current different cross-section $d\sigma/dQ^2_{QElike/QE}$ using data taken with the MINERνA detector in low neutrino energy mode (MINERνA playlist 1 and 13) has been presented. Results of four different analyses, CCQE/CCQE-like using old/new flux (Gen0/Gen2-thin), have been shown. The fact that the CCQE-like cross-section is slightly higher than the CCQE cross-section is as we expect. When doing the CCQE/CCQE-like analyses using the new flux, which predicts fewer events than the old flux, the cross-sections predicted by GENIE are lower than the ones from the actual data but agree with the ones predicted by GENIE using the old flux. This is also as we expect. In addition, comparisons of the measured results to various predictions made with GENIE and NuWro have been presented. For comparisons between the data and different NuWro configurations, the data distribution favors the NuWro prediction with $M_A = 0.99$ GeV including the MEC and RPA models for the CCQE-like channel. For the CCQE channel, the NuWro prediction with $M_A = 0.99$ GeV including the TEM model agrees with data the best.

The improvement on the measurement is exhibited in several ways. Michel vetoing is

implemented in both background template construction and the selection of signal events. More data files are included in this analysis (2.16×10^{20} POT) compared to the previous measurement (9.42×10^{19} POT). In addition, a wider range of neutrino energies has been analyzed. In order to fairly compare to the previous published results (CCQE), two intermedia stage analysis for the CCQE channel have been performed as well. The first analysis is to reduce the range of neutrino energy from 0-100 GeV to 1.5-10 GeV, which was used in the previous published analysis. The differential cross-section is measured to be 2.8% lower than my main CCQE analysis. Then the second analysis removes Michel veto from the first analysis, which shows the differential cross-section is 3.86% higher than that in the first analysis. The second analysis is an apple-to-apple comparison to the previous published analysis, since both of them measure the differential cross-section for neutrino with energy between 1.5-10 GeV and do not use Michel veto. The cross-section measured by the second analysis is 3.10% lower than the previous published result, which indicate they are comparable.

When estimating systematic errors, improvements to the procedure have been made and new systematic errors were introduced. For example, the previous procedure of estimating systematic errors in the group of muon reconstruction mis-calculated the lateral errors in the step of constructing the migration matrix. This mistake has been corrected. Another example is the estimation of systematic errors in the group of recoil energy. The previous method fails to take into account the events that fail the selection cuts in the universe of central values but pass the cuts in the universe of shifted values. The new systematic error, Michel veto, has also been added.

Similar analysis on this CCQE like channel are being performed on the data taken in the "medium energy" configuration of NuMI with an improved neutrino flux. Further study on the application of the `MichelTool` is encouraged. For example, using the `MichelTool` to categorize the low energy pion production is an interesting topic.

APPENDIX A

Additional Plots in the CCQE Analysis

This appendix presents the extraction of cross section for CCQE channel as well as the systematic estimation. Similar steps are taken as ones described in the main context, including background subtraction, unfolding, efficiency correction, and normalization. The first section shows the distribution of Q^2 in each step of the cross-section calculation. The values of the cross-section in each Q^2 bin as well as statistical errors and estimated systematic errors are listed at the end of the first section. The second section shows the estimation of systematic errors. Distributions of errors are shown for each systematic group. In addition, the systematic errors tables are presented at each stage.

A.1 Cross-section Extraction

The calculation begins with the distribution of Q^2 of selected events, shown in Fig. A.1.

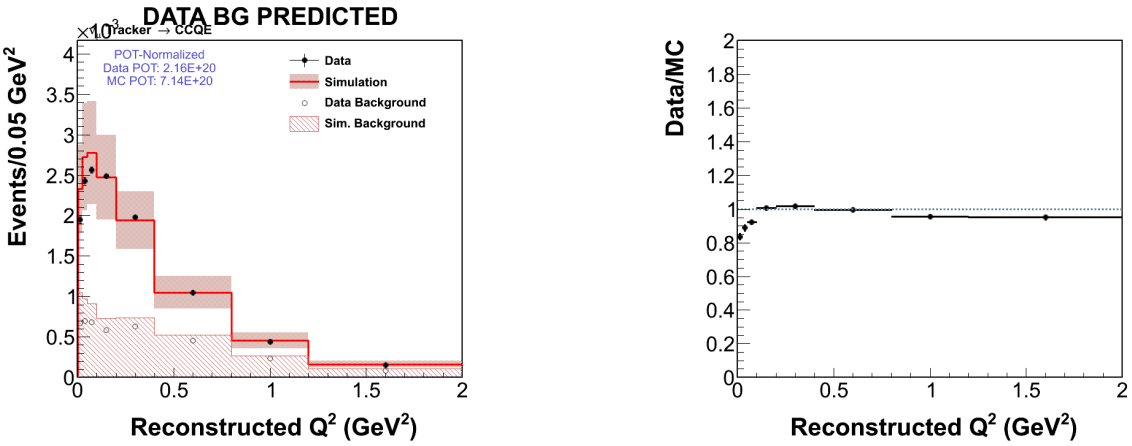

FIG. A.1: Left: Q^2 distribution for selected CCQE candidates in data and simulation, with predicted background events in shaded area. Right: ratio plot of Q^2 distribution

A.1.1 Background Subtraction

Recoil distributions in all Q^2 bins are used to measure scale factors of data and simulation. Thus, the background events in data are estimated. Fig. A.2 and Fig. A.3 are before fitting. Fig. A.4 and Fig. A.5 are after fitting.

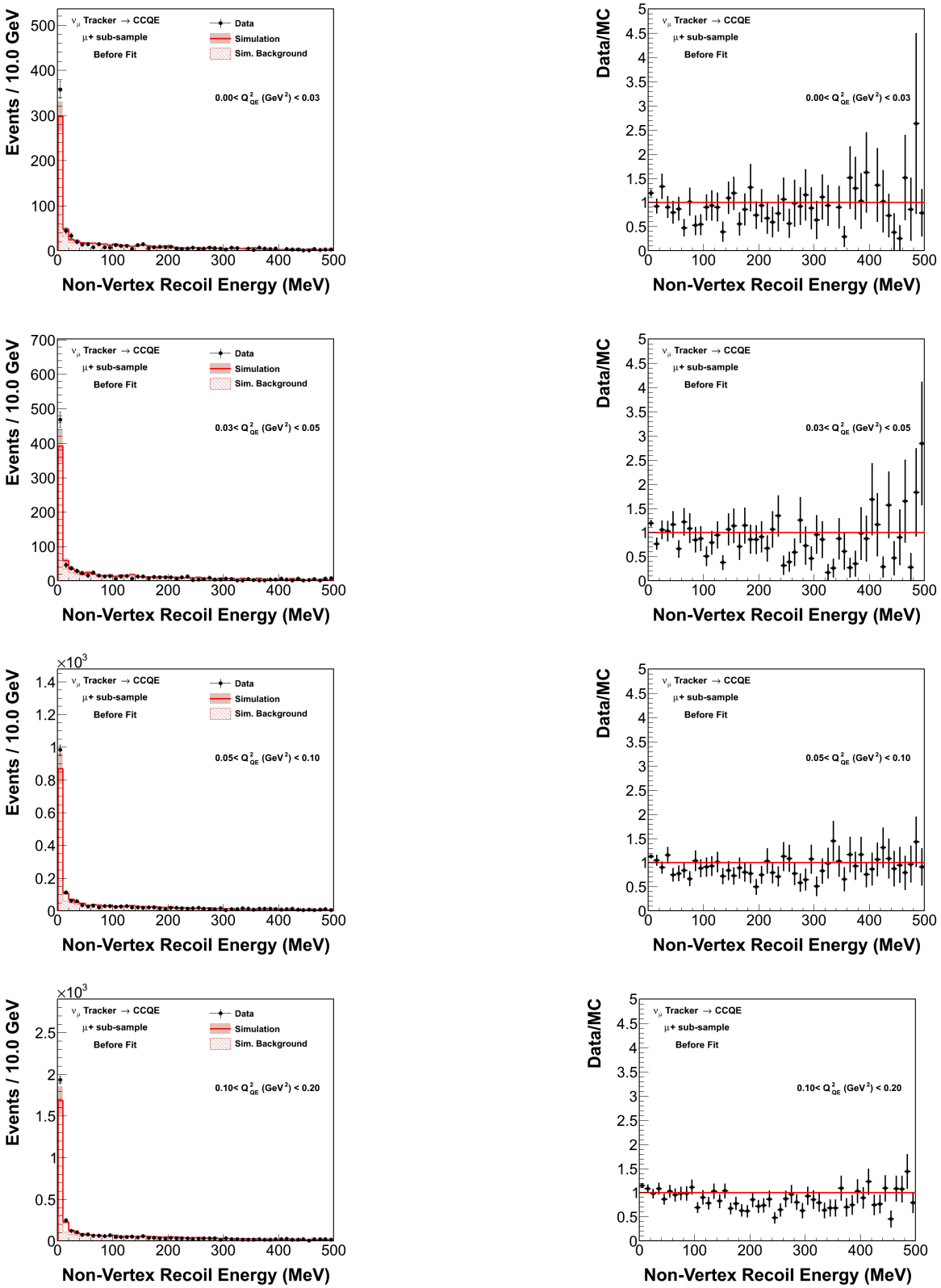

FIG. A.2: Area normalized data/MC overlays and ratios for the first four of eight Q^2 bins of recoil energy before the template fit. From top to bottom, the plots are for bin 1, bin 2, bin 3, and bin 4, respectively. The right plots are the ratio distributions between data and Monte Carlo.

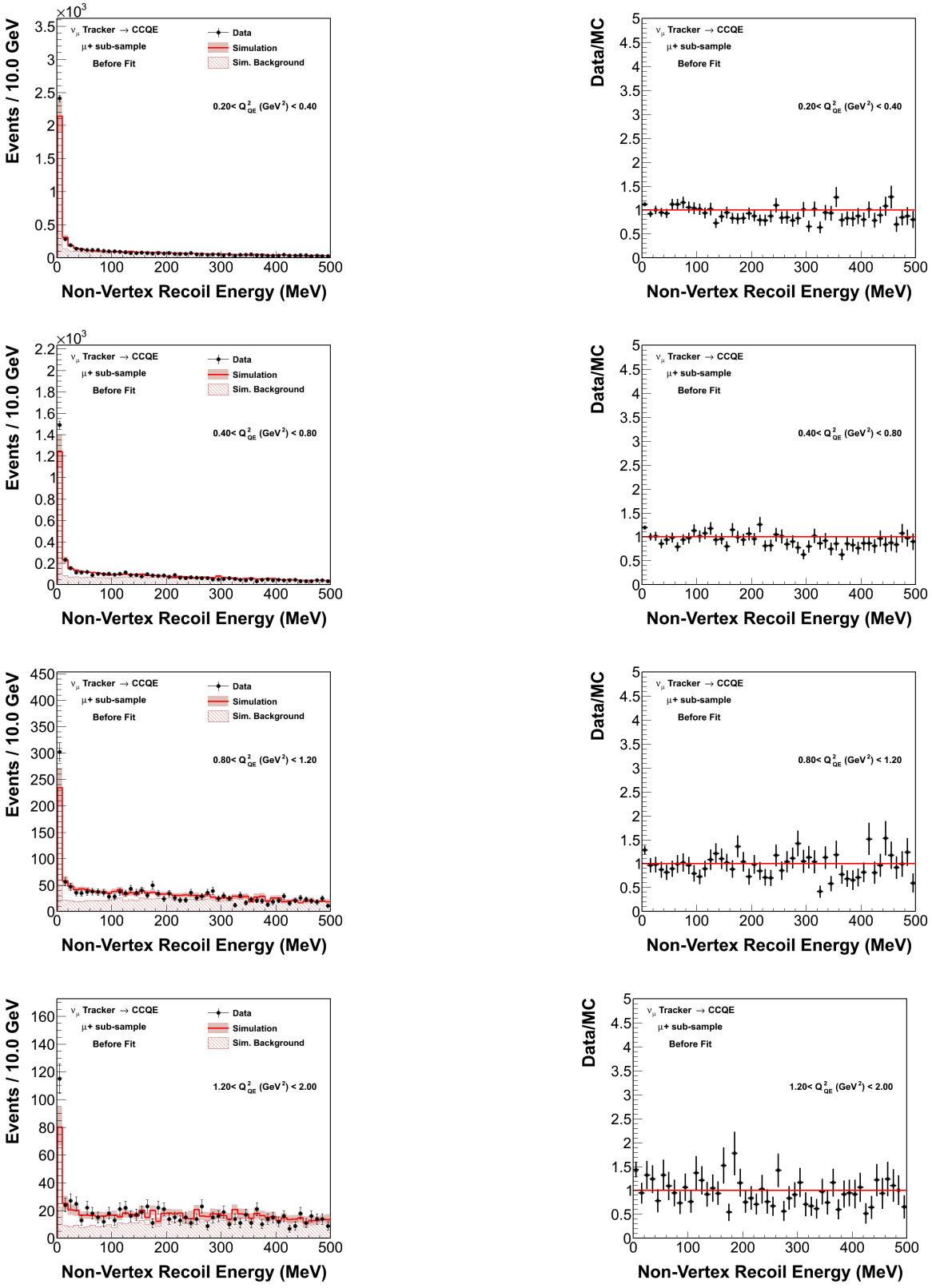

FIG. A.3: Area normalized data/MC overlays and ratios for the first four of eight Q^2 bins of recoil energy before the template fit. From top to bottom, the plots are for bin 5, bin 6, bin 7, and bin 8, respectively. The right plots are the ratio distributions between data and Monte Carlo.

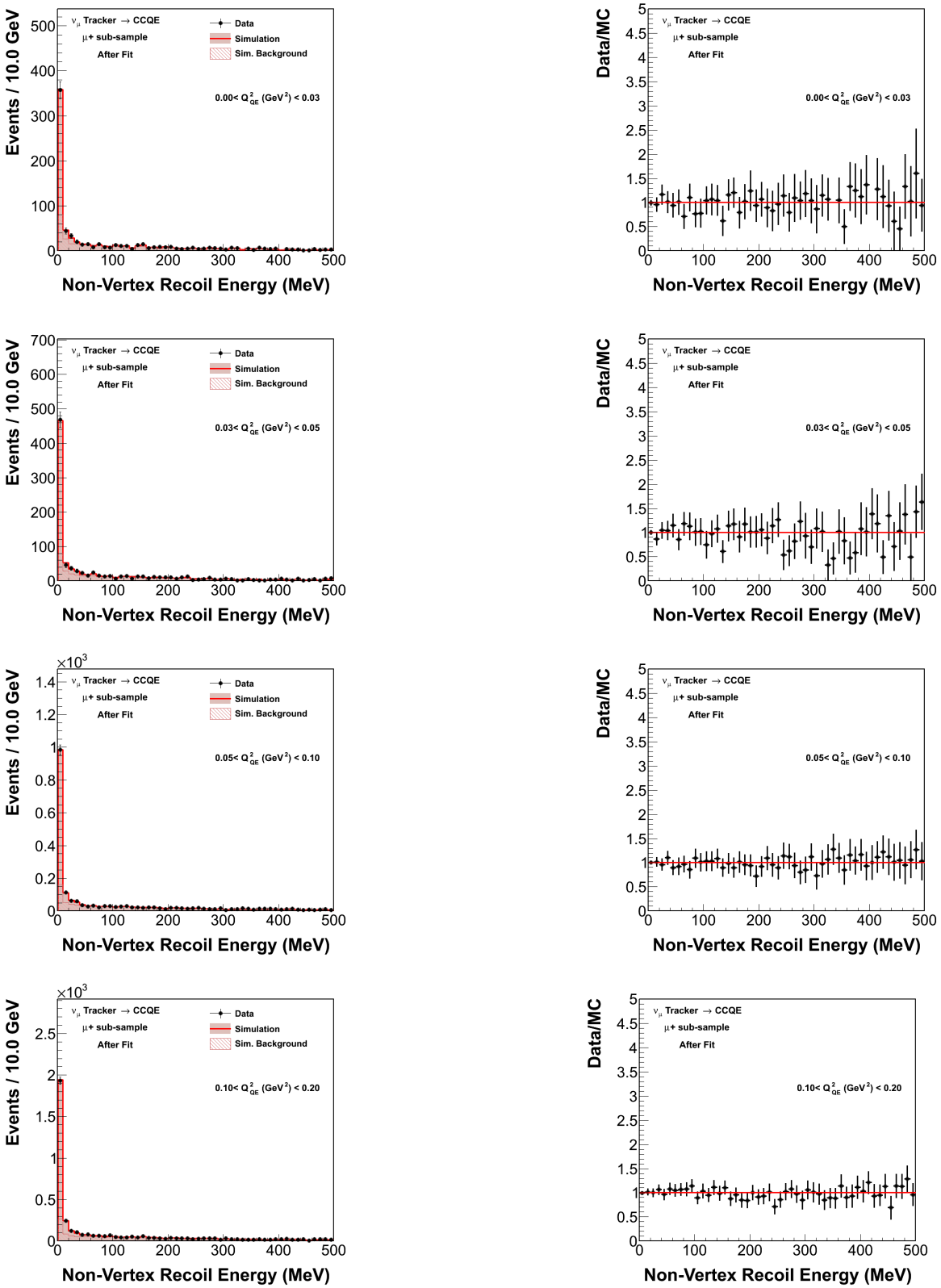

FIG. A.4: Area normalized data/MC overlays and ratios for the first four of eight Q^2 bins of recoil energy after the template fit. From top to bottom, the plots are for bin 1, bin 2, bin 3, and bin 4, respectively. The right plots are the ratio distributions between data and Monte Carlo.

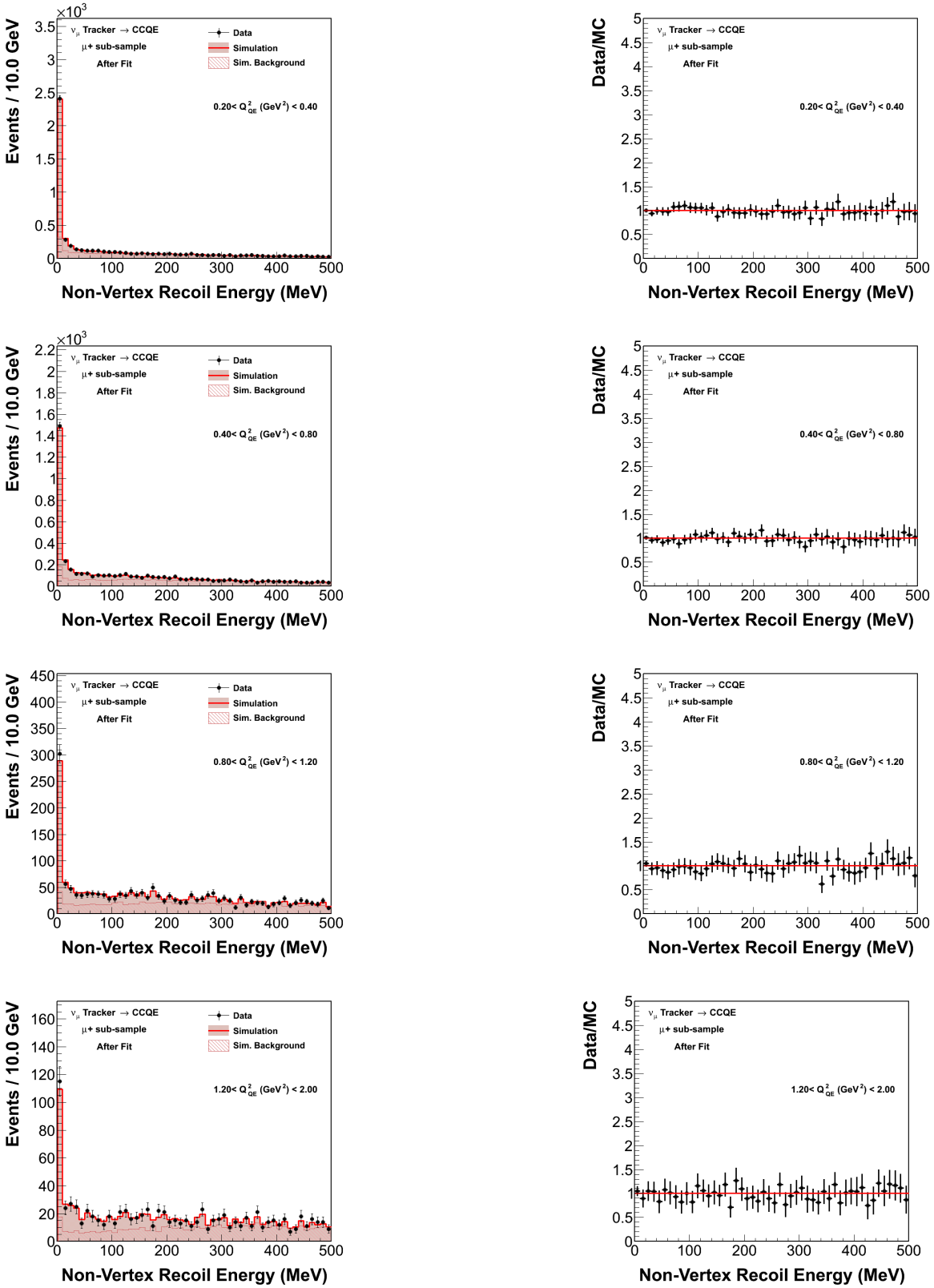

FIG. A.5: Area normalized data/MC overlays and ratios for the first four of eight Q^2 bins of recoil energy after the template fit. From top to bottom, the plots are for bin 5, bin 6, bin 7, and bin 8, respectively. The right plots are the ratio distributions between data and Monte Carlo.

The fitting procedure outcomes the best agreement between data and the simulation by assigning a scale factor to each Q^2 bin. The distribution of weights is in Fig A.6.

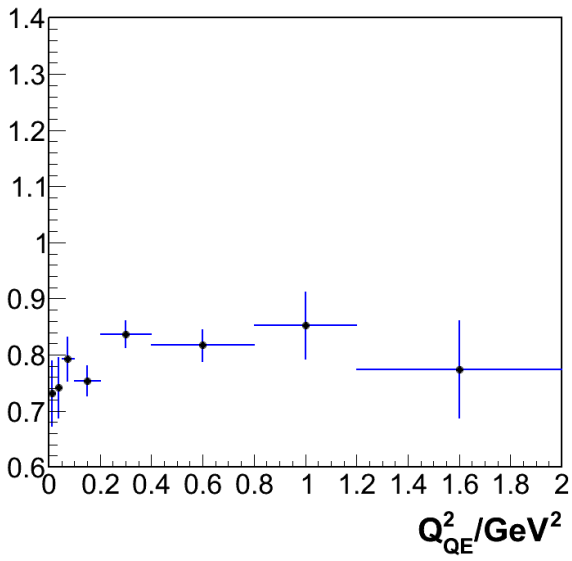

FIG. A.6: The fit results in each Q^2 bin, the same binning as Q^2.

After subtracting the estimated background, the Q^2 distribution of the selected sample is shown in Fig. A.7.

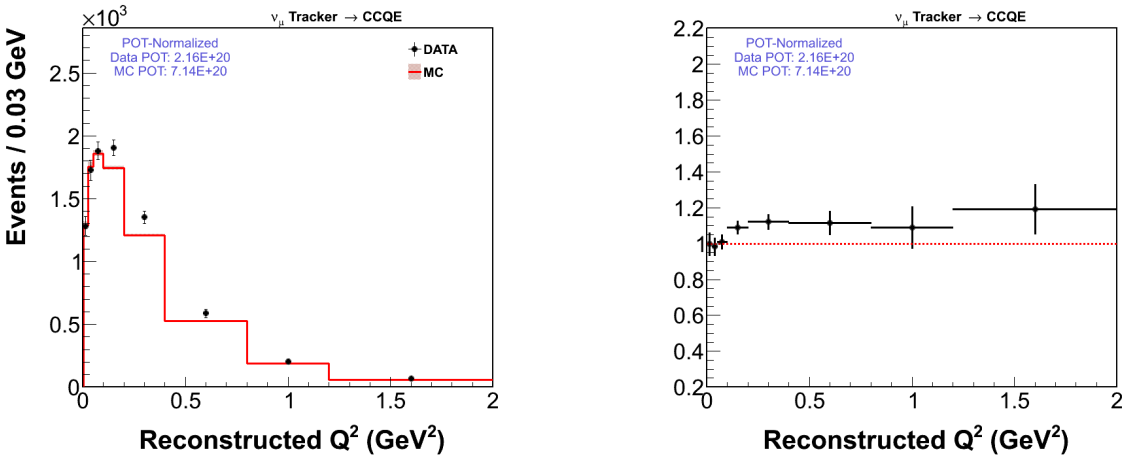

FIG. A.7: The left plot is Q^2 distribution for CCQE-like candidates after subtracting estimating background in data and simulation. The right plot is the ratio plot.

A.1.2 Bin Migration and Unfolding

Migration matrix is shown in Fig.A.8 and the distribution of Q^2 after unfolding is shown in Fig. A.9.

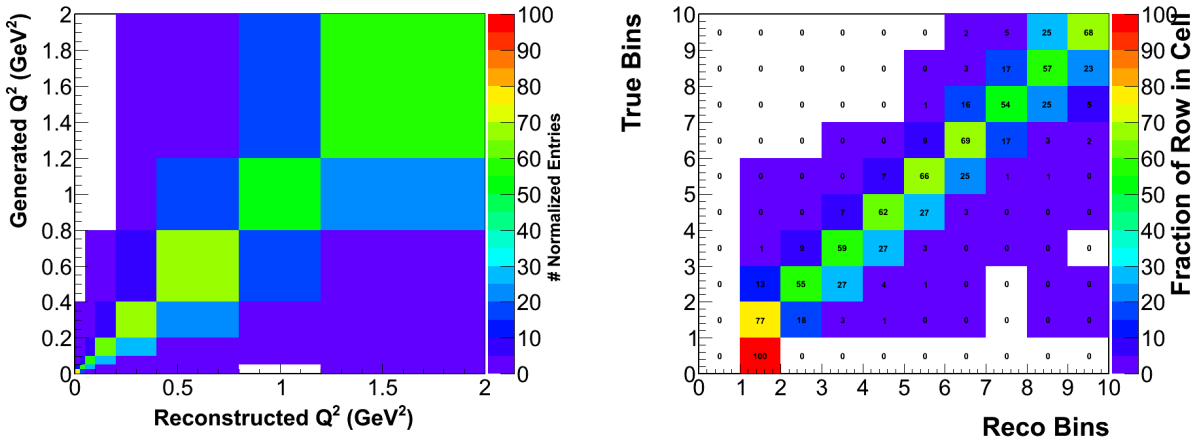

FIG. A.8: migration matrix

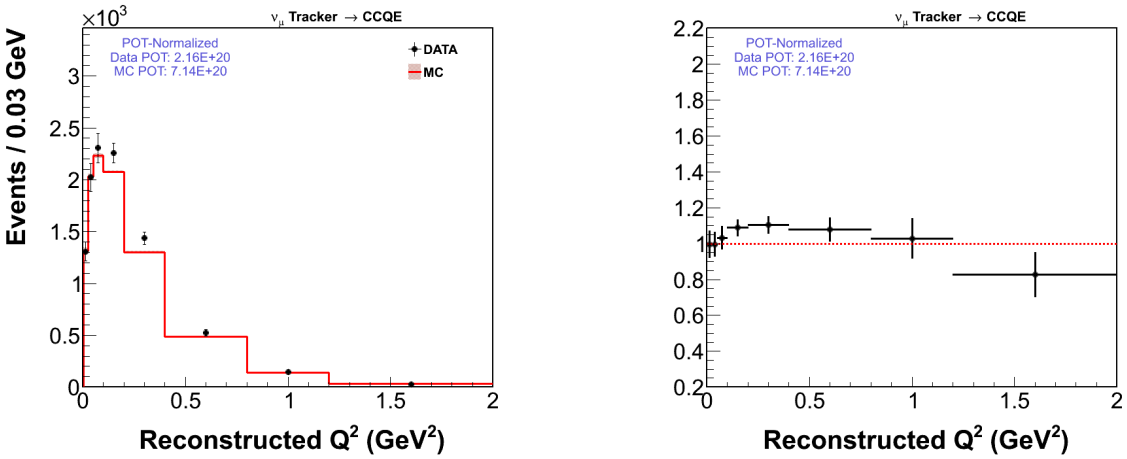

FIG. A.9: The left plot is Q^2 distribution for CCQE candidates after unfolding in data and simulation. The right plot is the ratio plot.

A.1.3 Efficiency and Acceptance Corrections

The plot of efficiency as a function of Q^2 is shown in Fig. A.10 and the Q^2 distribution after efficiency correction is shown in Fig. A.11.

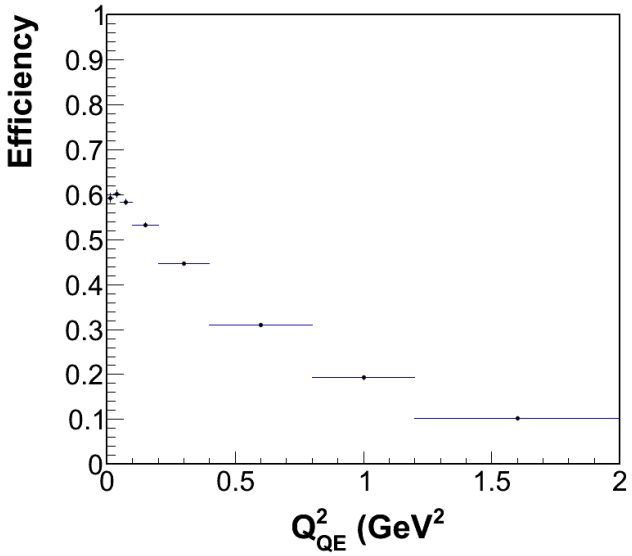

FIG. A.10: distribution of efficiency to reconstruct CCQE candidates as a function of Q^2

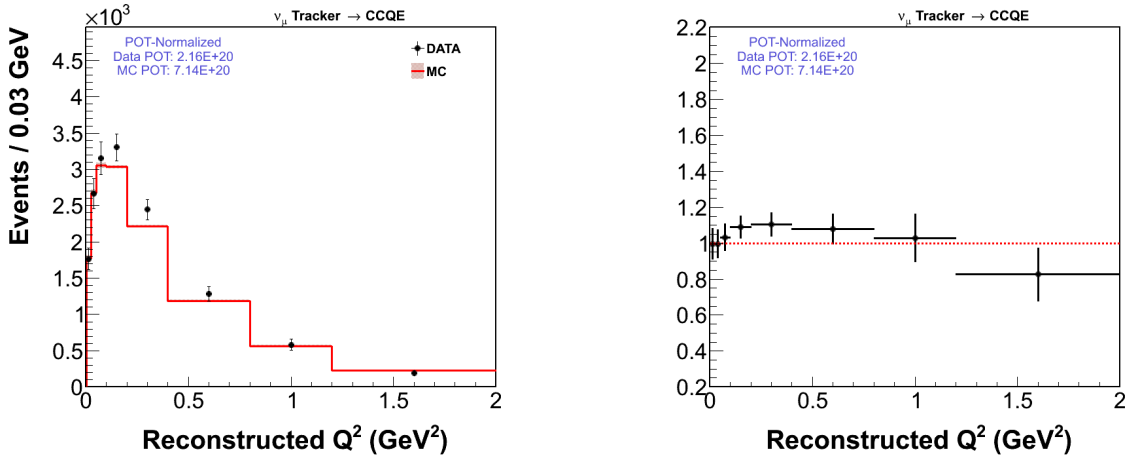

FIG. A.11: The left plot is Q^2 distribution for CCQE candidates after efficiency correction in data and simulation. The right plot is the ratio plot.

A.2 Systematic Estimation

A.2.1 Summary of Total Errors

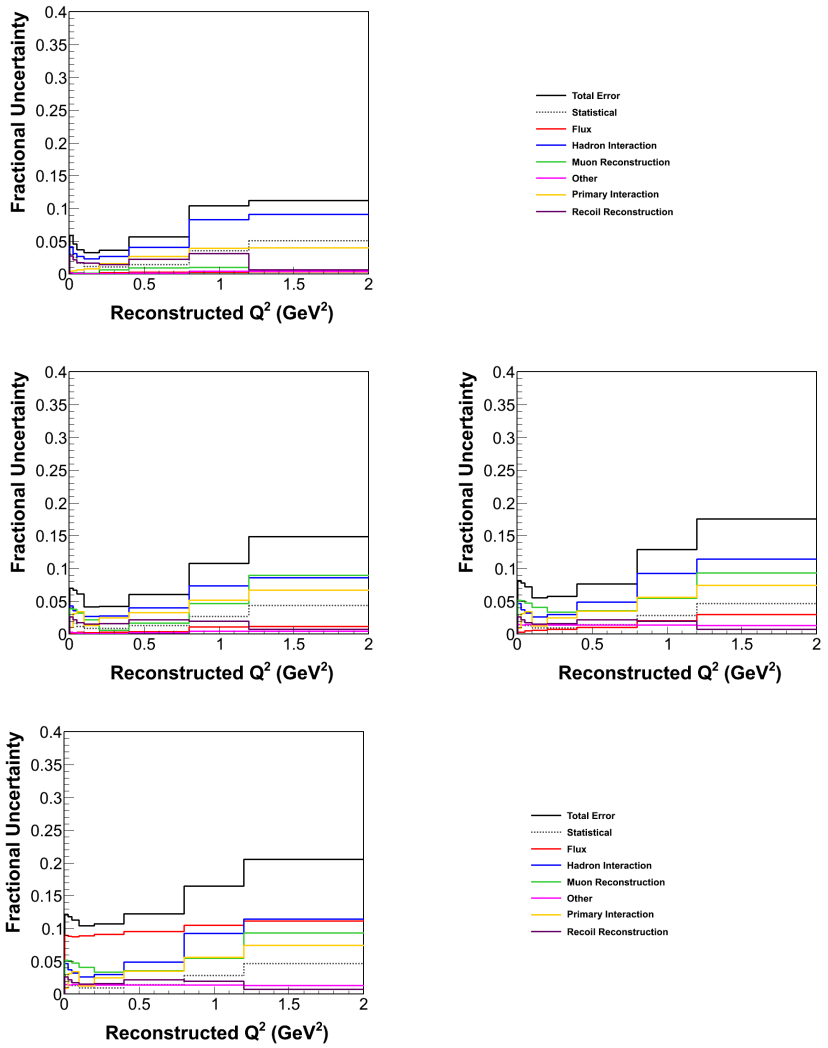

FIG. A.12: Total systematic errors for the neutrino mode CCQE one track analysis, with unstacked contributions from all six groups. Upper left: background subtraction stage. Upper right: unfolding stage. Lower left: efficiency correction stage. Lower right: final stage, all systematic errors on the double differential cross section.

A.2.2 Group of Flux

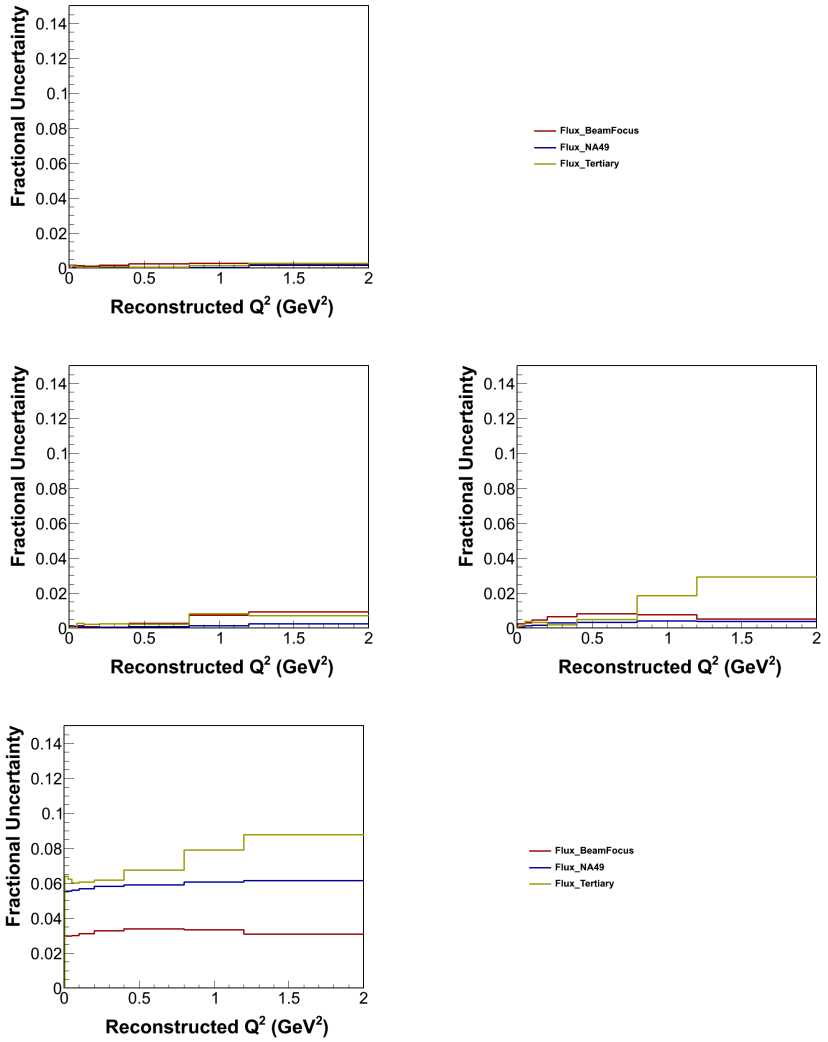

FIG. A.13: Systematic errors in **Group Flux** for the neutrino mode CCQE one track analysis. Upper left: background subtraction stage. Upper right: unfolding stage. Lower left: efficiency correction stage. Lower right: final stage, systematic errors in **Group Flux** on the double differential cross section.

A.2.3 Group of Primary Interaction

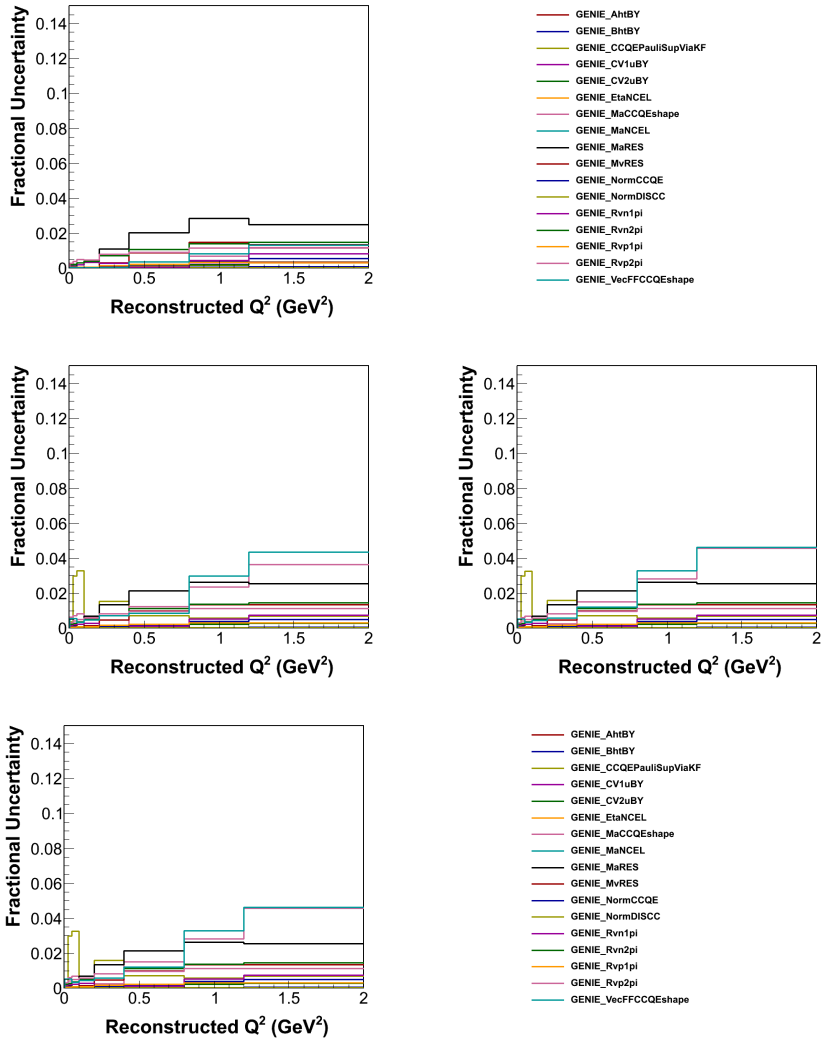

FIG. A.14: Systematic errors in **Group Primary Interaction** for the neutrino mode CCQE one track analysis. Upper left: background subtraction stage. Upper right: unfolding stage. Lower left: efficiency correction stage. Lower right: final stage, systematic errors in **Group Primary Interaction** on the double differential cross section.

A.2.4 Group of Hadron Interaction

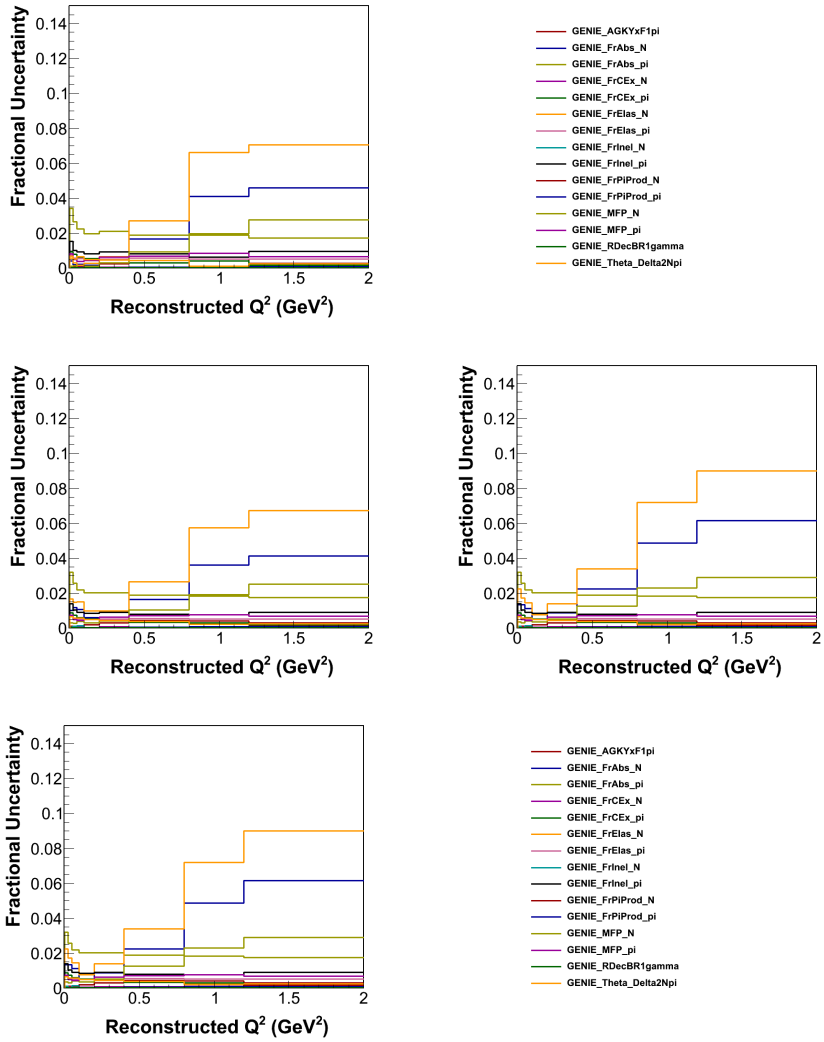

FIG. A.15: Systematic errors in **Group Hadron Interactions** for the neutrino mode CCQE one track analysis. Upper left: background subtraction stage. Upper right: unfolding stage. Lower left: efficiency correction stage. Lower right: final stage, systematic errors in **Group Hadron Interactions** on the double differential cross section.

A.2.5 Group of Muon Reconstruction

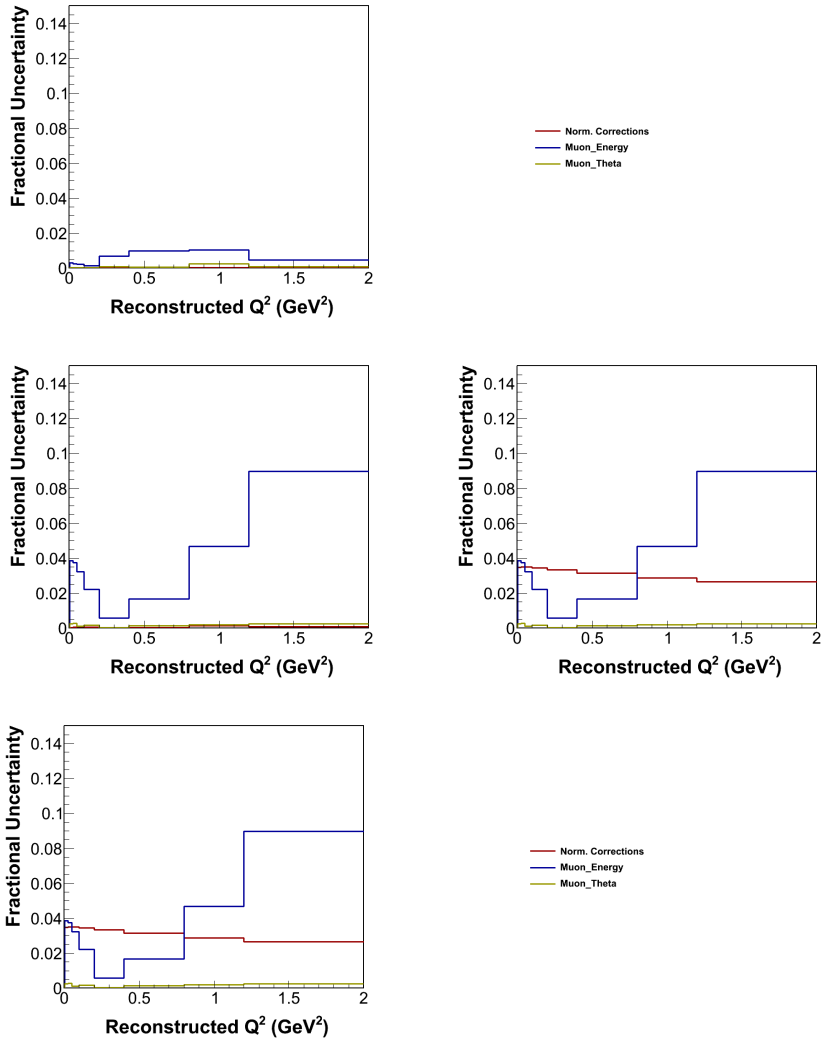

FIG. A.16: Systematic errors in **Group Muon Reconstruction** for the neutrino mode CCQE one track analysis. Upper left: background subtraction stage. Upper right: unfolding stage. Lower left: efficiency correction stage. Lower right: final stage, systematic errors in **Group Muon Reconstruction** on the double differential cross section.

A.2.6 Group of Recoil Reconstruction

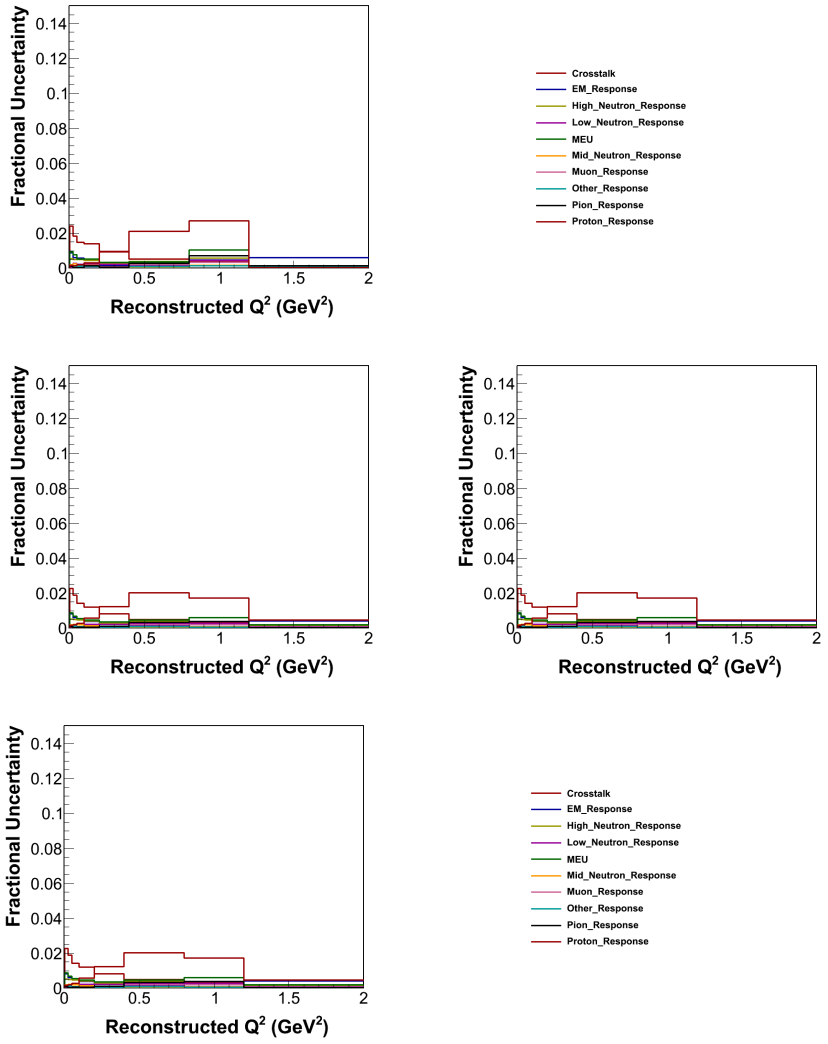

FIG. A.17: Systematic errors in **Group Recoil Reconstruction** for the neutrino mode CCQE one track analysis. Upper left: background subtraction stage. Upper right: unfolding stage. Lower left: efficiency correction stage. Lower right: final stage, systematic errors in **Group Recoil Reconstruction** on the double differential cross section.

A.2.7 Group of Other Errors

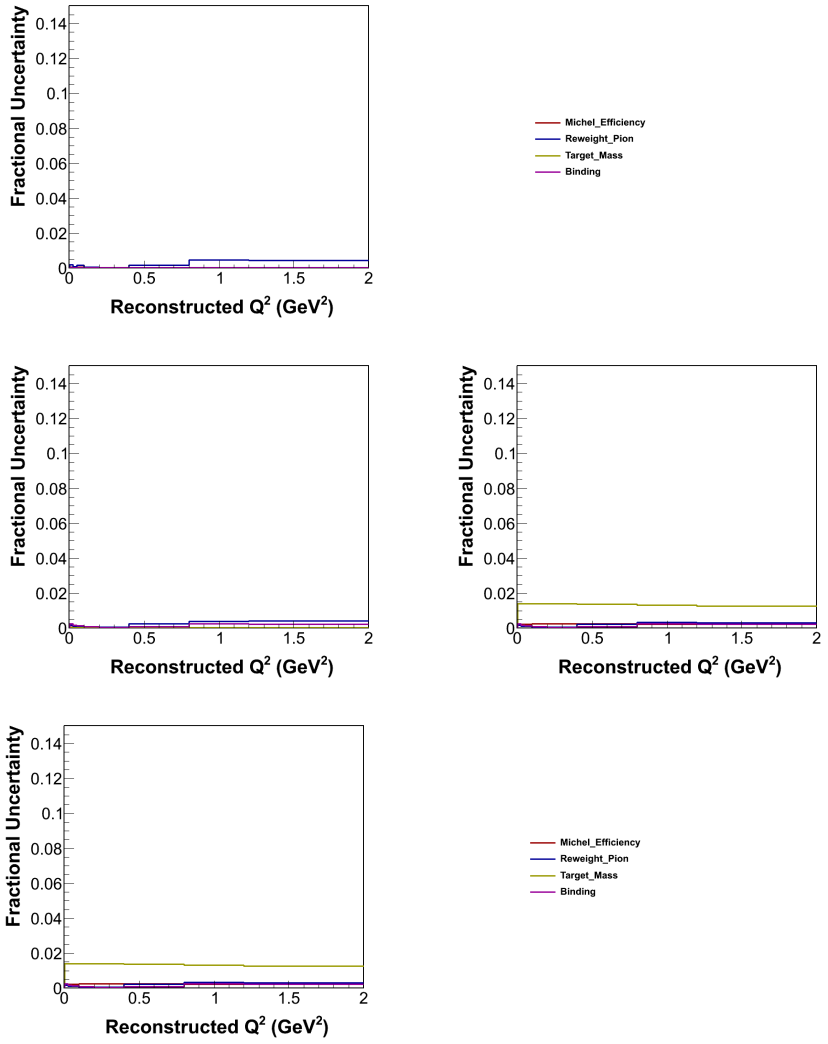

FIG. A.18: Systematic errors in **Group Other** for the neutrino mode CCQE one track analysis. Upper left: background subtraction stage. Upper right: unfolding stage. Lower left: efficiency correction stage. Lower right: final stage, systematic errors in **Group Other** on the double differential cross section.

A.2.8 Systematic Errors Tables

Table A.1 is the correlation table.

TABLE A.1: Total fractional systematic errors on the ν differential cross-sections and their correlation matrix

$Q^2_{QELike}(GeV^2)$	[0,0.025)	[0.025,0.05)	[0.05,0.1)	[0.1,0.2)	[0.2,0.4)	[0.4,0.8)	[0.8,1.2)	[1.2,2.0)	[2.0,∞)
σ_{sys}	0.12	0.12	0.12	0.11	0.11	0.12	0.16	0.21	0.26
$[0, 0.025)$	1.00	0.96	0.94	0.96	0.93	0.82	0.59	0.43	0.29
$[0.025, 0.05)$		1.00	0.99	0.97	0.90	0.79	0.55	0.37	0.25
$[0.05, 0.1)$			1.00	0.96	0.88	0.78	0.55	0.37	0.25
$[0.1, 0.2)$				1.00	0.97	0.86	0.61	0.43	0.34
$[0.2, 0.4)$					1.00	0.93	0.71	0.54	0.48
$[0.4, 0.8)$						1.00	0.91	0.79	0.73
$[0.8, 1.2)$							1.00	0.97	0.90
$[1.2, 2.0)$								1.00	0.94
$[2.0, \infty)$									1.00

Systematic errors summary tables are shown in the following part for each stage.

TABLE A.2: ν fractional systematic uncertainties on $d\sigma/dQ^2_{QE}$, background subtraction.

$Q^2_{QELike}(GeV^2)$	[0,0.025)	[0.025,0.05)	[0.05,0.1)	[0.1,0.2)	[0.2,0.4)	[0.4,0.8)	[0.8,1.2)	[1.2,2.0)	[2.0,∞)	total
Muon Reconstruction										
Muon Energy	0.003	0.003	0.003	0.000	0.005	0.010	0.007	0.005	0.000	0.005
Muon Theta	0.003	0.000	0.005	0.002	0.000	0.001	0.000	0.002	0.000	0.002
Norm.Correction	0.000	0.000	0.000	0.000	0.000	0.000	0.001	0.002	0.000	0.002
Group Total	0.004	0.003	0.005	0.002	0.005	0.010	0.007	0.006	0.000	0.005
Recoil Reconstruction										
CrossTalk	0.021	0.015	0.010	0.013	0.009	0.007	0.010	0.000	0.000	0.011
EM Response	0.009	0.005	0.006	0.005	0.002	0.002	0.003	0.006	0.000	0.005
High Neutron Response	0.006	0.004	0.003	0.003	0.003	0.003	0.012	0.001	0.000	0.004
Mid Neutron Response	0.000	0.003	0.002	0.002	0.001	0.000	0.005	0.000	0.000	0.002
Low Neutron Response	0.002	0.002	0.002	0.002	0.001	0.002	0.003	0.000	0.000	0.002
MEU	0.006	0.008	0.005	0.004	0.003	0.004	0.020	0.000	0.000	0.006
Muon Response	0.000	0.001	0.000	0.001	0.001	0.001	0.003	0.000	0.000	0.001
Other Response	0.001	0.001	0.001	0.001	0.001	0.000	0.000	0.001	0.000	0.001
Pion Response	0.007	0.000	0.001	0.002	0.001	0.001	0.006	0.002	0.000	0.002
Proton Response	0.002	0.001	0.001	0.003	0.009	0.016	0.025	0.000	0.000	0.007
Group Total	0.025	0.019	0.013	0.015	0.014	0.018	0.037	0.007	0.000	0.018
Primary Interaction Models										
AhtBY	0.000	0.000	0.000	0.000	0.000	0.000	0.002	0.003	0.000	0.001
BhtBY	0.000	0.000	0.000	0.000	0.000	0.001	0.003	0.005	0.000	0.001
CCQEPauliSupViaKF	0.012	0.011	0.009	0.004	0.002	0.001	0.000	0.001	0.000	0.005
CV1uBY	0.000	0.000	0.000	0.000	0.000	0.000	0.002	0.003	0.000	0.001
CV2uBY	0.000	0.000	0.000	0.000	0.000	0.000	0.002	0.003	0.000	0.001
EtaNCEL	0.000	0.000	0.000	0.000	0.000	0.000	0.000	0.000	0.000	0.000
MaCCQEshape	0.006	0.005	0.004	0.002	0.002	0.003	0.002	0.000	0.000	0.003
MaNCEL	0.000	0.000	0.000	0.000	0.000	0.000	0.000	0.000	0.000	0.000
MaRES	0.002	0.002	0.003	0.001	0.002	0.004	0.002	0.014	0.000	0.004
MvRES	0.000	0.001	0.002	0.002	0.001	0.001	0.001	0.007	0.000	0.002
NormCCQE	0.010	0.009	0.009	0.007	0.007	0.008	0.015	0.022	0.000	0.011
NormDISCC	0.000	0.000	0.000	0.000	0.000	0.000	0.000	0.000	0.000	0.000
Rvn1pi	0.002	0.002	0.004	0.006	0.007	0.009	0.002	0.005	0.000	0.005
Rvn2pi	0.002	0.002	0.003	0.004	0.006	0.007	0.015	0.010	0.000	0.006
Rvp1pi	0.001	0.000	0.000	0.000	0.002	0.003	0.002	0.004	0.000	0.001
Rvp2pi	0.002	0.003	0.004	0.004	0.006	0.006	0.008	0.009	0.000	0.005
VecffCCQEshape	0.001	0.000	0.001	0.001	0.002	0.004	0.004	0.002	0.000	0.002
Group Total	0.017	0.016	0.015	0.012	0.014	0.016	0.024	0.032	0.000	0.018
Final State Interactions										
AGKYxF1pi	0.002	0.002	0.001	0.002	0.001	0.003	0.003	0.004	0.000	0.002
FrAbs N	0.002	0.002	0.002	0.001	0.004	0.014	0.039	0.047	0.000	0.014
FrAbs π	0.023	0.024	0.022	0.019	0.027	0.031	0.039	0.035	0.000	0.028
FrCEx N	0.002	0.000	0.001	0.000	0.001	0.001	0.001	0.001	0.000	0.001
FrCEx π	0.008	0.003	0.005	0.004	0.002	0.000	0.001	0.004	0.000	0.004
FrElas N	0.004	0.006	0.001	0.000	0.005	0.023	0.071	0.079	0.000	0.024
FrElas π	0.001	0.000	0.000	0.000	0.001	0.001	0.002	0.003	0.000	0.001
FrInel N	0.001	0.000	0.000	0.000	0.000	0.000	0.000	0.000	0.000	0.000
FrInel π	0.040	0.036	0.036	0.030	0.036	0.037	0.046	0.032	0.000	0.037
FrPiProd N	0.000	0.000	0.000	0.000	0.000	0.001	0.003	0.003	0.000	0.001
FrPiProd π	0.001	0.000	0.000	0.000	0.000	0.000	0.000	0.001	0.000	0.000
Mean Free Path N	0.001	0.001	0.001	0.001	0.002	0.010	0.022	0.034	0.000	0.009
Mean Free Path π	0.003	0.001	0.003	0.001	0.004	0.005	0.006	0.004	0.000	0.003
RDecBR1gamma	0.000	0.000	0.000	0.000	0.000	0.000	0.000	0.000	0.000	0.000
Theta Delta 2Nπ	0.005	0.006	0.008	0.004	0.003	0.003	0.004	0.000	0.000	0.004
Group Total	0.048	0.044	0.044	0.036	0.046	0.056	0.104	0.110	0.000	0.061
Flux										
Flux BeamFocus	0.001	0.002	0.002	0.002	0.002	0.002	0.003	0.004	0.000	0.002
Flux Tertiary	0.004	0.001	0.002	0.001	0.001	0.002	0.009	0.015	0.000	0.004
Flux NA49	0.002	0.001	0.000	0.000	0.000	0.001	0.002	0.001	0.000	0.001
Group Total	0.004	0.003	0.003	0.002	0.002	0.003	0.010	0.016	0.000	0.005
Michel Efficiency	0.002	0.002	0.002	0.002	0.002	0.002	0.002	0.001	0.000	0.002
Pion Reweight	0.003	0.003	0.003	0.003	0.003	0.005	0.007	0.008	0.000	0.005
Target Mass	0.000	0.000	0.000	0.000	0.000	0.000	0.000	0.000	0.000	0.000
Binding Energy	0.000	0.000	0.000	0.000	0.000	0.000	0.001	0.000	0.000	0.000
Group Total	0.004	0.003	0.004	0.004	0.004	0.005	0.008	0.008	0.000	0.005
Total Systematic	0.057	0.051	0.049	0.041	0.051	0.062	0.113	0.116	0.000	0.068
Statistical	0.070	0.062	0.043	0.029	0.026	0.031	0.072	0.111	0.000	0.055
Total	0.091	0.080	0.065	0.050	0.057	0.070	0.134	0.160	0.000	0.088

TABLE A.3: ν fractional systematic uncertainties on $d\sigma/dQ^2_{QE}$, unfolding.

$Q^2_{QELike}(GeV^2)$	[0,0.025)	[0.025,0.05)	[0.05,0.1)	[0.1,0.2)	[0.2,0.4)	[0.4,0.8)	[0.8,1.2)	[1.2,2.0)	[2.0,∞)	total
Muon Reconstruction										
Muon Energy	0.040	0.044	0.040	0.023	0.006	0.022	0.061	0.104	0.164	0.043
Muon Theta	0.008	0.001	0.004	0.001	0.000	0.002	0.005	0.003	0.029	0.003
Norm.Correction	0.000	0.000	0.000	0.000	0.000	0.000	0.000	0.001	0.001	0.003
Group Total	0.040	0.044	0.041	0.023	0.007	0.022	0.061	0.104	0.167	0.043
Recoil Reconstruction										
CrossTalk	0.021	0.014	0.012	0.011	0.009	0.007	0.006	0.003	0.001	0.010
EM Response	0.008	0.006	0.005	0.004	0.001	0.001	0.000	0.004	0.005	0.004
High Neutron Response	0.006	0.004	0.003	0.003	0.003	0.005	0.007	0.003	0.003	0.004
Mid Neutron Response	0.001	0.002	0.002	0.002	0.001	0.001	0.003	0.001	0.001	0.001
Low Neutron Response	0.002	0.002	0.002	0.002	0.001	0.002	0.002	0.001	0.000	0.002
MEU	0.006	0.007	0.005	0.004	0.004	0.006	0.012	0.004	0.003	0.006
Muon Response	0.000	0.000	0.000	0.001	0.001	0.002	0.002	0.001	0.000	0.001
Other Response	0.001	0.001	0.001	0.001	0.000	0.000	0.000	0.001	0.001	0.001
Pion Response	0.006	0.001	0.001	0.001	0.001	0.001	0.003	0.000	0.001	0.002
Proton Response	0.002	0.001	0.002	0.005	0.010	0.016	0.016	0.005	0.004	0.007
Group Total	0.025	0.017	0.015	0.014	0.015	0.020	0.023	0.009	0.008	0.017
Primary Interaction Models										
AhtBY	0.000	0.000	0.000	0.000	0.000	0.001	0.002	0.003	0.003	0.001
BhtBY	0.000	0.000	0.000	0.000	0.000	0.001	0.003	0.005	0.005	0.001
CCQEPauliSupViaKF	0.013	0.013	0.022	0.003	0.015	0.005	0.002	0.002	0.002	0.009
CV1uBY	0.000	0.000	0.000	0.000	0.000	0.001	0.002	0.003	0.003	0.001
CV2uBY	0.000	0.000	0.000	0.000	0.000	0.001	0.002	0.003	0.003	0.001
EtaNCEL	0.000	0.000	0.000	0.000	0.000	0.000	0.000	0.000	0.000	0.000
MaCCQEshape	0.002	0.000	0.004	0.003	0.002	0.009	0.012	0.021	0.042	0.007
MaNCEL	0.000	0.000	0.000	0.000	0.000	0.000	0.000	0.000	0.000	0.000
MaRES	0.002	0.002	0.002	0.000	0.002	0.002	0.005	0.012	0.012	0.003
MvRES	0.001	0.001	0.002	0.001	0.000	0.000	0.003	0.005	0.005	0.002
NormCCQE	0.010	0.009	0.008	0.007	0.008	0.010	0.016	0.020	0.020	0.011
NormDISCC	0.000	0.000	0.000	0.000	0.000	0.000	0.000	0.000	0.000	0.000
Rvn1pi	0.002	0.003	0.005	0.006	0.008	0.007	0.004	0.005	0.005	0.005
Rvn2pi	0.002	0.002	0.003	0.005	0.006	0.008	0.012	0.011	0.011	0.006
Rvp1pi	0.001	0.000	0.000	0.000	0.002	0.003	0.003	0.003	0.004	0.001
Rvp2pi	0.002	0.004	0.004	0.005	0.006	0.006	0.008	0.009	0.008	0.006
VecffCCQEshape	0.003	0.005	0.005	0.003	0.005	0.007	0.019	0.028	0.029	0.009
Group Total	0.017	0.017	0.026	0.013	0.021	0.021	0.033	0.045	0.059	0.024
Final State Interactions										
AGKYxF1pi	0.002	0.002	0.002	0.002	0.002	0.003	0.004	0.004	0.004	0.002
FrAbs N	0.008	0.008	0.009	0.006	0.003	0.014	0.034	0.053	0.047	0.017
FrAbs π	0.023	0.023	0.022	0.022	0.028	0.032	0.037	0.036	0.036	0.028
FrCEx N	0.001	0.000	0.001	0.000	0.001	0.001	0.001	0.001	0.001	0.001
FrCEx π	0.007	0.004	0.005	0.004	0.002	0.000	0.001	0.003	0.003	0.003
FrElas N	0.018	0.006	0.015	0.009	0.004	0.024	0.064	0.089	0.089	0.029
FrElas π	0.001	0.000	0.000	0.000	0.001	0.001	0.003	0.003	0.003	0.001
FrInel N	0.002	0.003	0.000	0.000	0.000	0.000	0.000	0.001	0.001	0.001
FrInel π	0.040	0.036	0.034	0.033	0.036	0.038	0.041	0.035	0.034	0.037
FrPiProd N	0.000	0.000	0.000	0.000	0.000	0.001	0.003	0.004	0.006	0.001
FrPiProd π	0.000	0.000	0.000	0.000	0.000	0.000	0.000	0.001	0.001	0.000
Mean Free Path N	0.002	0.004	0.002	0.001	0.003	0.012	0.020	0.039	0.079	0.010
Mean Free Path π	0.003	0.002	0.002	0.002	0.004	0.005	0.005	0.004	0.004	0.003
RDecBR1gamma	0.000	0.000	0.000	0.000	0.000	0.000	0.000	0.000	0.000	0.000
Theta Delta 2Nπ	0.005	0.006	0.007	0.004	0.003	0.002	0.002	0.000	0.000	0.003
Group Total	0.051	0.045	0.045	0.041	0.046	0.059	0.093	0.122	0.137	0.063
Flux										
Flux BeamFocus	0.002	0.002	0.002	0.002	0.001	0.002	0.006	0.006	0.011	0.003
Flux Tertiary	0.003	0.002	0.002	0.000	0.001	0.001	0.009	0.021	0.014	0.005
Flux NA49	0.001	0.001	0.000	0.000	0.000	0.001	0.003	0.002	0.008	0.001
Group Total	0.003	0.002	0.003	0.002	0.001	0.003	0.011	0.022	0.019	0.006
Michel Efficiency	0.002	0.002	0.002	0.002	0.002	0.002	0.001	0.001	0.002	0.002
Pion Reweight	0.003	0.003	0.003	0.003	0.004	0.005	0.007	0.008	0.010	0.005
Target Mass	0.000	0.000	0.000	0.000	0.000	0.000	0.000	0.000	0.000	0.000
Binding Energy	0.003	0.002	0.001	0.001	0.000	0.001	0.003	0.003	0.002	0.002
Group Total	0.004	0.004	0.004	0.004	0.004	0.006	0.007	0.009	0.010	0.005
Total Systematic	0.071	0.068	0.068	0.051	0.054	0.069	0.119	0.168	0.225	0.084
Statistical	0.063	0.042	0.029	0.021	0.020	0.028	0.056	0.093	0.196	0.044
Total	0.096	0.079	0.074	0.055	0.058	0.074	0.132	0.193	0.298	0.095

TABLE A.4: ν fractional systematic uncertainties on $d\sigma/dQ^2_{QE}$, efficiency correction.

$Q^2_{QELike}(GeV^2)$	[0,0.025)	[0.025,0.05)	[0.05,0.1)	[0.1,0.2)	[0.2,0.4)	[0.4,0.8)	[0.8,1.2)	[1.2,2.0)	[2.0,∞)	total
Muon Reconstruction										
Muon Energy	0.040	0.044	0.040	0.023	0.006	0.022	0.061	0.104	0.164	0.043
Muon Theta	0.008	0.001	0.004	0.001	0.000	0.002	0.005	0.003	0.029	0.003
Norm.Correction	0.036	0.036	0.036	0.036	0.035	0.034	0.032	0.031	0.027	0.038
Group Total	0.054	0.056	0.055	0.043	0.036	0.040	0.069	0.109	0.169	0.058
Recoil Reconstruction										
CrossTalk	0.021	0.014	0.012	0.011	0.009	0.007	0.006	0.003	0.001	0.010
EM Response	0.008	0.006	0.005	0.004	0.001	0.001	0.000	0.004	0.005	0.004
High Neutron Response	0.006	0.004	0.003	0.003	0.003	0.005	0.007	0.003	0.003	0.004
Mid Neutron Response	0.001	0.002	0.002	0.002	0.001	0.001	0.003	0.001	0.001	0.001
Low Neutron Response	0.002	0.002	0.002	0.002	0.001	0.002	0.002	0.001	0.000	0.002
MEU	0.006	0.007	0.005	0.004	0.004	0.006	0.012	0.004	0.003	0.006
Muon Response	0.000	0.000	0.000	0.001	0.001	0.002	0.002	0.001	0.000	0.001
Other Response	0.001	0.001	0.001	0.001	0.000	0.000	0.000	0.001	0.001	0.001
Pion Response	0.006	0.001	0.001	0.001	0.001	0.001	0.003	0.000	0.001	0.002
Proton Response	0.002	0.001	0.002	0.005	0.010	0.016	0.016	0.005	0.004	0.007
Group Total	0.025	0.017	0.015	0.014	0.015	0.020	0.023	0.009	0.008	0.017
Primary Interaction Models										
AhtBY	0.000	0.000	0.000	0.000	0.000	0.001	0.002	0.003	0.003	0.001
BhtBY	0.000	0.000	0.000	0.000	0.000	0.001	0.003	0.005	0.005	0.001
CCQEPauliSupViaKF	0.014	0.013	0.022	0.004	0.016	0.005	0.002	0.002	0.002	0.010
CV1uBY	0.000	0.000	0.000	0.000	0.000	0.001	0.002	0.003	0.003	0.001
CV2uBY	0.000	0.000	0.000	0.000	0.000	0.001	0.002	0.003	0.003	0.001
EtaNCEL	0.000	0.000	0.000	0.000	0.000	0.000	0.000	0.000	0.000	0.000
MaCCQEshape	0.002	0.000	0.004	0.003	0.002	0.011	0.016	0.029	0.062	0.008
MaNCEL	0.000	0.000	0.000	0.000	0.000	0.000	0.000	0.000	0.000	0.000
MaRES	0.002	0.002	0.002	0.000	0.002	0.002	0.005	0.012	0.012	0.003
MvRES	0.001	0.001	0.002	0.001	0.000	0.000	0.003	0.005	0.005	0.002
NormCCQE	0.010	0.009	0.008	0.007	0.008	0.010	0.016	0.020	0.020	0.011
NormDISCC	0.000	0.000	0.000	0.000	0.000	0.000	0.000	0.000	0.000	0.000
Rvn1pi	0.002	0.003	0.005	0.006	0.008	0.007	0.004	0.005	0.005	0.005
Rvn2pi	0.002	0.002	0.003	0.005	0.006	0.008	0.012	0.011	0.011	0.006
Rvp1pi	0.001	0.000	0.000	0.000	0.002	0.003	0.003	0.003	0.004	0.001
Rvp2pi	0.002	0.004	0.004	0.005	0.006	0.006	0.008	0.009	0.008	0.006
VecffCCQEshape	0.003	0.005	0.004	0.003	0.005	0.010	0.022	0.031	0.020	0.010
Group Total	0.018	0.017	0.026	0.013	0.022	0.023	0.036	0.051	0.071	0.026
Final State Interactions										
AGKYxF1pi	0.002	0.002	0.002	0.002	0.002	0.003	0.004	0.004	0.004	0.002
FrAbs N	0.011	0.011	0.009	0.004	0.006	0.018	0.045	0.071	0.054	0.022
FrAbs π	0.023	0.023	0.022	0.022	0.028	0.032	0.037	0.036	0.036	0.028
FrCEx N	0.001	0.000	0.000	0.000	0.001	0.001	0.001	0.001	0.002	0.001
FrCEx π	0.007	0.004	0.005	0.004	0.002	0.000	0.001	0.003	0.003	0.003
FrElas N	0.022	0.012	0.012	0.005	0.009	0.028	0.075	0.113	0.094	0.034
FrElas π	0.001	0.000	0.000	0.000	0.001	0.001	0.003	0.003	0.003	0.001
FrInel N	0.002	0.002	0.001	0.000	0.001	0.000	0.000	0.000	0.003	0.001
FrInel π	0.040	0.036	0.034	0.033	0.036	0.038	0.041	0.035	0.034	0.037
FrPiProd N	0.000	0.000	0.000	0.000	0.000	0.001	0.002	0.001	0.003	0.001
FrPiProd π	0.000	0.000	0.000	0.000	0.000	0.000	0.000	0.001	0.001	0.000
Mean Free Path N	0.000	0.005	0.003	0.002	0.005	0.014	0.029	0.041	0.087	0.012
Mean Free Path π	0.003	0.002	0.002	0.002	0.004	0.005	0.005	0.004	0.004	0.003
RDecBR1gamma	0.000	0.000	0.000	0.000	0.000	0.000	0.000	0.000	0.000	0.000
Theta Delta 2Nπ	0.005	0.006	0.007	0.004	0.003	0.002	0.002	0.000	0.000	0.003
Group Total	0.053	0.047	0.044	0.040	0.047	0.062	0.107	0.148	0.147	0.069
Flux										
Flux BeamFocus	0.000	0.001	0.000	0.002	0.005	0.009	0.016	0.020	0.019	0.007
Flux Tertiary	0.003	0.002	0.002	0.002	0.002	0.004	0.012	0.011	0.012	0.005
Flux NA49	0.001	0.000	0.000	0.001	0.002	0.001	0.002	0.005	0.012	0.002
Group Total	0.004	0.002	0.002	0.003	0.006	0.010	0.020	0.023	0.026	0.009
Michel Efficiency	0.000	0.001	0.001	0.001	0.001	0.001	0.001	0.001	0.001	0.001
Pion Reweight	0.003	0.003	0.003	0.003	0.004	0.005	0.007	0.007	0.010	0.004
Target Mass	0.014	0.014	0.014	0.014	0.014	0.014	0.014	0.014	0.016	0.014
Binding Energy	0.003	0.002	0.001	0.001	0.000	0.001	0.003	0.003	0.002	0.002
Group Total	0.014	0.014	0.014	0.014	0.015	0.015	0.016	0.016	0.019	0.015
Total Systematic	0.083	0.079	0.078	0.063	0.067	0.082	0.137	0.193	0.238	0.098
Statistical	0.066	0.044	0.031	0.023	0.022	0.030	0.060	0.100	0.217	0.047
Total	0.106	0.090	0.083	0.067	0.070	0.087	0.150	0.218	0.322	0.109

TABLE A.5: ν fractional systematic uncertainties on $d\sigma/dQ^2_{QE}$, cross-section final result

$Q^2_{QELike}(GeV^2)$	[0,0.025)	[0.025,0.05)	[0.05,0.1)	[0.1,0.2)	[0.2,0.4)	[0.4,0.8)	[0.8,1.2)	[1.2,2.0)	[2.0,∞)	total
Muon Reconstruction										
Muon Energy	0.040	0.044	0.040	0.023	0.006	0.022	0.061	0.104	0.164	0.043
Muon Theta	0.008	0.001	0.004	0.001	0.000	0.002	0.005	0.003	0.029	0.003
Norm.Correction	0.036	0.036	0.036	0.036	0.035	0.034	0.032	0.031	0.027	0.038
Group Total	0.054	0.056	0.055	0.043	0.036	0.040	0.069	0.109	0.169	0.058
Recoil Reconstruction										
CrossTalk	0.021	0.014	0.012	0.011	0.009	0.007	0.006	0.003	0.001	0.010
EM Response	0.008	0.006	0.005	0.004	0.001	0.001	0.000	0.004	0.005	0.004
High Neutron Response	0.006	0.004	0.003	0.003	0.003	0.005	0.007	0.003	0.003	0.004
Mid Neutron Response	0.001	0.002	0.002	0.002	0.001	0.001	0.003	0.001	0.001	0.001
Low Neutron Response	0.002	0.002	0.002	0.002	0.001	0.002	0.002	0.001	0.000	0.002
MEU	0.006	0.007	0.005	0.004	0.004	0.006	0.012	0.004	0.003	0.006
Muon Response	0.000	0.000	0.000	0.001	0.001	0.002	0.002	0.001	0.000	0.001
Other Response	0.001	0.001	0.001	0.001	0.000	0.000	0.000	0.001	0.001	0.001
Pion Response	0.006	0.001	0.001	0.001	0.001	0.001	0.003	0.000	0.001	0.002
Proton Response	0.002	0.001	0.002	0.005	0.010	0.016	0.016	0.005	0.004	0.007
Group Total	0.025	0.017	0.015	0.014	0.015	0.020	0.023	0.009	0.008	0.017
Primary Interaction Models										
AhtBY	0.000	0.000	0.000	0.000	0.000	0.001	0.002	0.003	0.003	0.001
BhtBY	0.000	0.000	0.000	0.000	0.000	0.001	0.003	0.005	0.005	0.001
CCQEPauliSupViaKF	0.014	0.013	0.022	0.004	0.016	0.005	0.002	0.002	0.002	0.010
CV1uBY	0.000	0.000	0.000	0.000	0.000	0.001	0.002	0.003	0.003	0.001
CV2uBY	0.000	0.000	0.000	0.000	0.000	0.001	0.002	0.003	0.003	0.001
EtaNCEL	0.000	0.000	0.000	0.000	0.000	0.000	0.000	0.000	0.000	0.000
MaCCQEshape	0.002	0.000	0.004	0.003	0.002	0.011	0.016	0.029	0.062	0.008
MaNCEL	0.000	0.000	0.000	0.000	0.000	0.000	0.000	0.000	0.000	0.000
MaRES	0.002	0.002	0.002	0.000	0.002	0.002	0.005	0.012	0.012	0.003
MvRES	0.001	0.001	0.002	0.001	0.000	0.000	0.003	0.005	0.005	0.002
NormCCQE	0.010	0.009	0.008	0.007	0.008	0.010	0.016	0.020	0.020	0.011
NormDISCC	0.000	0.000	0.000	0.000	0.000	0.000	0.000	0.000	0.000	0.000
Rvn1pi	0.002	0.003	0.005	0.006	0.008	0.007	0.004	0.005	0.005	0.005
Rvn2pi	0.002	0.002	0.003	0.005	0.006	0.008	0.012	0.011	0.011	0.006
Rvp1pi	0.001	0.000	0.000	0.000	0.002	0.003	0.003	0.003	0.004	0.001
Rvp2pi	0.002	0.004	0.004	0.005	0.006	0.006	0.008	0.009	0.008	0.006
VecffCCQEshape	0.003	0.005	0.004	0.003	0.005	0.010	0.022	0.031	0.020	0.010
Group Total	0.018	0.017	0.026	0.013	0.022	0.023	0.036	0.051	0.071	0.026
Final State Interactions										
AGKYxF1pi	0.002	0.002	0.002	0.002	0.002	0.003	0.004	0.004	0.004	0.002
FrAbs N	0.011	0.011	0.009	0.004	0.006	0.018	0.045	0.071	0.054	0.022
FrAbs π	0.023	0.023	0.022	0.022	0.028	0.032	0.037	0.036	0.036	0.028
FrCEx N	0.001	0.000	0.000	0.000	0.001	0.001	0.001	0.001	0.002	0.001
FrCEx π	0.007	0.004	0.005	0.004	0.002	0.000	0.001	0.003	0.003	0.003
FrElas N	0.022	0.012	0.012	0.005	0.009	0.028	0.075	0.113	0.094	0.034
FrElas π	0.001	0.000	0.000	0.000	0.001	0.001	0.003	0.003	0.003	0.001
FrInel N	0.002	0.002	0.001	0.000	0.001	0.000	0.000	0.000	0.003	0.001
FrInel π	0.040	0.036	0.034	0.033	0.036	0.038	0.041	0.035	0.034	0.037
FrPiProd N	0.000	0.000	0.000	0.000	0.000	0.001	0.002	0.001	0.003	0.001
FrPiProd π	0.000	0.000	0.000	0.000	0.000	0.000	0.000	0.001	0.001	0.000
Mean Free Path N	0.000	0.005	0.003	0.002	0.005	0.014	0.029	0.041	0.087	0.012
Mean Free Path π	0.003	0.002	0.002	0.002	0.004	0.005	0.005	0.004	0.004	0.003
RDecBR1gamma	0.000	0.000	0.000	0.000	0.000	0.000	0.000	0.000	0.000	0.000
Theta Delta 2Nπ	0.005	0.006	0.007	0.004	0.003	0.002	0.002	0.000	0.000	0.003
Group Total	0.053	0.047	0.044	0.040	0.047	0.062	0.107	0.148	0.147	0.069
Flux										
Flux BeamFocus	0.031	0.030	0.031	0.032	0.034	0.038	0.043	0.047	0.047	0.036
Flux Tertiary	0.060	0.059	0.057	0.056	0.056	0.055	0.048	0.049	0.066	0.055
Flux NA49	0.055	0.056	0.056	0.056	0.058	0.057	0.058	0.061	0.070	0.057
Group Total	0.087	0.086	0.085	0.086	0.088	0.088	0.087	0.091	0.107	0.087
Michel Efficiency	0.000	0.001	0.001	0.001	0.001	0.001	0.001	0.001	0.001	0.001
Pion Reweight	0.003	0.003	0.003	0.003	0.004	0.005	0.007	0.007	0.010	0.004
Target Mass	0.014	0.014	0.014	0.014	0.014	0.014	0.014	0.014	0.016	0.014
Binding Energy	0.003	0.002	0.001	0.001	0.000	0.001	0.003	0.003	0.002	0.002
Group Total	0.014	0.014	0.014	0.014	0.015	0.015	0.016	0.016	0.019	0.015
Total Systematic	0.120	0.117	0.115	0.107	0.110	0.119	0.161	0.212	0.259	0.133
Statistical	0.066	0.044	0.031	0.023	0.022	0.030	0.060	0.100	0.217	0.047
Total	0.137	0.125	0.119	0.109	0.112	0.123	0.172	0.235	0.338	0.142

APPENDIX B

The MichelTool Pseudo-code

```
MichelTool(x,y,z,t)
{
  bool found_Michel_candidate = false;
  loop over TimeSlice with time > t
  {
    /**** search stage ****/
    if not found_QC(TimeSlice)
    continue;
    count number_of_views with QC;
    if number_of_views == 1
    {
      sum energy_Michel_prong;
      if energy_Michel_prong > 10
      found_Michel_candidate = true;
      }
    else
    found_Michel_candidate = true;
```

```
    if not found_Michel_candidate
    continue;
    /**** reconstruction stage ****/
    loop over clusters in the TimeSlice
    {
      if not pass_prior_selection
      continue;
      if not pass_reconstruction_selection
      continue;
      add cluster to Michel_prong;
      }
    if Michel_prong not pass_cleaning_selection
        continue;
        return Michel_Prong;
        }
  return 0;
}

found_QC(TimeSlice)
{
  bool found_tight_view = false;
  loop over clusters in the TimeSlice
  {
    if not pass_prior_selection
    continue;
    if pass_tight_selection in any view
    {
      found_tight_view = true;
      loop over clusters in other two views
      {
        if not pass_prior_selection
```

```
        continue;
        pass_loose_selection;
      }
      return found_QC_in_X/U/V_view;
      }
  }
  if not found_in_tight_view
  {
    loop over clusters in the TimeSlice
    {
      if not pass_prior_selection
      continue;
      if pass_moderate_selection
      return found_QC_in_X/U/V_view;
      else
      return 0;
      }
    }
}
```

BIBLIOGRAPHY

[1] G. A. Fiorentini et al. (MINERvA), Phys. Rev. Lett. **111**, 022502 (2013), 1305.2243.

[2] J. D. Devan, Ph.D. thesis, Coll. William and Mary (2015), URL http://lss.fnal.gov/archive/thesis/2000/fermilab-thesis-2015-29.pdf.

[3] J. Beringer et al. (Particle Data Group), Phys. Rev. **D86**, 010001 (2012).

[4] C. Amsler et al. (Particle Data Group) (2008).

[5] Q. R. Ahmad et al. (SNO), Phys. Rev. Lett. **89**, 011301 (2002), nucl-ex/0204008.

[6] J. Chvojka, Ph.D. thesis, University of Rochester (2012).

[7] T. Walton, Ph.D. thesis, Hampton U. (2014), URL http://lss.fnal.gov/archive/thesis/2000/fermilab-thesis-2014-11.shtml.

[8] K. Abe et al. (T2K), Nucl. Instrum. Meth. **A659**, 106 (2011), 1106.1238.

[9] D. S. Ayres et al. (NOvA) (2004), hep-ex/0503053.

[10] L. M. Magro, AIP Conf. Proc. **1743**, 050010 (2016).

[11] G. D., *Introduction to Elementary Particles* (John Wiley and Sons, Inc, 1987).

[12] C. H. Llewellyn Smith, Phys. Rept. **3**, 261 (1972).

[13] A. Bodek, S. Avvakumov, R. Bradford, and H. S. Budd, Eur. Phys. J. **C53**, 349 (2008), 0708.1946.

[14] S. Galster, H. Klein, J. Moritz, K. H. Schmidt, D. Wegener, and J. Bleckwenn, Nucl. Phys. **B32**, 221 (1971).

[15] A. J. R. Puckett, AIP Conf. Proc. **1182**, 925 (2009).

[16] M. L. Goldberger and S. B. Treiman, Phys. Rev. **110**, 1178 (1958).

[17] V. Bernard, L. Elouadrhiri, and U.-G. Meissner, J. Phys. **G28**, R1 (2002), hep-ph/0107088.

[18] R. A. Smith and E. J. Moniz, Nucl. Phys. **B43**, 605 (1972), [Erratum: Nucl. Phys.B101,547(1975)].

[19] A. Bodek and J. L. Ritchie, Phys. Rev. **D23**, 1070 (1981).

[20] J. T. Sobczyk, Phys. Rev. **C86**, 015504 (2012), 1201.3673.

[21] P. A. Rodrigues et al. (MINERvA), Phys. Rev. Lett. **116**, 071802 (2016), 1511.05944.

[22] P. Rodrigues, *Rpa and 2p2h in neutrino carbon interactions*, MINERvA Internal Document Docdb-11338-v6 (2015), URL http://minerva-docdb.fnal.gov:8080/cgi-bin/RetrieveFile?docid=11338&filename=rpamec.pdf&version=6.

[23] L.Fields, *An Analysis of Muon Neutrino Charged Current Quasi-Elastic Interactions*, MINERvA Internal Note (2013), URL http://minerva-docdb.fnal.gov:8080/cgi-bin/RetrieveFile?docid=8716&filename=CCQEAntiNu_TechNote.pdf&version=1.

[24] L. Aliaga Soplin, Ph.D. thesis, William-Mary Coll. (2016), URL http://lss.fnal.gov/archive/thesis/2000/fermilab-thesis-2016-03.pdf.

[25] S. Holmes, R. S. Moore, and V. Shiltsev, JINST **6**, T08001 (2011), 1106.0909.

[26] S. Kopp et al., Nucl. Instrum. Meth. **A568**, 503 (2006), physics/0607229.

[27] Z. Pavlovic, Ph.D. thesis, Texas U. (2008), URL http://lss.fnal.gov/archive/thesis/2000/fermilab-thesis-2008-59.pdf.

[28] P. Adamson et al., Nucl. Instrum. Meth. **A806**, 279 (2016), 1507.06690.

[29] B. G. Tice, Ph.D. thesis, Rutgers U., Piscataway (2014-01), URL http://lss.fnal.gov/archive/thesis/2000/fermilab-thesis-2014-01.pdf.

[30] L. J. Loiacono, Ph.D. thesis, Texas U. (2010), URL http://lss.fnal.gov/cgi-bin/find_paper.pl?thesis-2010-71.

[31] L. Aliaga et al. (MINERvA), Nucl. Instrum. Meth. **A743**, 130 (2014), 1305.5199.

[32] B. M. Eberly, Ph.D. thesis, Pittsburgh U. (2014), URL http://d-scholarship.pitt.edu/20853/.

[33] A. Pla-Dalmau, A. D. Bross, V. V. Rykalin, and B. M. Wood (MINERvA), in *2005 IEEE Nuclear Science Symposium and Medical Imaging Conference El Conquistador Resort, Puerto Rico, October 23-29, 2005* (2005), URL http://lss.fnal.gov/cgi-bin/find_paper.pl?conf-05-506.

[34] G. N. Perdue et al. (MINERvA), Nucl. Instrum. Meth. **A694**, 179 (2012), 1209.1120.

[35] R. Fruhwirth, Nucl. Instrum. Meth. **A262**, 444 (1987).

[36] W. Waltenberger (2008).

[37] D. E. Groom, N. V. Mokhov, and S. I. Striganov, Atom. Data Nucl. Data Tabl. **78**, 183 (2001).

[38] D. E. Groom (2008).

[39] S. Agostinelli et al. (GEANT4), Nucl. Instrum. Meth. **A506**, 250 (2003).

[40] L. Aliaga, *MINERvA Flux: Current Uncertainties And Future Plans*, Flux Measurement and Determination in the Intensity Frontier Era Neutrino Beams Worshop (2012).

[41] R. P. Feynman, R. D. Field, and G. C. Fox, Phys. Rev. **D18**, 3320 (1978).

[42] M. Kordosky et al., *A brief documentation of the flux used in the may 2013 analyses*, MINERvA Internal Note (2013).

[43] C. Alt et al. (NA49), Eur. Phys. J. **C49**, 897 (2007), hep-ex/0606028.

[44] T. Anticic et al. (NA49), Eur. Phys. J. **C68**, 1 (2010), 1004.1889.

[45] B. Baatar et al. (NA49), Eur. Phys. J. **C73**, 2364 (2013), 1207.6520.

[46] D. S. Barton et al., Phys. Rev. **D27**, 2580 (1983).

[47] C. Andreopoulos et al., Nucl. Instrum. Meth. **A614**, 87 (2010), 0905.2517.

[48] R. Bradford, A. Bodek, H. S. Budd, and J. Arrington, Nucl. Phys. Proc. Suppl. **159**, 127 (2006), [,127(2006)], hep-ex/0602017.

[49] S. L. Adler, Phys. Rev. **135**, B963 (1964).

[50] D. Rein and L. M. Sehgal, Annals Phys. **133**, 79 (1981).

[51] A. Bodek and U. K. Yang, in *2nd International Workshop on Neutrino-Nucleus Interactions in the Few GeV Region (NuInt 02) Irvine, California, December 12-15, 2002* (2003), hep-ex/0308007.

[52] L. Alvarez-Ruso et al., *The GENIE Neutrino Monte Carlo Generator: Physics and User Manual* (2013).

[53] J. B. Birks, Proc. Phys. Soc. **A64**, 874 (1951).

[54] C. Caso et al. (Particle Data Group), Eur. Phys. J. **C3**, 1 (1998).

[55] C. Bouchiat and L. Michel, Phys. Rev. **106**, 170 (1957), [,89(1957)].

[56] NIST, *Pysics Measurement Laboratory*, `http://http://physics.nist.gov/cgi-bin/Star/e_table.pl`, [Online; accessed 23-September-2016].

[57] R. Ransome, *strip density discussion*, MINERvA Internal Document Docdb-6016 (2011), URL `http://minerva-docdb.fnal.gov:8080/cgi-bin/ShowDocument?docid=6016`.

[58] L. Fields et al. (MINERvA), Phys. Rev. Lett. **111**, 022501 (2013), `1305.2234`.

[59] E. J. Moniz, I. Sick, R. R. Whitney, J. R. Ficenec, R. D. Kephart, and W. P. Trower, Phys. Rev. Lett. **26**, 445 (1971).

[60] J. W. Van Orden and T. W. Donnelly, Annals Phys. **131**, 451 (1981).

[61] R. J. Barlow and C. Beeston, Comput. Phys. Commun. **77**, 219 (1993).

[62] R. P. Feynman, Phys. Rev. Lett. **23**, 1415 (1969).

[63] J.Wolcott, *Uncertainties due to Feynman scaling of NA49 data to NuMI energy*, MINERvA Internal Note (2013), URL `http://mnvevd1.fnal.gov/Glaucus/web/view_technote.cgi?technote_id=15`.

[64] H.Gallagher, *Summary of minerva estimates of genie systematics*, MINERvA Internal Document Docdb-7578v3 (2012), URL `http://minerva-docdb.fnal.gov:8080/cgi-bin/ShowDocument?docid=7578&version=3`.

[65] S. Dytman, H. Gallagher, and M. Kordosky (2008), `0806.2119`.

[66] D. G. Michael et al. (MINOS), Nucl. Instrum. Meth. **A596**, 190 (2008), 0805.3170.

[67] J. S. Dytman and A. Gago, *Geant4 Hadronic Uncertainties*, http://minerva-docdb.fnal.gov:8080/cgi-bin/RetrieveFile?docid=8249&filename=velasquez-HadronicUncert-nov12.pdf&version=1 (2012), mINERvA Internal Document Docdb-8249.

[68] R.Gran, *Testbeam summer 2012 Pion response figures*, MINERvA Internal Document Docdb-7529 (2012), URL http://minerva-docdb.fnal.gov:8080/cgi-bin/ShowDocument?docid=7529.

[69] R.Gran, *Proton range, birks constant*, MINERvA Internal Document Docdb-8945 (2013), URL http://minerva-docdb.fnal.gov:8080/cgi-bin/ShowDocument?docid=8945&version=1.

[70] B.Eberly, *Charged Pion Update*, MINERvA Internal Document Docdb-9523v1 (2014), URL http://minerva-docdb.fnal.gov:8080/cgi-bin/ShowDocument?docid=9523&version=1.

[71] J. Żmuda, K. M. Graczyk, C. Juszczak, and J. T. Sobczyk, Acta Phys. Polon. **B46**, 2329 (2015), 1510.03268.

VITA

Dun Zhang

Dun Zhang was born on August 8, 1986 in a small village of Lianyungang City, Jiangsu Province, P.R.China. He started to show his curious about math and natural science at early age, especially after he began his formal eduction in his village. In 2000, he entered Donghai Middle school in the same county and graduated as the top student in 2003. In the same year, he joined the University of Science and Technology of China in Hefei City, Anhui Province, which is 10-hour-driving away from his hometown, and chose physics as his major, focusing on the theoretical part. He enjoyed his undergraduate research project, which was about the Quantum Game Theory. In 2007, he continued his graduate study in the Department of Physics of the College of William and Mary in Williamsburg, Virginia and received a Master of Science in physics in two years. Then he joined the high energy physics research group and was supervised by Professor Mike Kordosky. During 2011 and 2012, he was based at Fermi National Accelerator Laboratory in Batavia, Illinois and conducted his research on an experiment named MINERνA. He contributed to the experiment in many ways, such as tuning the threshold of discriminators, maintaining FEBs database, modeling afterpulsing, and some hardware repairing duty. His work in developing a tool to tag Michel electrons benefits collaborators and improves the measurement of differential cross-sections. After graduation, he will keep curious about physics all the time.